Experimental Apparatus for Quantum Pumping with a Bose-Einstein Condensate

Megan K. Ivory

Sidman, Pennsylvania

Master of Science, College of William and Mary, 2009
Bachelor of Science, Saint Vincent College, 2007

A Dissertation presented to the Graduate Faculty
of the College of William and Mary in Candidacy for the Degree of
Doctor of Philosophy

Department of Physics

The College of William and Mary
January 2016

APPROVAL PAGE

This Dissertation is submitted in partial fulfillment of
the requirements for the degree of

Doctor of Philosophy

_____
Megan K. Ivory

Approved by the Committee, September, 2015

_____
Committee Chair
Associate Professor Seth Aubin, Physics
The College of William and Mary

_____
Professor John B. Delos, Physics
The College of William and Mary

_____
Associate Professor Irina Novikova, Physics
The College of William and Mary

_____
Professor William Cooke, Physics
The College of William and Mary

_____
Professor Kunal Das, Physics
Kutztown University

ABSTRACT

Quantum pumping is a method of transporting particles through a circuit without an external applied voltage or chemical potential, but instead with localized time-varying potentials. Ballistic quantum pumping has been theorized in mesoscopic solid state systems, but experimental verifications have been challenging due to the capacitive coupling and rectification inherent to electronic systems. Using ultracold neutral atoms to test and verify the theoretical predictions of quantum pumping reduces these challenges while providing the advantages of easy confinement and manipulation, a high degree of coherence, and bosons as well as fermions. In addition, ultracold atoms allow smooth tunability between classical thermal gases and quantum gases. Here, we design, build, characterize, and optimize a dual-species experimental apparatus capable of quantum pumping experiments with Bose-Einstein condensates on an atom chip. We produce quasi-pure ^{87}Rb Bose-Einstein condensates of $\approx 10^4$ atoms and successfully laser-cool ^{39}K. We lay the experimental groundwork for quantum pumping experiments with ultracold atoms and characterize the classical dynamics of the system. These classical dynamics are supported with theoretical modeling that we have developed to compare the dramatic differences between the classical and quantum results of a double barrier turnstile pump as well as its single barrier building blocks.

TABLE OF CONTENTS

iv

ACKNOWLEDGMENTS

To Callao, who teaches me daily what it means to be brave and to love unconditionally.

LIST OF TABLES

LIST OF FIGURES

x

EXPERIMENTAL APPARATUS FOR QUANTUM PUMPING WITH A

BOSE-EINSTEIN CONDENSATE

CHAPTER 1

Introduction

Electric current is the backbone of the thriving electronics industry and an area of intense research in condensed matter physics. One active study is the flow of charge between two reservoirs due to a localized, time-dependent potential or *pump* within a wire [1, 2] rather than an applied voltage bias. There is particular interest in exploiting the quantum effects of such a pump to produce highly controlled, reversible, and coherent electron transport in mesoscopic systems, potentially on the level of a single-electron [3, 4]. Such an adiabatic or ballistic *quantum pump* was first proposed by Thouless in 1983 as a way of creating electric current. Despite some recent experimental success with non-adiabatic quantum pumps the adiabatic or ballistic quantum pumps have met significant experimental challenges in the forms of spurious capacitive coupling and rectification effects [5, 6, 7].

This thesis describes the first steps in developing an alternative method of exploring and verifying biasless pumping based on ultracold neutral atoms rather than electrons. The utilization of neutral atoms has a number of advantages over the electron counterparts. First, it eliminates electromagnetic interactions which often mask the quantum pumping

signatures in electronic configurations. Second, it allows one to tune between classical and quantum regimes such that one can understand the fully classical effects and therefore distinguish the fully quantum features of pumping. In addition, ultracold atoms are easily confined in 1D to 3D potentials, controlled and manipulated with laser and magnetic fields, and have tunable interactions, allowing them to mimic their electronic counterparts. They also display a high degree of coherence, are available in both bosonic and fermionic species, and can be tuned in energy, momentum, and position for spectroscopically probing these dependencies.

A schematic for exploring quantum pumping with ultracold atoms is shown in Figure 1.1. The basic setup consists of two reservoirs of ultracold atoms connected by a 1D potential. In the center of the 1D channel potential, the localized pump is created with a dynamically varied potential, shown here as two repulsive Gaussian potentials. The atoms are launched towards the pump with an initial momentum, and a current is measured as an imbalance in the final number of atoms in each reservoir.
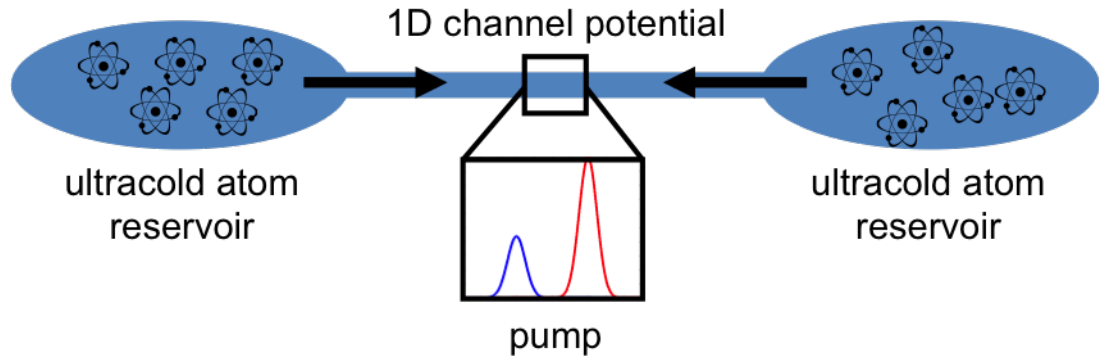
FIG. 1.1: Quantum pumping of ultracold atoms. The basic pumping setup consists of two reservoirs of ultracold atoms connected by a 1D channel potential. Atoms in each reservoir are launched towards the pump with an initial momentum. The pump, for example the double barrier turnstile pump, is a localized potential between the two reservoirs that is dynamically varied in time to create a current without a difference in potential between the reservoirs.

In this thesis, we perform a detailed theoretical study of the classical effects in a

particular pump referred to as the turnstile pump. In addition, we prepare the key elements of an experimental apparatus with neutral ultracold atoms for testing these theoretical predictions and modeling quantum pumping in the future. To do so, we have built an apparatus dedicated to the study of quantum gases and demonstrated the production of Bose-Einstein condensates (BEC) of ^{87}Rb.

1.1   Background and history

While the classical effects of pumping can be studied with a thermal cloud of atoms, phase coherence is essential for observing quantum effects. BECs are coherent macroscopic quantum states first theorized in 1924 by Bose and Einstein and eponymously termed [8, 9, 10]. At that time, physicists had just begun to understand the quantum statistical differences between integer spin particles (bosons) and half integer spin particles (fermions). While Fermi statistics and the Pauli exclusion principle forbid fermions from occupying the same state when cooled, Einstein's theory supposed that an ultracold gas of bosons would condense into the same lowest energy state. This phase transition to condensation occurs at extremely low temperatures and has the advantage of forming a cloud of atoms which all share the same wavefunction. This 'superatom' is both macroscopic and quantum mechanical, providing for the first time a window for probing the nature of quantum mechanics with a macroscopic number of atoms.

Despite its early theoretical development, it was not until 1995 that physicists demonstrated BEC in a laboratory. Indeed, the 2001 Nobel Prize in physics was awarded to Eric Cornell, Carl Weiman, and Wolfgang Ketterle for the experimental realization of a BEC of rubidium and sodium atoms [11, 12]. These first demonstrations (and two decades worth of demonstrations that follow) were only made possible by several preceding advances and breakthroughs in laser development, atom cooling and trapping techniques, and ultrahigh

vacuum (UHV) methods.

Cooling an atom to its ground state first requires complete isolation from its environment so as to minimize the heating caused by collisions with background gases. This is only possible in a UHV environment, typically requiring pressures below 10^{-10} Torr. Modern vacuum technology includes roughing pumps, turbo pumps, ion pumps, titanium sublimation pumps, gettering materials, and cleaning and vacuum processing techniques which make UHV a relatively straightforward engineering task rather than a physics problem.

Once in a vacuum apparatus, atoms are cooled using a technique called laser cooling. This method relies upon the development of narrow linewidth lasers which are used to address an energy transition between the ground and excited states of an atom. This breakthrough technique of laser cooing was demonstrated first in ions in 1978 [13, 14] and later in neutral atoms in 1985 by William Phillips [15] and Steven Chu [16], for which they along with Claude Cohen-Tannoudji were awarded the 1997 Nobel Prize in physics [17]. With this technique, atoms can be cooled to temperatures as low as $10 - 100\mu$K, corresponding to velocities in the range of $\approx$ 1-100 cm/s depending on the atomic mass [16]. Finally, the laser-cooled neutral atoms are moving slow enough to trap.

Cold atoms can be trapped with both optical and magnetic traps. Optical traps take the form of far-detuned dipole traps such as those used in optical tweezers experiments [18] or optical lattices produced by standing light fields [19]. The earliest conservative neutral atom traps were magnetic traps produced with current-carrying coils which form magnetic field minima. Magnetic traps function on the simple basis of low-field seeking Zeeman energy levels. They were discussed as early as the 1950's, with hints of experimental demonstration by 1975 [20]. While many BEC experiments still rely on the early magnetic trap configurations, there is a growing community of physicists developing BEC-producing apparatuses based on relatively new 'atom chip' technology [21, 22, 23, 24, 25]. Atom chips are substrates, typically silicon or aluminum nitride, with copper or gold wires

imprinted on the surface using standard photo lithography techniques. By passing currents through the wires, one can produce compact magnetic fields at a distance from the surface of the chip where cold atoms can be trapped. Traps produced with the chip fields are more tightly confined than their coil counterparts, leading to higher collision rates, lower rethermalization times, and generally more efficient evaporation to BEC. In addition, chip-based apparatuses are compelling choices for application development due to their potential for miniaturization.

1.2 Applications

Applications for ultracold atoms range from precision sensing and timekeeping to quantum information to simulating otherwise intractable models of solid state many-body systems. Ultracold atoms have also been elemental in some of the world's most sensitive gyroscopes, magnetic gradiometers, and gravity gradiometers [26, 27, 28]. This is due to the coherence of ultracold atoms and their small deBroglie wavelength. The atoms within a Bose-Einstein condensate are coherent with one another, meaning they share a common phase, similar to photons in a laser. With coherent atoms, one can begin to explore applications previously developed only with coherent light, such as interferometry. Light interferometers split a coherent wave of light along two paths and then recombine them. The interference pattern of the light after recombination gives the user information about the path differences. With coherent atoms acting as deBroglie waves, this same concept can be applied to measure a large breadth of interactions due to the high sensitivity of the atoms. For example, atoms are sensitive to gravitational fields, electric fields, magnetic fields, and a host of other fields and corresponding forces. In addition, the deBroglie wavelength of cold atoms is tens of thousands of times smaller than optical wavelengths making them inherently more precise sensors than their optical wave counterparts.

Cold atoms are also the basis of today's most precise atomic clocks. When one considers that the energy spacing between levels in an atom corresponds to a frequency, it is easy to see how each individual atom acts as a oscillator. The identical atomic structure from one atom to the next makes every atom (of the same species) oscillate at the exact same frequency. When isolated from environmental fluctuations and collisions and when cooled below the Doppler temperature, the frequency or time associated with these natural oscillations between energy levels can be measured very precisely. To date, the most precise and accurate atomic clocks in the world are laser-cooled neutral atoms held in optical lattices and operating on optical transitions (10^{15} oscillations each second) [29, 30]. These clocks operate with a precision on the order of a part in 10^{18}, meaning they lose a second only once in every 5 billions years or so.

The energy splitting between ground and excited state and the ability to accurately control state preparation and manipulation in cold atoms is also the basis of several quantum information efforts in recent years [31, 32, 33]. In such experiments, a quantum bit of information or qubit can be represented by a two-level system. A longer coherence time in ultracold atoms means quantum information stored in the atom is preserved longer, allowing more time for memory, processing, and read-out.

Perhaps the most appropriate and compelling application of ultracold atoms in the context of this thesis is the modeling of solid state systems. Ultracold atoms have already been used to study challenging condensed matter physics phenomena and theories such as superfluidity, the Bose-Hubbard model, Mott insulators, and superconductivity [34, 35, 36, 37]. Atoms confined in optical lattices form perfect crystals with easily tuned parameters that are otherwise fixed and imperfect in their solid crystal counterparts. This makes them ideal for modeling and exploring elusive or difficult physical concepts in solid state systems, such as the concept of quantum pumping described above.

1.3　Structure of the thesis

Here I present the design, construction, optimization, and performance of a dual-species apparatus built literally from the ground up for rubidium and potassium ultracold atom experiments on a chip. This apparatus has been developed for (among other things) the experimental demonstration of the classical and quantum features of quantum pumping – a mesoscopic transport mechanism. For the work in this thesis, I present the theoretical findings of the classical aspects of pumping, while demonstrating cooling of atoms to Bose-Einstein condensate on an atom chip, and laying the groundwork for future experiments in quantum pumping. The use of an atom chip for the final trapping and evaporation to BEC makes this apparatus potentially miniaturizable to integrated chip-scale devices, making the realization of deployable application solutions a conceivable goal.

The work presented in this thesis has resulted in the following publications:

1. M. K. Ivory, et al., "Ballistic atom pumps",Phys. Rev. A90, 023602 (2014).

2. M. K. Ivory, et al., "Atom chip apparatus for experiments with ultracold rubidium and potassium gases",Rev. Sci. Instrum.85, 043102 (2014).

3. C. Chen, M. K. Ivory, et al., "Dynamical Monodromy",Phys. Rev. E89, 012919 (2014).

4. T. A. Byrd, M. K. Ivory, et al.,"Scattering by an oscillating barrier: quantum, classical, and semiclassical comparison",Phys. Rev. A86, 013622 (2012).

5. S. Martinez, L. Hernandez, D. Reyes, E. Gomez, M. Ivory, C. Davison, and S. Aubin, "Note: Fast, small, and low vibration mechanical laser shutters",Rev. Sci. Instrum.82, 046102 (2011).

This thesis is structured as follows. In Chapter 2, I introduce the relevant theoretical background needed for trapping and cooling a cloud of atoms to quantum degeneracy.

In Chapter 3, I discuss optical dipole traps and optical lattices. Chapter 4 describes the design, construction, operation, and performance of the experimental apparatus, with emphasis on the components and demonstrations in which I played a significant role. Chapter 5 covers the final cooling stage and achievement of BEC in the Aubin lab. Chapter 6 is a thorough discussion of the classical features of scattering from single and double oscillating rectangular and Gaussian barriers necessary for understanding the classical and quantum features of quantum pumping. In Chapter 7, I describe the experimental infrastructure for a simple demonstration of classical scattering in a scheme we call "The Discriminator". Finally, I conclude with an outlook towards improving the experimental demonstration of quantum pumping.

CHAPTER 2

Ultracold atom theory

2.1   Introduction

As described in the previous chapter, Bose-Einstein condensates (BECs) make possible a number of advanced sensing, timekeeping, and navigational applications in which quantum mechanics can provide advantages over classical physics approaches. BEC is its own state of matter, which occurs as a phase transition when the atomic phase space density–i.e. density distribution in both momentum or temperature and position) reaches a critical value. Therefore, the phase transition occurs at some related temperature and peak atom number density given by the phase space density (PSD):

$$PSD = n\lambda_{dB}^3 \tag{2.1}$$

where n is the atom density and λ_{dB} is the thermal deBroglie wavelength. When the deBroglie wavelength approaches the length scale of the atomic separation in the cloud, a condensate will begin to form amidst the surrounding thermal atoms. This transition

occurs when PSD $\gtrsim 2.612$.

The advent of laser cooling made Bose-Einstein condensates an achievable goal in alkali atoms. 3D laser cooling of neutral atoms was first demonstrated in 1985 by Phillips and Chu [15, 16]. This method of laser cooling was soon paired with a confining magnetic field to produce the first magneto-optical trap in 1987 by Chu and Pritchard [38]. Due to physical limitations on the achievable temperatures using optical cooling techniques (primarily the recoil limit), a number of magnetic trapping techniques were explored. These included quadrupole traps using anti-Helmholtz coils, which were the first magnetic traps to confine neutral atoms [39]. However, the zero-crossing of the magnetic field is problematic for achieving BEC, as the undefined quantization axis at the zero-crossing leads to severe Majorana losses [40]. As a solution, Ioffe-Pritchard traps offer magnetic confinement without a zero-crossing. Ioffe-Pritchard traps have been produced in both macroscopic coil assemblies [41, 42] and microfabricated atom chips [21, 22, 23, 24, 25]. The final cooling stage in most BEC experiments is evaporative cooling, which was first demonstrated by both Cornell and Ketterle in 1994 [43, 44] and utilized for the first demonstration of BEC by Cornell and Weiman in 1995 in ^{87}Rb [45].

In this chapter, I describe the theoretical background for the various stages of cooling and trapping employed for achieving BEC in the Aubin Lab. Creating an ultracold quantum degenerate gas in our system is a multi-step process involving laser cooling in a magneto-optical trap (MOT), optical molasses, transfer to a magnetic trap after optical pumping, a magnetic transport sequence, and finally evaporative cooling in a chip-produced magnetic trap. The basic steps which we describe in the following sections are:

1. Magneto-optical trapping,

2. Optical molasses or polarization gradient cooling,

3. Magnetic trapping,

4. Optical pumping,

5. Atom chip trapping,

6. RF evaporative cooling,

7. Imaging, and

8. Temperature and atom number measurements.

Steps 1-6 are steps towards cold atom preparation, while steps 7 and 8 are destructive diagnostic techniques.

For reference, the atomic structure of ^{87}Rb and ^{39}K atoms can be found in Figures 2.1 and 2.2 [46, 47]. In addition, several relevant constants that will be introduced in this chapter are summarized in Table 2.1 [46, 47]. Throughout this thesis, we refer to the ground levels (nS$_{1/2}$) by F and the excited levels (nP$_{3/2}$) by F'.

TABLE 2.1: ^{87}Rb and ^{39}K constants.

	Symbol	^{87}Rb Value	^{39}K Value	Units
Linewidth	$\Gamma/2\pi$	6.065	6.035	MHz
Saturation Intensity	I_{sat}	1.67	1.75	mW/cm^2
Resonance Cross Section	σ_0	0.29	0.28	μm^2
Wavelength	λ	780.241	766.701	nm
Doppler Temperature	T_D	146	145	μK

2.2   Magneto-optical trapping

As its name suggests, this first cooling step requires both magnetic and optical fields. The "optical" refers to the process of laser cooling. The "magneto" refers to an external magnetic quadrupole field that spatially controls the strength of the optical force. Each of these concepts is explored in more detail in the subsections that follow.
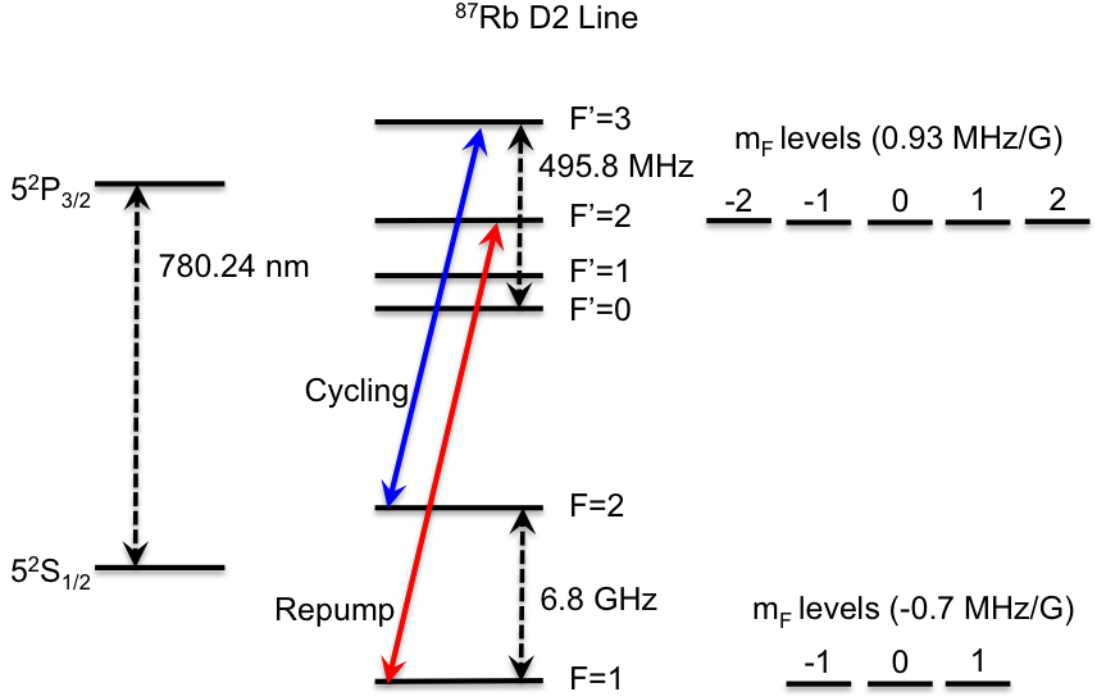
FIG. 2.1: ^{87}Rb D2 line energy diagram. The D2 line of ^{87}Rb is shown above with hyperfine levels. The cycling (cooling) and repumping transitions are shown in blue and red, respectively. The Zeeman levels and splittings of the F=1 and F'=2 hyperfine levels are also shown.

2.2.1 Laser cooling

When it comes to laser cooling, atomic physicists primarily choose alkali atoms (left-most column of the periodic table), and have only recently been branching out to other more exotic elements such as strontium [48], ytterbium [49], chromium [50], dysprosium [51], etc. The reason for this is the single valence electron in the alkali atoms: The D2-line level structure of these atoms can be well-approximated as a two-level system, making these atoms well suited for laser cooling techniques. The basic principle of laser cooling [52] relies on atomic absorption of a photon from a laser beam and the associated momentum kick from that photon absorption. We begin with a two-level atom with resonant frequency $\omega_0 = \frac{E_0}{\hbar}$, where E_0 is the energy difference between the ground
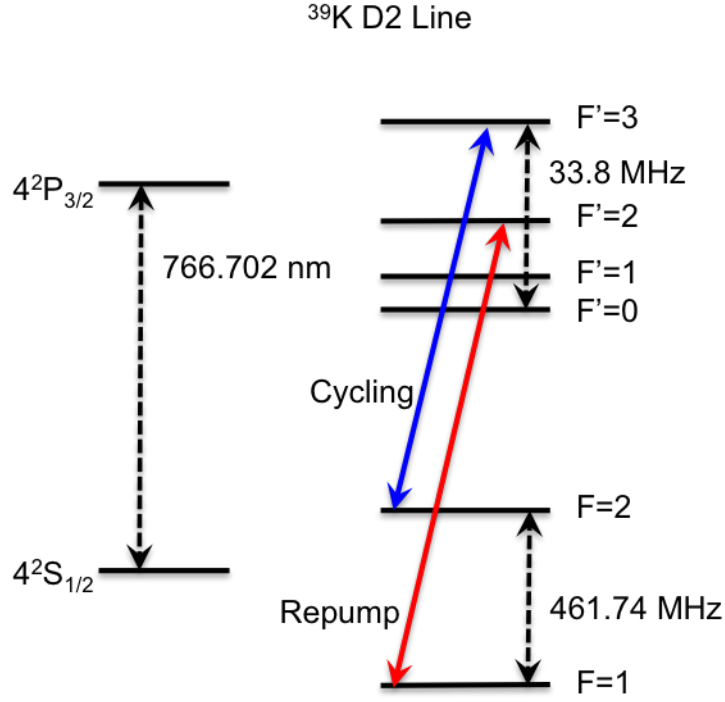
FIG. 2.2: ^{39}K D2 line energy diagram. The D2 line of ^{39}K is shown above with hyperfine levels. The cycling (cooling) and repumping transitions are shown in blue and red, respectively.

and excited states and $\hbar$ is Planck's constant. If a laser beam that is slightly red-detuned (a few linewidths) from ω_0 is pointed towards a moving atom such that the atom and the photons are moving in opposite directions, the laser beam will appear Doppler shifted closer to resonance in the frame of the atom (see Figure 2.3). For this reason, laser cooling is also known as Doppler cooling. With the laser beam appearing closer to resonance, the atom will be more likely to absorb a photon and receive a momentum kick that opposes the original velocity of the atom. The photon is then re-emitted in a random direction. Meanwhile, the red-detuned laser beam propagating along the same direction as a moving atom will appear Doppler shifted even further from resonance (more red-detuned) and becomes less likely to be absorbed. The overall effect is that the atom will slow down,

thereby losing energy and effectively becoming cooler.
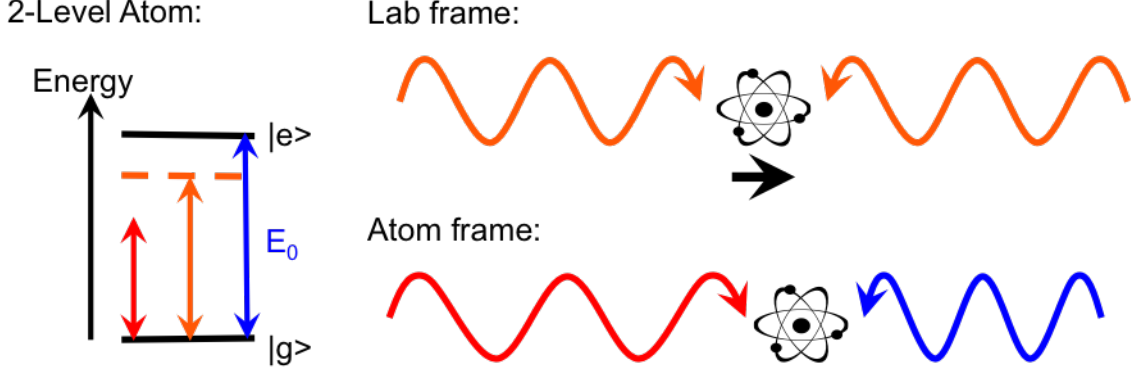
FIG. 2.3: Doppler cooling. In the basic Doppler cooling description, we assume a 2-level atom with ground and excited states separated by an on-resonant energy $E_0 = \hbar\omega_0$ (blue). By applying a red-detuned laser beam (orange), the frequency appears shifted towards (away from) resonance for atoms moving toward (away from) the propagating beam in the frame of the atom due to the Doppler shift.

Laser cooling is applied using six counter-propagating beams (two along each of three spatial axes), producing cooling in all three dimensions. The process is Doppler limited, meaning it is limited by the natural linewidth of the atomic transition. In the case of ^{87}Rb, the width of the D2 atomic transition is $\Gamma/2\pi = 6$ MHz wide (see Table 2.1). Therefore, laser cooling can cool rubidium atoms from room temperature to $T_D = \frac{\hbar\Gamma}{4\pi k_B} = 146$ μK.

In our experiment we use the F=2 to F'=3 cycling transition to cool our atoms. While this is mostly a closed transition, there is a small chance that atoms will be excited off-resonantly to the F'=2 level. In this case, atoms can decay into the F=1 level, which is "dark" since those atoms will not scatter cooling light. With only the cooling laser, these atoms would be lost. For this reason, we also employ a repump beam in our MOT between the F=1 to F'=2 transition to extract atoms from the F=1 dark level and put them back in the F=2 level via the F'=2→F=2 decay channel.

2.2.2 Spatial confinement with a magnetic field

To produce a MOT, laser cooling beams are overlapped with a weak, spatially-dependent magnetic field, allowing the atoms to be spatially confined as well as cooled. This combined magnetic confinement and optical cooling is known as the MOT. Typically, MOTs are capable of reaching temperatures on the order of 100 μK and phase space densities on the order of 10^{-6}.

The magnetic field is produced with two coils in anti-Helmholtz configuration along one of the cooling axes. The coil geometry produces a spatial magnetic gradient that is quadrupole in nature. That is, it is zero at the center with a linear non-zero field elsewhere. This field Zeeman shifts the atomic hyperfine levels as shown in Figure 2.4.
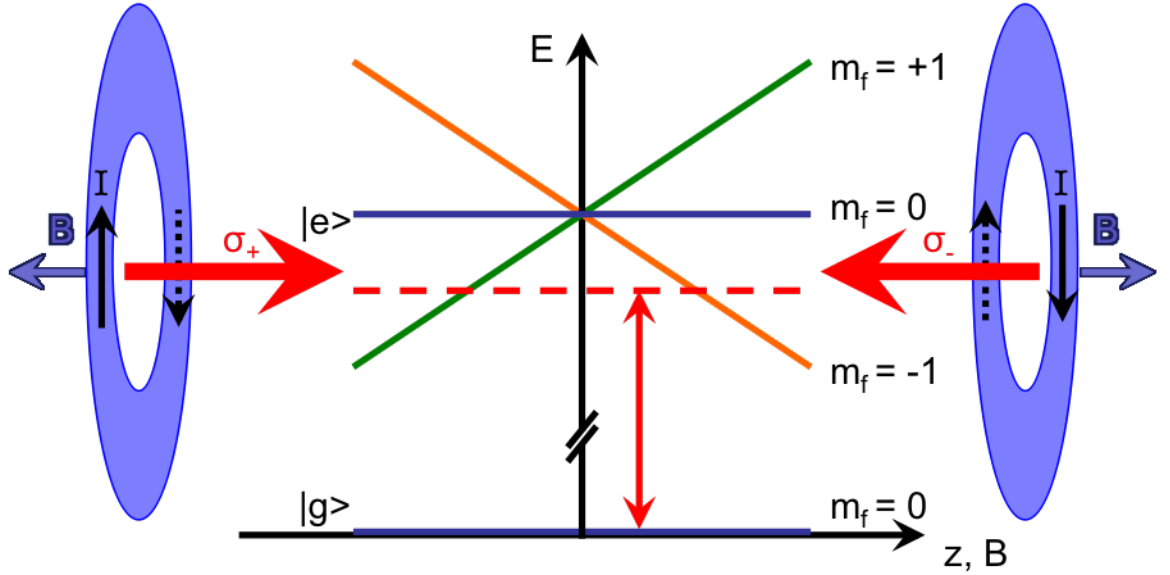
FIG. 2.4: Magnetic confinement in a MOT. The presence of the magnetic field causes the Zeeman levels to split. This, coupled with the laser detuning, causes atoms with $m_f = -1$ on the right to preferentially absorb the σ_- beam, getting a kick towards the trap center, and atoms with $m_f = +1$ on the left to preferentially absorb the σ_+ beam.

Figure 2.4 shows the Zeeman shifts in the presence of a quadrupole magnetic field.

The $m_F = -1$ level (in orange) is shifted to a lower energy on the right-hand side of the cartoon and to a higher energy on the left-hand side of the cartoon. It is important that the counter-propagating laser beams along this axis have opposite handed circular polarization with respect to the +z-axis (however, they have some polarization helicity). If the polarizations are chosen appropriately with respect to the direction of the current through the coils, an atom at rest on the right-hand side of the cartoon will preferentially absorb the beam with σ^-−polarization. This is because the $m_F = -1$ level is shifted closer to resonance of the beam. The momentum kick associated with this absorption creates a restoring force back towards the zero position. An atom at rest on the left-hand side of the cartoon experiences a similar restoring force towards the zero position due to its tendency to absorb the σ^+−polarization beam. The magnetic quadrupole field does not confine the atom on its own, but instead tunes the optical force, thus giving it a spatial dependence.

2.3 Optical molasses

The presence of polarized light fields has additional cooling advantages when the magnetic gradient is absent. This was recognized early on in laser cooling experiments when researchers unexpectedly and inexplicably reached temperatures well below the Doppler limit [16]. This fortunate phenomena arises from the fact that our atoms are not in fact strictly two-level atoms. The hyperfine structure advantageously complicates our previous picture.

Here we consider the case of two counter-propagating beams with orthogonal linear polarizations (lin ⊥ lin). The resulting polarization of the standing wave produced by the overlapping beams varies spatially as shown in Figure 2.5: The electric field polarization alternates between left and right circularly polarization. The light field shifts the hyperfine atomic levels depending on the polarization via the AC Stark effect. In the cartoon, an

atom beginning in the $m_F = -1/2$ level at z = 0 will climb the AC Stark potential with its initial kinetic energy. When it has traveled a quarter wave, the field is σ^+-polarized and the atom is preferentially pumped to the $m_F = +1/2$ level. From here, if the atom's remaining kinetic energy is sufficient, it will climb the next quarter wave hill until the field becomes σ^--polarized and it is pumped back to the $m_F = -1/2$ level. This continues until the atom no longer has sufficient kinetic energy travel up the optical "hill". This sub-Doppler cooling phenomenon is broadly known as Sisyphus cooling, and is included in optical molasses and polarization gradient cooling mechanisms. The experiments described in this thesis utilize a sub-Doppler cooling scheme similar to the one described above using two counter-propagating beams with orthogonal circular polarizations in our molasses stage.

Employing optical molasses can decrease temperatures in the atom cloud to the order of 5-30 μK or so. Importantly, the local magnetic field must be reduced to zero, so that the polarization gradient AC Stark effect is the dominant energy shift seen by the atoms. Optical molasses cooling can increase the PSD of the atoms to the $10^{-5} - 10^{-6}$ range. In order to go colder in temperature and to higher PSD, evaporative cooling in a conservative magnetic trap must be employed.

2.4   Magnetic trapping

In the description of the MOT above, a weak magnetic field gradient is used to help confine atoms undergoing laser cooling to a region centered around the magnetic zero. For certain hyperfine states, magnetic field gradients can also be used without the presence of an optical field to hold atoms against gravity and trap them. A common way to do this is to use the anti-Helmholtz coils of the MOT operating at a gradient strong enough to counter gravity. The field produced by a pair of anti-Helmholtz coils oriented along the
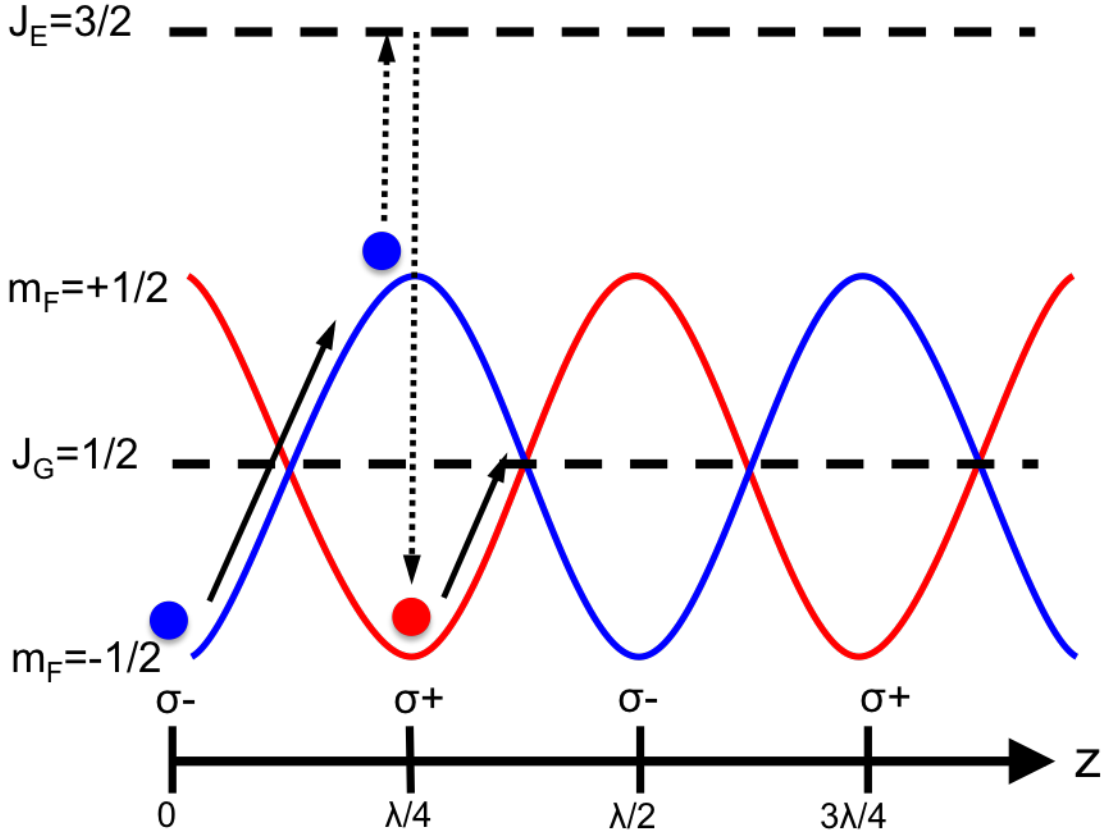
FIG. 2.5: Sisyphus cooling. The spatial variation of the polarization leads to an additional cooling effect known as Sisyphus cooling. An atom beginning in the $m_F = -1/2$ level at the origin travels up the AC Stark potential hill. At the top, the overall polarization is now $\sigma+$ and the atom is pumped preferentially into the $m_F = +1/2$ level at the bottom of a hill. This process repeats until the atom no longer has sufficient kinetic energy to travel up the hill.

z-axis to first order is given by:

$$\vec{B} = B'(\frac{x}{2}\hat{x} + \frac{y}{2}\hat{y} - z\hat{z}) \tag{2.2}$$

where x, y, and z, are positions along the three axes $\hat{x}, \hat{y}$, and $\hat{z}$, respectively, and B' is the magnetic field gradient along the strong (z-) axis. The potential due to a magnetic field,

as seen by an atom with mass m and magnetic moment μ, is

$$U_{Zeeman} = -\vec{\mu} \cdot \vec{B} = m_F g_F \mu_B |\vec{B}|. \tag{2.3}$$

Here, g_F is the hyperfine Landé g-factor, μ_B is the Bohr magneton, and m_F is the magnetic quantum number. We seek to magnetically trap ^{87}Rb and ^{39}K atoms in the $|$F=2,m$_F$=2$\rangle$ ground state where $g_F = 1/2$. To do so, the magnetic gradient B' must be greater than mg/μ_B = 15.36 G/cm in the direction of gravity (g=9.8 m/s^2). In our case, gravity is along a weak axis of the anti-Helmholtz coils. Therefore, we require B' larger than 30.72 G/cm to hold atoms against gravity. For sufficiently strong gradients, the $|$F=2,m$_F$=1$\rangle$ and $|$F=1,m$_F$=-1$\rangle$ states are also trappable.

2.4.1 Optical pumping

The presence of the magnetic field also breaks the degeneracy of the Zeeman sublevels: For ^{87}Rb atoms in the $F = 2$ level, there are 5 Zeeman states. Therefore, in order to trap as many atoms as possible, we apply a pumping pulse prior to turning on the magnetic trap in order to pump the atoms into the desired trapped state. We call this optical pumping because it is done with a short optical pulse of light directed along a quantization axis created by a magnetic field, and it pumps the atoms preferentially into the $|$F=2,m$_F$=2$\rangle$ ground state. The optical pumping pulse is produced with a single circularly polarized beam. Due to the selection rules, an atom absorbing $\sigma+$ light will undergo a transition with $\Delta m_F = +1$, and an atom absorbing $\sigma-$ light will undergo a transition with $\Delta m_F = -1$. The atom can undergo spontaneous emission transitions with $\Delta m_F = -1, 0$, or $+1$. The net result is that atoms accumulate in the highest positive (lowest negative) m_F level for $\sigma+$ ($\sigma-$) light. Because of this, optical pumping is a sort of internal state cooling – it reduces the entropy of the atoms by placing them in the same

19

internal state. A cartoon showing the allowable transitions for the F=2 to F'=2 levels of ^{87}Rb is shown in Figure 2.6.
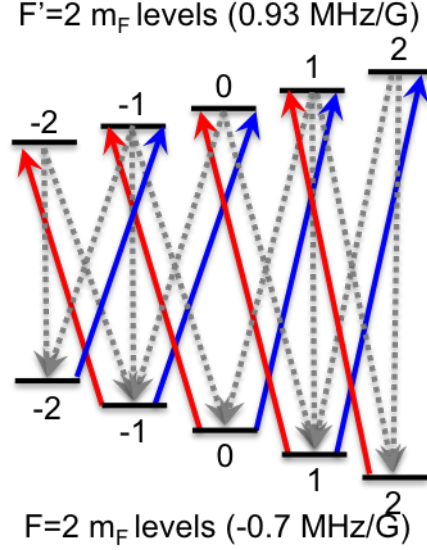
FIG. 2.6: Optical pumping. The F=2 and F'=2 Zeeman levels are shown for ^{87}Rb. The red (blue) lines show allowable excitations for light, while gray dashed lines show allowable decays. For $\sigma-$ light, atoms will accumulate in the $|F=2, m_F=-2\rangle$ level. For $\sigma+$ light, atoms will accumulate in the $|F=2, m_F=2\rangle$ level.

We pump our atoms to the $|F=2, m_F=2\rangle$ state. The 30 G/cm field is sufficient to hold these atoms against gravity, but is not sufficient to hold $|F=2, m_F=+1\rangle$ or $|F=2, m_F=-1\rangle$ atoms. This allows us to distill the spins and produce a pure spin-polarized cloud of ^{87}Rb atoms.

2.4.2 Magnetic transport

Once in the magnetic trap, atoms can be transported between locations using a series of magnetic quadrupole traps. Our magnetic transport system consists of 7 pairs of overlapping anti-Helmholtz coils in an L-shape path covering a distance of about 60 cm between the MOT region and the second vacuum chamber containing the atom chip. By

carefully ramping the currents in the 7 coil pairs, one can create a moving magnetic trap so as to translate the atoms. Three coil pairs are powered at any given time to ensure that the trap keeps its shape (gradient and aspect ratio) throughout the translation process [53, 21, 54].

We use this method to transport the atoms from the MOT region of the vacuum apparatus to the science region. The transport process produces little heating and atomic population loss (beyond vacuum lifetime losses). At the end of the sequence, we ramp down the transport magnetic fields while simultaneously ramping on the atom chip magnetic fields to load the atoms onto the atom chip.

2.5   Atom chip trapping

The atom chip is a silicon wafer with a lithographically deposited copper wire pattern. The large trapping frequencies produced by the atom chip trap lead to higher collision rates and shorter rethermalization times than their larger-scale optical and magnetic trap counterparts, leading to shorter evaporation times and lowering the trap lifetime requirements. (Though recently, hybrid magnetic optical traps have produced fast evaporation times as well [55].) By running current through wires on a chip and applying an external magnetic bias field, one can create a harmonic magnetic trap located hundreds of microns below the chip with very tight confinement. The particular chip we are working with contains a Z-wire trap (see Figure 2.7 and 2.8). The current through the center portion of the Z creates a magnetic field directly below the wire that is in the plane of the chip but perpendicular to the wire. Adding an external magnetic bias field (B_{Hold}) in the direction opposite the wire-produced field creates a magnetic minimum below the chip. Increasing B_{Hold} moves this minimum closer to the chip because it balances a stronger field from the wire. Therefore, we can control the vertical positioning of the atoms by varying either

FIG. 2.7: Atom chip metalization. The left image illustrates the various wire patterns on our atom chip generously donated by the Thywissen Lab at the University of Toronto. A zoomed in image of the center portion, outlined in black/white, is shown in the upper right corner. Here the z-wire, shown in blue, is very evident. Further zooming in shows further structure in the bottom right image. For the work carried out in this thesis, the blue Z-wire trace is used for trapping and one of the red U-wires is used for RF evaporation.

B_{Hold} or the wire current. In addition, the other legs of the Z-wire have the advantage of producing end-caps for our trap, providing axial confinement in addition to the radial confinement of the external field.

Our Z-wire consists of two end-caps that are 200 μm wide and several mm long. The central portion of the Z is 50 μm wide and 2.8 mm long. During the experiment, we apply 1 A of current to the Z-wire and a B_{Hold} field of 20 G perpendicular to the central leg of the Z-wire. We also add a small field parallel to the central leg of the Z-wire: B_{Ioffe}=4.9 G. The presence of this field shifts the trap minimum so that it avoids crossing zero.
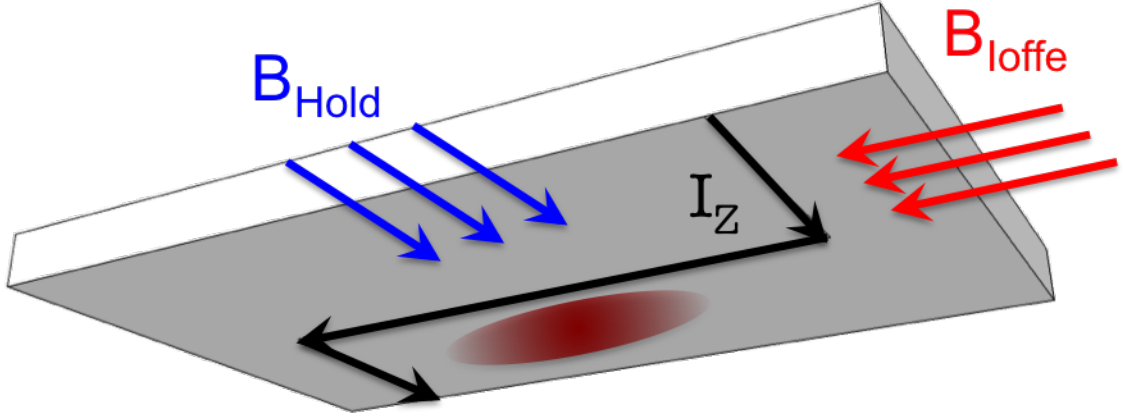
FIG. 2.8: Atom chip fields. Shown are the direction of current I_Z through the Z-wire, as well as the directions of the B_{Hold} (blue) and B_{Ioffe} (red) fields required to trap atoms below the chip.

This reduces the possibility of Majorana losses due to spin flips in the presence of a zero magnetic field. The resulting trap potential can be seen in Figure 2.9.

These magnetic fields $\vec{B}$ are calculated using the Biot-Savart Law for a current carrying conductor, given a current I along direction $\vec{l}$ at a position $\vec{r}$ from the conductor:

$$\vec{B} = \frac{\mu I}{4\pi} \int \frac{d\vec{l} \times \hat{r}}{|\vec{r}|^2}. \tag{2.4}$$

For metalized traces on the atom chip, we assume a rectangular conductor with width $\Delta y = y_2 - y_1$ and length $\Delta x = x_2 - x_1$ and current running along the length of the conductor. The resulting magnetic field along each axis is:

$$\vec{B} = \frac{\mu I}{4\pi} \left[-\tan^{-1}\left(\frac{xy}{z\sqrt{x^2+y^2+z^2}}\right)\hat{y} - \tanh^{-1}\left(\frac{\sqrt{x^2+y^2+z^2}}{x}\right)\hat{z} \right] \tag{2.5}$$

evaluated at the limits $x = x_1$ to x_2 and at $y = y_1$ to y_2. To model the fields from the

23
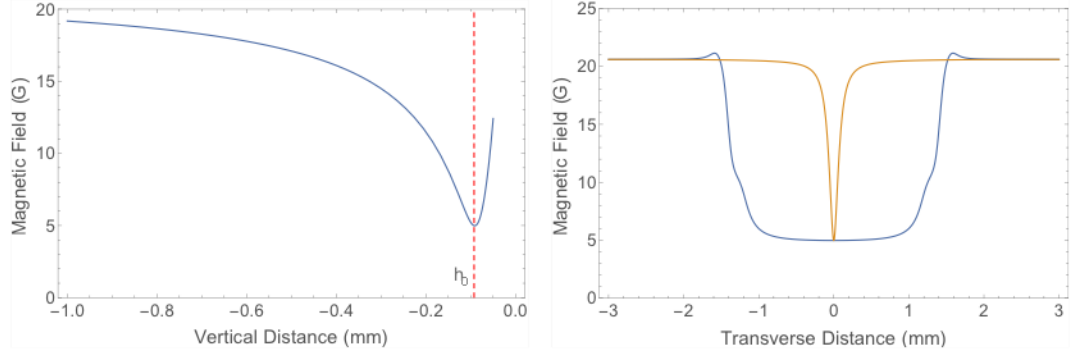
FIG. 2.9: Atom chip potential. The left image plots the resulting trap potential along the vertical radial axis directly below the Z-wire. The right image plots the resulting trap potential along the axial (blue) and horizontal radial (yellow) axes for a vertical distance of h_0 from the chip. The presence of the Ioffe field has shifted the minimum away from zero.

chip's Z-wire, we sum the magnetic field from three rectangular conductors (representing each leg of the Z) using Equation 2.5.

2.6   Evaporative cooling

Once the atoms are held in the atom chip trap, we begin the final step towards BEC: evaporative cooling. At this stage, the $|F=2, m_F=2\rangle$ atoms are entirely confined by the magnetic fields of the chip in a magnetic bowl (see the cartoon in Figure 2.10). There also exist four additional m_F states, three of which are untrapped. The m_F states are separated by RF frequencies. In the F=2 ground state of ^{87}Rb, the Zeeman splitting is 0.7 MHz/G between m_F states. Evaporative cooling operates by applying an RF field which couples the m_F levels of the atoms. If the RF frequency starts high, it will only match the energy splitting of the m_F levels at positions far from the center of the trap. Only atoms with sufficient kinetic energy to reach those positions will be driven to the untrapped states and leave the trap. Therefore, hotter atoms will reach the outer edge of the trap, spin flip, and fall away, leaving an overall cooler cloud of atoms behind.

Typically, experiments achieve evaporative cooling by starting with a high RF frequency (or "RF knife"), and adiabatically sweeping the field to lower frequencies as the cloud cools. For example, in the experimental system described in this thesis, we achieve evaporative cooling by sweeping the frequency from 20 MHz to 3.3 MHz in approximately 6 s.

There is no guaranteed formula for a successful evaporative path to BEC. In practice, we monitor the temperature, density, collision rate, and phase space density of our atoms throughout the evaporative path. Temperature is monitored with standard time-of-flight measurements which are described in Section 2.9. Density is a standard atom number density measurement which we know from the number of atoms and the volume of our trap (estimated from the trap frequencies):

$$n = \frac{N X_r^2 X_z}{(2\pi)^{3/2}}. \tag{2.6}$$

Here, N is the number of atoms, and $X_{r,z}$ is the size of the cloud along the radial or axial axes determined from $\frac{1}{2}mv^2 = \frac{1}{2}m\omega_{r,z}^2 X_{r,z}^2$ with m the mass of the atoms, $\omega_{r,z}$ the trap frequency, and v the velocity of our atoms (determined from time-of-flight measurements in Section 2.9). Collision rate is a measure of the number of atom-atom elastic collisions occurring per second:

$$CR = \frac{8\pi n v a_s}{2\sqrt{2}}, \tag{2.7}$$

where a_s is the scattering length of the atoms. (Values of a_s for ^{87}Rb and ^{39}K can be found in [56, 57, 47, 58], respectively. Conveniently, for ^{87}Rb, $a_s \approx 99a_0$, where a_0 is the Bohr radius.) Phase space density is calculated from Equation 2.1.

As mentioned previously, evaporative cooling allows experimentalists to reach BEC.

It should come as no surprise that this technique is capable of reaching temperatures in the nK range and phase space densities larger than 2.612.
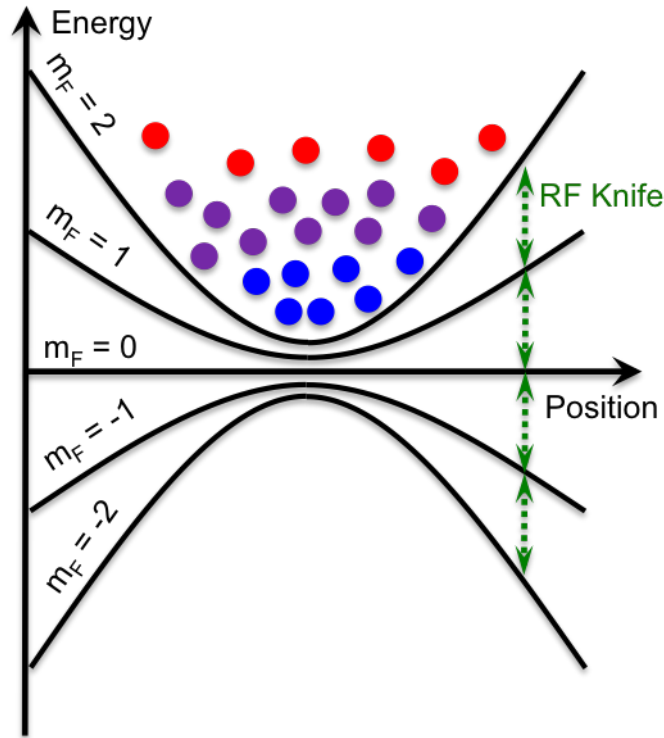
FIG. 2.10: Evaporative cooling for F=2 ground level. m_F=1,2 atoms are trapped, while m_F=0,-1,-2 atoms are untrapped. An RF magnetic field (known as an RF knife) can be swept from large frequencies to small frequencies which ejects the most energetic atoms to the untrapped states. This results in an overall cooler cloud of atoms remaining trapped.

2.7 Bose-Einstein condensate

Atoms obey both classical and quantum mechanical properties, depending on the characteristics of the cloud. At high temperatures, they act as a thermal gas and obey Maxwell-Boltzmann statistics. However, as they are cooled, it is useful to think of the atoms quantum mechanically as wavepackets with an associated thermal deBroglie wave-

length, given by:

$$\lambda_{dB} = \left(\frac{2\pi\hbar^2}{mk_BT}\right)^{1/2}.$$

(2.8)

Here, k_B is the Boltzmann constant and T is the temperature of the atoms. As the atoms are cooled, the deBroglie wavelength increases until λ_{dB} is on the order of the separation of atoms. When this happens, the atomic waves overlap and form a Bose-Einstein condensate (BEC) for a cloud of bosonic atoms. As a BEC, all of the atoms are in the same quantum state and can be described by the same macroscopic wavefunction. This transition to BEC occurs when the phase space density, defined in Equation 2.1 exceeds the value 2.6.

Quantum mechanical systems are described by the Schrodinger equation:

$$i\hbar\frac{d}{dt}\Psi(r,z,t) = \left(-\frac{\hbar^2}{2m}\nabla^2 + U(r,z,t)\right)\Psi(r,z,t).$$

(2.9)

In this equation, the potential energy $U(r,z,t) = U_{ext} = U_{int}$ is the sum of both the external trap potential U_{ext} and the atomic mean-field interaction potential U_{int}. In the experiments presented in this thesis, ultracold atoms are produced in a harmonic trapping potential given by:

$$U_{ext} = \frac{1}{2}m(\omega_r^2 r^2 + \omega_z^2 z^2)$$

(2.10)

where m is the atomic mass, ω_r is the radial trap frequency, and ω_z is the axial trap frequency. The atomic mean-field interaction potential is given by a non-linear self-interaction term:

$$U_{int} = gN|\psi(r,z)|^2$$

(2.11)

where N is the number of atoms and g is an interaction parameter given by $g = 4\pi\hbar a_s/m$ with a_s the scattering length of the atoms [56, 57, 47, 58]. Conveniently, for ^{87}Rb, $a_s \approx 99a_0$, where a_0 is the Bohr radius.) Note that the sign of g is determined by the sign of the scattering length. g (and therefore the scattering length) must be positive (repulsive) or the condensate will implode. Because of this non-linear interaction potential, the Schrodinger equation becomes non-linear and is sometimes referred to as the Gross-Pitaevskii (GP) equation after its discoverers.

In the stationary case, the GP equation is written:

$$\mu\psi(r,z) = \Big(-\frac{\hbar^2}{2m}\nabla^2 + U_{ext} + gN|\psi(r,z)|^2 \Big)\psi(r,z), \tag{2.12}$$

given $\Psi(r,z,t) = \psi(r,z)e^{-i\mu t/\hbar}$ [59]. Here, μ is defined as the chemical potential or mean-field energy of the atoms. For large enough N, we can assume the kinetic energy term is negligibly small (Thomas-Fermi approximation), and for a harmonic trap the equation reduces to:

$$\mu\psi(r,z) = \Big(\frac{1}{2}m(\omega_r^2 r^2 + \omega_z^2 z^2) + gN|\psi(r,z)|^2 \Big)\psi(r,z). \tag{2.13}$$

From this equation, we can solve for the ground state energy distribution/atom number density $(\rho(r,z))$, which is given by:

$$N|\psi(r,z)|^2 = \frac{\mu - \frac{1}{2}m(\omega_r^2 r^2 + \omega_z^2 z^2)}{g} = \rho(r,z), \tag{2.14}$$

for $\mu > U_{ext}$ and zero elsewhere. Spatially, the Thomas-Fermi distribution is an upside

down paraboloid with radius:

$$R_{r,z} = \frac{1}{\omega_{r,z}}\sqrt{\frac{2\mu}{m}}. \tag{2.15}$$

To determine the chemical potential or mean-field energy μ, one need only to integrate Equation 2.14 over r and z and solve for μ:

$$\mu = \frac{\hbar\overline{\omega}}{2}\left[\frac{15Na_s}{\overline{a_{ho}}}\right]^{2/5}, \tag{2.16}$$

where $\overline{\omega} = (\omega_r^2\omega_z)^{1/3}$ is the geometric mean frequency of the trap and $\overline{a_{ho}} = \sqrt{\frac{\hbar}{m\overline{\omega}}}$ is the geometric mean of the harmonic oscillator. Alternatively, if the trapping frequencies $\omega_{r,z}$ and Thomas-Fermi radii $R_{r,z}$ are known, one can calculate μ from Equation 2.15.

Below the critical temperature at which atoms begin to condense, the atom distribution will be bimodal in nature. The thermal atoms will have a Gaussian distribution, and the condensed atoms will have the Thomas-Fermi distribution described above. This bimodal distribution is one of two signatures of BEC which we seek during the optimization of our evaporative cooling.

The second signature is anisotropic expansion after some time-of-flight, which derives from the dynamics of the condensate upon being released from the trap. These dynamics depend on the aspect ratio of the trap frequencies. The time-of-flight expansion can be described by [60]:

$$r_0(t) = r_0(0)\sqrt{1 + \tau^2},$$
$$z_0(t) = \epsilon^{-1}r_0(0)(1 + \epsilon^2[\tau\arctan\tau - \ln\sqrt{1+\tau^2}]). \tag{2.17}$$

Here, r_0 and z_0 are the radial and axial cloud sizes at time t, ϵ is the ratio ω_z/ω_r, and

$\tau = \omega_r t.$

Equation 2.17 results in three different time stages [60]:

1. For $t \lesssim 1/\omega_r$, radial acceleration as mean-field energy is converted to kinetic energy,

2. For $1/\omega_r \lesssim t \lesssim \omega_r/\omega_z^2$, radial expansion but little axial expansion, and

3. For $t \gtrsim \omega_r/\omega_z^2$, radial and axial expansion at asymptotic aspect ratio.

In our system, stage 1 takes place within the first 130 μs of being released from the trap, and stage 3 does not begin until 4 s after being released. Therefore, we only ever observe the atoms after undergoing stage 1 and in the midst of stage 2. The result of this stage is a cloud that nearly maintains its initial axial size but quickly expands radially during a typical 5-30 ms time-of-flight period. This anisotropic expansion was demonstrated experimentally and can be found in the quasi-pure condensate image in Figure 5.6.

2.8 Imaging

Most measurements of cold and ultracold atom samples are usually done by way of imaging the atomic cloud. Imaging is done using near- or on-resonant light collected on a precisely triggered CCD camera. There are two main varieties of imaging: absorption and fluorescence. Absorption imaging is a photon-efficient method that allows users to determine atom number without any knowledge of the quantum efficiency of the CCD camera. It is best used for denser atom clouds.

For less dense clouds or even single atom imaging [61], fluorescence imaging is often used. This method collects photons that have been spontaneously emitted from an excited atom when it decays. The signal depends on the collection time and the numerical aperture

of the collection optics. In order to accurately determine an atom number, one needs to know the quantum efficiency of the camera, or the number of photons required to produce one count of signal.

In the following subsections, I discuss the physics behind each of these methods.

2.8.1 Absorption imaging

Most data for this thesis is acquired with absorption imaging, which essentially looks at the shadow produced by a cloud of atoms in a beam of resonant light as it shines into the camera. This method requires two images: an image of the shadowed beam with atoms ("atom image") and an image of the beam alone after the atoms have fallen away or dispersed ("laser image"). You can extract the optical depth OD on a pixel using:

$$OD = \ln\left(\frac{C_{laser}}{C_{atom}}\right), \tag{2.18}$$

where C_{laser} and C_{atom} are the detector counts for the laser image and atom image, respectively. The intensity of the light after passing through a cloud of atoms is given by:

$$I = I_0 e^{-OD} \tag{2.19}$$

where I_0 is the initial intensity of the light. From Beer's Law, the OD can also be written as a function of atom density $n(r)$, the absorption cross section σ, and the length Δz of the atomic medium [52]:

$$OD = n(r)\sigma\Delta z \tag{2.20}$$

where σ is defined as:

$$\sigma = \frac{\sigma_0}{1 + 4(\frac{\Delta}{\Gamma})^2 + \frac{I_0}{I_{sat}}} \qquad (2.21)$$

In the above equation, σ_0 is the on-resonance cross section, Δ is the detuning from resonance, Γ is the decay rate, and I_{sat} is the saturation intensity. For absorption imaging, we typically use an on-resonance beam with $I_0 \ll I_{sat}$. Therefore, the absorption cross section reduces to $\sigma \approx \sigma_0$, given by:

$$\sigma_0 = \frac{3\lambda^2}{2\pi}. \qquad (2.22)$$

where λ is the wavelength of the imaging light. With this description, we can easily convert our absorption images to atoms per pixel. For on-resonant imaging, substituting Equation 2.22 into Equation 2.20 and applying Equation 2.23 gives the atom number at each pixel:

$$N_{pixel} = \int_{x,y} \int_0^{\Delta z} n(\vec{r})dz = n(r)\Delta z = \ln\left(\frac{C_{laser}}{C_{atom}}\right)\frac{2\pi}{3\lambda^2} \times A_{pixel}, \qquad (2.23)$$

where A_{pixel} is the area of each pixel. Further image analysis is detailed in Chapter 5.

2.8.2 Fluorescence imaging

Fluorescence imaging detects the photons re-emitted by the atoms when an on-resonance pulse of light is applied. This method of imaging is better suited for lower atom numbers and is fairly straightforward. When on- or near-resonance light is applied to the atoms, they scatter (absorb and re-emit) photons, emitting into the full solid angle. Placing a camera near the atoms, one can collect a fraction of the scattered photons. In principle, one can determine the atom number from fluorescence imaging if one knows the

collection efficiency of the imaging system and the quantum efficiency of the camera (the number of photons corresponding to a single count). An atom scatters photons at a rate R given by:

$$R = \frac{s_0 \Gamma/2}{1 + 4(\frac{\Delta}{\Gamma})^2 + s_0} \qquad (2.24)$$

where s_0 is the on-resonance saturation parameter, defined as $s_0 = 2|\Omega|^2/\Gamma^2 = I/I_{sat}$. Here, Ω is the Rabi frequency. In both Equation 2.21 and Equation 2.24, $I_{sat} = \frac{\pi hc\Gamma}{3\lambda^3}$. Therefore, the atom number at each pixel given by the fluorescence imaging method is:

$$N_{pixel} = \frac{4\pi}{\Theta} \frac{1}{Q} \frac{C}{t_{exp}} \frac{1}{R}, \qquad (2.25)$$

where Θ is the collection solid angle of the imaging system, Q is the quantum efficiency of the camera, C is the number of CCD counts, and t_{exp} is the exposure time.

2.9   Temperature measurement

Throughout the entire MOT to BEC process, we monitor the temperature of our atom cloud. Temperature is monitored by way of a process called time-of-flight imaging. Essentially, at the point in the experiment at which we would like to know the temperature of our atoms, we quickly turn off all optical and magnetic fields and allow our atoms to free fall under gravity for a period of a few milliseconds. This period of free fall is known as the time-of-flight.

During this period, the atoms expand ballistically. The rate of the expansion is governed by the thermal momentum distribution. (Note: For this reason, temperature can only be measured with the thermal atoms in the cloud – not with condensed BEC atoms.)

Therefore, temperature measurements are made with a series of images of increasingly longer times-of-flight. In each of these images, the thermal atom distribution is fit to a Gaussian distribution along the vertical and/or horizontal axis. The fitted atom distribution can either be a slice through the cloud or a summed distribution over some region of interest, and is frequently well-described by a Gaussian distribution for thermal clouds. The camera image records a Gaussian distribution in the x-y plane given by:

$$n(y, z) = n_0 e^{-\frac{1}{2}\frac{(x-x_0)^2}{\sigma_x^2}} e^{-\frac{1}{2}\frac{(y-y_0)^2}{\sigma_y^2}} \tag{2.26}$$

where n_0 is the peak density (atoms per pixel), x_0 and y_0 are the position of the centroid, and σ_x and σ_y are the widths of the distribution along x and y. We determine the temperature along either the y (z) axis by plotting σ_x (σ_y) vs the time-of-flight. The $\sigma_{x,y}(t)$ relationship takes the form:

$$\sigma_{x,y}(t) = \sqrt{\sigma_i^2 + v^2 t^2} \tag{2.27}$$

where σ_i is the initial size of the cloud before time-of-flight expansion, $v = \sqrt{k_B T/m}$ is the average ballistic expansion velocity, and t is the time-of-flight. It is fun to note that for ^{87}Rb, $\frac{k_B}{m}$=0.9498 cm^2/(s$^2\mu$K). Therefore, if you wish to know the temperature of your cloud in μK, you need only to square the expansion velocity given in cm/s for an approximate temperature in μK within 5% of the actual value.

The plot of an expansion under time-of-flight takes on the general form in Figure 2.11. In order to obtain an accurate temperature measurement, it is important to have a cloud size from the linear regime. For this reason, in hotter clouds such as the MOT and magnetic trap, we usually take several images and reproduce the plot from Figure 2.11 to determine temperature. An example of this type of temperature measurement is

shown later in Figure 4.13 in Chapter 4 to compare the temperature of potassium atoms before and after a molasses stage was implemented. For colder temperatures, when our initial cloud size has significantly smaller σ_0, we are able to do single image temperature measurements after sufficiently long time-of-flight. We use this single image method once our atoms have begun to evaporatively cool in the magnetic chip trap.
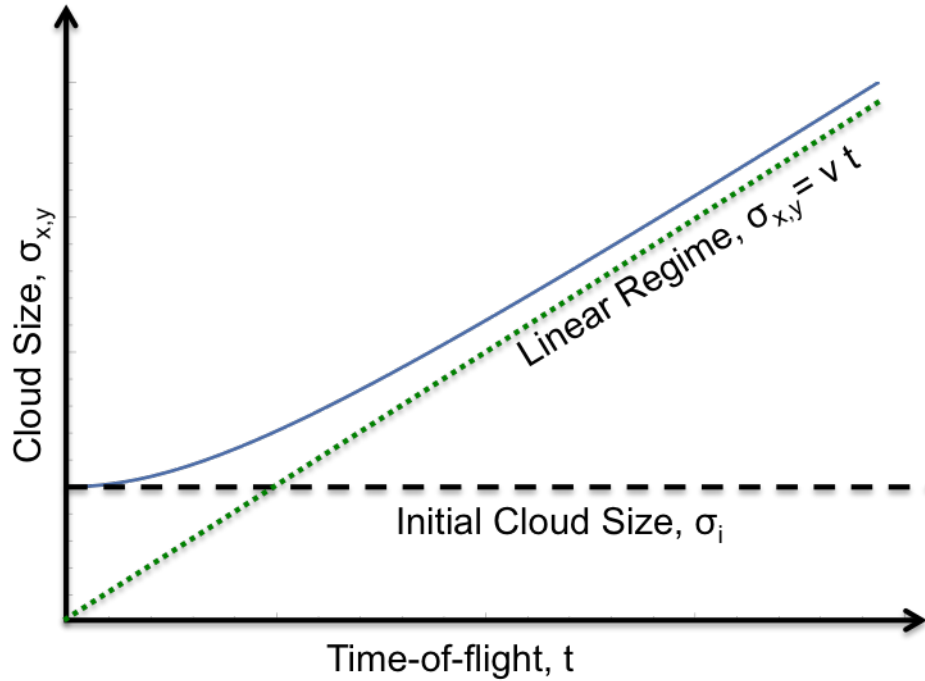
FIG. 2.11: Time-of-flight measurements for determining temperature. This is the general form of the thermal cloud expansion under time-of-flight, described by Equation 2.27. If a full fit is not done, it is important to be in the linear regime before approximating temperatures. The slope of the linear regime is $v = \sqrt{\frac{k_B T}{m}}$

CHAPTER 3

Optical dipole traps

3.1   Introduction

A single focused red-detuned laser beam can be used to form a dipole trap for ultracold atoms. Due to the interaction of the dipole moment of the atom and the electric field of the light, the energy levels of the atom will experience a shift known as the AC Stark shift. These shifts in energy can produce attractive trapping potentials for ground state atoms in a red-detuned beam and repulsive potentials for ground state atoms in a blue-detuned beam [62]. Furthermore, the addition of a counter-propagating beam produces an optical lattice potential. Each of these has found a multitude of uses in cold/ultracold atomic physics laboratories. In general, optical traps are conservative traps that are easy to implement experimentally. They are preferred for magnetic field sensing applications, since magnetic traps overwhelm and distort the very thing one is trying to measure [63]. Blue-detuned beams in a variety of geometries can be used when the experimentalist seeks to trap atoms without the presence of the energy shift. Utilizing the blue-detuned repulsive potential will cause the atom to seek the low intensity regions where shifts are minimal [64].

The tight confinement of the optical lattice, which reduces the motion of the atoms and provides a more uniform potential site-to-site, is the preferred choice for the most precise atomic clock experiments in the world [29].

In this chapter, I introduce the theory behind optical dipole and optical lattice traps. I begin with the dressed atom theory, which describes the energy shifts of the atom in the presence of a light field. Many of the following calculations have been derived in detail in [52]. Here I cover the highlights of the dressed atom theory which lead us to the AC Stark shift. I then describe the method of calculating a trap potential from the intensity of a light field. Finally, I derive the lattice potential and note some significant differences between the lattice and dipole potentials.

3.2   Two-level atom theory for a dipole trap

We begin with the Hamiltonian of the full system as a sum of the field-free Hamiltonian H_0 for a two-level atom, the Hamiltonian H_{EM} for the electromagnetic field of the laser light, and the interaction Hamiltonian H_{int} describing the coupling between the two. We write these Hamiltonians in the basis of the dressed atom theory: $|g, N+1\rangle$ and $|e, N\rangle$. In this basis, the ground state $|g, N+1\rangle$ exists when the atom is in the ground state with $N+1$ photons available, and the excited state $|e, N\rangle$ exists when an atom has absorbed a photon and is in the excited state.

The standard atomic Hamiltonian for a two-level atom can be written as:

$$H_0 = \begin{bmatrix} 0 & 0 \\ 0 & E_0 \end{bmatrix} = \hbar \begin{bmatrix} 0 & 0 \\ 0 & \omega_0 \end{bmatrix} \tag{3.1}$$

where $E_0 = \hbar\omega_0$ is the energy difference between the excited and ground state (see Figure 3.1). When we place the two-level atom in a light field, we can consider a very simplified

FIG. 3.1: Two-level energy diagram. (left) A two-level atom is assumed to have two energy levels: a ground state $|g\rangle$ and excited state $|e\rangle$ separated by energy $\hbar\omega_0$. For optical dipole trapping, a far off-resonance detuned wavelength is chosen, represented by energy detuning $\hbar\Delta$. (right) A red-detuned beam results in atoms being confined in the high intensity region of the beam, often formed simply by focusing the beam. Note that $\hbar\Delta$ in the left figure is shown with $\hbar\Delta < 0$ (red-detuning) to match the right figure.

case where the atom interacts with a single longitudinal mode of the EM field with:

$$H_{EM} = \hbar\omega_l \begin{bmatrix} N+1 & 0 \\ 0 & N \end{bmatrix}. \tag{3.2}$$

Here, the frequency of the light field mode ω_l is detuned from the resonance by some amount Δ such that $\Delta = \omega_l - \omega_0$ and N represents some number of photons.

Due to the charge q of the single valence electron at position $\vec{r}$ from the center of the atom (the origin) interacting with the electric field of the EM wave $\vec{\mathbb{E}_0}$, the dressed atom energy states will be coupled by an interaction Hamiltonian given by:

$$H_{int} = \hbar \begin{bmatrix} 0 & \frac{\Omega}{2} \\ \frac{\Omega^*}{2} & 0 \end{bmatrix}, \tag{3.3}$$

where

$$\Omega = -\frac{q}{\hbar}\langle e|\vec{r}\cdot\vec{\mathbb{E}_0}|g\rangle \tag{3.4}$$

is defined as the Rabi frequency. Calculating the dipole matrix element $\langle e|\vec{r}\cdot\vec{\mathbb{E}_0}|g\rangle$ requires explicit knowledge of the atomic wavefunction but has been done for both rubidium and potassium [46].

If we redefine the energy origin by subtracting $\hbar\omega_l N + \hbar\omega_0$, then we can write the full Hamiltonian of the dressed atom as:

$$H_{total} = H_0 + H_{EM} + H_{int} = \hbar \begin{bmatrix} \Delta & \frac{\Omega}{2} \\ \frac{\Omega^*}{2} & 0 \end{bmatrix} \tag{3.5}$$

Solving the above Hamiltonian, we find eigenvalues $E_\pm$ equal to:

$$E_\pm = \frac{1}{2}\hbar\Delta(1 \pm \sqrt{1 + \frac{|\Omega|^2}{\Delta^2}}). \tag{3.6}$$

For a far off resonance trap (FORT), we can assume $|\Delta| >> |\Omega|$ and approximate the square root such that:

$$E_\pm = \frac{1}{2}\hbar\Delta \pm \frac{1}{2}\hbar\Delta \pm \frac{\hbar|\Omega|^2}{4\Delta}. \tag{3.7}$$

The diagonalized Hamiltonian is therefore:

$$H = \begin{bmatrix} -\frac{\hbar|\Omega|^2}{4\Delta} & 0 \\ 0 & \hbar\Delta + \frac{\hbar|\Omega|^2}{4\Delta} \end{bmatrix} \tag{3.8}$$

39
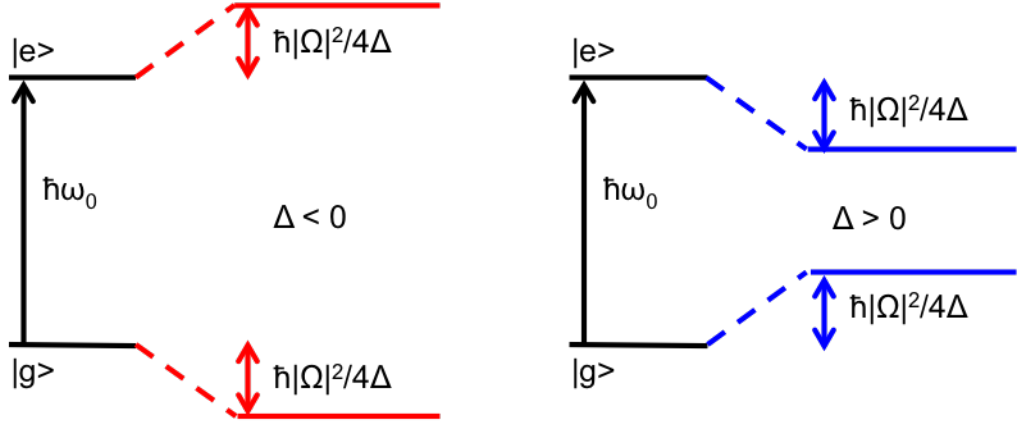
FIG. 3.2: Two-level energy diagram of the dressed atom. (left) The shifts of the ground $|g\rangle$ and excited $|e\rangle$ states of a two-level atom in a red-detuned ($\Delta < 0$) light field. (right) The shifts of the ground $|g\rangle$ and excited $|e\rangle$ states of a two-level atom in a blue-detuned ($\Delta > 0$) light field.

One can see that there is an added term to the original energy levels of the ground and excited states which now gives us the new energy levels in the light field (see Figure 3.2). This term is $\pm\frac{\hbar|\Omega|^2}{4\Delta}$ and is attributed to the action of the light field on the atoms. Particularly, $|\Omega|^2$ is proportional to the peak intensity of the light field I. Recall that $I = \frac{1}{2}c\epsilon_0\vec{\mathbb{E}}_0^{\,2}$, such that rewriting and squaring 3.4 gives us:

$$|\Omega|^2 = \frac{2Iq^2|\langle e|\vec{r}|g\rangle|^2}{c\epsilon_0\hbar^2}. \tag{3.9}$$

Here, c is the speed of light in vacuum and ϵ_0 is the permittivity of free space. From Section 2.8.2, we can also rewrite this as $|\Omega|^2 = \frac{\Gamma^2}{2}\frac{I}{I_{sat}} = \frac{3I\Gamma\lambda^3}{2\pi hc}$.

3.3 Calculating dipole trap potentials

We will now transition from quantum mechanics and atomic energy levels to classical optics and Gaussian beams. For calculating the potential from a detuned, focused, Gaussian laser beam, it is convenient to recall that the Rabi frequency in the above derivation

is proportional to the beam intensity or square of the electric field. Therefore, we will base the following calculations on the intensity of the beam rather than the Rabi frequency.

Far-off resonance traps produce a potential which looks like:

$$U(r, z) = U_0 I(r, z) \tag{3.10}$$

In the above equation, U_0 is the peak potential and is given by [62]:

$$U_0 = \frac{3\pi c^2 \Gamma}{2\omega_0^3 \Delta}. \tag{3.11}$$

The intensity $I(r, z)$ is the irradiance of the beam as a function of position given by [65]:

$$I(r, z) = \frac{I_0}{w(z)^2} \exp\left(-\frac{2r^2}{w(z)^2}\right) \tag{3.12}$$

where $I_0 = \frac{2P}{\pi}$, P is the power of the beam, r is the radial distance from the center of the beam, and $w(z)$ is the spot size of the beam given by [66]:

$$w(z) = w_0\left(1 + \left(\frac{\lambda z}{\pi w_0^2}\right)^2\right)^{\frac{1}{2}} \tag{3.13}$$

where w_0 is the beam waist of the focused beam, λ is the wavelength of the beam, and z is the distance from the focal point along the axis of beam propagation. Knowing the focal length of the lens f and the input beam diameter d, one can calculate the full divergence angle of the beam to be $\Theta = 2\tan^{-1}(\frac{d}{2f})$ and the beam waist at the focus to be $w_0 = \frac{2\lambda}{\pi\Theta}$.

We can convert the potential to temperature by:

$$T = \frac{U(r, z)}{k} \tag{3.14}$$

where k is Boltzmann's constant.

The trapping potentials seen by an ^{87}Rb atom along the r and z axes produced by a 1064 nm beam focused to $w_0 = 60$ μm with 100 mW of power is shown in Figure 3.3. Such a trap has a depth of approximately 1.5 μK per 100 mW of power.
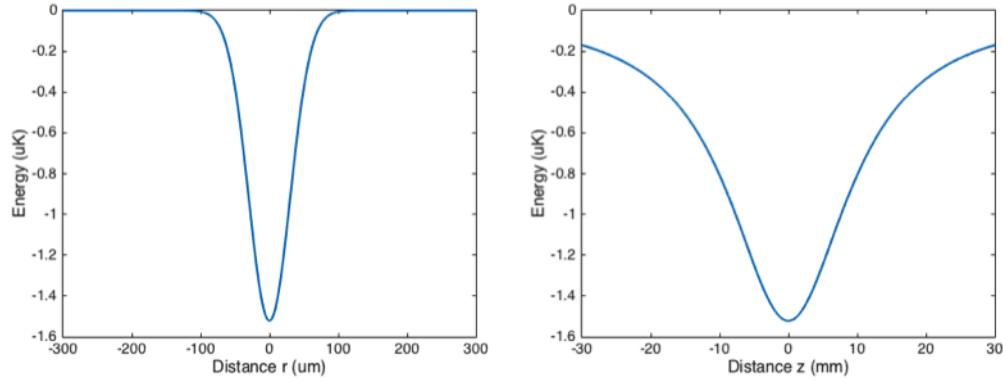
FIG. 3.3: Dipole potential. left) The potential produced in the r direction for a $\lambda = 1064$ nm beam focused to $w_0 = 60\mu$m with $P = 100$ mW as seen by ^{87}Rb atoms. The potential is computed with Equation 3.10 - 3.12. right) The potential produced in the z direction for the same beam and atoms.

3.3.1 Calculating the frequency of oscillation

To calculate the frequency of oscillation along one dimension, for example along the r-axis, we expand $U(r, z = 0)$ about the location of minimum potential, r_{min}. This gives us an expansion of the form:

$$U(r, z = 0) = C_0 + C_1(r - r_{min}) + C_2(r - r_{min})^2 + C_3(r - r_{min})^3 + ... \tag{3.15}$$

with coefficients $C_{0,1,2,3...}$. If all coefficients are negligible compared to C_2, we can equate the non-vanishing term to a simple harmonic oscillator potential:

$$\frac{1}{2}m\omega_r^2(r - r_{min})^2 = C_2(r - r_{min})^2 \tag{3.16}$$

where m is the mass of the atom (or oscillator), ω_r is the frequency of oscillation, and $C_2 = \frac{1}{2}\frac{d^2U}{dr^2}$ evaluated at $r = r_{min}$. This allows us to solve for the frequency of oscillation:

$$\omega_r = \sqrt{\frac{2C_2}{m}}, \tag{3.17}$$

3.4   Optical lattices

A special case of an optical dipole potential occurs when a laser beam is retro-reflected to produce a standing wave. The potential of the standing wave in one dimension as experienced by the atoms goes like $\cos^2(kz)$ where $k = \frac{2\pi}{\lambda}$ is the wave number of the beam and z is the axis of propagation. The periodicity of this potential produces an optical lattice with lattice constant $\lambda/2$. The ability to tailor the depth, spacing of, and number of atoms in each lattice site makes the optical lattice a desirable test bed for simulating solid state crystal lattices which tend to have fixed properties and impurities. Optical lattices have also proven to be useful in a number of atomic physics applications including gravimetry [63], atomic clocks [29], and quantum computing [67]. While making an optical lattice was not an aim of the research presented in this thesis, I will still discuss them briefly here since they unintentionally caused some complications in alignment of the dipole beam.

To understand where the above-mentioned $\cos^2(kz)$ potential comes from, we can use the simple model of the electric field $\vec{\mathbb{E}}$ of a plane-wave traveling through free space in the

z-direction with frequency ω_l as:

$$\vec{\mathbb{E}} = \vec{\mathbb{E}}_0 \cos(kz - \omega_l t). \tag{3.18}$$

Keeping in mind that an optical lattice forms with the overlap of two counter propagating fields, we can write the sum of both fields simply as:

$$\vec{\mathbb{E}}_{total} = \vec{\mathbb{E}}_0 \cos(kz - \omega_l t) + \sqrt{R}\vec{\mathbb{E}}_0 \cos(-kz - \omega_l t) \tag{3.19}$$

where the reflection amplitude $\sqrt{R}$ is less than one for a less than 100% reflection. Atoms will respond to the intensity of the light rather than the raw electric field, which goes like the electric field squared. In addition, the response time of the atom is several orders of magnitude slower than one period of the light field $\frac{2\pi}{\omega_l}$, so, in fact, the intensity from the atoms perspective will appear as the time average of the electric field squared:

$$I = \frac{c\epsilon}{2} \langle \vec{\mathbb{E}}_0^2 \cos^2(kz - \omega_l t) + R\vec{\mathbb{E}}_0^2 \cos^2(-kz - \omega_l t) + 2\sqrt{R}\vec{\mathbb{E}}_0^2 \cos(kz - \omega_l t) \cos(-kz - \omega_l t)\rangle_t. \tag{3.20}$$

Some additional simplification using trigonometric identities and time averaging yields:

$$I = I_0 + RI_0 + 2\sqrt{R}I_0 \cos(2kz) = I_0 + RI_0 + 2\sqrt{R}I_0(\cos^2(kz) - 1). \tag{3.21}$$

In the straight-forward case of a dipole trap, $\sqrt{R} = 0$ and we are left with $I = I_0$. Alternatively, for a perfectly reflected beam with $\sqrt{R} = 1$, the intensity becomes $I = 4I_0 \cos^2(kz)$. In this case, the presence of the optical lattices increases the peak intensity, and therefore the trap potential, by a factor of 4.

It is also fun to note that the force on the atom due to the potential goes like the

44
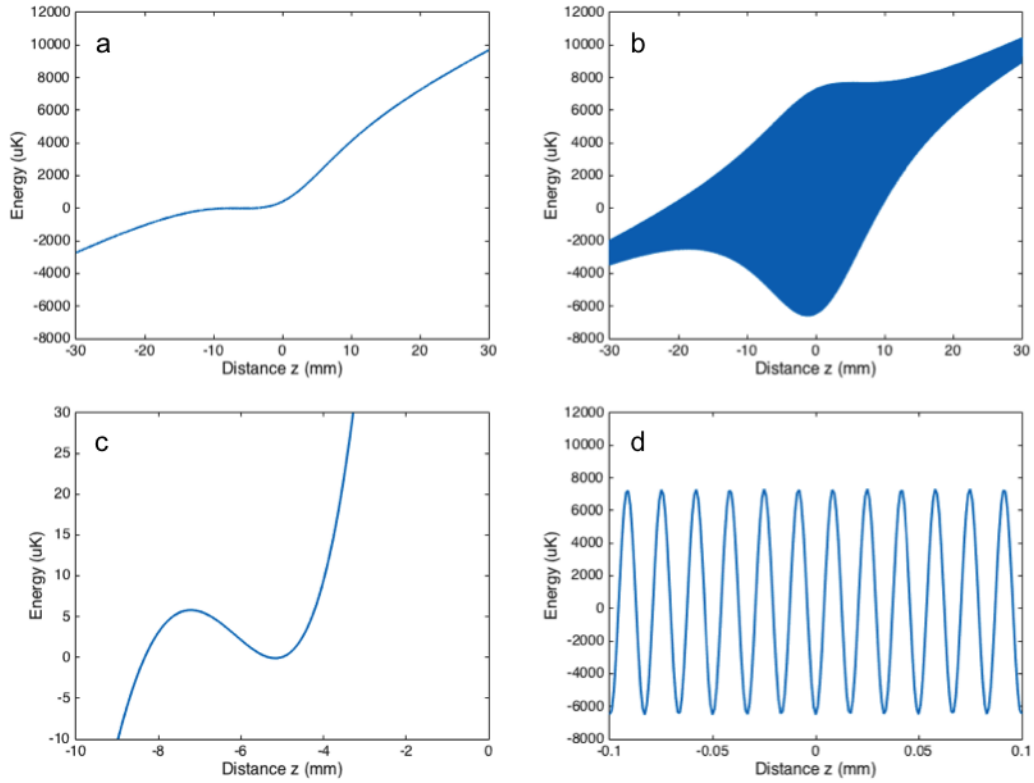
FIG. 3.4: Dipole and lattice trapping. a) A vertically oriented dipole beam with $w_0 = 60$ μm beam waist radius creates a potential depth of 5 μK against gravity with 227 W of power. b) This same power produces a lattice depth on the order of 10 mK. c) Zooming in on a), one can see the 5 μK potential depth more easily. d) Zooming in on b), one can see the lattice wells with a spacing of $\lambda/2=532$ nm.

change in potential over distance, $-\frac{dU}{dz}$. In addition to having an overall potential difference four times greater than the dipole trap, the optical lattice sees that potential difference over the distance of a quarter of a wavelength, as opposed to a distance on the order of the Rayleigh length. The result is a tremendous force from the optical lattice. To put this into perspective, let us consider a vertical beam with a waist radius $w_0=60$ μ m. In order to form a dipole trap of ^{87}Rb atoms 5 μ K deep in the vertical axis against gravity, one would need 227 W of 1064 nm laser power (see resulting trap shape in Figure 3.4 a and c). In the presence of an optical lattice, this same laser power produced a tremendous lattice

depth shown in Figure 3.4 b and d. In fact, the same 5 μK lattice depth can be formed with only 100 mW of power (see resulting lattice in Figure 3.5).
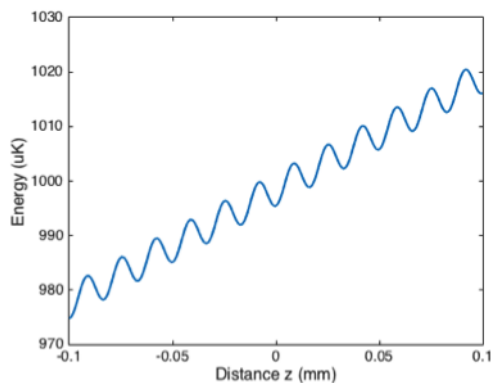
FIG. 3.5: Low power lattice trapping. A 5μK lattice depth can be produced with only 100 mW of power. The slope is due to the presence of gravity.

For the experiments carried out in Chapter 7, we originally planned to have an elongated dipole trap in which the atoms could slowly slosh back and forth as if in a 1D channel. Upon aligning the dipole trap and applying a force which was expected to make the atoms begin to slosh, we saw no movement of the atoms. Since our glass vacuum cell was not anti-reflection coated, it is reasonable to expect 4% reflection per surface. If we consider only the inner surface of the glass, with $R = 0.04$, the fringes on the $\cos^2(kz)$ lattice term are 40% on top of the single beam dipole trap. This was certainly more significant than ever expected, and large enough of an effect to prevent the atoms from sloshing in the trap. Realigning the beam to have a small angle of incidence with respect to the glass reduces this effect.

CHAPTER 4

Experimental apparatus

Actually producing ultracold atoms in the lab requires a number of systems integrated in space and time in a single apparatus. These systems include the ultra-high vacuum (UHV) system with various pumps, laser systems with corresponding locking electronics, shutters, frequency modulators, amplifiers, and optical fibers, magnetic field producing coils and their associated control electronics, and additional system components such as the atomic source, atom chip, and imaging systems. All of these are used synchronously and controlled by an overall timing sequencer to produce a magneto-optical trap (MOT), followed by optical molasses, optical pumping, magnetic trapping, magnetic transport, chip trapping, and RF evaporative cooling. In this chapter, I will describe most of these systems in detail, paying particular attention to ones in which I played a significant role in designing, building, and optimizing.

A sketch of the full vacuum apparatus with coils and the final laser beams that interact with the atoms can be found in Figure 4.1. Here one can see the dual chamber setup with horizontal MOT chamber and vertically oriented chip chamber. I played a significant role in the following:

1. Design layout of the lab;

2. UHV system cleaning, assembly, pumping, and baking;

3. Locking the repump laser;

4. Construction and alignment of the Rb and K tapered amplifier (TA) mounts;

5. Alignment of Rb and K laser systems from laser output, through AOMs, shutters, TAs, and fibers, to the apparatus table, through beam splitting cubes, waveplates, and telescopes, to the 3D MOT;

6. Imaging systems, including demonstration of fluorescence and absorption imaging in both chambers;

7. Design, construction, installation of bias-coils at the chip;

8. Demonstration of 3D MOTs for Rb and K;

9. Demonstration of Rb molasses;

10. Demonstration of Rb (and K) magnetic trap;

11. Demonstration of Rb optical pumping;

12. Alignment and demonstration of Rb dipole trap at the chip.

Additionally, in later chapters I will also discuss my work on: Chip trap characterization (and discovery of dimple trap); RF evaporation to BEC; and laying the groundwork for quantum pumping experiments.

Magnetic Coils
- ◎ MOT
- ◎ Transport/Push (P1, P2)
- ▭ Chip Bias

Laser Beams
- ➡ MOT
- ➡ OP/Probe
- → Chip Imaging

DC feedthrough

SMA feedthroughs

P2

Atom Chip

Dispenser feedthroughs

Ion Pump MOT Coils

Ti-Sub Pump

P1

Transport Coils

Turbo Pump

RGA

Ion Pump

Shutter

x   z   y

10cm
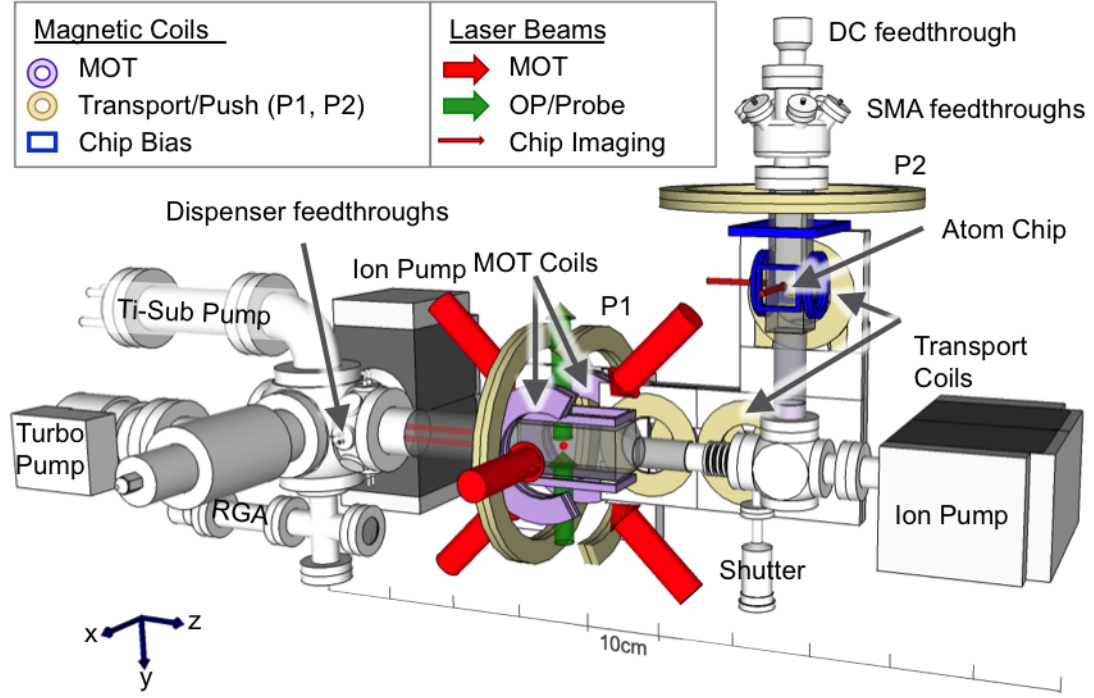
FIG. 4.1: Experimental apparatus. This figure shows the two-chamber vacuum apparatus for producing dual-species cold and ultracold atoms. The vacuum system components are shown in gray, while magnetic coils and laser beams are shown in color and labeled in the key at the top left. In addition to the vacuum system itself, I payed a significant role in the technology development for components shown in red, blue, and green (more detail given in text). This figure is a modification of the master apparatus CAD file created by Austin Ziltz.

4.1 Lab layout

One of the unique challenges experienced during my tenure in the Aubin lab was building an apparatus from scratch, only to have to move it and associated infrastructure to a completely different lab when Small Hall was renovated in 2010. This also served as a unique opportunity to re-think the layout of the lab. I was in charge of the layout design, one of which can be found in Figure 4.2. This design, nearly final, shows final positions of the large optics tables (apparatus table and laser table) and the Unistrut (dark green) that supports the electronics "cloud" over the tables. Also drawn are workbench areas (light

49

green) and the desk space/shelving area (orange/brown) (which eventually changed).

FIG. 4.2: Lab layout (post 2010). When Small Hall was renovated in 2010, the Aubin lab moved from one location to another, giving us the opportunity to redesign the layout of the lab. Here is a nearly final layout. The left figure shows the positioning of electrical and lighting infrastructure. The right figure shows final positions of two large optics tables (apparatus table and laser table) and the Unistrut (dark green) that supports the electronics "cloud" over the tables. Also drawn are workbench areas (light green) and the desk space/shelving area (orange/brown) (which eventually changed)

Our lab is designed with two optics tables (see Figure 4.2 and 4.3): The frequency stabilization and most of the power control occurs on one, while the main vacuum apparatus is on the other. Beams for the MOT and probes are sent from one table to the second apparatus table via optical fibers. Separate tables give us several advantages. The laser

control alignment is decoupled from the MOT alignment. The apparatus is magnetically and mechanically decoupled from the laser systems and vice-versa. The region of the vacuum apparatus is less likely to have stray beams which can significantly affect the lifetime of our magnetic trap. The increased distance between the chip and the AOMs reduces stray RF. There is also sufficient extra table space to conceivably add additional lasers for future experiments. The disadvantage of separate laser tables is the increased risk of ground loops, which is minimized by analog and digital isolation.

4.2 Vacuum system

The vacuum system is comprised of two chambers in an L-shaped geometry. This geometry was chosen such that the first chamber containing the atomic dispensers would not have direct line-of-sight to the second chamber where very low pressures are beneficial for BEC production and future atom-surface force measurements are planned (and not part of this thesis). The first chamber–the MOT chamber–is a rectangular Pyrex cell measuring 17 cm long and 6.3 cm in height and width. The MOT chamber is directly attached to several additional components including: a residual-gas analyzer (RGA) (ExTorr XT100), a 55 l/s ion pump (Varian StarIon Plus 55), a titanium-sublimation pump (Gamma Vacuum), and an all-metal angle valve which optionally connects a 60 l/s turbo pump (Pfeiffer) for initial pump down and bake out. The ion pump continually operates at 7 kV and provides the primary pumping for the MOT chamber. The titanium-sublimation pump provides occasional additional pumping of about 60 l/s, but in practice is only activated about once per year. The RGA typically indicates pressures in the low 10^{-10} range in the MOT chamber. In addition, four dispensers ($2 \times$ Rb and $2 \times$ K) (SAES and Alvatec) on electrical feedthroughs protrude into the MOT cell and dispense the requested species/element when heated by a current. One of the K dispensers is enriched with ^{40}K in anticipation of

fermionic experiments in the future.

The second chamber–the science chamber–is a rectangular Pyrex cell measuring 7.7 cm high by 4.6 cm in width and length. This chamber contains the atom chip where the BEC is produced, so better vacuum pressures are desired. This chamber is primarily pumped by an additional 60 l/s ion pump connected at the corner of the L. While we did not have a vacuum gauge in this chamber to directly measure resulting pressure, we are capable of producing magnetic traps with lifetimes above 7 s, more than adequate for BEC production.

4.3 Laser system and locks

The first cooling step towards Bose-Einstein condensation is laser cooling, which consists of a magneto-optical trap (MOT) followed by molasses, optical pumping, and optional probing before being loaded into a magnetic trap. The MOT is formed in the first of two vacuum cells in our apparatus with six independent counter-propagating beams comprised of two near-resonant lasers locked to the cycling and repump transitions of the atoms. Our apparatus is capable of cooling ^{85}Rb, ^{87}Rb, ^{39}K, ^{40}K, and ^{41}K, each of which start out in a MOT. (Disclaimer: While we have not demonstrated cooling of ^{40}K or ^{41}K, the system we have built should be capable of doing so.) The trap laser, which is locked to the cycling transition, is red-detuned from resonance using an acousto-optical modulator (AOM) and then combined with the on-resonance repump laser to be sent to the MOT. The repump laser "re-pumps" the atoms which have fallen into the dark ground state back into the cycling transition. The MOT beams should be large so as to affect a greater number of atoms, but the intensity of the trap beam must approach the saturation regime. After loading the MOT, there is a brief (5-12 ms) period of molasses followed by a short (1 ms) optical pumping pulse. During the optical molasses stage, the trap laser is further

red-detuned from resonance with the AOM. The optical pumping pulse is tuned to a resonance and circularly polarized to pump atoms into a single magnetic sublevel for magnetic trapping in the next step. (For theoretical details on these stages, please see Chapter 2). Our laser system is designed with all of these requirements in mind, as well as sufficient probe beams to monitor atoms in both the MOT and atom chip trap, with beams available for both absorption and fluorescence imaging at the chip.

Except for our Rb repump laser (which is discussed later), our K and Rb laser systems consist of master extended cavity diode lasers (ECDLs) (New Focus) at 767 nm and 780 nm respectively which seed more powerful diode lasers (see Figure 4.3). The master lasers are locked using standard saturation spectroscopy with a lock-in amplifier to generate the error signal. The saturating beam is dithered at 99 kHz, achieving a lock stability on the order of the laser linewidth. The master trap lasers are injected into respective slave lasers after passing through a double pass AOM setup to allow us to make frequency adjustments without angular or power alterations of the final beam. These locking schemes also allow us to easily choose frequencies for trapping additional species of K and Rb.

Our laser system has a switchyard architecture using a combination of single-pass AOMs as well as mechanical shutters to control the presence of the beam at the apparatus (see Figure 4.3). Both the trap and repump beams pass through their respective single-pass AOMs before the first-order deflected beams are combined on a cube and sent to the apparatus table via fiber. When the single-pass AOMs are switched off, only the zero-order undeflected beams remain, and are not coupled to the MOT fiber. The single-pass AOMs allow us to control the beam powers at speeds up to the microsecond time scale, or possibly faster. Lab-made mechanical shutters [68] are also strategically placed at the focal points of telescopes to provide an additional on/off switch such that the AOMs are off for only short periods of time to reduce beam steering associated with AOM temperature variations.
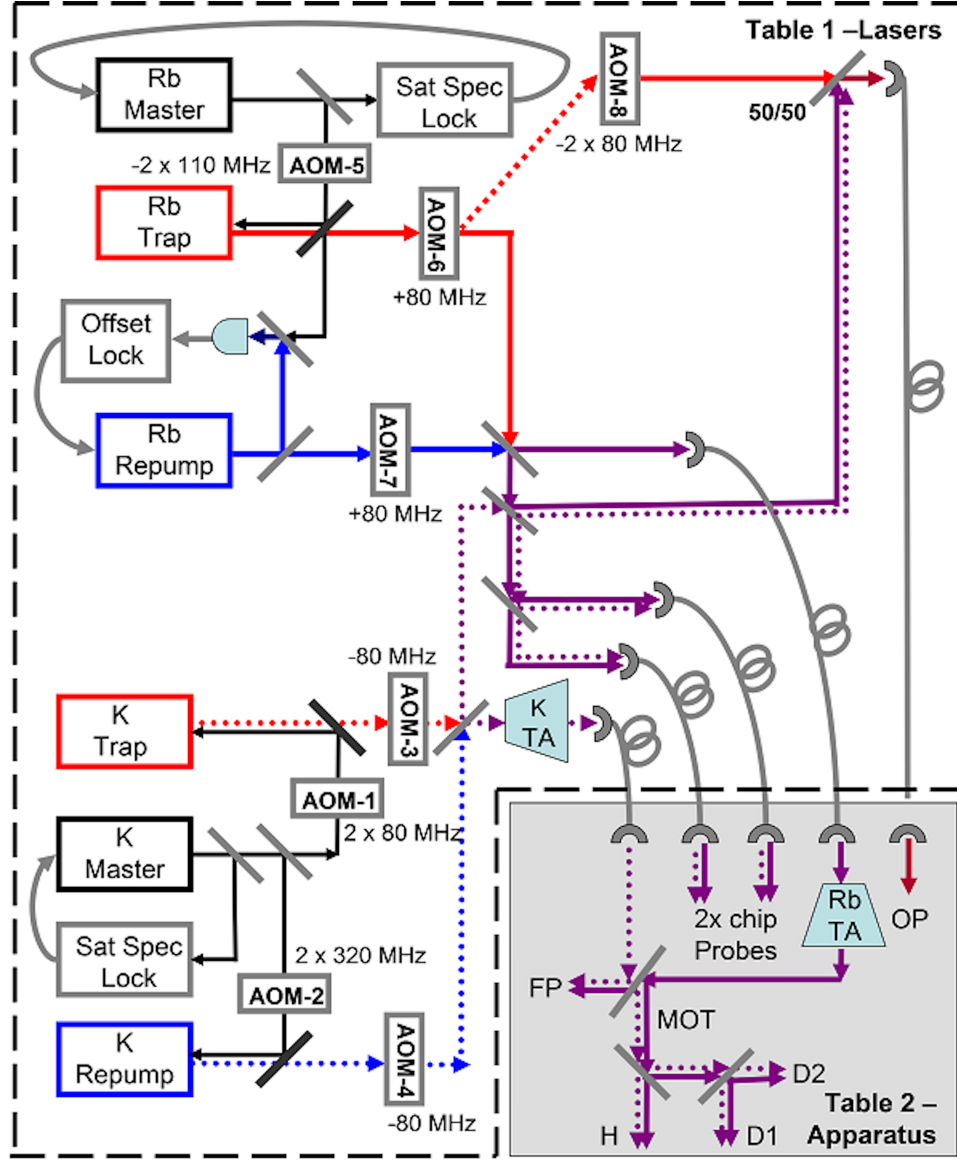
FIG. 4.3: Laser scheme. Our laser system for the dual-species apparatus consists of 6 lasers, 8 AOMs, 2 tapered amplifiers, 5 fiber optical cables, and numerous shutters to produce appropriately tuned and timed trap, repump, pump, and probe beams for the experiment spanning two optics tables.

The combined trap and repump beams for K and Rb travel via separate fibers to the apparatus. The Rb beams are amplified through a TA after passing through the fiber and arriving at the apparatus table. The K beams are amplified through a separate TA on the laser table, immediately before coupling to the fiber. On the apparatus table, two mirrors

54

align each beam to overlap on a single cube, allowing the K and Rb systems to maintain some independence from one another. The single resulting beam is split into the six counter-propagating beams for the MOT such that the power of the counter-propagating beams along one dimension is balanced using a single waveplate. The beams as large as possible in order to cool as many atoms as possible, while keeping the beam intensity in the vicinity of the saturation regime. The last optic before the vacuum cell is a 1:5 telescope, providing approximately 5 cm diameter beams for the MOT.

Our probe beams are generated on the laser table at the beamsplitter cube where the trap and repump beam are combined before the main MOT fiber (see Figure 4.3). The port of the cube that is not sent to the MOT has both trap and repump present, and this light encounters a second beamsplitter cube which splits the beam to produce two probe beams. The remaining unused port on this second cube is used to mix both Rb and K trap and repump beams for the two probes. The two probe beams are sent to the apparatus table and directed at the atom chip via individual fibers. One additional probe beam is available and directed at the MOT vacuum chamber for optical pumping, which also has the option of containing repump beams.

While the K and Rb systems are very similar in the above-outlined manner, there are several key differences which we will discuss below.

4.3.1 Rubidium laser system

Our rubidium laser system consists of two ECDLs (New Focus Vortex) at 780 nm: one trap laser operating on the $5S_{1/2}$ F=2 $\rightarrow$ $5P_{3/2}$ F'=3 D2 line cycling transition of ^{87}Rb and one repump laser for the F=1 $\rightarrow$ F'=2 transition (see Figure 4.4). The master trap laser is locked +125 MHz above the transition line. The locked beam passes through a double-pass -110 MHz AOM before seeding the second injection-locked diode laser (Sanyo

DL7150-201W). This second diode laser has an output of about 50 mW, which passes through a +80 MHz AOM before it is combined with the repump beam for amplification.
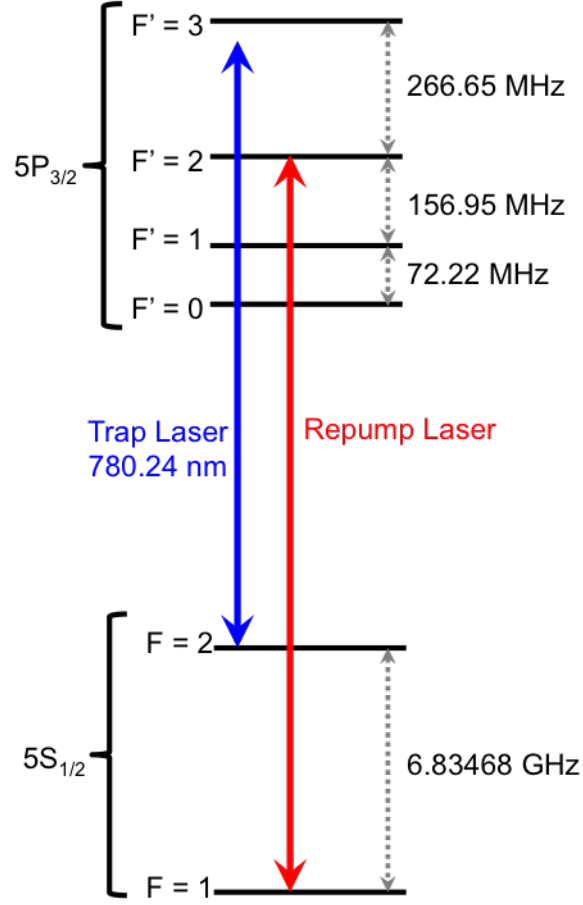
FIG. 4.4: Trap and repump level diagram for ^{8}7Rb. The trap laser is red-detuned from the $5S_{1/2}$ F=2 $\rightarrow$ $5P_{3/2}$ F'=3 D2 line cycling transition, while the repump laser is locked to the F=1 $\rightarrow$ F'=2 transition. The latter re-pumps atoms that may have fallen into F=1 back into the cycling/cooling transition. Spectroscopic numbers found in [46].

The repump laser in our Rb laser system is locked with the offset lock scheme shown in Figure 4.5. The optical beat note between the trap and repump lasers is converted to an electrical signal via a Receiver Optical Sub Assembly (ROSA) (Finisar, HFD6180-418). The electrical signal is then converted to a digital signal with a limiting amplifier

(Hittite, HMC750LP4), divided by eight in frequency (Hittite, HMC363G8), amplified, and compared to a known desired frequency (HP Agilent 8657) with a phase frequency detector (PFD) (Hittite, HMC439QS16G). The error signal from the PFD is sent through proportional-integral (PI) feedback to both current and piezo controls of the ECDL repump laser. The locking scheme is sufficiently robust that it rarely, if ever, falls out of lock, despite mechanical disturbances and the lock failure of the trap laser. In addition, the locking circuit is mostly assembled from evaluation boards, making it a low-cost locking solution ($\approx$ \$1500 not including labor). Prior to combining with the trap beam, the repump beam also passes through a +80 MHz single-pass AOM. The 80 MHz AOMs used for these beams provide fast on/off shuttering and amplitude control.
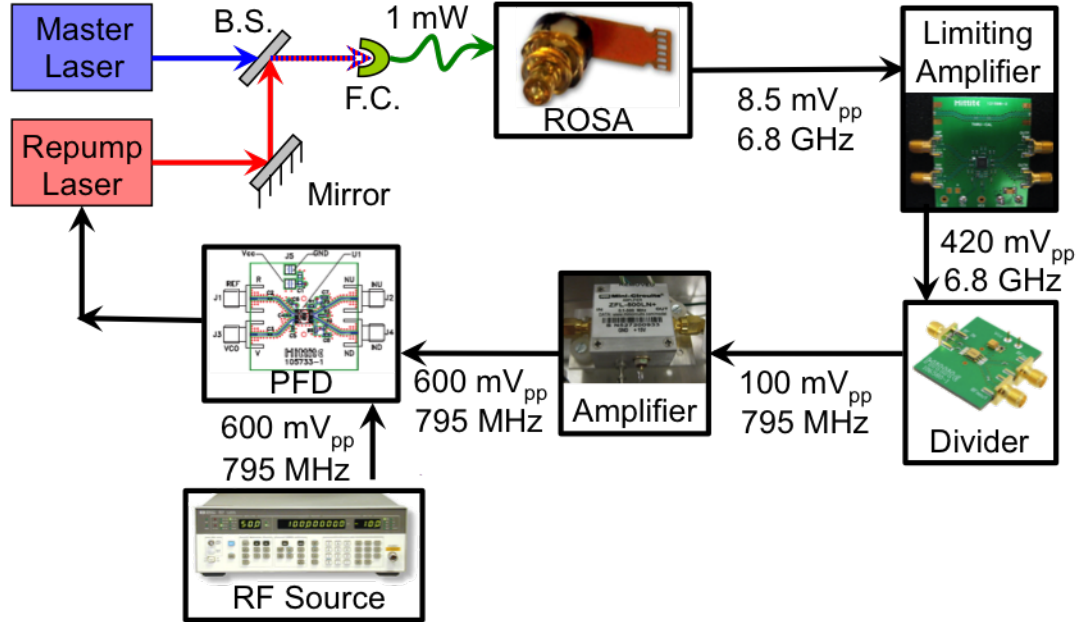
FIG. 4.5: Repump lock scheme. The repump laser is offset lock to the trap laser by overlapping the two beams and detecting the beat note The beat note is converted to an electrical signal which is digitized, divided, amplified, and compared to the desired frequency with the phase frequency detector (PFD). In the figure, B.S. is a non-polarizing 50/50 beamsplitter. The polarizations of the master and repump lasers are parallel at the fiber coupler (F.C.).

The exact frequency offset of the repump laser is dictated by the chosen frequency

from the RF source. The beat note is the difference between the master laser (which is locked 125 MHz to the blue of the F=2 → F'=3 transition) and the repump laser. To choose the frequency of the RF source, we use:

$$f_{RF} = \frac{1}{8} \times (f_{GS} - 266.65 - 125 - 80) \tag{4.1}$$

where f_{GS} is the ground state splitting, f_{RF} is the RF frequency, and units are in MHz. For ^{87}Rb, f_{GS} is 6.835 GHz, and the F'=2 to F'=3 splitting is 266.65 MHz, so we choose f_{RF} around 795.4 MHz. In practice, the optimized MOT occurs for $f_{RF} = 796.2$ MHz. The fast-Fourier transform of the beat note signal, when picked off after the amplifier and locked to 794 MHz, is shown in Figure 4.6. Table 4.1 shows calculated values for offset locking to other transitions, assuming the master laser is locked to the same transition.
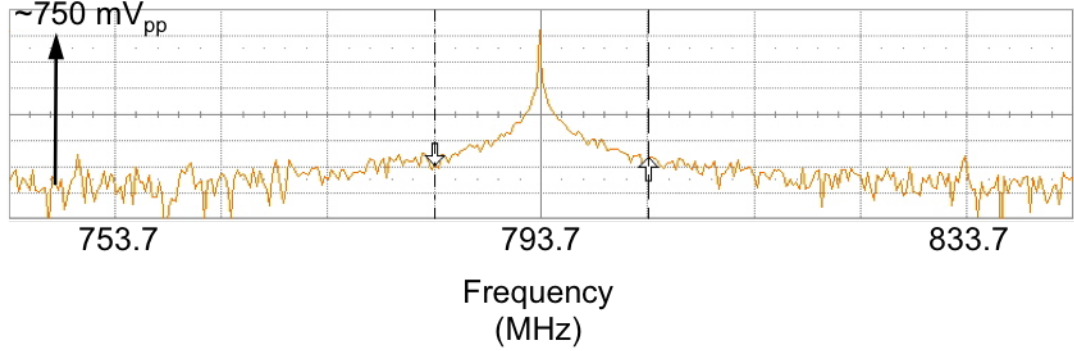
FIG. 4.6: Fast-Fourier transform (FFT) of the beat note signal. We monitor the divided and amplified beat note FFT signal on an oscilloscope. Typical signals are around 750 mV$_{pp}$.

TABLE 4.1: Offset lock frequencies.

Atom	Transition	Frequency (calc)	Frequency (exp)	Amplitude
^{87}Rb	F=1 to F'=2	795.4 MHz	796.2 MHz	0 dBm
^{87}Rb	F=1 to F'=1	775.8 MHz	n/a	0 dBm
^{85}Rb	F=2 to F'=3	338.8 MHz	338.75 MHz	7 dBm
^{85}Rb	F=2 to F'=2	330.9 MHz	330.5 MHz	7 dBm

58

The trap and repump beams are combined on a polarizing beam-splitting cube and then coupled to an optical fiber that bridges the two optics tables. Once on the apparatus table, the Rb combined trap-repump beam is sent through a tapered amplifier (TA) (Eagleyard EYP-TPA-0780-01000). Approximately 15 mW of power are input to the TA, and up to 400 mW output are realized with 1.60 A of current across the TA. After beam shaping and spatial filtering, approximately 320 mW of power is sent to the MOT, with an intensity of 1.4 mW/cm^2 in each overlapping beam in the MOT cell.

4.3.2 Potassium laser system

The K system has one master ECDL laser (New Focus Vortex) at 767 nm which seeds two higher power diode lasers (Eagleyard EYP-RWL-0770-00025) for the trap and repump beam. The hyperfine splitting of the ground level is small enough that a single frequency stabilized master laser can be used and the individual trap and repump frequencies can be produced with AOMs for the $4S_{1/2} \rightarrow 4P_{3/2}$ cycling and repump transitions of ^{39}K. We use a double-pass 80 (320) MHz AOM for the trap (repump) beam before seeding the second diode lasers.

Similar to the rubidium laser setup, the combined potassium trap-repump beam is amplified with a TA (Eagleyard EYP-TPA-0765-01500). However, the amplification for the potassium beam occurs on the laser optics table, prior to being coupled to an optical fiber. For this reason, output power from the TA is limited so as not to damage the optical fiber. This not only limits the power sent to the optical fiber, but also the power available at the K MOT. It should be noted that the beam quality from both the Rb and K TA output is not Gaussian (though it is advertised to be Gaussian – this could be a problem with our input coupling to the TA). This makes efficient coupling of the TA output to an optical fiber quite challenging. Therefore, the best fiber coupling that I was able to

achieve was approximately 30%. This led to only ≈ 60 mW of power available for MOT beams. Nonetheless, as is shown later in the chapter, this power is sufficient for producing a ^{39}K MOT.

4.3.3 Tapered amplifiers

Our laser amplification was done with two Eagleyard TAs with wavelengths centered at 780 and 765 nm for Rb and K, respectively. The amplifiers are capable of producing up to 1 W of output power with a seed power of only 10-15 mW when operated with sufficient current. We purchased the TA, OEM driver (ITC133), display unit (ITC100D), and faceplate (ITC100F), and constructed the mount and protection circuit in-house.

Figure 4.7 shows the mount design, based on similar designs by [69]. The mount is machined out of copper to provide heat sinking for the TA chip. It is also designed to be water cooling compatible, though we found water cooling was not necessary for our current implementation. The TA chip is held in the center with a screw and the pressure from either side of the mount. Plenty of thermal paste was used to ensure good contact between the TA chip and the copper mount. On either side of the TA chip, a lens screws into the mount to provide optical coupling to and from the amplifier. While these tapped lens holders were designed to allow adjustability of the focal point along the beam propagation axis, we found that the taps themselves did not provide sufficient stability for smooth adjustments. Therefore, if you change the focal point of an input or output lens, significant realigning of the beam to the lens is required for proper coupling with the amplifier.

The TA runs at a variable current between 0 and 2.5 A. In practice, we rarely ran the TA above 1.6 A. The documentation for the TA specifies that it has zero tolerance for reverse voltage, so a protection circuit incorporating a diode was implemented at the
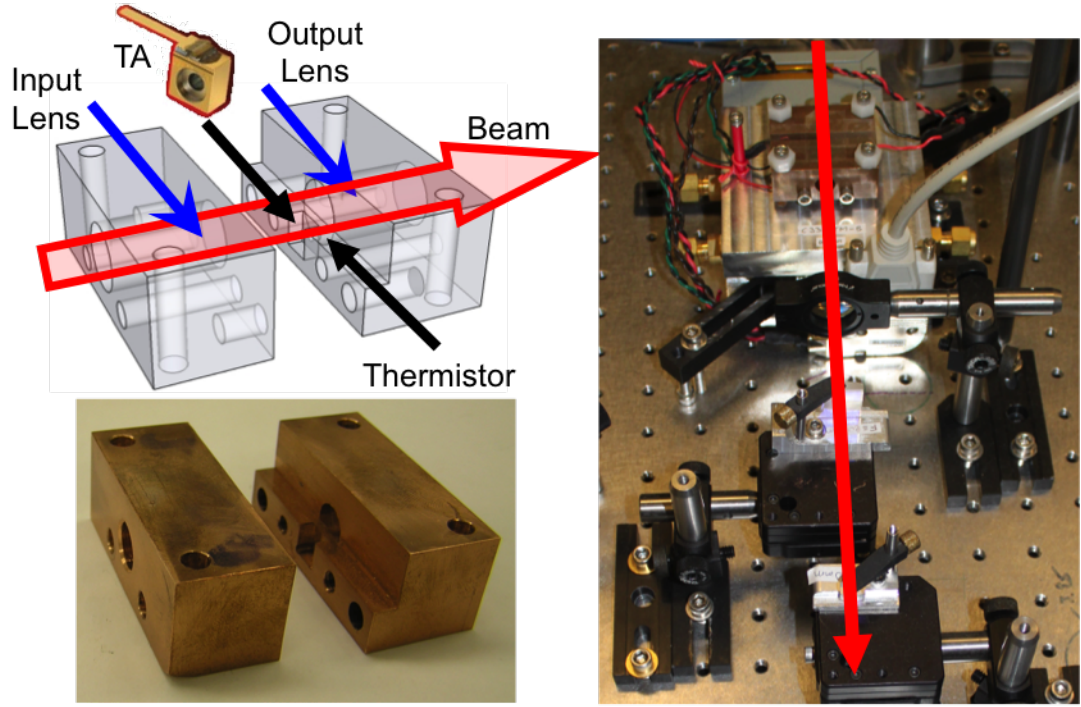
FIG. 4.7: Tapered amplifier mount. The tapered amplifier chips were mounted in a copper block which provided both a heat sink and mount for the TA chip and coupling optics.

input to the TA as shown in Figure 4.8.

The controller monitors the temperature of the TA via a thermistor placed directly adjacent to it on the mount. The mount itself sits on top of a Peltier thermoelectric cooler (TEC) which allows the user to temperature-tune the TA. The gain curve of the TA is temperature dependent. We therefore tune the temperature such that our desired wavelength is at the top of the gain curve. This not only gives the most power output, but also provides the most stability.
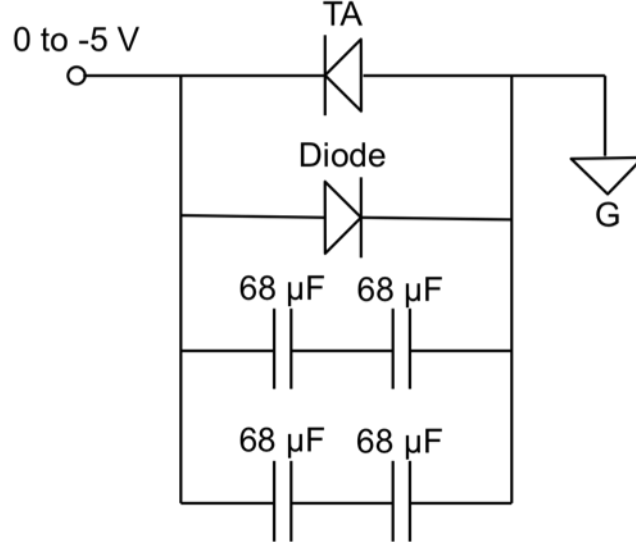
FIG. 4.8: Tapered amplifier protection circuit. The tapered amplifiers were electrically protected from negative voltage and noise through the implementation of the above circuit. The diode (Diodes Inc 6A05) provides a path to ground for reverse current, while the capacitors provide a filter for AC noise.

4.4 Experimental procedure

4.4.1 Magneto-optical trap and molasses

Once on the apparatus table, the combined and amplified trap and repump beam passes through two linear waveplates and two corresponding polarizing beam splitting cubes to separate the beam for each of the three cooling axes of the MOT. Each of these three separated beams is split into two counter-propagating beams with an additional polarizing beam splitting cube. Immediately before entering the MOT vacuum chamber, the beams pass through a final circular polarizing waveplate ($\lambda/4$) and a telescope. The presence of the telescope as the last element before the vacuum chamber allows us to use one inch optics up to that point. The 1:5 telescope expands the input beam to fill the 2 inch diameter of the telescope.

Initial formation of the MOT was done by retro-reflecting three pencil beams (without

the presence of the telescopes). Care was taken to ensure the correct circular polarization of the beams with respect to one another so that the overall polarity of the magnetic field could be easily flipped to match the beam polarization. Since overlapping the quadrupole minimum with the small pencil beams was expected to be challenging, we used a hand-held bar magnet to shift the magnetic minimum when first identifying the MOT. Once we were convinced of the retro-reflected beam alignment, we added in the counter-propagating beams one at a time, verifying that the MOT was still operational after each addition. With the three counter-propagating beams properly aligned, we inserted the six telescopes and optimized the alignment and polarization of the beams using the MOT.
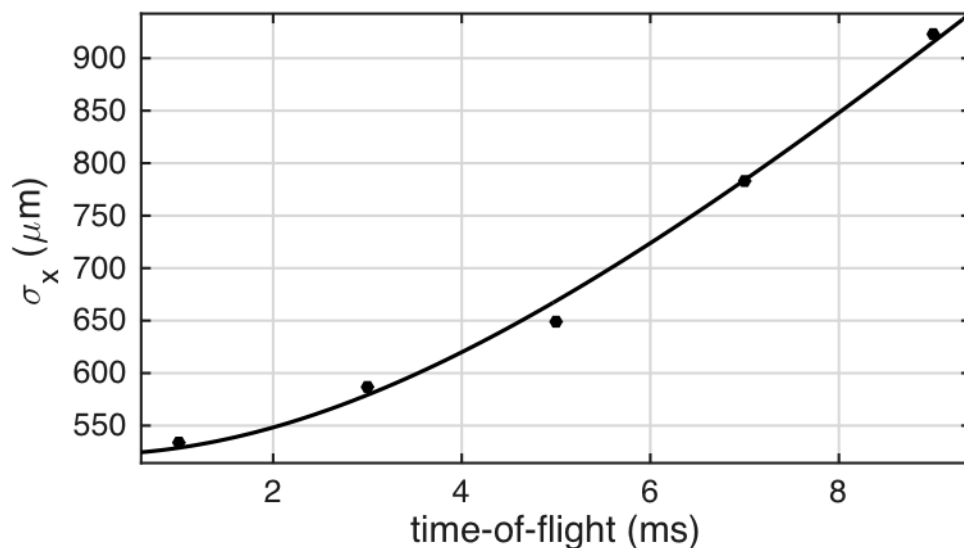
FIG. 4.9: ^{87}Rb MOT temperature. Expansion over time-of-flight gives a temperature measurement fit in this case of $T = 74\mu$K, $v = 8.4$ cm/s, and $\sigma_0 = 522\mu$m. Here, σ_x is given in Equation 2.27 and the general method is described in Figure 2.11 and Section 2.9.

The ^{87}Rb MOT loads several 10^8 atoms after 25 s at temperatures around 60 μK. Figure 4.9 shows a typical temperature measurement for a ^{87}Rb MOT. This particular measurement gives $T = 74\mu$K, $v = 8.4$ cm/s, and $\sigma_0 = 522\mu$m (see section 2.9 for pa-

rameter definitions). A fluorescence image of a ^{87}Rb MOT produced in our system is shown in Figure 4.10. We typically load the MOT using light induced atomic desorption (LIAD) [70], which is essentially an assortment of 405 nm LEDs pointing at the MOT region. Akin to the photoelectric effect, the UV light causes rubidium atoms which have stuck to the walls of the vacuum apparatus to desorb, giving them another opportunity to be cooled and trapped by the MOT. The effect on the ^{87}Rb MOT loading rate of the LIAD vs using the dispenser for loading vs using neither LIAD nor dispenser are shown in Figure 4.11.
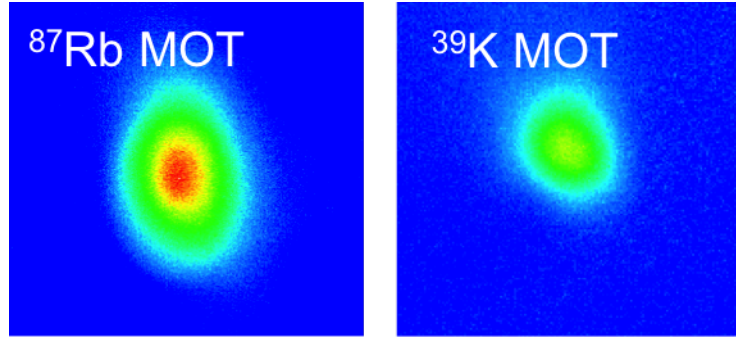
FIG. 4.10: Magneto-optical traps. Fluorescence images of a ^{87}Rb MOT (left) and ^{39}K MOT (right) produced with our apparatus.

We combine our potassium trap and repump beam with the output from the rubidium TA on the apparatus table. This combination occurs before splitting along various MOT beamlines. For the polarization of the potassium beams, an additional dichroic linear waveplate ($\lambda/2$ for 767 nm light, λ for 780 nm light) is placed before each polarizing beam splitting cube. This setup is convenient in that all the alignment of the potassium MOT beams is accomplished with only two mirrors. In addition, we can readily switch between rubidium, potassium, and combined MOTs simply by shuttering the appropriate lasers. Due to the reduced power in the potassium MOT beams, we produce ^{39}K MOTs with $\approx 10^7$ atoms after 30 s.
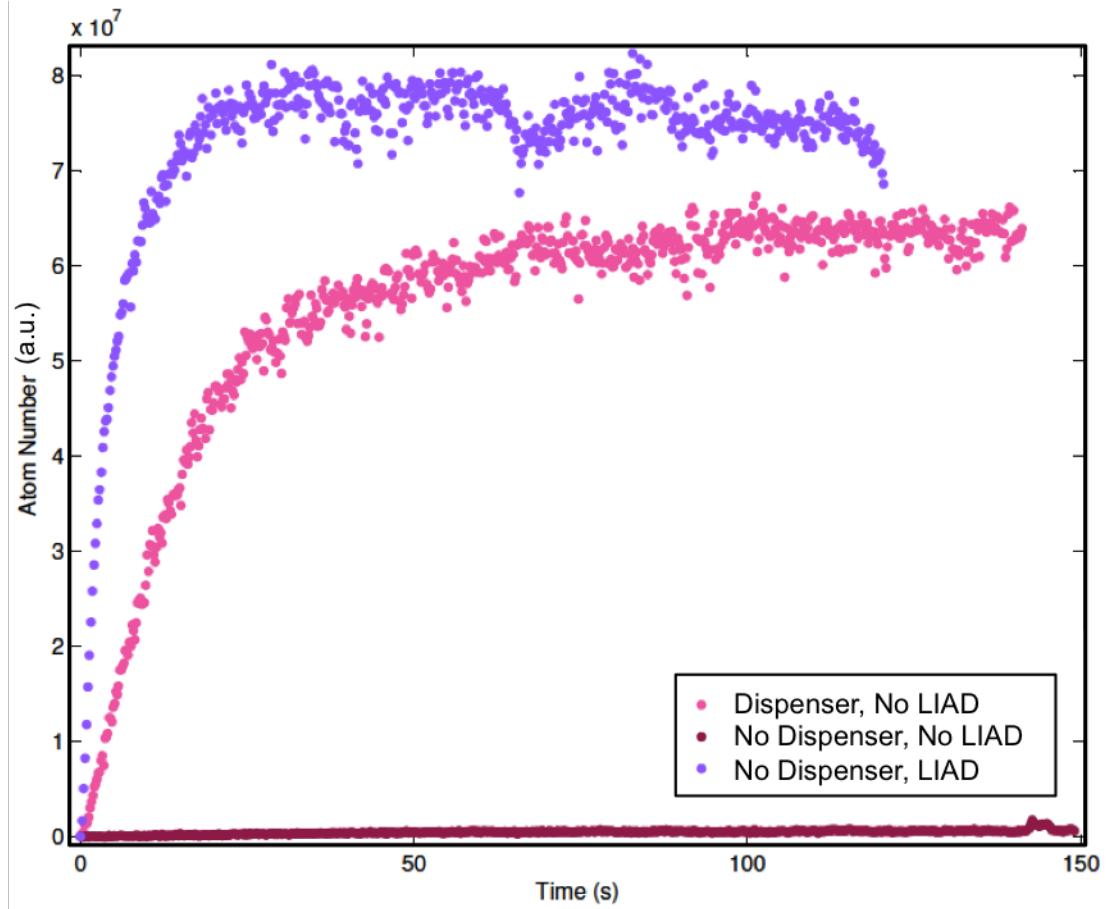
FIG. 4.11: MOT loading with LIAD. Number of atoms estimated in early (July 2009) ^{87}Rb MOTs as a function of loading time. Loading rates are shown with no dispenser or LIAD, with only the dispenser, and with only LIAD. Both the loading rate and the final number of atoms improves with LIAD over using only the dispenser.

The optical molasses stage of the experiment is implemented by quickly turning off the MOT light and magnetic fields. The MOT beams are then switched back on at reduced power and additional detuning of 56 MHz (for a total detuning of 71 MHz to the red of the F=2 to F'=3 transition) for a period of 5-12 ms. The repump light is also switched on at reduced power.

The optical molasses is more sensitive to alignment and power imbalances than the MOT is. Therefore additional care was taken to ensure the molasses beams (which are

the same as the MOT beams) were properly aligned. When we first began attempts at optical molasses, we started by watching the MOT on a security camera as we switched off the MOT coils. Power imbalance causes the MOT cloud to disperse directionally. Therefore, we balanced the power of the beams such that the MOT remained stationary as we turned off the coils. From this point, optimization is done using a long time-of-flight fluorescence image while further adjusting alignment, power balancing, and bias fields until the temperature (size of cloud at long time-of-flight) is minimized. The molasses was shown to reduce temperatures to as low as 4 μK along one axis in ^{87}Rb when working with reduced atom numbers. During typical use, the molasses reached temperatures around 30 μK.
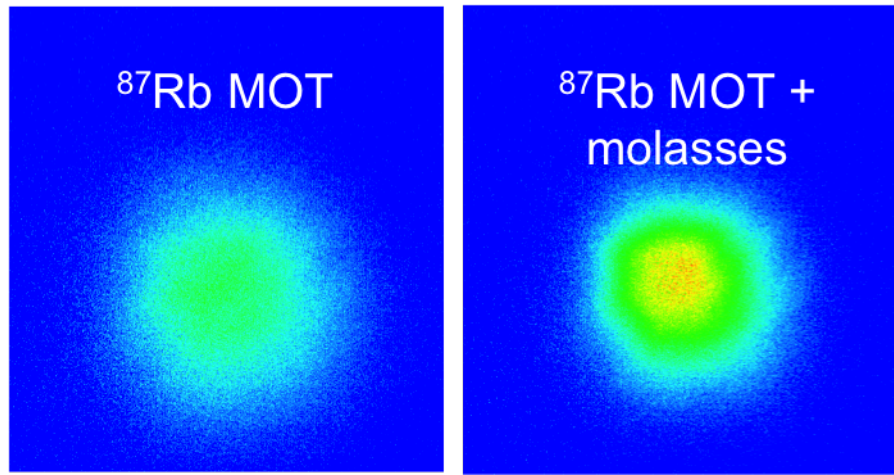
FIG. 4.12: Rb optical molasses. Fluorescence images of a ^{87}Rb cloud of atoms left to expand for $\approx$ 10 ms time-of-flight after early molasses demonstration. The left image shows a $\approx 60\mu$K MOT expanding, while the right image shows the same cloud expanding after a brief molasses period with temperatures $\approx 30\mu$K. The cloud on the right shows a denser, more compact cloud, indicating cooler temperatures.

Potassium is more challenging to cool to sub-Doppler temperatures due to the smaller splitting of the hyperfine structure. If you recall from Figures 2.1 and 2.2, the ^{87}Rb 5^2P$_{3/2}$ hyperfine levels are split over 495.8 MHz, while the ^{39}K 4^2P$_{3/2}$ level spread is 33.8 MHz

66

[46, 47]. Nonetheless, following a procedure akin to [71] we were able to significantly improve the temperature of our cold potassium cloud. Figure 4.13 below shows the TOF temperature measurement documenting an improvement from 1550 μK to 240 μK during my tenure.
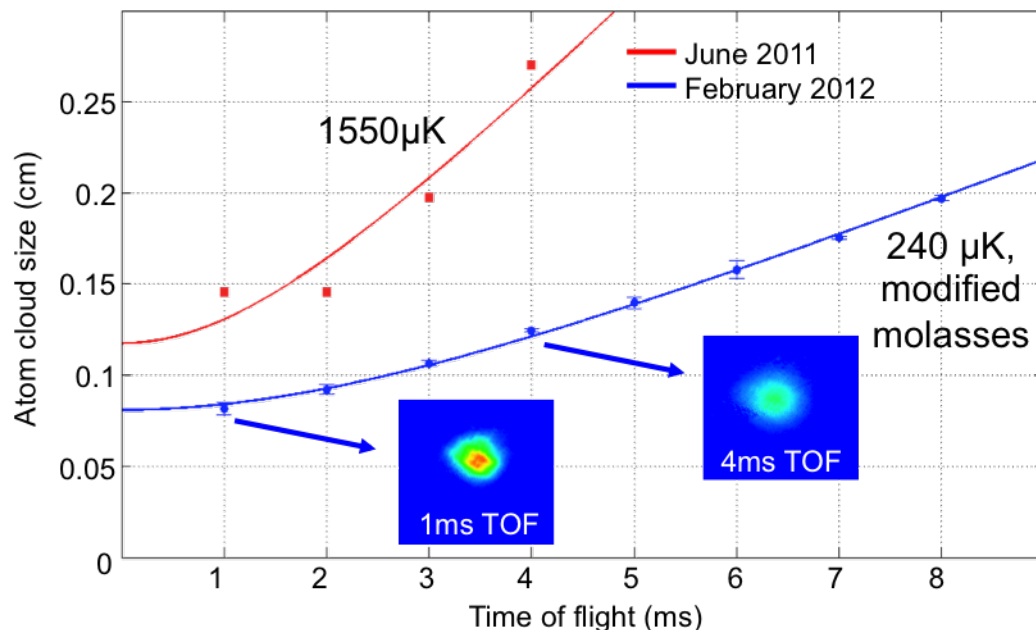
FIG. 4.13: K cooling. By implementing a cooling scheme inspired by [71], we were able to further cool potassium from temperatures around 1550 μK to a temperature of 240 μK.

4.4.2 Optical pumping, magnetic trapping, and transport

After the molasses stage, a brief ($\approx$ 1 ms) optical pumping pulse is applied to preferentially populate the $|F = 2, m_F = 2\rangle$ ground state. The pulse is tuned to $|F = 2, m_F = 2\rangle$ resonance, though the energy level is shifted by 5.8 MHz to the red due to the presence of a 9.1 G vertical bias field used to create a quantization axis. The polarization and alignment of the optical pumping beam is tuned to maximize the number of atoms in the magnetic trap. This is done by comparing the number of atoms in the magnetic trap

when the optical pumping beam is present and blocked. As long as the beam is hitting the atoms, there should be some effect from the presence of the beam. At this point, one can choose to either maximize or minimize the number of atoms in the magnetic trap. It is sometimes easier to optimize towards zero signal rather than a maximum signal. If the zero signal case is chosen, after optimizing the polarization and alignment, one needs only to switch the polarity of the magnetic field in order to maximize the number of atoms in the magnetic trap. Once this is done, further optimization of the beam power, detuning, and timing scheme is straightforward.

After the optical pumping pulse, we quickly switch on the magnetic trap. Our magnetic trap is a quadrupole trap formed with two anti-Helmholtz coils producing a gradient of 80 G/cm. When initially demonstrating magnetic trapping, we followed a spin distillation scheme to ensure we are only trapping the $m_F = 2$ atoms. In this scheme, we rapidly turn on the magnetic trap coils to approximately 30 G/cm on the weak axis for 500 ms (long enough for untrapped atoms to leave), thus trapping $|F=2, m_F = 2\rangle$ and $|F=2, m_F = 1\rangle$ atoms. Then, we ramp the gradient to a set point until we see a change in atom number before ramping the gradient back up to the maximum 80 G/cm. If we plot the atom number vs. that set point, we obtain the plot shown in Figure 4.14. Based on this data, we pick a quadrupole coil current such that only $|F=2, m_F = 2\rangle$ atoms are trapped during the normal operation of our magnetic trap.

With only the $m_F = 2$ atoms in the magnetic trap, and with the optimized optical pumping pulse, we are able to load up to 3×10^8 atoms into the magnetic trap at a temperature of approximately 50 μK and with lifetimes well over 10 s and phase space densities on the order of 10^{-6}. Figure 4.15 shows a magnetically trapped cloud of ^{87}Rb atoms and a lifetime measurement showing a 14.7 s lifetime. Despite water cooling the coils, they can only be left on for ≈ 30 s before the temperature rises above 46 C (above which a temperature sensor attached to the coils turns the current off), which limits the
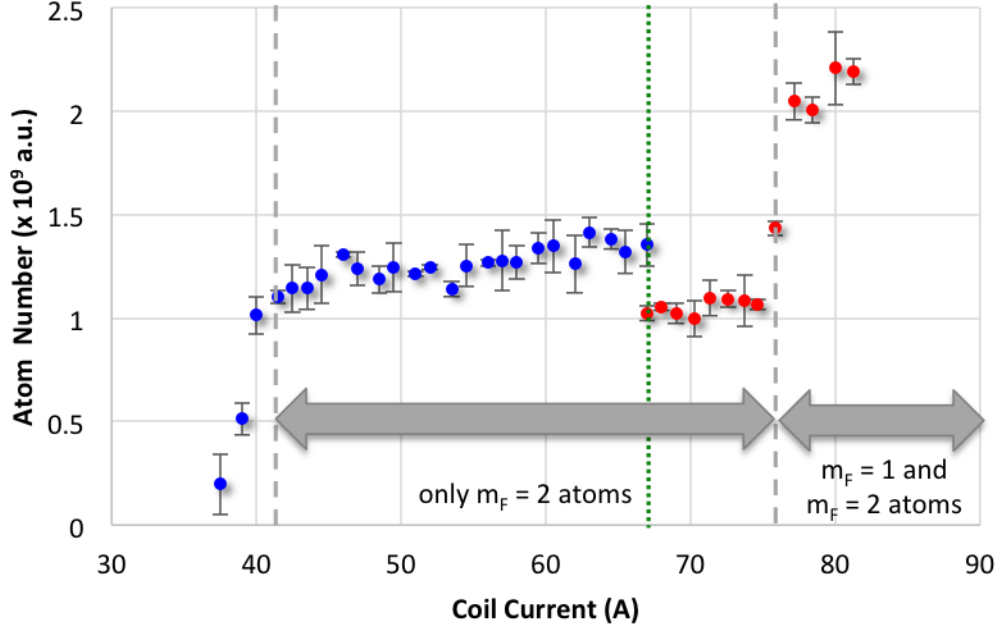
FIG. 4.14: Spin distillation of magnetically trapped ^{87}Rb. Number of atoms in the magnetic trap as a function of magnetic trap coil current. We begin at the green dashed line and decrease the current until we see no atoms in the trap. We begin again at the green dashed line and increase the current until we see an increase of atoms. This increase is the result of trapping both $m_F = 1$ and $m_F = 2$ atoms in the magnetic trap. Therefore, the region indicated between the gray dashed lines produces a gradient sufficient to hold only the $m_F = 2$ atoms. The error bars represent the standard deviation of 3 data points.

accuracy of our long lifetime measurements.

The atoms are transferred from the initial magnetic trap to a magnetic transport system which shuttles atoms from the MOT chamber to the chip chamber. The transport system consists of 7 pairs of coils in anti-Helmholtz configuration. Current through these coils is ramped such that the magnetic minimum is transferred along the 60 cm path over the course of 8 s. More details on the magnetic transport system can be found in [54, 21].
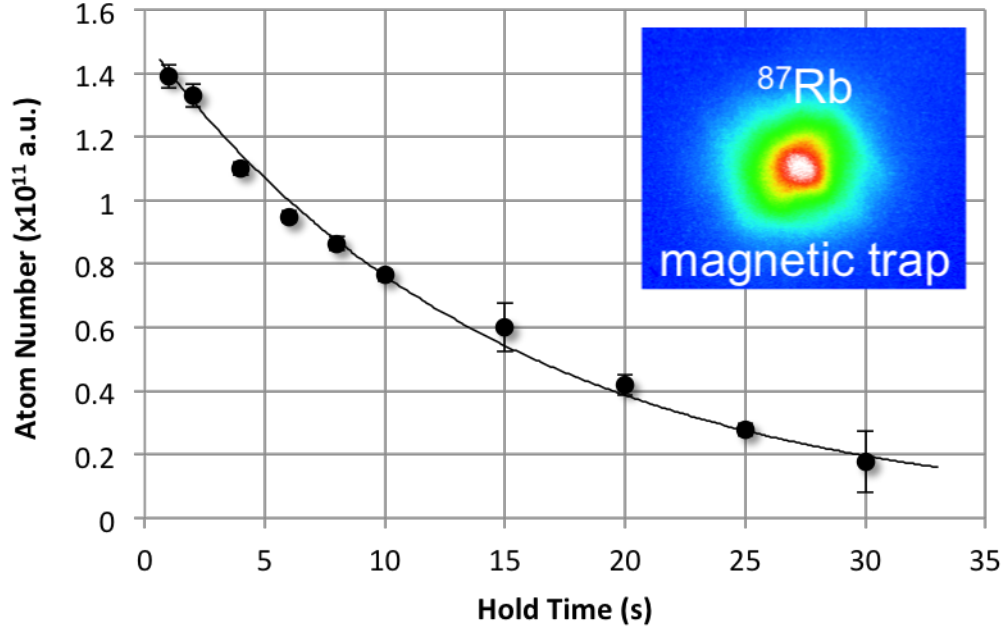
FIG. 4.15: Lifetime of magnetically trapped ^{87}Rb in the $|$F=2,m$_F$=2$\rangle$ state. This figure shows a lifetime measurement of ^{87}Rb atoms magnetically trapped in the $|$F=2,m$_F$=2$\rangle$ state based on fluorescence imaging. The fitted curve shows a lifetime of 14.7 s. The error bars represent the standard deviation of three separate data sets. The inset shows a fluorescence image of magnetically trapped ^{87}Rb atoms.

4.4.3 Chip trap

At the end of the transport cycle, we transfer over 5×10^6 atoms into the Z-wire chip trap. The trap is produced with 1 A of current from a floating High Finesse current driver (BCS-5/5) with galvanically isolated analog and TTL controls. A home-built "kill box" allows a maximum of 1 A of current through the Z-wire for no longer than 10 s. The chip itself is grounded through the chip stack, which is grounded to the rest of the apparatus through a braided strip. Current passes through the chip's Z-wire and an external hold field of B$_{hold}$=20 G is applied. A Ioffe field of B$_{Ioffe}$=4.9 G raises the trap bottom to minimize spin-flip loss. Figure 2.8 in Chapter 2 shows the orientation of these magnetic fields with respect to the atom chip. The field calibrations can be found in Table 4.2 below.

TABLE 4.2: Magnetic field calibration of the chip bias coils.

Coil	Magnetic Field (G/A)	Inductance (μH)	Impedance (Ω)
Horizontal Bias	2.9	35	0.1
Ioffe	2.66	29	0.036
Vertical Bias	1.64	n/a	n/a

Figure 4.16 shows the hand-off between the magnetic transport trap and the chip trap. The chip-trapped atoms have an initial phase space density of 5×10^{-6} and a lifetime approaching 7 s (shown in Figure 4.17).

From here, we can evaporatively cool our atoms to quantum degeneracy and/or load into a dipole trap. The evaporative cooling stages to BEC are detailed in the following chapter.

4.4.4 Dipole trapping at the atom chip

We efficiently load atoms from the atom chip magnetic trap to an elongated dipole trap aligned with the axial direction of the chip trap. This provides sufficient mode matching between the two traps that most of the atoms can be transferred with limited heating when aligned properly.

We use several alignment tricks to perform the transfer. The dipole beam is formed by about 1 W at 1064 nm from a NovaWave Technologies fiber laser. The beam passes through an 80 MHz AOM for amplitude control, a shutter, and a 50 cm achromat lens for focusing, before combining it with the pump/probe beam path in the same direction on a dichroic mirror (see Figure 4.18). Alignment control is done via two mirrors prior to combining on the dichroic mirror.

Alignment is done in the following manner. Initial alignment is done without the focusing lens. We simply overlap the dipole beam along the probe path. Next we align the lens positioning along the vertical axis and the horizontal axis transverse to the axis
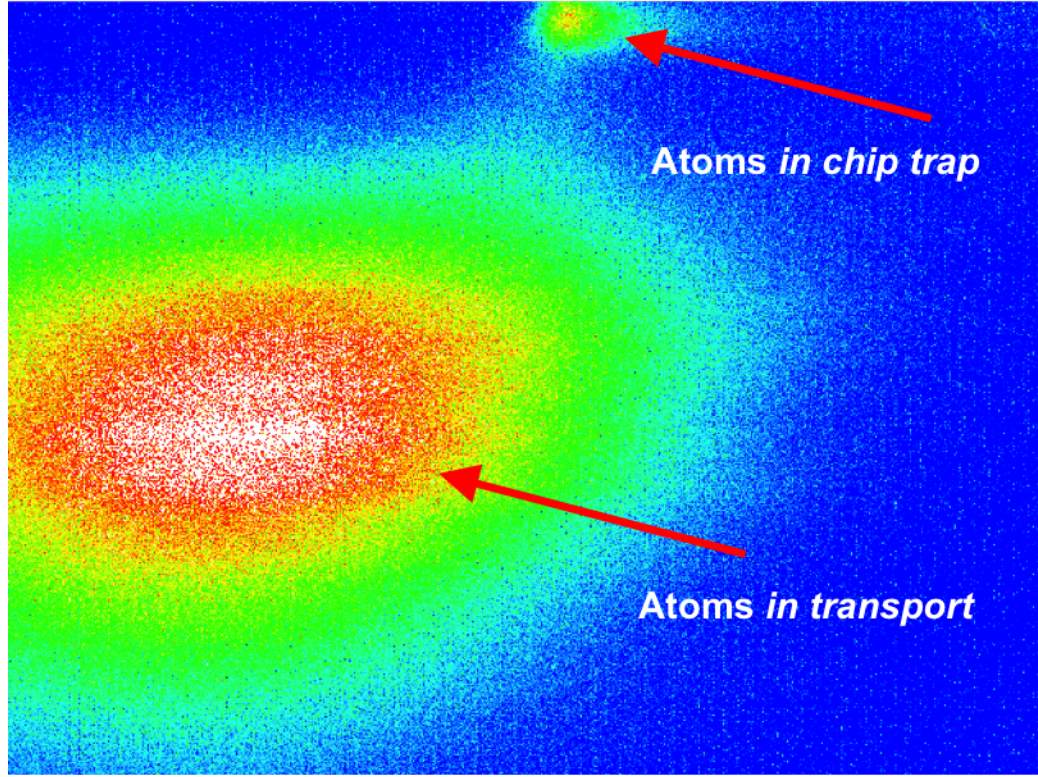
FIG. 4.16: Transport trap to atom chip trap transfer. This figure shows one of the first demonstration of chip-trapped ^{87}Rb atoms. The large cloud at the bottom left are atoms at the end of the transport cycle. The small cloud at the top right is trapped by the atom chip. Here the chip is horizontally along the top of the image, but out of the fram of the image in order to capture the atoms in transport in the field of view. Photo courtesy of Austin Ziltz.

of propagation so as to overlap the dipole trap with the atom cloud. This is done by first ensuring that the radial camera is well focused on the position of the atoms in the magnetic chip trap, and then recording this position with a cursor on the screen. With the experiment off, the camera free-running, and the dipole beam amplitude extremely low, we insert the lens and overlap the position of the focused dipole spot onto the camera position where the atoms were previously recorded. In a similar manner, we then adjust the lens along the axis of propagation: The dipole beam spot size imaged by the camera will appear smallest when the focal point of the beam overlaps with the focal plane of the
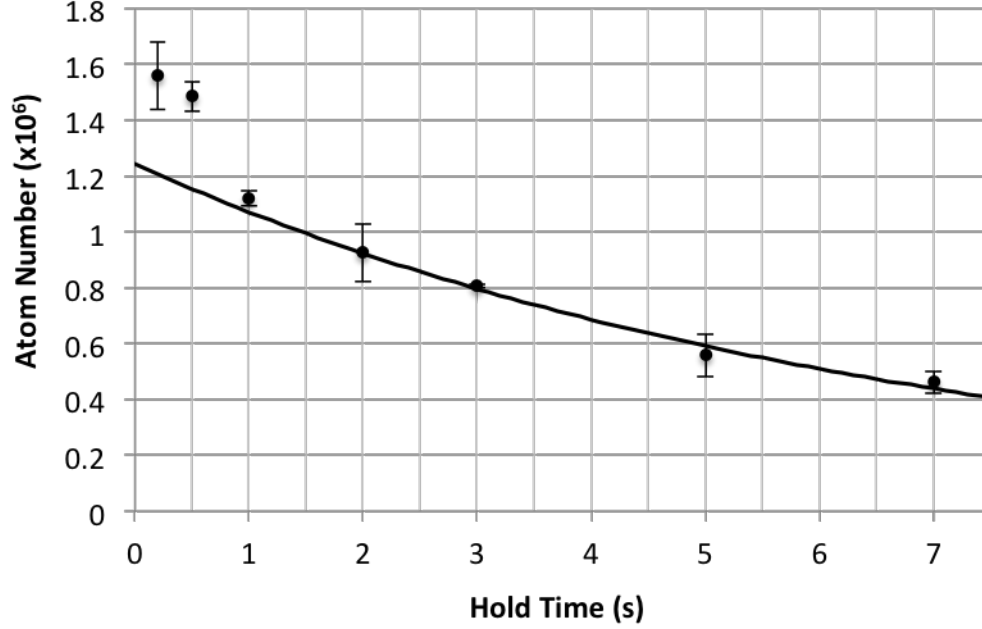
FIG. 4.17: Chip lifetime measurement. This figure shows a lifetime measurement of our atoms in the chip trap. The exponential curve drawn shows a lifetime of 6.7 s, fitted to the data points at Hold Time = 2, 3, 5, and 7 s. The steep decline in atom number in the first points is a product of free evaporation in the trap. Error bars drawn here are the standard deviation of 3-5 data points.

camera imaging system, and which also corresponds with the location of the atoms. The idea is that this process will get the alignment close enough to at least see a small signal of dipole trapped atoms when the magnetic chip trap has been switched off for some time. Fine tuning of the alignment adjustments can be done to optimize this signal.

We estimate a dipole beam waist radius of 60 μm and a trap depth of 20 μK. We load the dipole trap from a relaxed magnetic chip trap. This is done such that the magnetic chip trap is far from the chip ($\approx$465 μm) which allows us to 1) avoid alignment tragedies like burning out a chip wire with a high intensity beam, and 2) avoid clipping the dipole beam on the chip which would detract from good dipole beam quality. We also turn on the dipole beam slowly over the course of 100 ms in order to minimize heating. As you

73
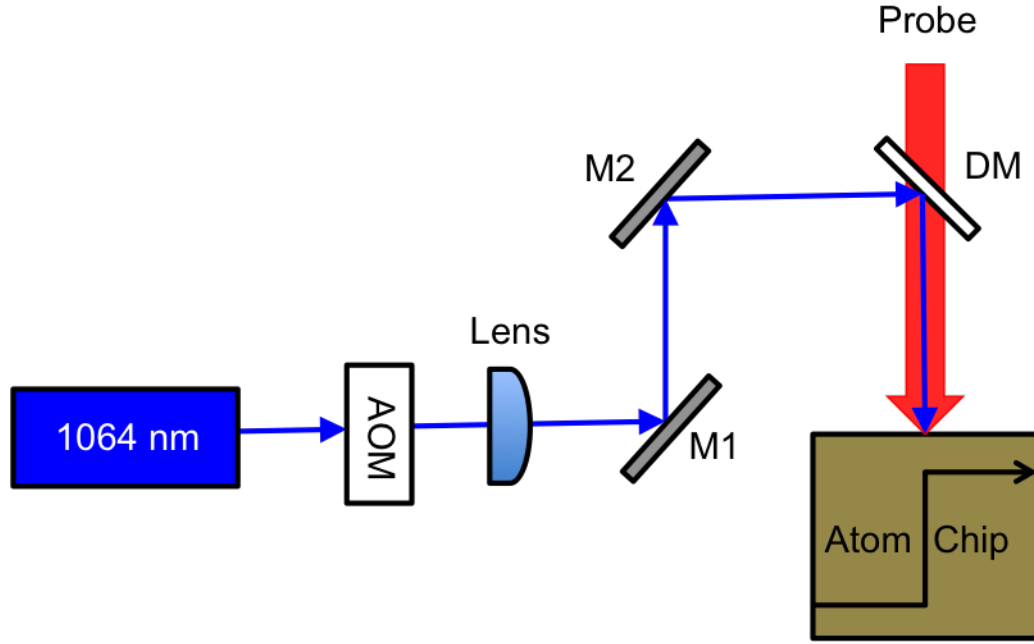
FIG. 4.18: Dipole laser scheme. The dipole trap is formed with a 1064 nm laser beam focused to a 60 μm waist radius and directed along the axial direction of the chip trap. The lens is a 50 cm achromat lens, M1 and M2 are mirrors, and DM is a dichroic mirror (Thorlabs DMSP1000) that reflects the dipole trap beam while passing the pump/probe beam. Note: This figure is a schematic only and does not indicate the actual layout or order of the optical elements.

can see from Figure 4.19, these methods allow for successful loading into the dipole trap.

Here I will take a moment to warn experimentalists of the importance of anti-reflection coatings on glass cells. Later, we explain that we dipole trap the atoms to produce a 1D channel in which the atoms can travel. The idea is to pull the atoms to one end of the elongated trap and then sling-shot them to the other end. When we attempted to implement this, the atoms did not budge. This was due to unanticipated reflections from the glass cell producing a small but powerful lattice potential (recall Chapter 3). Note that uncoated glass typically reflects 4%. This was sufficient to immobilize atoms at $< 5\mu$K temperatures. It was only after tilting the input beam several degrees so as to minimize the overlap of the incident and spuriously retro-reflected beam that the lattice was weak enough to allow the atoms to translate along the long axis of the dipole trap.
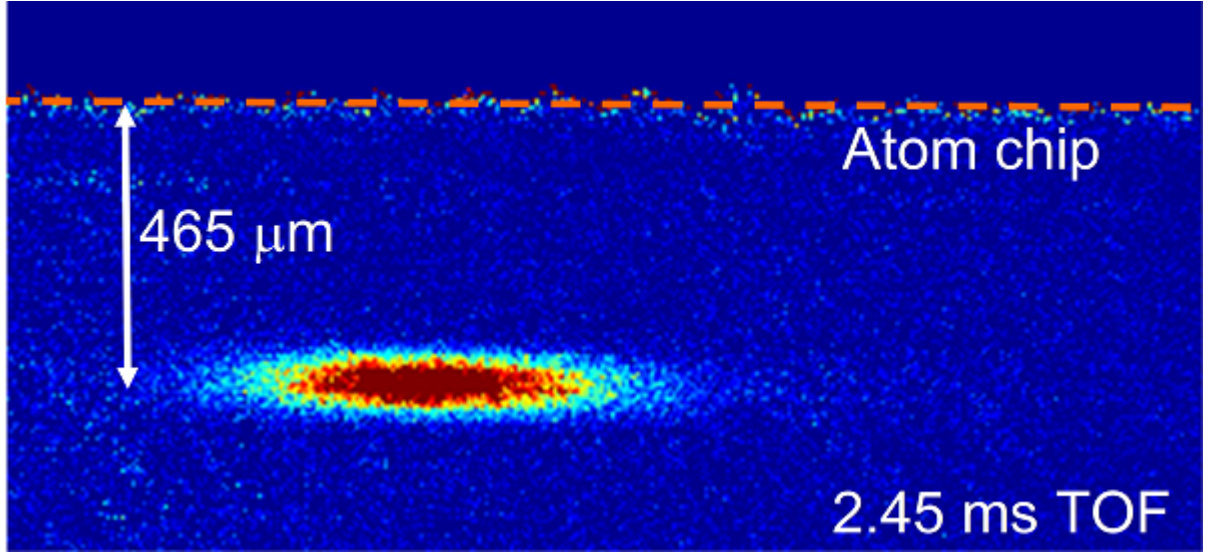
FIG. 4.19: Dipole trapped atoms. We trap approximately 6×10^4 ^{87}Rb atoms in this image at a distance of approximately 465 μm from the surface of the chip. Atoms are loaded from the magnetic chip trap after some initial evaporative cooling stages. The image was taken after 2.45 ms time-of-flight.

4.5   Imaging systems

At the atom chip, our apparatus is designed with several imaging choices, including both fluorescence and absorption imaging along both the axial and radial directions. In Figure 4.20, the imaging axes are defined such that axial imaging allows one to image from the side such that the entire length of the cigar-shaped trap can be resolved, while radial imaging looks "down the barrel" of the cigar-shaped trap. While radial absorption imaging is useful in initial chip trap loading due to the higher signal from the larger optical density of the atoms along that axis, you will see in the following chapter that axial imaging allows us to gain additional information about the spatial uniformity of our cloud in the atom chip trap. Figure 4.20 depicts these axes with respect to the chip region of the apparatus. The green arrows represent the circular polarization of the beam. We also apply a small magnetic field as a quantization axis: For radial (axial) imaging, we use the round Ioffe

(square hold) coils in Figure 4.20.
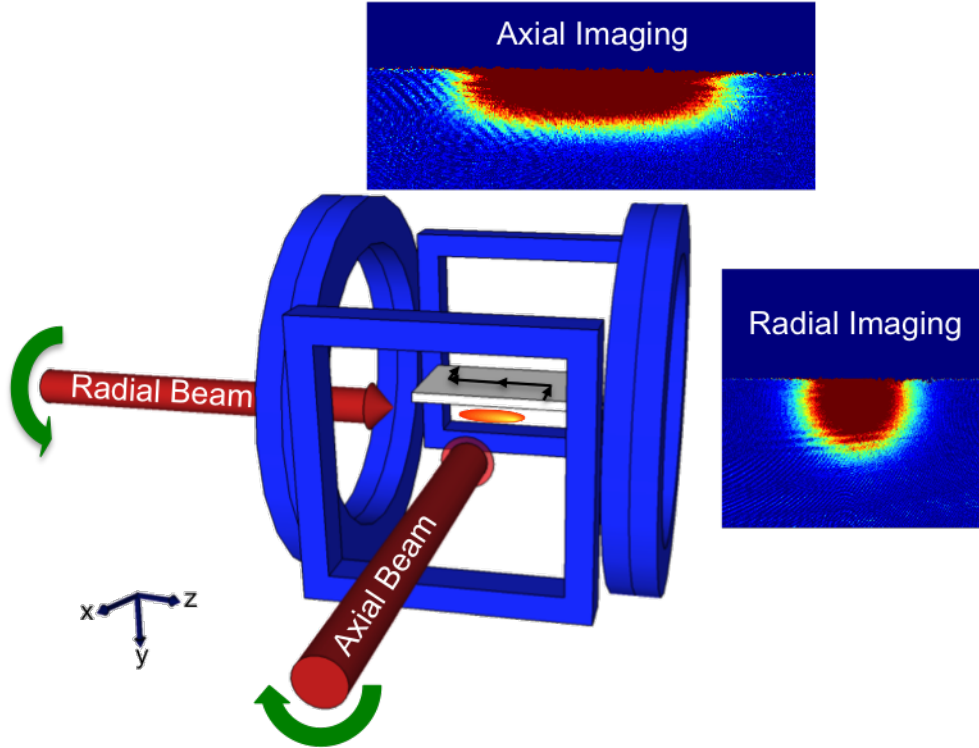
FIG. 4.20: Imaging axes at the chip. Our system is capable of both absorption and fluorescence imaging along both the radial and axial axes of the cigar-shaped chip trap. Radial imaging images "down the barrel" of the cigar, providing higher optical density for imaging at higher temperatures. Axial imaging shows the length of the cigar and is useful at colder temperatures for detecting the bimodal distribution signature of BEC.

Most of the data acquired in this thesis was taken using absorption imaging. In practice, we apply two very short (0.1μs) pulses of on-resonance light for absorption imaging. The first pulse produces the atom image, and is usually taken after some reasonable (2-20 ms) time-of-flight. The second pulse produces the laser image, and is applied after the atoms have had enough time to fall out of the frame of the image (typically 200-500 ms). We apply Equation 2.23 from Chapter 2 to determine the OD, and then divide by the atom-photon cross-section σ_0 to determine the atoms per pixel.

We also have the ability to image atoms with fluorescence in each of the chambers.

In the MOT chamber, we use the MOT beams to excite the atoms and collect the emitted photons with a nearby camera. The beams and shutter can be left on for 10's of ms if needed.

The imaging system itself is a CCD camera (Unibrain) that has had the on-chip window of the CCD removed (to reduce laser imaging fringes). Each of these cameras are 12-bit and are connected to the desktop computers using the Firewire communication standard IEEE 1394b. The properties of the chip radial and axial cameras as well as the MOT camera can be found in Table 4.3. The chip cameras are each attached to a lens tube that houses a single achromat lens pair (Thorlabs MAP10100100-B) at two focal lengths away from both the CCD and the atoms to be imaged (see the 2f-2f imaging configuration in Figure 4.21). The MOT camera has two achromat lenses set-up in the style of the Thorlabs MAP lens pair. The properties of the imaging systems can be found in Table 4.4. Magnification, and depth-of-focus provided by Anuraag Sensharma.

TABLE 4.3: Camera properties.

Camera	Model	Number of Pixels	Pixel Size (μm)
Chip Radial	Unibrain Fire-i 530b	640×480	7.4×7.4
Chip Axial	Unibrain Fire-i 701b	1280×960	4.65×4.65
MOT	Unibrain Fire-i 530b	640×480	7.4×7.4

TABLE 4.4: Imaging System properties.

Camera	Focal Length	Magnification	Resolution	Depth of Field
Chip Radial	5 cm	-1.00	6.1 μm	$\pm$ 0.5 mm
Chip Axial	5 cm	-1.00	6.1 μm	$\pm$ 0.5 mm
MOT	3.75 cm	-0.489	unknown	$\pm$ 0.76 mm
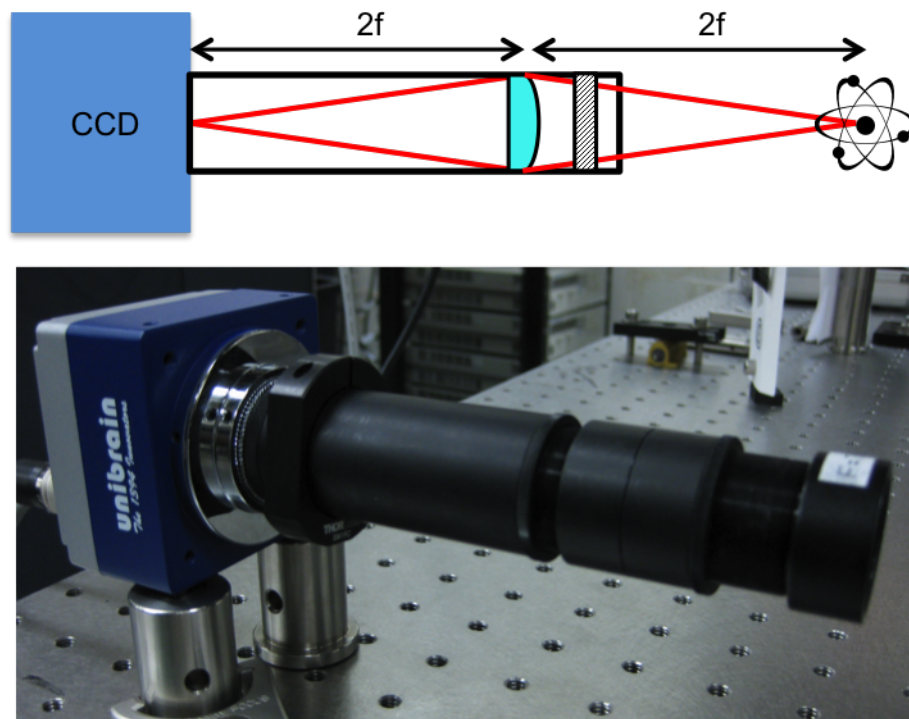
FIG. 4.21: Imaging system camera. We image atoms by way of a CCD camera (blue) with a lens tube housing a single achromat lens (cyan) and any necessary filters (gray hash).

CHAPTER 5

Production of Bose-Einstein condensates

This chapter covers the production and observation of BEC in our atom chip trap. In our system, we use radio frequency (RF) evaporation to cool our ultracold ^{87}Rb atoms while varying the atom chip trap potential. I provide details about the various trapping frequencies used for the loading, compression, and decompression stages, along with the RF sweep properties. I also outline the characterization of the chip trap (including an unexpected dimple trap), as well as image analysis methods for determining atom number, temperature, and phase space density. Finally, I describe the three defining signatures of BEC that we use: 1) bimodal distribution, 2) anisotropic expansion, and 3) phase space density ≥ 2.612.

5.1 Evaporative cooling

The final cooling method for achieving BEC is evaporative cooling (recall Section 2.6). Our evaporative cooling takes place in the atom chip Z-wire trap using an RF field through an adjacent U-wire for the RF magnetic field (see Figure 2.7). Both the RF magnetic field and the trap itself can be adjusted for optimization. We evaporate using 7 RF knife sweeps in 4 different chip traps. Once the ^{87}Rb atoms are loaded into the Z-wire trap, we apply our RF knife and sweep it from larger to smaller frequencies, first in the initial chip loading trap, then in a compressed trap, then in a final trap in which we do the imaging, and finally in a "dimple trap" which is discovered as atoms are further cooled (see Section 5.2). While sweep parameters (initial and final RF values, times for sufficient rethermalization, etc) could be estimated using various trap parameters, this is a complex optimization problem. In practice, optimization is always done via trial and error.

We begin our evaporative cooling by applying a 20 MHz RF knife to our atoms confined in the trap into which they are initially loaded. During a period of free evaporation (i.e., no RF sweep, but atoms are ejected simply because the trap is not deep enough), we also compress the trap. Once the trap is fully compressed, we perform three RF sweeps over 6 s before decompressing into our final "maging trap". In this decompressed trap, two additional RF sweeps bring us to condensation. A summary of the chip current, B_{Hold}, B_{Ioffe}, axial and radial trap frequencies, trap depth, and trap bottom can be found in Table 5.1. These values are determined by modeling the magnetic trap produced by a given wire pattern and current, as in Equation 2.5. In addition, the timing of the RF sweeps and the trap compression/decompression can be visualized in Figure 5.1.

Both Table 5.1 and Figure 5.1 are the successful results of much trial and error and optimization of the system parameters. Of course when we set out from our initial chip trap to begin evaporative cooling, we had to start somewhere. The results of early RF

TABLE 5.1: Calculated chip trap parameters with $I = 1$ A through a rectangular conductor, as given by Equation 2.5.

Trap	B_{Hold}	B_{Ioffe}	ω_{rad} (Hz)	ω_{ax} (Hz)	Distance
Initial	20 G	4.9 G	$2\pi \times 1040$	$2\pi \times 9.1$	91 μm
Comp	46.4 G	9.2 G	$2\pi \times 2810$	$2\pi \times 5.7$	22 μm
Final	20 G	4.9 G	$2\pi \times 1040$	$2\pi \times 9.1$	91 μm

TABLE 5.2: Measured chip trap parameters with $I = 1$ A through a rectangular conductor, by fitting the density images described in Equation 5.1 ("Image Fits") or by using the sloshing method described in Section 5.2 and Figure 5.4 ("Sloshing").

Trap	Method	ω_{rad} (Hz)	ω_{ax} (Hz)
Final	Image Fits	n/a	$2\pi \times 8.5$
Dimple	Image Fits	n/a	$2\pi \times 51$
Dimple	Sloshing	$2\pi \times 1034$	$2\pi \times 53$

evaporation paths were unsuccessful. We also needed a way to diagnose our progress, as well as a basic figure of merit for charting our progress towards BEC. Our method of diagnosing the success and efficiency of our RF evaporation path was by plotting phase space density as a function of atom number. Evaporative cooling will naturally decrease the number of atoms in the trap. The goal is to simultaneously increase the phase space density as much as possible for a given atom number loss.

We also monitor temperature, density, and collision rate of our atoms as an additional diagnostic tool, given from the time-of-flight temperature measurements described in Section 2.9 and Equations 2.6 and 2.7. Generally one would seek an evaporation path in which temperature continuously decreases and density and collision rates continually increase. When choosing an evaporative path, there is a trade-off between a slow efficient evaporation and a fast lossy evaporation. At first glance, slow efficient evaporation sounds preferred. However, recall there is a limited lifetime in the chip trap due to the quality of the vacuum, so we use a less efficient but quicker evaporation. Similarly, it would seem that as large a density as possible would be desired. However, for large enough density, one will begin to experience three-body losses leading to an atom number decrease without
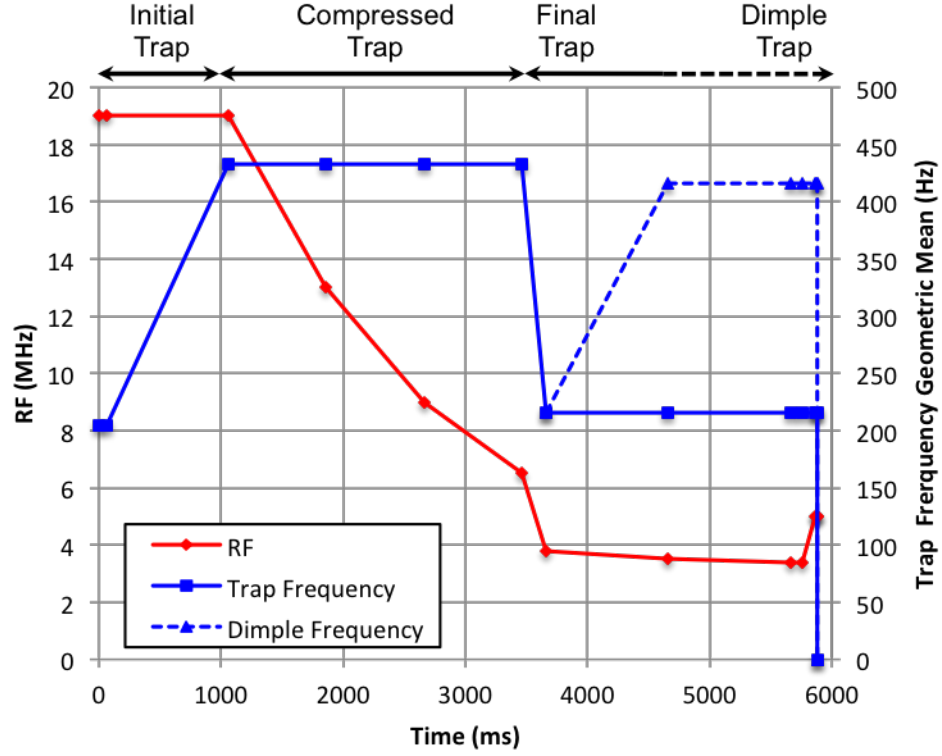
FIG. 5.1: RF sweeps and trap ramps. The final RF values (red) and mean trapping frequency (blue) as a function of time. The dimple trap parameters (described later in Section 5.2) are shown as the dashed blue line.

an increase in phase space density.

Within the first few months after loading atoms onto the chip, we made significant efforts to efficiently evaporate to BEC. Much to our frustration, our evaporation paths looked like the example path in Figure 5.2. As you can see in this figure, our climb in PSD plateaus around a phase space density on the order of PSD $\approx 10^{-1}$. The data for this plot was taken by radial absorption imaging. It was not until we decided to image the cloud axially that we discovered the reason behind our plateau.
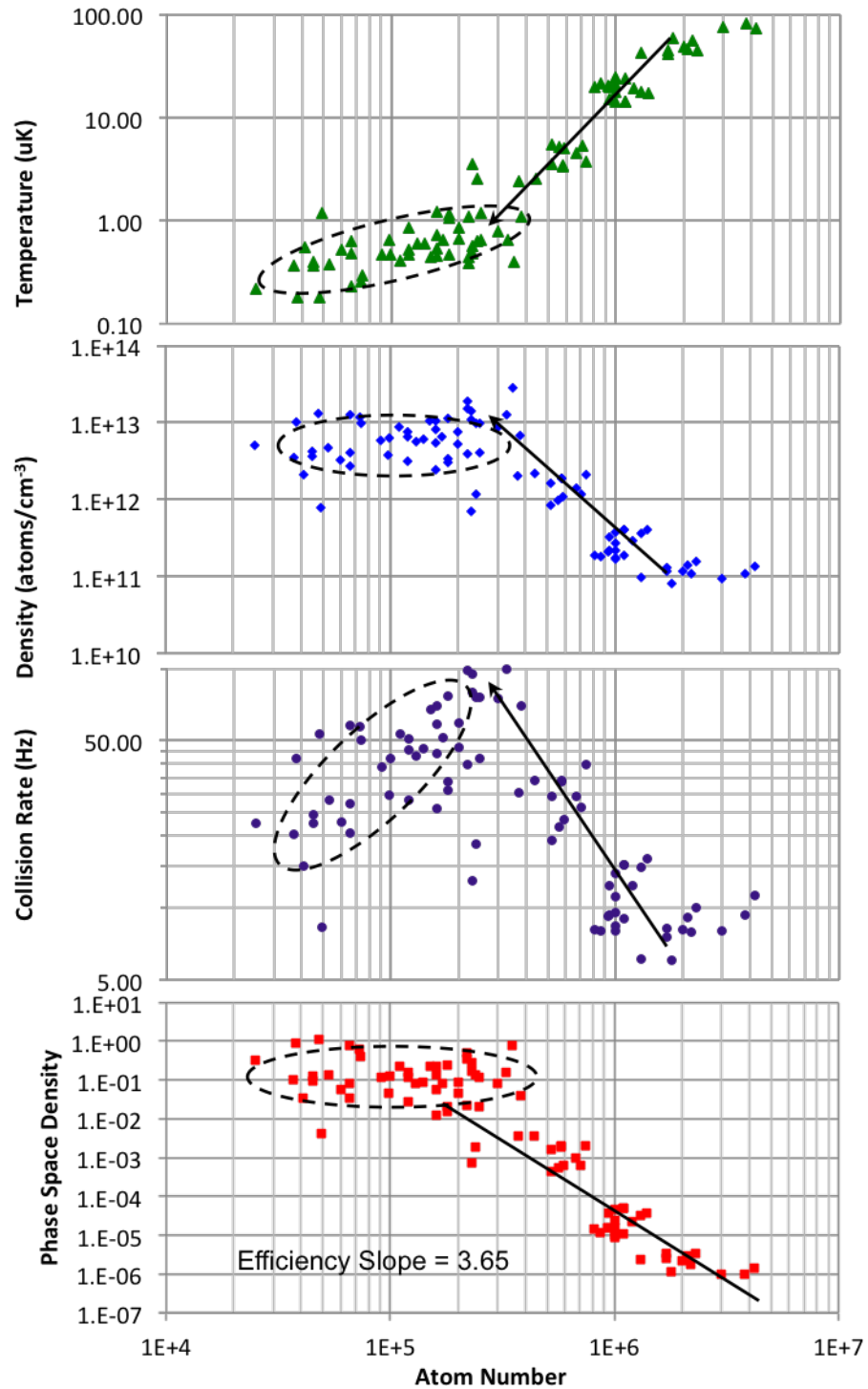
FIG. 5.2: Unsuccessful path to BEC. Temperature, density, collision rate, and PSD as a function of atom number as atoms are evaporated. The arrows are meant to guide the eye along the successful and efficient evaporation beginning. The dashed circles show failure points - atom loss without PSD etc gain. The line in the bottom plot represents a fit of points from the first evaporation stages, showing an efficiency slope of 3.65.

5.2 Dimple trap

Although we expect an evaporative path through atom number and phase space density to have the steep linear progression in Figure 5.2, the kink visible when PSD reaches 10^{-1} is an obvious sign of problematic behavior. It is important to note that the data for Figure 5.2 was entirely taken with the radial imaging system, which looks down the barrel of the cigar-shaped atom cloud. Data was initially taken with this imaging system due to the higher optical density along this axis which gives larger signal-to-noise ratios for the hotter atom clouds that tend to be more dispersed after a short time-of-flight due to the higher temperatures. However, at the PSD near the kink, it was reasonable to assume we would have sufficient density and signal-to-noise to view the atoms with the axial imaging system which views the cigar-shaped atom cloud from the side, so as to see the entire length of the cigar. What we discovered can be seen in Figure 5.3 below.

In this image, we determine the trap potential from the density distribution of our atoms. Bagnato et al. show that the trap potential along the longitudinal axis (z-axis in Figure 4.20) is a function of temperature, deBroglie wavelength, and atom number density n [72]:

$$U(z) = -k_B T \log(\lambda_{dB}^3) - k_B T \log(n(z)). \tag{5.1}$$

Therefore, if we know the temperature of our atoms, we can convert the atom number density plots to trapping potential plots such as the ones given in Figure 5.3. Not only does this method help to identify the trap frequencies of the dimple, it also helps us to characterize laser-induced potential barriers introduced in the remaining chapters of this thesis.

The presumably smooth spatial distribution of atoms in the trap was not so smooth
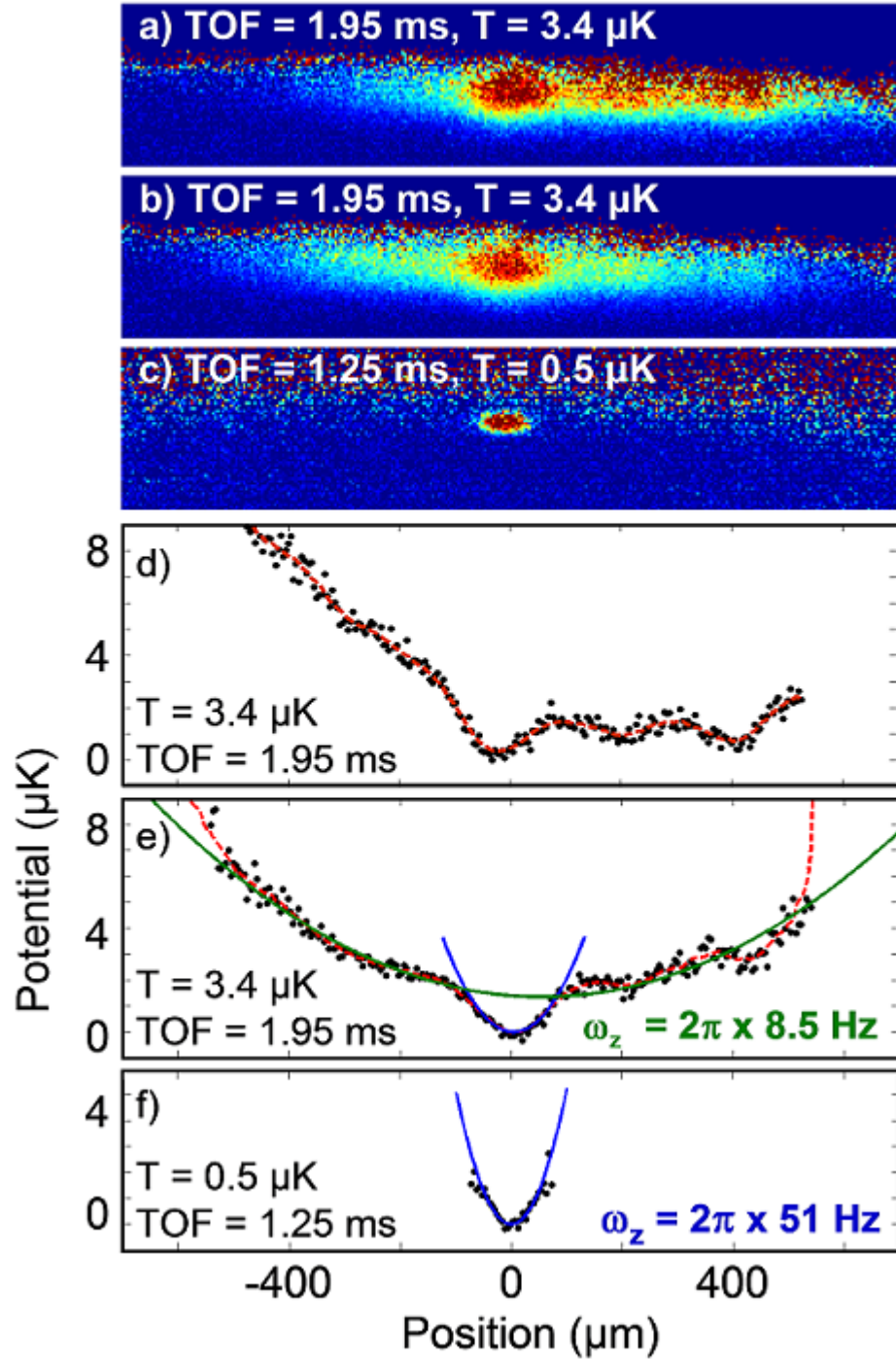
FIG. 5.3: Dimple trap. a-c) Absorption images of ^{87}Rb atoms in a dimple chip trap and d-f) corresponding potential plots. a) Atoms in the chip trap with no additional bias. b) Atoms in the chip trap with an additional magnetic field gradient to center the atoms on the dimple. c) Atoms centered on the dimple after additional evaporation. d-f) Plots of the trap potential based on the atom number density from the images in a-c).

at all, as is shown in Figure 5.3. The energy potential is shown below the absorption image with atom column density from which it is calculated. A very clear dimple is visible in the potential, causing the atoms to gather together while breaking up the cloud somewhat. This is problematic for the evaporative cooling because it reduces the collision rate and rethermalization and results in independent atomic clouds with different temperatures and PSD.

However, with clever use of our coils, we can shift the trap minimum such that it is centered on the dimple and use it to our advantage. The shift is done by applying a magnetic gradient to push the atoms into the dimple using the quadrupole magnetic field of the last transport coil.

The trap frequency in the dimple is larger than the measured and predicted axial trap frequency without the dimple. We can exploit this larger trap frequency at lower temperatures when the atoms fall into the dimple to obtain larger collision rates and more efficient evaporation times. You can see that with a small magnetic gradient, we can do just this. From the fitted curves in this figure, we can extract the measured trap frequencies of $\omega_z = \pi \times 8.5(4)$ Hz and $\omega_{dimple} = 2\pi \times 51(3)$ Hz.

We also verify the trap frequencies by intentionally inducing sloshing of the atoms in the trap and measuring their oscillation frequency. The sloshing is induced by applying a magnetic gradient using the bias coils to push the atoms up the wall of the trap. We then quickly turn off the gradient, allowing the atoms to roll down the side of the trap and slosh. We vary the amount of time the atoms are held in the trap, and then image the atoms and track their position. These results are shown in Figure 5.4 for both the axial and radial axes. The atoms used for this data are condensed and have been pushed into the dimple, therefore, the frequencies measured are the frequencies of the dimple trap. The fitted axial frequency in Figure 5.4 is $2\pi \times 53(1)$ Hz, and the fitted radial frequency is $2\pi \times 1034(6)$ Hz.
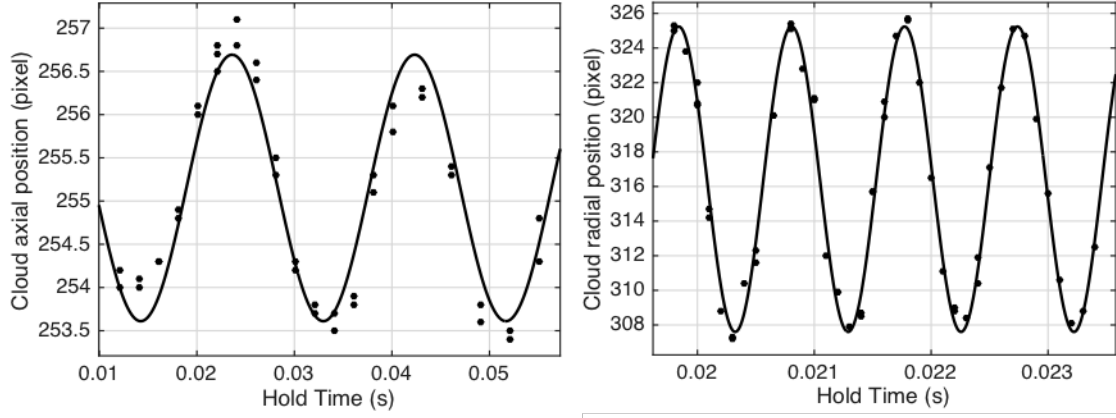
FIG. 5.4: Dimple trap frequency measurement with the sloshing method. Once sloshing is induced in the dimple trap, we plot the position of the condensed cloud as a function of the time spent sloshing (hold time). The fitted curves show $\omega_z = 2\pi \times 53(1)$ Hz and $\omega_r = 2\pi \times 1034(6)$ Hz.

5.3   Bose-Einstein condensate

Once we apply the magnetic gradient to center our atoms on the dimple, we continue with evaporation towards BEC in the tighter trap. As you can see from the evaporation path below, this method eliminates the problematic kink which was preventing us from efficiently continuing evaporation to BEC. We now have a smooth linear progression to a PSD ≤ 2.612 as calculated in Equation 2.1. We calculate the efficiency slope of our evaporation to be 2.7. The colored circles behind each data point represent the temperature of the atoms from the colorbar inset. Each point is the average of 10 data points, and the error bars represent the statistical standard deviation from the mean. This PSD ≥ 2.612 is one of three signatures of BEC introduced in Chapter 2. The other two (the bimodal Gaussian + Thomas-Fermi distribution and anisotropic expansion) are described below.

Figure 5.6 shows images of the time-of-flight anisotropic expansion of the BEC during the very final stages of evaporative cooling and their associated bimodal distributions. The Thomas-Fermi distribution can be clearly seen emerging from the Gaussian thermal cloud.

87
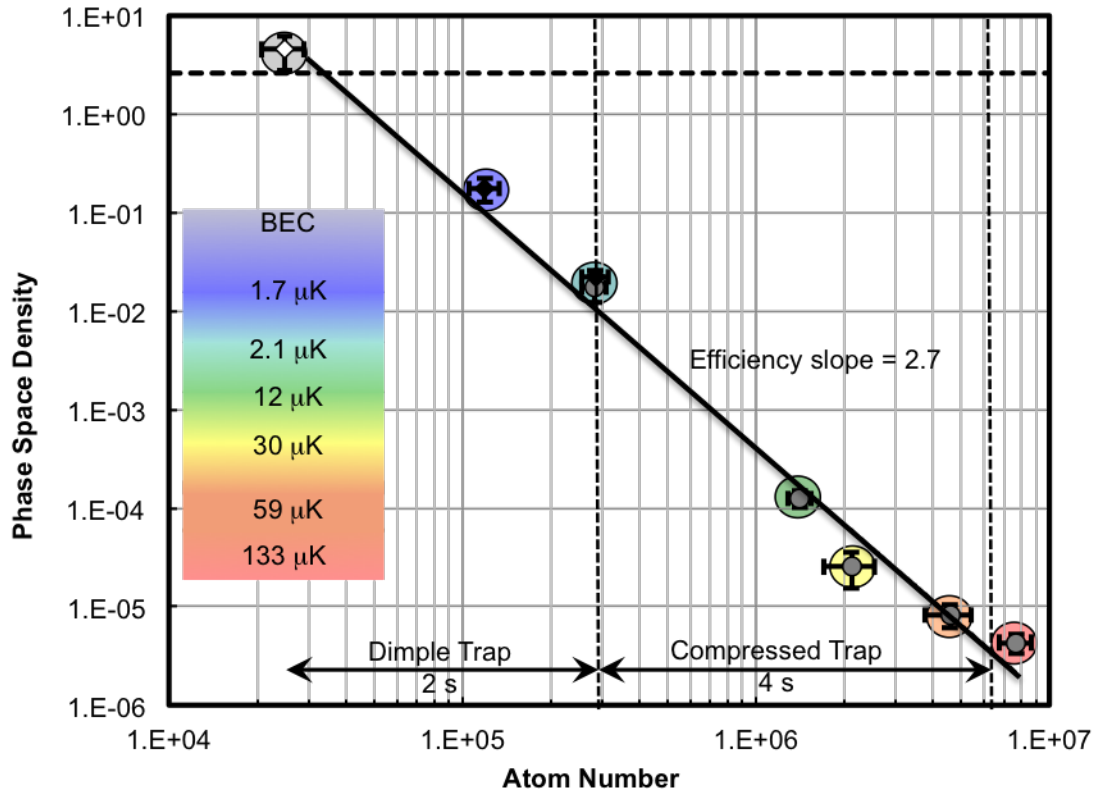
FIG. 5.5: Successful path to BEC. Phase space density vs atom number plot showing successful evaporation to BEC. Here we load the atoms, compress the trap, and then transfer into the dimple trap by applying a push to center the cloud on the dimple potential all the while applying RF evaporation. The evaporation path occurs over 6 seconds.

Only the Gaussian distribution of the thermal atoms is present for temperatures above the critical temperature. Slightly below the temperature of ≈410 nK, one can see the more pointed Thomas-Fermi distribution of the BEC begin to emerge from the thermal distribution. At even colder temperatures, we almost completely eliminate the presence of the thermal distribution to produce a quasi-pure BEC of 13,000 atoms.

It should be noted that one can never guarantee that there are no thermal atoms in the cloud. Even when the thermal tail is not visible, there is likely some small percentage of thermal atoms in the cloud. Thus, we refer to the BEC as quasi-pure.

Also present in Figure 5.6 is the final signature of BEC: anisotropic expansion. The time-of-flight for these axial absorption images is 8.45 ms. The chip is above the top of the images shown, with gravity in the vertical down direction. The axial axis of the cigar-shaped trap lies horizontally across the top of the images for very short times-of-flight. You can see in these images, however, that the time-of-flight is sufficient to produce a condensate that is instead elongated vertically. In other words, the radial axis of the trap (vertical and in/out of the page) has expanded much more rapidly than the axial axis (horizontal on the page). This is exactly the kind of dynamic behavior we expect from a BEC, as described in Chapter 2, but not from a dilute thermal gas.

5.4   Image analysis

The images of our BEC are obtained via absorption imaging, described in Chapter 2. Here, I will briefly describe the fitting and image analysis from which we determine atom number, Thomas-Fermi radii, and temperature.

Our raw data consists of pixel arrays of optical depths (ODs). The array corresponds to the user-chosen "Region of Interest" (ROI) and stores the ODs based on the pixel location on the CCD. Since absorption imaging requires both a laser image (the image of
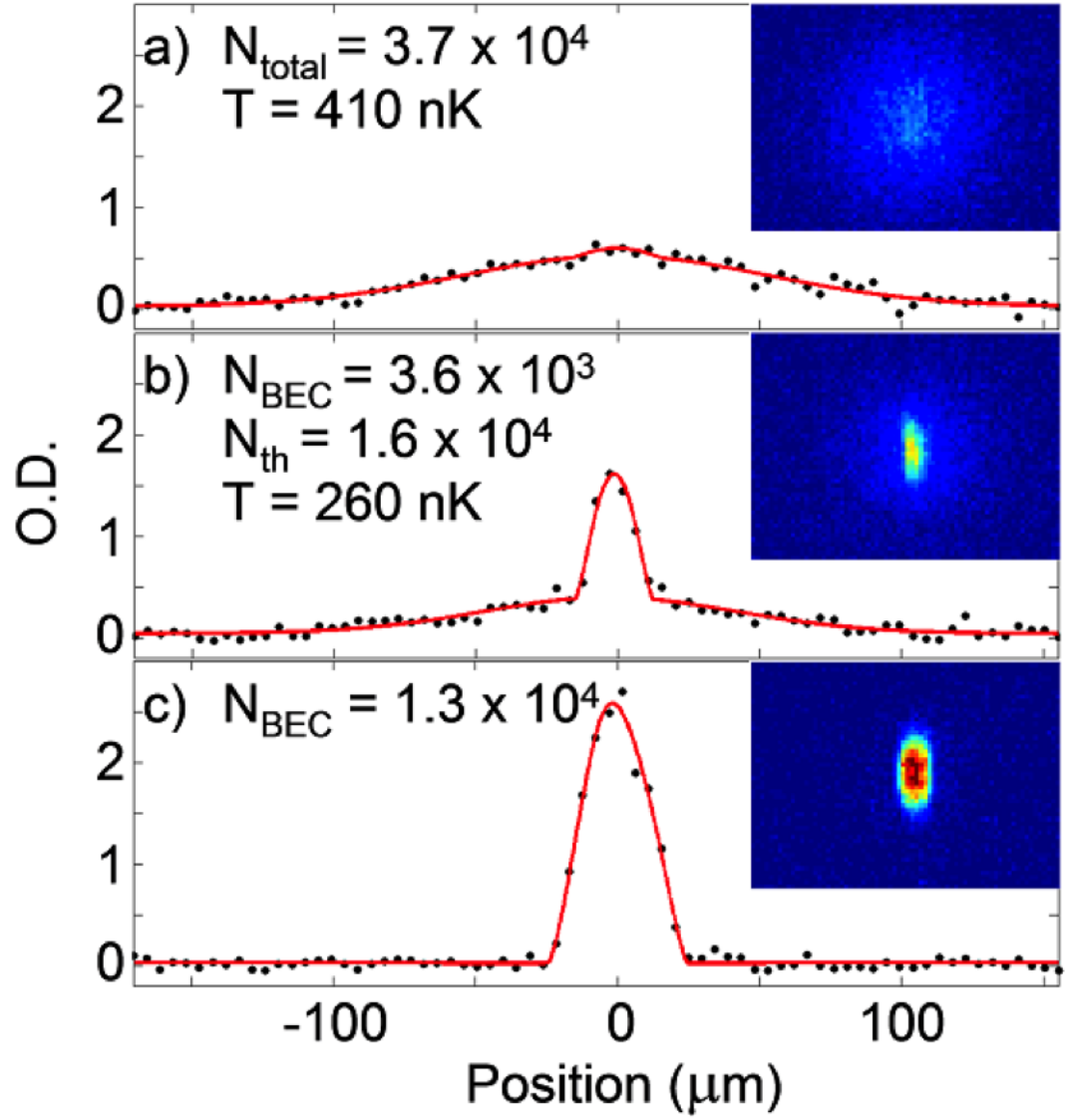
FIG. 5.6: Optical density plots of BEC and corresponding absorption images (insets). a) $T > T_c$: Thermal cloud of 3.7×10^4 atoms. b) $T \lesssim T_c$: The condensate begins to form. c) $T << T_c$: Quasi-pure BEC of 13,000 atoms.

the laser illuminating the CCD in the presence of zero atoms) and an atom image (the image of the shadow in the laser beam produced by the presence of atoms), we have two arrays of data. We pull the OD from these images using Equation 2.20 and determine the atom number density by dividing the OD by the on-resonance cross section σ_0 given in Equation 2.22.

The 3D density distribution of the condensate will be:

$$n_{3D}(x, y, z) = Max\left[n_0\left[1 - \frac{x^2}{R_x^2} - \frac{y^2}{R_y^2} - \frac{z^2}{R_z^2}\right], 0\right] \tag{5.2}$$

Our data is a single array with each element equaling the column atom number density of each pixel. The column atom number density along the z-axis (the absorption probe laser axis) is obtained by integrating Equation 5.2 with respect to z from 0 to z_0 and multiplying it by 2. The integration is straightforward, so long as one remembers that $z_0 = R_z\sqrt{1 - (\frac{x}{R_x})^2 - (\frac{y}{R_y})^2}$ for a paraboloid, giving:

$$n_{2D}(x, y) = \frac{4}{3}R_z n_0\left[1 - \frac{x^2}{R_x^2} - \frac{y^2}{R_y^2}\right]^{3/2}. \tag{5.3}$$

Summing (integrating) the array across another axis will give a 1D distribution. Once again, we integrate with respect to y from 0 to y_0 and multiply by 2, remembering that $y_0 = R_y\sqrt{1 - (\frac{x}{R_x})^2}$:

$$n_{1D}(x) = \frac{\pi}{2}R_z R_y n_0\left[1 - \frac{x^2}{R_x^2}\right]^2. \tag{5.4}$$

Summing (integrating) along the final axis will give the total atom number:

$$N = \frac{8\pi}{15}R_x R_y R_z n_0. \tag{5.5}$$

In the above Equations, R_i is the Thomas-Fermi radius along the i axis and η_0 is the peak atom number density. Since we have a cylindrically symmetric trap, two of the axes will have the same Thomas-Fermi radius. By fitting the appropriate density distribution, we can determine the peak atom number density and Thomas-Fermi radii. By summing the column density at each camera pixel, we can determine the total atom number N. Temperature is determined from the Gaussian thermal pedestal distribution via single image time-of-flight measurements described in Chapter 2. The thermal atoms can be easily fitted using a Gaussian distribution, which is a good approximation of the hot Bose gas.

In Figure 5.6, the red curves are a fit to a single slice of data through the middle of the corresponding images in the insets:

$$OD = \log\left(\frac{C_{laser}}{C_{atom}}\right) = \frac{3\lambda^2}{2\pi}n(y, z = 0) = \frac{3\lambda^2}{2\pi}\left[n_{0,BEC}\frac{4}{3}R_x\left(1 - \frac{y^2}{R_y}^2\right)^{3/2} + n_{0,thermal}e^{-\frac{1}{2}\frac{(y)^2}{\sigma_y^2}}\right]$$

(5.6)

5.5 Conclusion

While the achievement of BEC was a very time-consuming and arduous task taking the Aubin group nearly 5 years, the work of 1 professor, 4 graduate students, and (seemingly) countless undergraduate and summer students, it in fact is not the end point but the starting line for scientific research. Many of the required tools to this point are engineering tools, and many of the methods implemented to this point are well-understood and established in ultracold physics labs around the world. Therefore, it is fortunate that throughout the design, construction, and implementation of the BEC apparatus described to this point, we were careful to do our more far-sighted theoretical homework in the mean-

time. While the Aubin group has numerous research goals, some of which were discussed previously in the introduction, the first to be seriously pursued was quantum pumping. This is the subject of the remainder of this thesis.

CHAPTER 6

Classical aspects of quantum pumping

6.1 Introduction

Quantum pumping is a proposed method for generating highly controlled and reversible electron transport in mesoscopic systems without applying an external voltage bias [1, 2, 73]. Instead, localized time-varying potentials are used to pump an electron current through a 1D wire and ultimately a circuit.

A basic model for a quantum pump is shown in Figure 6.1: It consists of two reservoirs connected by a 1D nanowire with a localized potential in the middle for the quantum pump. The reservoirs are cooled such as to produce a Fermi sea of electrons in which only those at the Fermi level participate in the transport. The reservoirs are held at the same chemical potential – i.e. there is no externally applied voltage, bias, or battery–and yet pumping action occurs due to the presence of a time-varying potential in the center of the 1D nanowire. The desired outcome is that as the electrons at the top of the Fermi sea

travel back and forth through the connecting 1D channel, they encounter the potential in such a way that they are preferentially pumped in one direction through the channel over the other. This preferential directional flow of electrons is an electrical current.
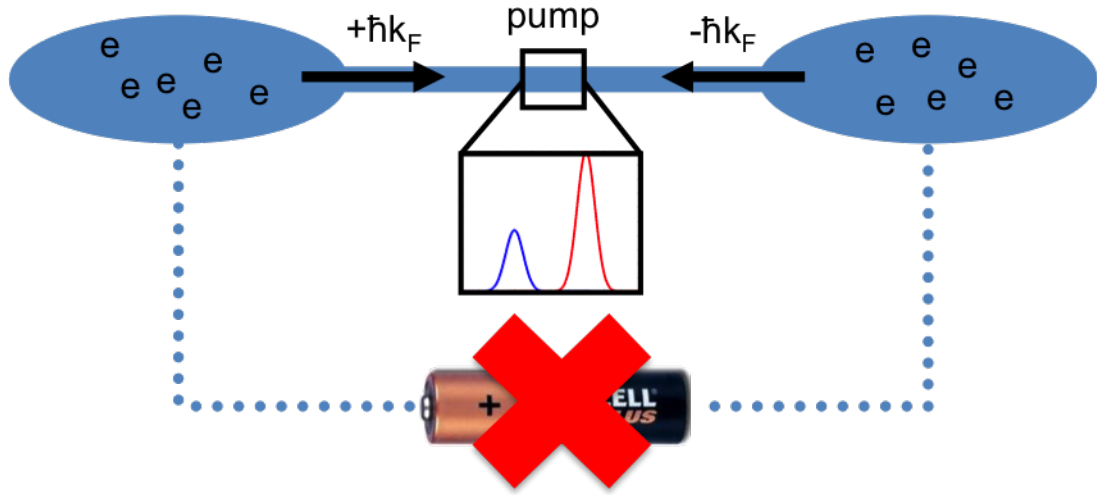
FIG. 6.1: Quantum pumping of cooled electrons. The basic quantum pumping setup consists of two reservoirs of cooled electrons connected by a nanowire. Electrons at the top of the Fermi sea are free to move from the reservoir to the nanowire. A pump, such as the double barrier turnstile pump, is a localized time dependent potential between the two reservoirs which generates a controlled, reversible current without an applied external voltage bias.

Interest in quantum pumping has arisen on a number of levels. Practically, quantum pumping promises a method of producing very controlled and reversible currents, possibly down to the single electron level [74]. This is particularly intriguing as applications such as quantum computing become more realistic, requiring the shuttling of electrons (or ions, or atoms) to various processing regions. Later, if quantum devices and processing matures toward early electronics devices, a battery or method of producing current in such a device will become necessary. This is also true in atomic quantum devices. Already, significant work has been done towards the realization of various "atomtronics" devices which are the analogs of their electronics counterparts [75, 76, 77, 78]. On a more fundamental level, quantum pumping allows the exploration of symmetry effects on dynamics as well

as the probing of classical and quantum regimes and the boundary between them. This chapter introduces the fundamental concepts for modeling and understanding the classical dynamics in a quantum pump in preparation for ultracold atom experiments that will tune from a classical thermal gas to a quantum BEC.

Quantum pumping was first conceived by Thouless in 1984 as a way of adiabatically transporting charge using a cyclic potential. Non-adiabatic quantum pumping was recently observed in 2008 [3]. Though several efforts towards an experimental realization of ballistic quantum pumping have been made, spurious capacitive coupling and rectification effects complicate the studies in mesoscopic semiconductor and hybrid normal-superconducting systems [6, 7, 79].

In addition to these challenges, many signatures of pumping are classical in nature. Therefore, in order to understand which pumping effects are entirely quantum, the classical effects must be fully understood. Ultracold atomic physicists can make significant contributions to this study by simulating quantum pumping systems using neutral atoms. In addition to avoiding electromagnetic interactions, our ultracold atoms display a high degree of coherence, allowing us to study the quantum aspects of pumping in addition to the classical aspects. Ultracold atom experiments also permit smooth tuning between classical thermal gases and quantum gases simply by decreasing the temperature of the atoms. Use of ultracold atoms also allows precision control of the initial momentum of particles and their momentum spread, as well as precision imaging of the transport [80]. Other advantages include choice between bosons and fermions and tuning of atom-atom interactions with Feshbach resonances. For this theoretical work, we deal only with non-interacting bosons. Finally, we have a variety of cooling, trapping, and manipulation techniques at our disposal.

The initial exploration of the work presented in this thesis was motivated by [81, 82] which explored quantum pumping mechanisms for ultracold atoms with a double barrier

turnstile pump. In these works, the authors discovered that significant classical pumping mechanisms were present in the study, in addition to the quantum mechanisms. Therefore, we set out to fully model the purely classical behavior of a turnstile pump, only to find the classical dynamics of the system to be quite rich and interesting on their own. In this chapter, we present the classical dynamics of a turnstile pump with both rectangular and Gaussian barriers. Then, in order to understand the quantum dynamics, we first compare classical and quantum results of scattering from a single oscillating barrier and then from the full double barrier turnstile pump.

This chapter is structured as follows. In section 6.2 we present the physical model that we use for the rectangular barrier studies as well as the Gaussian barrier studies. We include notes on our chosen scaled units as well as our methods of quantifying pumping, tools for examining classical dynamics, a symmetry theorem, and a description of our numerical methods. In section 6.3 we study the single rectangular barrier, a double rectangular barrier system with barriers flush against one another, and finally a double rectangular barrier system with spaced barriers. Section 6.4 uses similar methods and builds upon what we learn in the previous section to study the single and double Gaussian barrier cases. At this point, we have a clear grasp of the classical dynamics of the system, so we are prepared to make a comparison between the classical and quantum cases. Section 6.5 describes the analogous quantum results for single and double Gaussian barrier systems. We conclude with possible applications and an outlook to the experimental demonstration which will be covered in the next chapter.

6.2   Model

A number of pumps have been previously proposed for the simulation of this phenomenon in both solid state and ultracold atomic systems, including the snowplow or

translating barrier, paddle wheel, appropriately timed rising and falling delta barriers, and double-barrier turnstile pumps [83, 82, 84]. These pumps rely upon scattering from one or more time dependent potential barriers. In this thesis, I focus on the turnstile pump, which consists of two potential barriers with amplitude oscillations that are $\pi/2$ out of phase with one another. These pumps display a rich variety of complicated classical dynamics including signatures of chaos.

We begin modeling a double-barrier turnstile pump with a simplified case using rectangular barriers. The rectangular barriers are defined by:

$$U_{left}(t) = \begin{cases} U_0(1 + \cos(\omega t)), & \text{for } x_{0left} - W/2 < x < x_{0left} + W/2 \\ 0, & \text{elsewhere} \end{cases} \tag{6.1}$$

$$U_{right}(t) = \begin{cases} U_0(1 + \cos(\omega t + \phi)), & \text{for } x_{0right} - W/2 < x < x_{0right} + W/2 \\ 0, & \text{elsewhere} \end{cases} \tag{6.2}$$

where U_0 is the maximum height of the barrier, ω is the frequency of the amplitude oscillation, ϕ is an additional phase term, $x_{0left,right}$ is the center of the left or right barrier, and W is the full width of the barrier. A schematic of the rectangular barrier case is shown in Figure 6.2 with $U_{left}(t = 0)$ drawn in blue and $U_{right}(t = 0)$ drawn in red.

This is a simplified case for two reasons: 1) challenges associated with producing an actual rectangular potential in the lab make it unrealistic for experimental demonstrations, and 2) analytic modeling is easily accessible since there are no spatially varying potentials. Due to the first reason, we also examine the case of a double Gaussian barrier turnstile pump. Gaussian potentials are straightforward to produce in the lab with focused laser beams in comparison to rectangular potentials. Recall from Chapter 3 that a light field detuned from atomic resonance will produce a potential experienced by the atoms. Detuned
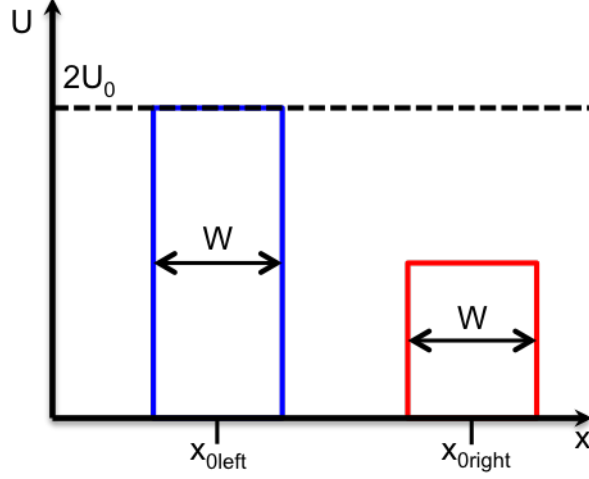
FIG. 6.2: Rectangular barrier schematic. $U_{left}(t = 0)$ is drawn in blue centered on location x_{0left}. $U_{right}(t = 0)$ is drawn in red centered on location x_{0right}. The barriers oscillate $\pi/2$ out of phase with one another with maximum height $2U_0$.

Gaussian light fields are readily available with the lasers in the lab.

For the case of the Gaussian turnstile pump, we model the resulting potential as follows:

$$U_{left}(x, t) = U_0(1 + \cos{(\omega t)}) \exp(-\frac{1}{2}\frac{(x - x_{0left})^2}{\sigma^2}) \tag{6.3}$$

$$U_{right}(x, t) = U_0(1 + \cos{(\omega t + \phi)}) \exp(-\frac{1}{2}\frac{(x - x_{0right})^2}{\sigma^2}) \tag{6.4}$$

where, in the Gaussian case, σ^2 is the variance of the Gaussian distribution. In order to ease the leap between rectangular and Gaussian barriers and to make the results more relate-able, I refer to the full-width half-max (FWHM) of the barriers rather than the variance σ^2. These two are related as follows: FWHM $= 2\sqrt{2\ln 2}\sigma$.

Pumping action for a particular initial momentum is expected due to the $\pi/2$ phase shift between the left and right barriers. The time-lapse below is helpful to see the relative

height of the barriers over one cycle.
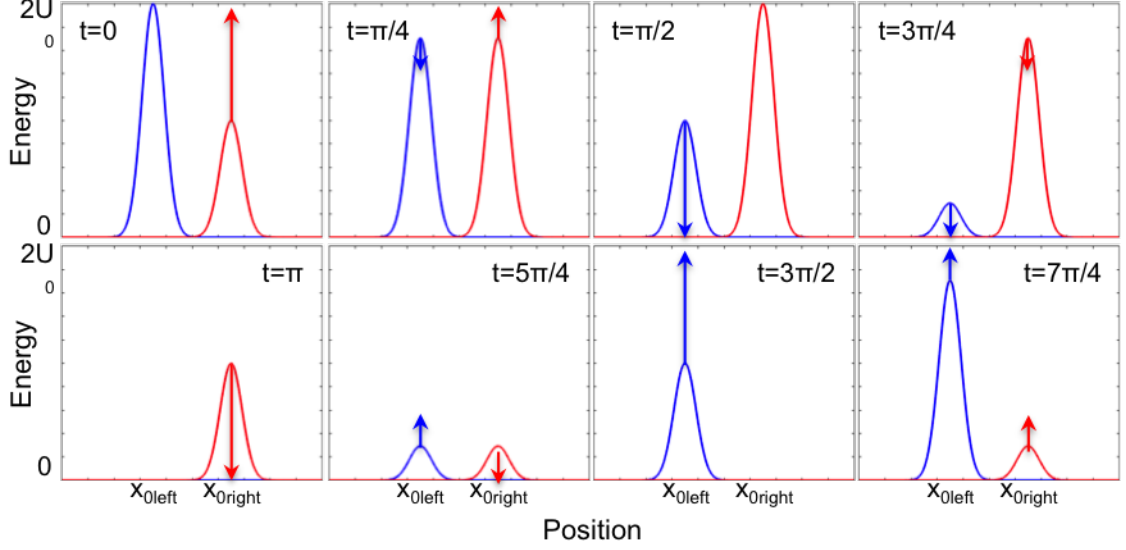
FIG. 6.3: Time-lapse of double Gaussian barriers. The barriers oscillate $\pi/2$ out of phase with one another in order to break the spatial symmetry and induce pumping for particular momenta. The arrows indicate the direction of amplitude change.

6.2.1 Scaled units

For simplicity's sake, we employ a theoretical unit convention throughout this chapter based on selecting an arbitrary frequency unit ω_u and related length unit $l_u = \sqrt{\frac{\hbar}{\omega_u m}}$ with $\hbar = 1.054 \times 10^{-34}$ J s. The corresponding energy unit is $E_u = \hbar \omega_u$, while the mass unit is that of the particle, $m_u = m$. We obtain these units by reducing the 1D Schrodinger equation to a dimensionless form.

Practically speaking, these theoretical units need to be converted to real units to do anything of use in the lab. The conversion of the dimensionless theoretical units to real units is the following: Our length scale l_u is set by the ratio of the experimental barrier width to the theoretical barrier width; With this ratio, we can then calculate the experimental $\omega_{exp} = \frac{\hbar}{ml_u^2}\omega_{th}$ in units rad/s; The experimental barrier height can be

determined by $U_{exp} = E_u U_{th}$ in units of J; Finally, the experimental momentum can be found by $p_{exp} = \frac{\hbar}{l_u} p_{th}$ in units of kg m/s.

6.2.2 Methods

Here I introduce our methods for quantifying pumping, examining the surface of section, considering symmetry roles, and numerically calculating results.

Quantifying pumping

First, we quantify pumping by simply determining the net particles pumped (and the direction) and the net momentum or energy pumped (and the direction). This is done by launching atoms from both sides of the pump and waiting until all the atoms have exited the pumping region. Then, we calculate the difference in number that end up on one side vs the other.

This can be determined from several distributions of atoms. For the classical calculations, we either use a distribution in position and momentum, or we use a position distribution at a single momentum. The initial distribution in position and momentum will be a block of non-interacting particles launched with momentum ranging from 0 to 3. The initial launch times t_0 of the particles are chosen such that for a given momentum, a line of evenly distributed particles arrives at the first edge of the first barrier over the course of a full period. We choose the initial position of the particles to be far enough away that the barrier potential drops to 0.0001 of its maximum U_0.

For the quantum calculations, the initial distribution has a single momentum. We model atoms in the 1D "nanowire" channel as a wave packet consisting of a plane wave of

initial momentum p_0 with a longitudinal Gaussian envelope of width β given by:

$$\psi(x, t = 0) = \frac{1}{(2\pi)^{\frac{1}{4}}} e^{-\frac{1}{4}\frac{(x-x_0)^2}{\beta^2}} e^{ip_0 x} \tag{6.5}$$

We consider initial packets of atoms with a sufficiently broad position envelope such that it takes several oscillations of the barrier for the entire packet to encounter the barrier.

We determine the overall current of our system by the following: 1. Launch a distribution of particles from *left-to-right* and look at the number of transmitted and reflected particles, as well as the final momentum of each particle. 2. Launch the same distribution of particles from *right-to-left* and look at the number of transmitted and reflected particles, as well as the final momentum of each particle. 3. Sum the results of each of these to look at the net particle current and momentum current for every initial momentum and time. 4. Average over all initial phase (which can be thought of as initial positions or initial times).

Surface of section

Due to the oscillatory nature of the barrier, atoms can end up with a final momentum greater than or less than their initial momentum, depending on the time and phase of a barrier when they encounter it. The surface of section or Poincaré map is a useful tool for visualizing the complexity of the dynamics in phase space. These tools plot the particles in phase space (position and momentum) as the system is strobed once every pump cycle. A surface of section plot for a single oscillating Gaussian barrier can be found in Figure 6.4. In this figure, particles that begin in the upper left quadrant (red, pink, and orange lines) are launched left-to-right. Particles that begin in the lower right quadrant (blue, cyan, and green lines) are launched right-to-left. Particles with larger initial momentum (red and blue) will pass over the barrier to the upper right or lower left quadrant. The

oscillations in the momentum in these final quadrants are a product of the oscillatory nature of the barrier. Similarly, particles with very small initial momentum (orange and green) will be reflected from the barrier with changes in their final momentum due to the oscillating barrier. Particles with momenta that fall between these categories (pink and cyan) will experience some transmission and some reflection, depending on their initial position.
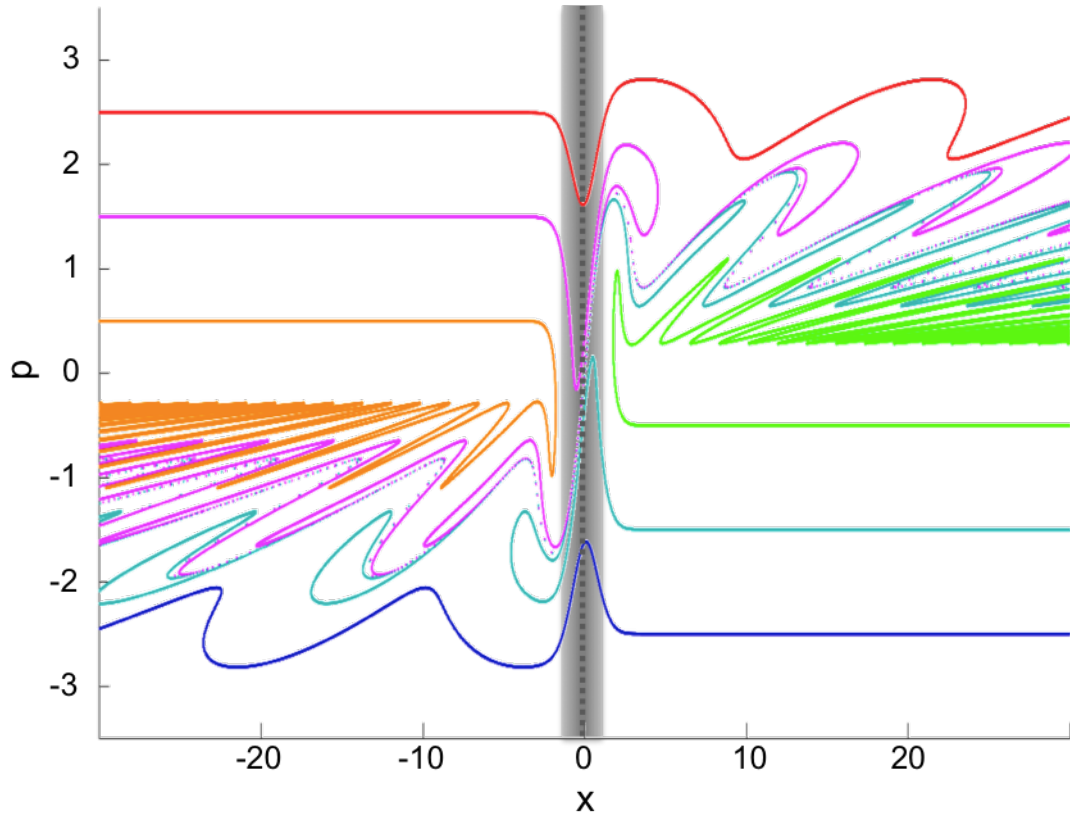
FIG. 6.4: Surface of section for a single oscillating Gaussian barrier. This surface of section plot for atoms launched towards a single oscillating Gaussian barrier with $U_0 = 1$, $\omega = 1$, FWHM=2, located at $x = 0$. The shaded region indicates the FWHM size of the Gaussian barrier in the plot.

It is also important to note from Figure 6.4 that the results are symmetric as x goes to -x and p goes to -p. The symmetry of the single oscillating barrier prevents any pumping

from occurring.

Symmetry

Less intuitively, symmetry will also prevent pumping in certain conditions for the double barrier turnstile pump we have described. This is counter-intuitive because of the phase shift between the barriers (in our case, the right barrier U_{right} is shifted $3\pi/2$ from the left barrier U_{left}). Looking at Figure 6.3, one can see that U_{right} lags behind U_{left}, similar to a leftward moving wave. One might expect then that this particular pump would produce an overall particle current from right to left.

Theorem: Due to the symmetry of the pump (barriers with equal width and height), a case considering a uniform distribution of all possible initial energies and positions, will have a particle ending on the right for every particle ending on the left. Therefore, the symmetry, even with the phase shift between the barriers, prevents any pumping in this case. This is explored in more detail in [85].

Fortunately for us, the quantum pumps which we are trying to simulate in our neutral atom system do not employ uniform distributions of particles with all possible energies and positions. Rather, they begin with particles with a narrow band of initial momentum representing electrons at the top of the Fermi sea. Therefore, it is perfectly reasonable to anticipate pumping in our simulations using particles with a narrow band of initial momenta.

Numerical methods

In the case of Gaussian barriers, I have developed a numerical code to calculate the position and momentum as a function of time using MATLAB. The code calculates the force on particles due to potential barriers over a very short time-step, i.e. the Euler method. Given an initial position x_0 and momentum p_0 of a particle and initial phase ωt_0

104

of the system, I calculate the potential due to the barriers at the position of the particle after a time step δt:

$$U(x = x_0, t = t'_0) = U_{left}(x = x_0, t = t'_0) + U_{right}(x = x_0, t = t'_0) \tag{6.6}$$

where $U_{left}(x, t)$ and $U_{right}(x, t)$ are given in Equation 6.3 and 6.4 with $x = x_0$ and $t = t'_0 = t_0 + \delta t$. The force F (and therefore acceleration since m=1) can easily be calculated to be:

$$F(x = x_0, t = t'_0) = \frac{x_0 - x_{0left}}{\sigma^2} U_{left}(x = x_0, t = t'_0) + \frac{x_0 - x_{0right}}{\sigma^2} U_{right}(x = x_0, t = t'_0). \tag{6.7}$$

From here, I use basic kinematic equations to determine the new position x'_0 and momentum p'_0 after the time step δt (remembering that in our units, mass $m = 1$):

$$x'_0 = x_0 + p_0 \delta t + \frac{1}{2} F(x = x_0, t = t'_0) \delta t^2$$
$$p'_0 = p_0 + F(x = x_0, t = t'_0) \delta t \tag{6.8}$$

I then begin again with the new $x_0 = x'_0$, $p_0 = p'_0$, and $t_0 = t'_0$, looping through this process until the particle has exited the pumping region.

The accuracy of this method depends on the time step δt chosen. I evaluated the accuracy by monitoring the resultant particle current as a function of δt. By decreasing δt until the particle current converged, I was able to determine the size of δt required for minimizing the effect of numerical errors. I also compared my numerical results with results obtained using MATLAB's built-in ODE solvers. Several of the solvers returned splotchy or erroneous results, while others returned results that matched my own. The latter of these validated the correctness of my code, and I chose to continue using my own

code out of familiarity, stubbornness, and pride.

6.3   Rectangular barrier(s)

As mentioned previously, rectangular barriers represent a very simple potential that we can analytically model. For pedagogical reasons, we begin with these more simplistic models and build up to the Gaussian turnstile pump. The most simple case we examine is a single oscillating rectangular barrier.

6.3.1   Classical single rectangular barrier

The physics of a single oscillating rectangular barrier is the most straightforward to understand. An incident particle will either reflect off or transmit over the barrier. If the particle has enough energy to transmit over the barrier, it can gain or lose energy during the time it spends in the barrier region due to the time oscillations of the barrier. We call the process of gaining or losing energy in the region of the barrier the "elevator effect". Due to this effect, a particle with very small momentum that reaches the barrier when it is at its minimum can hop onto the barrier and gain a large momentum boost from the barrier. The opposite can also happen. If a particle makes it onto the barrier as the barrier is decreasing in amplitude, the particle will lose energy as it crosses the barrier. This effect causes the final momentum to be extremely dependent upon initial conditions, especially for those particles that barely have sufficient energy to make it onto the barrier.

We analytically calculate the height of the barrier versus the momentum of the particle to determine on which side the particle ends and with what final momentum. For this case, we assume only U_{left} is present and centered at $x_{0left} = 0$. Since the barrier is rectangular, the particles will only experience acceleration at the barrier boundaries and will travel with constant velocity at all other regions, including the flat top region of the barrier. Therefore,

it is straightforward to calculate the total energy of the particles and compare it to the height of the upcoming barrier. For example, a particle beginning to the left of the barrier is launched left-to-right with initial momentum p_0. The particle arrives at the leftmost edge of U_{left} at time t_0. We know the height of the barrier $U_{left}(t_0)$ from 6.1 and the total energy of the particle is $E_{total}(t_0) = \frac{1}{2}p_0^2$ (mass=1 in our units). If $E_{total}(t_0) \geq U_{left}(t_0)$, the particle is reflected from the barrier with $p_{final} = -p_0$. Otherwise, the particle transmits over the barrier with momentum

$$p_a = \sqrt{2(U_{left}(t_0) - E_{total}(t_0))}. \tag{6.9}$$

With this momentum, we can calculate the time at which the particle will reach the opposite edge of the barrier:

$$t_a = \frac{W}{p_a} + t_0 \tag{6.10}$$

and the corresponding $U_{left}(t_a)$ and the final total energy of the particle given by:

$$E_{total}(t_a) = U_{left}(t_a) + \frac{1}{2}p_a^2. \tag{6.11}$$

The results of this calculation for particles scattering from a single oscillating rectangular barrier with $W = 1$, $\omega = 1$, $U_0 = 1$, and $x_{0left} = 0$ are shown in Figure 6.5. Each pixel in the plots represents a single particle with initial momentum p_0 on the y-axis and arriving at the edge of the first barrier at initial phase ωt_0 on the x-axis. p_0 has an even distribution ranging from 0 to a momentum sufficiently large that all particles transmit over the barrier – in this case we choose 3, as the maximum barrier height is 2. t_0 ranges from 0 to $\frac{2\pi}{\omega}$ to cover a full period of the pump. In Figure 6.5, the color corresponds to

FIG. 6.5: Final side of particles scattered from single rectangular barrier. The results of a grid of particles with initial momentum $p_0 = 0$ to 3 and launched over $\omega t_0 = 0$ to 2π. The color of each pixel corresponds to the final side (left or right) of a particle at the particular initial position and launch time. The left (right) surface plot represents particles launched from left-to-right (right-to-left). Red (blue) correspond to particles which end on the right (left) side of the pump. In this case, $W = 1$, $\omega = 1$, $U_0 = 1$, and the barrier is centered at $x_{0left} = 0$.

the side of the pump on which the particle ends up. Red (blue) means the particle ends up on the right (left).

There are several features of which to take note. First, particles with $p_0 > 2$ will always transmit over the barrier. This is because the maximum achievable height of the barrier is $U_{left} = 2$. Second, based on our definition of U_{left} in Equation 6.1, the barrier starts and ends at its maximum height at $\omega t_0 = 0, 2\pi$. At $\omega t_0 = \pi$, the barrier will be at its minimum zero height. This is all evident in Figure 6.5 in the boundary between the particles with positive and negative final momentum. This boundary indeed traces out the height of the barrier over time. The point at $\omega t_0 = \pi$ shows that when the barrier height is zero, even particles with minimal momentum can transmit if they arrive at the barrier at $\omega t_0 = \pi$. Finally, the left and right plots are the opposite of one another, displaying the symmetry that prevents any pumping from occurring in this case.

FIG. 6.6: Final momentum of particles scattered from single rectangular barrier. The results of a grid of particles with initial momentum $p_0 = 0$ to 3 and launched over $\omega t_0 = 0$ to 2π. The color of each pixel corresponds to the final momentum of a particle at the particular initial position and launch time. The left (right) surface plot represents particles launched from left-to-right (right-to-left). Red and warm (blue and cool) shades correspond to particles which end with positive (negative) final momentum. In this case, $W = 1$, $\omega = 1$, $U_0 = 1$, and the barrier is centered at $x_{0left} = 0$.

Figure 6.6 is the corresponding final momentum plot to the final side plot in Figure 6.5. The same features are present, but the pixel colors are scaled to represent their final momentum. Dark red and blue correspond to large momenta, and green corresponds to zero momenta. Particles that are reflected from the barrier see only a sign change in momentum. Particles that transmit over the barrier, however, experience a change in the momentum, evidenced by the color scheme in this figure. Near the boundaries, there are more dense fluctuations in momentum, as these are the particles with barely enough energy to hop on the barrier, so they experience strong dependency on initial conditions. This dependence will play an even more significant role in the next sections.

6.3.2 Classical double rectangular barrier turnstile

We now proceed to the double rectangular barrier case, first with barriers that are touching one another, $|x_{0right}| + |x_{0left}| = W$, and then with some space between. We once again calculate analytically on which side of the pump particles end up and with what final momentum when we launch uniform distributions of particles in position and momentum from both sides of the pump.

Rectangular barriers with no space between

We first examine the simplest of turnstile pumps - two rectangular barriers given by 6.1 and 6.2 with no space between them. The physics of this case is straightforward. An incident particle will either reflect off the first barrier, reflect off the second barrier, or transmit over both of them.

The final position of the particles is determined with the same algorithm as the single rectangular barrier case above. The calculations for the first barrier the particle encounters is the same. A particle will either transmit over the first barrier with momentum given by Equation 6.9, or it will reflect with momentum $-p_0$. Those particles which transmit over the first barrier will also transmit over the second barrier if $E_{total}(t_a) \geq U_{right}(t_a)$. Otherwise, they will be reflected from the second barrier with $p = -p_a$, spend another time $\frac{W}{p_a}$ transmitting over U_{left}, and finally fall off U_{left} onto the left-hand side of the pump with

$$p_{final} = -\sqrt{2\left(U_{left}(t_a + \frac{W}{p_a}) + \frac{1}{2}p_a^2\right)}. \tag{6.12}$$

110

The particles that transmit over the second barrier will do so with momentum

$$p_b = \sqrt{2(U_{right}(t_a) - E_{total}(t_a))}. \tag{6.13}$$

Again, we can calculate the time at which the particle will fall off the second barrier:

$$t_b = \frac{W}{p_b} + t_a \tag{6.14}$$

and the corresponding $U_{right}(t_b)$, to determine

$$p_{final} = \sqrt{2(U_{right}(t_b) + \frac{1}{2}p_b^2)}. \tag{6.15}$$

A similar algorithm is followed for particles beginning on the right of the pump with negative initial momentum, keeping in mind that they will first encounter the rightmost barrier and then, given sufficient energy, the leftmost barrier.

The results of our simulations for barriers with $W = 1$, $\omega = 1$, $U_0 = 1$, $\phi = \frac{3\pi}{2}$, $x_{0left} = -1/2$, and $x_{0right} = 1/2$ are shown in Figures 6.7 and 6.9. Once again, each pixel represents a single particle with initial momentum p_0 on the y-axis and arriving at the edge of the first barrier at initial phase ωt_0 on the x-axis. p_0 has a uniform distribution ranging from 0 to a momentum sufficiently large that all particles transmit over the barrier - we again choose 3. t_0 ranges from 0 to $\frac{2\pi}{\omega}$ to cover a full period of the pump. In Figure 6.7, the color corresponds to the side of the pump on which the particle ends up. Red (blue) means the particle ends up on the right (left).

There are obvious similarities and differences between this double rectangular barrier case and the previous single rectangular barrier case. First, the region in the plot representing the particles that immediately reflect from the first encountered barrier (in
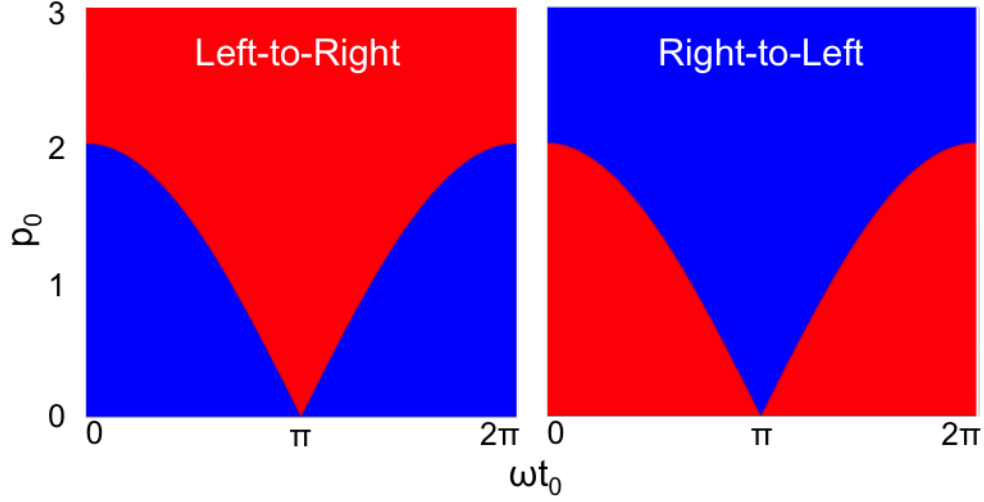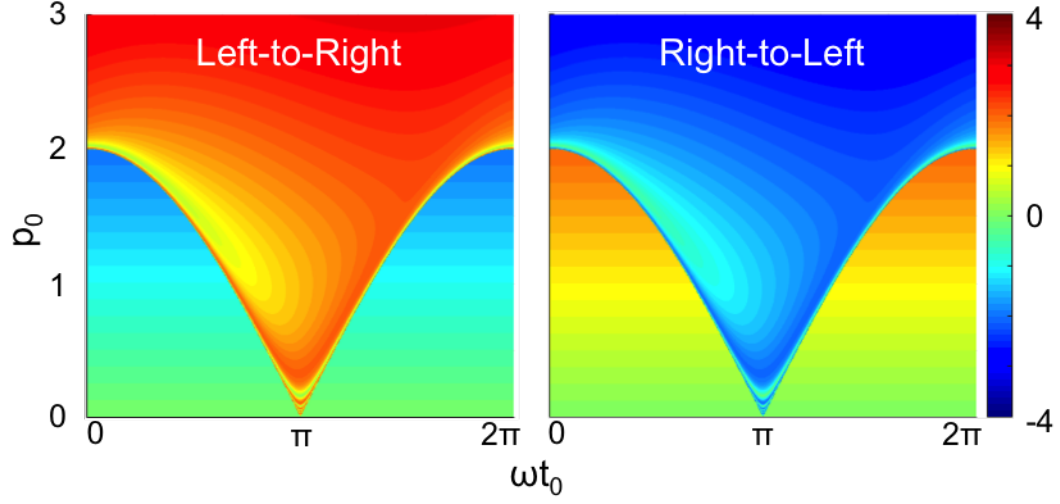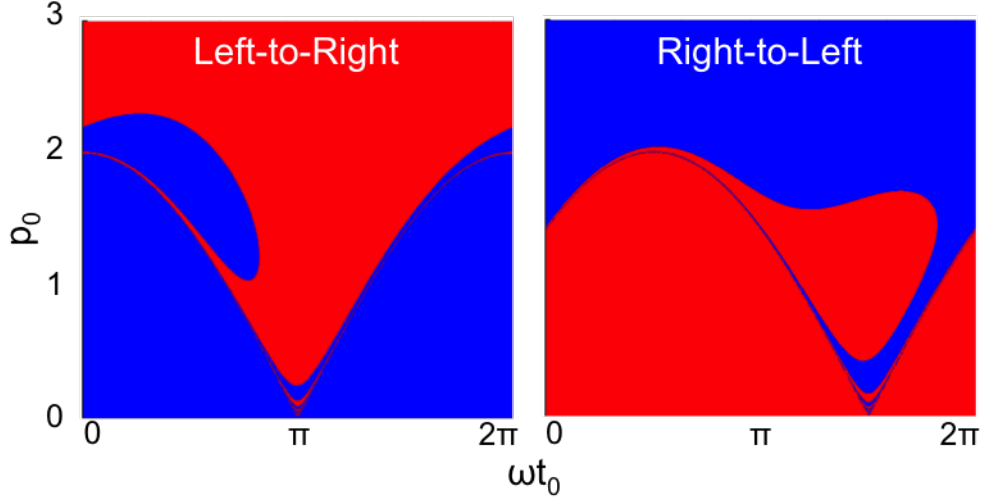
FIG. 6.7: Final side of particles scattered from double rectangular barrier. The results of a grid of particles with initial momentum $p_0 = 0$ to 3 and launched over $\omega t_0 = 0$ to 2π. The color of each pixel corresponds to the final side (left or right) of a particle at the particular initial position and launch time. The left (right) surface plot represents particles launched from left-to-right (right-to-left). Red (blue) correspond to particles which end on the right (left) side of the pump. In this case, $W = 1$, $\omega = 1$, $U_0 = 1$, and the barriers are centered at $x_{0left} = -1/2$ and $x_{0right} = 1/2$.

the previous case, the only barrier) remains the same. The lowermost blue region in the left plot and red region in the right plot are defined by the results of a single leftmost or rightmost barrier, respectively. This blue (red) region represents the particles approaching from the left (right) that do not make it over the initial leftmost (rightmost) barrier. Without the second barrier, the region above this lowermost boundary would be entirely red (blue). However, for the particles that formerly transmitted smoothly to the opposite side of the "pump", there is now a protruding lobe of particles that do not transmit. This lobe is due entirely to the presence of the second barrier.

The second major difference is that there is no longer a clear boundary between the transmitted and reflected particles. In fact, zooming in on the region near $p_0 = 0$ and $\omega t_0 = \pi$, as in Figure 6.8, shows evidence of extreme dependence on initial conditions. This dependence produces stripes of red and blue near the boundary from Figure 6.6. The
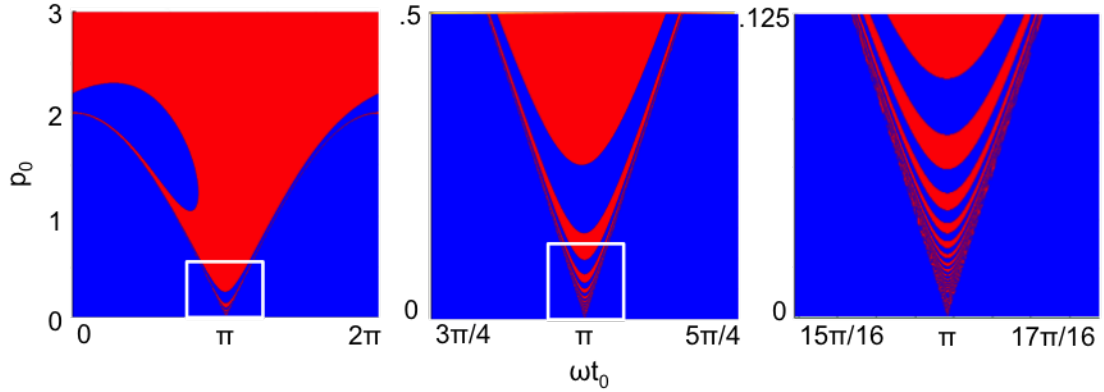
FIG. 6.8: Rectangular double barrier - "Elevator Effect". As we zoom in on the region near $p_0 = 0$ and $\omega t_0 = \pi$, we see that the side of the pump on which a particle ends has a clear fractal behavior. This dependence manifests as stripes of red and blue near what was a clear boundary in Figure 6.6. This is because particles that barely have enough energy to transmit over the first barrier will ride the first barrier over several cycles with very small momentum until they reach the second barrier. We call this the 'Elevator Effect'. The white box in the leftmost plot shows the region of the middle plot. The white box in the middle plot shows the region of the rightmost plot.

reason for these stripes is what we call the 'Elevator Effect'. Particles just beyond this boundary have barely enough energy to transmit over the first barrier, and will do so with very small momentum. Therefore, the barrier oscillates at timescales much faster than the particle translates. The particle may ride the elevator for several cycles before reaching the second barrier. This causes the resultant side (red or blue) to be extremely sensitive to initial conditions.

For this same simulation, we can also examine the final momentum of the particles. This is shown in Figure 6.9. The color scheme is similar to that in Figure 6.6. However, due to the second barrier, a lobe exists in each of the plots and the right-to-left plot is no longer obviously symmetric to the left-to-right plot as in the single barrier case. It now becomes feasible to consider what happens if we sum these plots to look at the net momentum gained or lost at each pixel.

This sum is shown in Figure 6.10. The plot on the left shows the sum of the two plots

FIG. 6.9: Final momentum of particles scattered from a rectangular double barrier. The results of a grid of particles with initial momentum $p_0 = 0$ to 3 and launched over $\omega t_0 = 0$ to 2π. The color of each pixel corresponds to the final momentum of a particle at the particular initial position and launch time. The left (right) surface plot represents particles launched from left-to-right (right-to-left). Red and warm (blue and cool) shades correspond to particles which end with positive (negative) final momentum. In this case, $W = 1$, $\omega = 1$, $U_0 = 1$, and the barriers are centered at $x_{0left} = -1/2$ and $x_{0right} = 1/2$.

in Figure 6.9. The plot in the middle is the average momentum for each p_0 averaged over all possible ωt_0. The plot on the right is the average particles pumped for each p_0 averaged over all possible ωt_0. Net momentum is defined by $\left[\sum_{\omega t_0} p_f(p_0) \right]/N$ where N is the total number of particles, while net particles pumped simply counts the number of particles on the left vs the number on the right for a single value of p_0 and normalizes the result with respect to N. It is obvious that for regions of p_0, there can be both momentum and particle pumping from the double barrier turnstile. What is not obvious is that integrating the right plot over all p_0 will yield zero pumping. This is the case only when considering the sum of all possible p_0 and ωt_0 due to the symmetry in the system.

The choice of barrier width is important in these results. Even with no space between the barriers, one sees the resulting figures above change as we choose broader or narrower barriers. These effects are illustrated in Figure 6.11 for left-to-right launched particles with

114
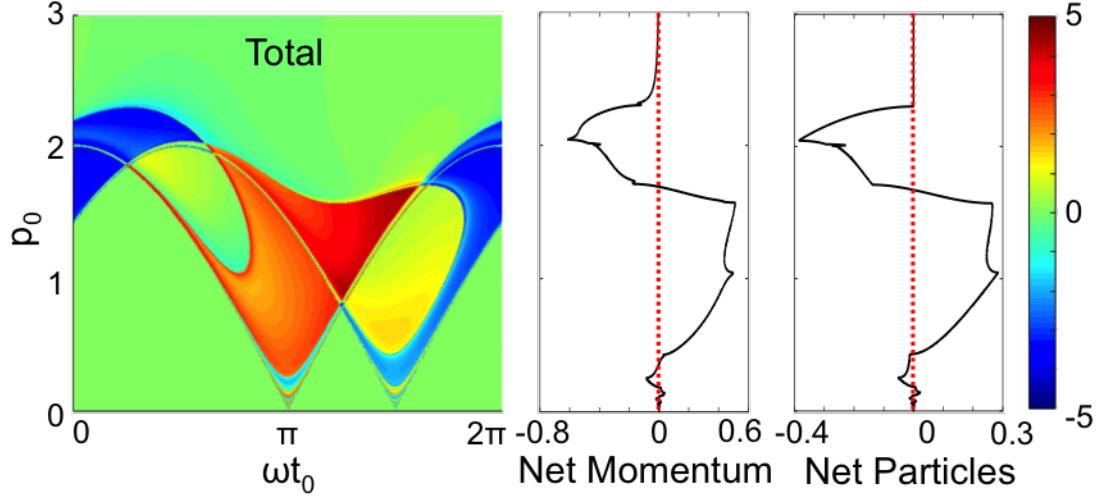
FIG. 6.10: Rectangular double barrier total and average momentum and particle pumping. The left plot shows the sum of each plot from Figure 6.9. The center plot shows the average momentum for each p_0 on the y-axis summed over all possible ωt_0 on the x-axis. The left plot shows the average particles pumped for each p_0 on the y-axis summed over all possible ωt_0 on the x-axis. Regions of pumping for particular p_0 are obvious (where the color is not green in the left plot or where the net momentum or particles are not zero in the center and right plots).

all other parameters unchanged ($\omega = 1$, $U_0 = 1$, $\phi = \frac{3\pi}{2}$, $x_{0left} = -1/2$, and $x_{0right} = 1/2$). The plots begin with barriers quite narrow ($W = 0.1$) in the top left and increase in size to the largest barriers ($W = 10$) in the bottom right. For very narrow barriers, ($W = 0.1$), the lobe begins to trace out the height of the second barrier over time. As the barriers become wider, the "Elevator Effect" plays a larger role, as is evidenced by the increased striping and sensitivity to initial conditions.

Rectangular barriers with space between

Separating the rectangular barriers by some space maintains the qualitative features of the above results, while increasing the chaotic region and effects. Since there still exists no acceleration in our system except at the barrier edges, a calculation of the final momentum is similar to the above case where there is no space between the particles. If a particle
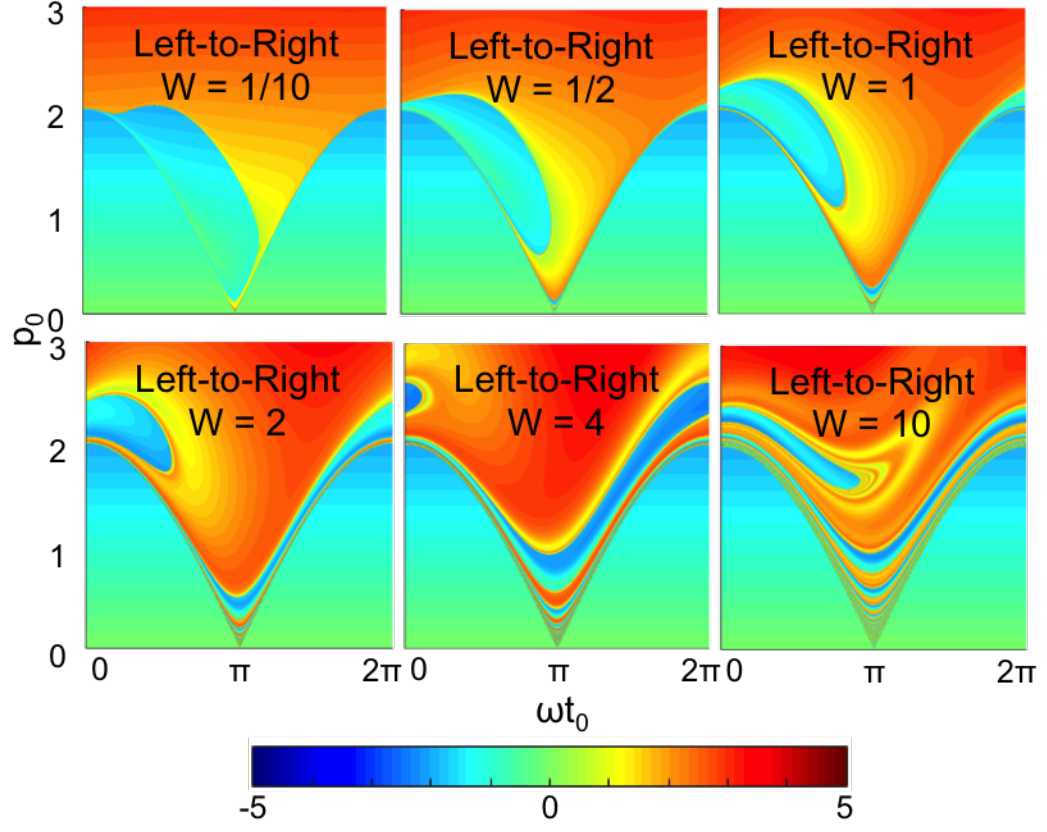
FIG. 6.11: Rectangular double barrier - effect of width. Resulting momentum of left-to-right launched particles as the barrier width W increases from 0.1 to 10. As the barriers become wider, the "Elevator Effect" dominates, shown here with increased striping and sensitivity to initial conditions.

beginning on the left of the pump with positive momentum has enough energy to hop onto the first barrier, we calculate the momentum of each particle over the first barrier p_a and the time t_a it reaches the end of the first barrier using 6.9 and 6.10. However, at this point, the particle falls off the first barrier into the region between barriers with momentum

$$p_N = (-1)^{N-1}\sqrt{2(U_{left}(t_a) + \frac{1}{2}p_a^2)}, \tag{6.16}$$

116

where the N in the exponent is a counter which we explain below. At this point, we consider the particle to be trapped in the region between the barriers. While the particle is trapped, we will count the number of times it traverses back and forth in the gap, as it reflects between the barriers. During the first pass through the gap, our trap counter N=1. If when the particle reaches the second barrier at time

$$t_N = N \frac{x_{0right} - x_{0left} - 4\sigma}{p_N} + t_a, \tag{6.17}$$

the particle has energy $\frac{1}{2}p_N^2 \leq U_{right}(t_N)$, then it will reflect from the second barrier and N will increment by 1. We continue to compare the kinetic energy of the particle $\frac{1}{2}p_N^2$ with the height of the encountered barrier - for N=odd, we compare with $U_{right}(t_N)$, and for N=even, we compare with $U_{left}(t_N)$, until the particle has sufficient energy to make it over one of the barriers. The remainder of the calculation is straightforward:

$$p_b = \pm\sqrt{2(\frac{1}{2}p_N^2 - U_{right,left}(t_N))}, \tag{6.18}$$

where the (+) corresponds to U_{right} and the (-) corresponds to U_{left}. Then, the particle will spend time

$$t_b = \frac{4\sigma}{p_b} + t_N \tag{6.19}$$

traversing the barrier, after which it will fall off the last barrier with

$$p_{final} = \pm\sqrt{2(\frac{1}{2}p_b^2 + U_{right,left}(t_b))}. \tag{6.20}$$

Once again, the algorithm is similar for particles originating on the right side of the

117

pump with negative initial momentum. The results of these calculations for the same particles launched previously at the same two barriers ($W = 1$, $\omega = 1$, $U_0 = 1$, $\phi = \frac{3\pi}{2}$) but with $x_{0left} = -1$ and $x_{0right} = 1$ are shown in Figure 6.12 below. Several qualitative features remain the same. However, we note the presence of a new lobe due to particles undergoing one back and forth bounce between the barriers. This complexity is due to the dynamics associated with the space between the barriers, allowing particles to bounce back and forth between them for significant time before exiting the pumping region. Even more so than the previous cases, the outcome is extremely dependent upon initial conditions of the particles.
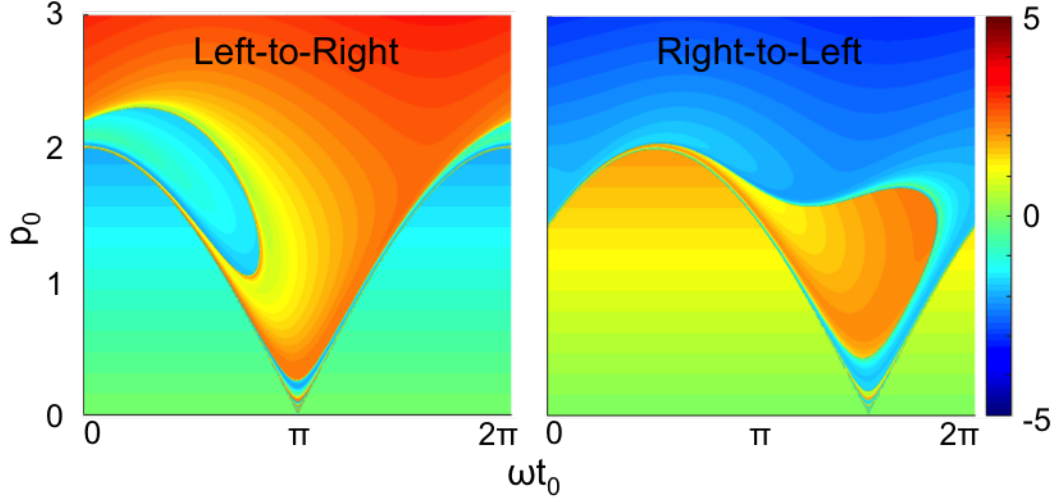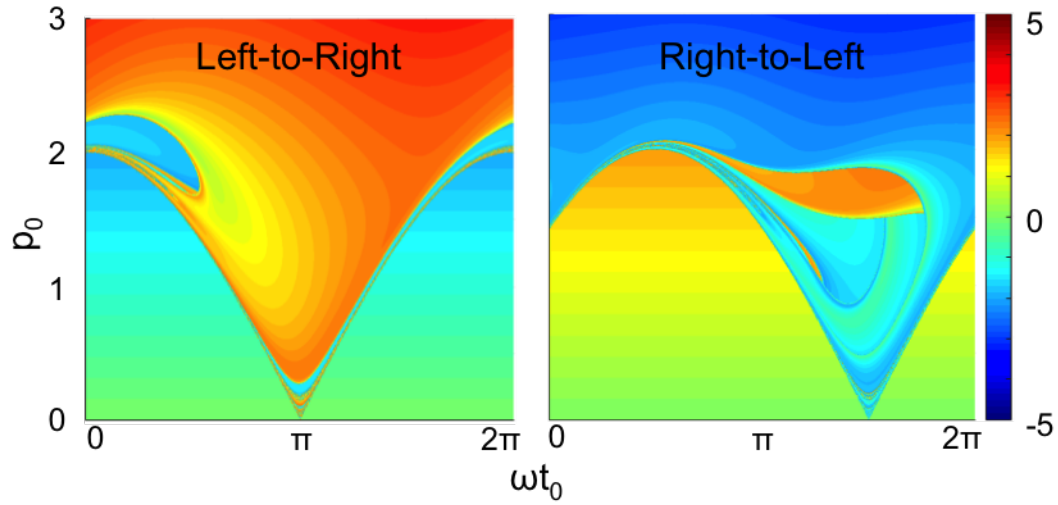

FIG. 6.12: Final momentum of particles scattered from a rectangular double barrier with space. The results of a grid of particles with initial momentum $p_0 = 0$ to 3 and launched over $\omega t_0 = 0$ to 2π. The color of each pixel corresponds to the final momentum of a particle at the particular initial position and launch time. The left (right) surface plot represents particles launched from left-to-right (right-to-left). Red and warm (blue and cool) shades correspond to particles which end with positive (negative) final momentum. In this case, $W = 1$, $\omega = 1$, $U_0 = 1$, and the barriers are centered at $x_{0left} = -1$ and $x_{0right} = 1$

In Figure 6.13, we examine the overall effect of the particles launched left-to-right while varying the width of the barriers and the space between them. Just as we saw that increasing the width of the barriers increased the striping due to the 'Elevator Effect',

increasing the space between the barriers also increases the chaotic region producing additional sensitivity to initial conditions. Increasing the space adds lobes within lobes and noticeably alters the area of the lobe.

6.3.3   Rectangular barrier conclusions

The classical dynamics of the rectangular barrier cases are extremely rich. For the single barrier case, particles can either be reflected from the barrier with only a change in the sign of the momentum, or they can transmit over the barrier and experience increases or decreases in momentum due to the oscillation of the barrier. Particles that hop onto the barrier with barely sufficient energy will experience variations in final momentum that are extremely dependent on the initial ωt_0.

With the addition of a second barrier, this dependence becomes even more noticeable, and clear fractal behavior can be seen around the class of particles that barely make it onto the first barrier. A lobe also appears which represents particles that transmit over the first barrier but reflect from the second. The structure of both the lobe and the fractal behavior becomes more complicated as the width of the barriers is increased due to the increased number of barrier oscillations that occur as particles transmit over them. Adding space between the barriers further complicates the lobe. Increasing this space between them increases the chaotic region.

6.4   Gaussian barriers

Armed with our foundation of understanding of the rectangular barrier systems, we can now examine Gaussian barrier systems. Gaussian potentials are an excellent choice for experimental implementations of pumping because they are readily available without implementing additional technology such as spatial light modulators. We expect to see
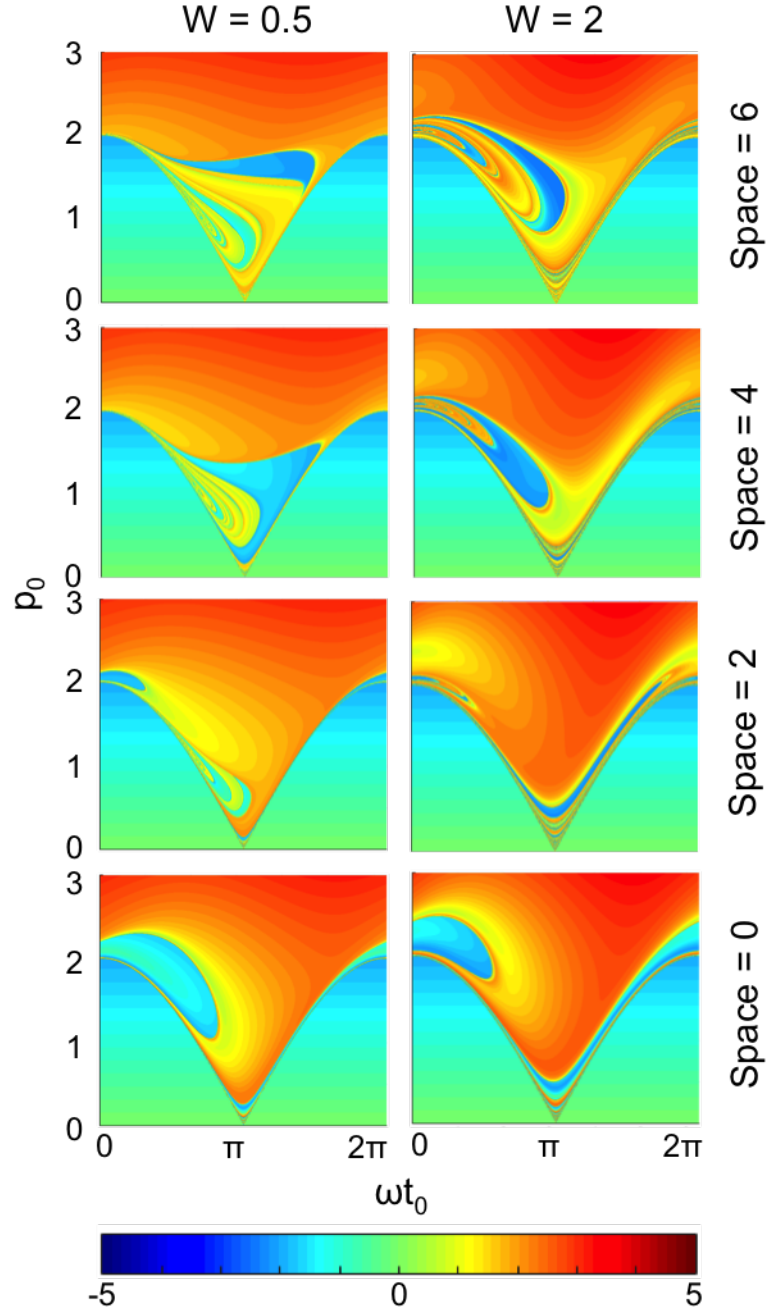
FIG. 6.13: Rectangular double barrier - effect of spacing. As we increase the space between the barriers, we also increase the chaotic region. This manifests as lobes within lobes and a further increased sensitivity to initial conditions.

some similarities between the Gaussian and rectangular cases, and relate the differences to the barrier shape. Once again, we begin with the single barrier dynamics and build up to the double barrier case.

6.4.1 Classical single Gaussian barrier

The methods for simulating particles scattering from a single Gaussian barrier were described previously in the Numerical Methods section (6.2.2). For the single Gaussian barrier case, we assume only one barrier, say U_{left} centered at $x_{0left} = 0$. To maintain consistency with the previous sections, we choose a FWHM $= 2$, $\omega = 1$, and $U_0 = 1$. The relationship between FWHM and σ is provided in the Model section previously. We launch the same block of atoms ($p_0 = 0$ to 3, $\omega t_0 = 0$ to 2π) towards the barrier from either side. The resulting final momentum of each particle is shown in Figure 6.14.
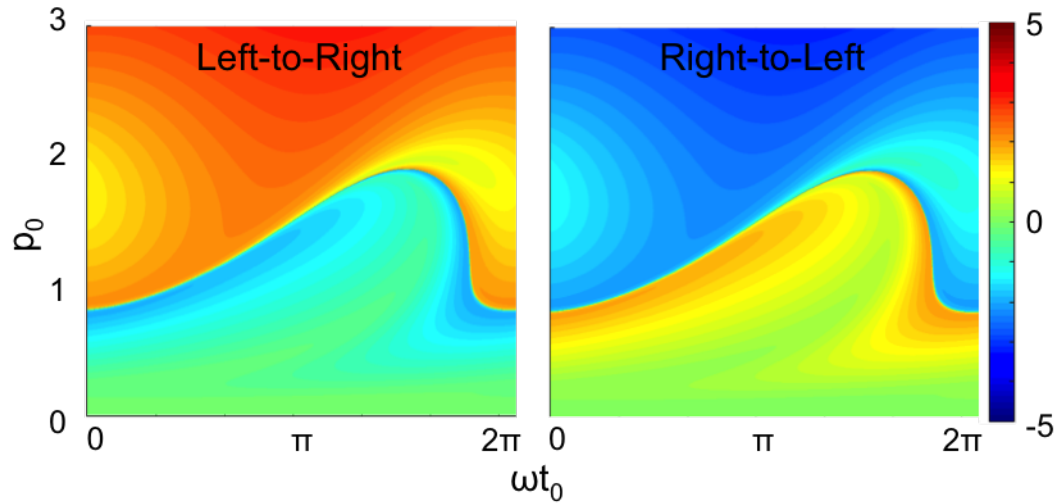
FIG. 6.14: Final momenta of particles scattering from a single oscillating Gaussian barrier. The results of a grid of particles with initial momentum $p_0 = 0$ to 3 and launched over $\omega t_0 = 0$ to 2π. The color of each pixel corresponds to the final momentum of a particle at the particular initial position and launch time. The left (right) surface plot represents particles launched from left-to-right (right-to-left). Red and warm (blue and cool) shades correspond to particles which end with positive (negative) final momentum. In this case, FWHM $= 2$, $\omega = 1$, $U_0 = 1$, and the barrier is centered at $x_{0left} = 0$.

121

Similar to the single rectangular barrier case, all particles with $p_0 > 2$ will transmit over the single Gaussian barrier. However, the boundary between positive and negative final momentum no longer follows the height of the barrier over time. Neither does it dip to $p_0 = 0$ for $\omega t_0 = \pi$. This is due to the Gaussian shape of the barrier and the fact that we launch our distribution from a further distance from the pumping region where the Gaussian tail is $< 0.0001 U_0$. Rather than having sharp edges, the Gaussian barrier has a smooth spatial distribution that creates a force on the particles at distances beyond the FWHM. It is literally an uphill battle for all particles as they approach the barrier. This particularly affects the low momentum particles, and no particle with $p_0 \lesssim 0.8$ will transmit over the barrier. Note that the two plots are symmetric, though the color scaling masks this symmetry a little. Once again, due to the symmetry of this case, there will be no resultant pumping.

One can gain a better understanding of the classical dynamics using a surface of section plot or Poincaré map, as was shown in Figure 6.4. As with every surface of section, we begin with several lines of particles in position space each with a single initial momentum. For a periodic, time dependent system, we strobe the path through phase space once every cycle. The surface of section in Figure 6.4 uses the parameters for the case described above, with FWHM = 2, $\omega = 1$, and $U_0 = 1$. As was described previously in the Surface of Section section (6.2.2) and description of Figure 6.14, some of the particles (for example, the red and blue curves in the plot with $p_0 = \pm 2.5$) easily transmit over the barrier region. It is also easy to see that particles with $p_0 = \pm 0.5$ (the orange and green curves) are simply reflected from the barrier. The reflection or transmission of particles that begin with $p_0 = \pm 1.5$ is dependent on the initial position of the particles, i.e. the time at which the particles reach the barrier. Depending on the height of the barrier, the particles may or may not have enough energy to transmit, thus the lines for these particular initial momenta end up tangled between both the top right and bottom left

quadrants.

In nearly all cases, when particles scatter off the oscillating barrier, they end with a final momentum that is greater than or less than their initial momentum. This change in momentum is entirely attributed to the presence of the single barrier. Particles that traverse the barrier as it is rising (falling) will end up with greater (less) momentum than that with which they began.

A histogram of the final momenta of the scattered particles represents the final momentum probability distribution. In Figure 6.15, we choose a simple case in the classical regime where all particles transmit over the barrier: An initial packet with $p_0 = 2.5$ will give a final momentum distribution between ≈ 2.05 and 2.82. This histogram is a result of the red curve in the top right quadrant of Figure 6.4, with parameters FWHM = 2, $\omega = 1, U_0 = 1$, and $x_{0left} = 0$. As one can see, there is a very clearly defined classically allowed region of final momentum. The boundaries are marked by sharp peaks in the histogram of final momentum. The presence of the sharp peaks is due to the sinusoidal nature of the barrier oscillations.

6.4.2   Classical double Gaussian barrier turnstile

Next we move to the double Gaussian barrier turnstile, which we expect to show the same qualitative features of the single oscillating Gaussian barrier, but with added complexity such as the lobes and striping effects we saw in the double rectangular barrier turnstile. Due to the shape of the Gaussian barriers, we cannot place the barriers immediately against one another as we first did to the double rectangular barriers. Unless they are completely overlapped, there will always be some space between the Gaussian barriers. Therefore, we should always expect to see signatures of a chaotic region as we did with the spaced rectangular barriers.
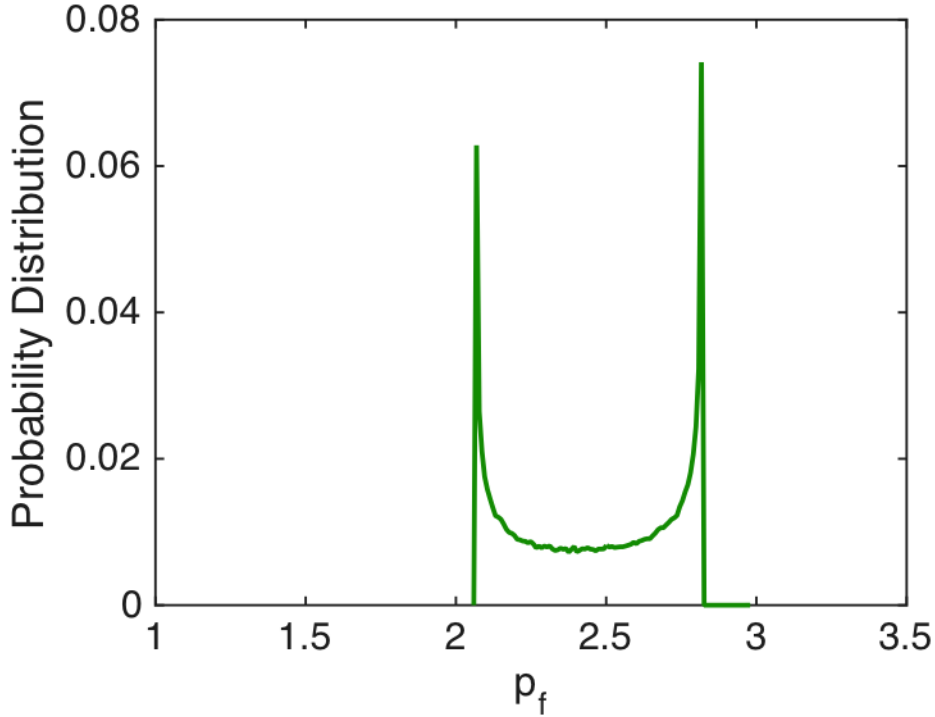
FIG. 6.15: Final momentum distribution of particles scattering from a single oscillating Gaussian barrier. This is a histogram of the final momenta of particles launched with $p_0 = 2.5$ and FWHM $= 2$, $\omega = 1, U_0 = 1$, and $x_{0left} = 0$. Particles gain or lose energy as the traverse the oscillating barrier, giving them a spread of final momenta. This spread has a clearly defined classically allowed region, marked by sharp peaks at the boundaries. The sharp peaks are due to more particles ending up with the maximum or minimum momentum, a product of the sinusoidal nature of the barrier. The y-axis is the probability distribution, or number of particles per final momentum value, which is normalized such that integrating over all final momenta in this plot gives 1.

The results for the double Gaussian turnstile pump with U_{left} centered at $x_{0left} = -3$ and U_{right} centered at $x_{0right} = 3$ are shown in Figure 6.16. To maintain consistency with the previous sections, we choose a FWHM $= 2$, $\omega = 1$, and $U_0 = 1$. We once again launch the same block of atoms ($p_0 = 0$ to 3, $\omega t_0 = 0$ to 2π) towards the barrier from either side.

Sure enough, the once clear boundaries between transmission and reflection are now disrupted with lobes and stripes in the double Gaussian case shown in Figure 6.16. This should not be a surprise to us, given what we learned in the rectangular barrier case study.

124
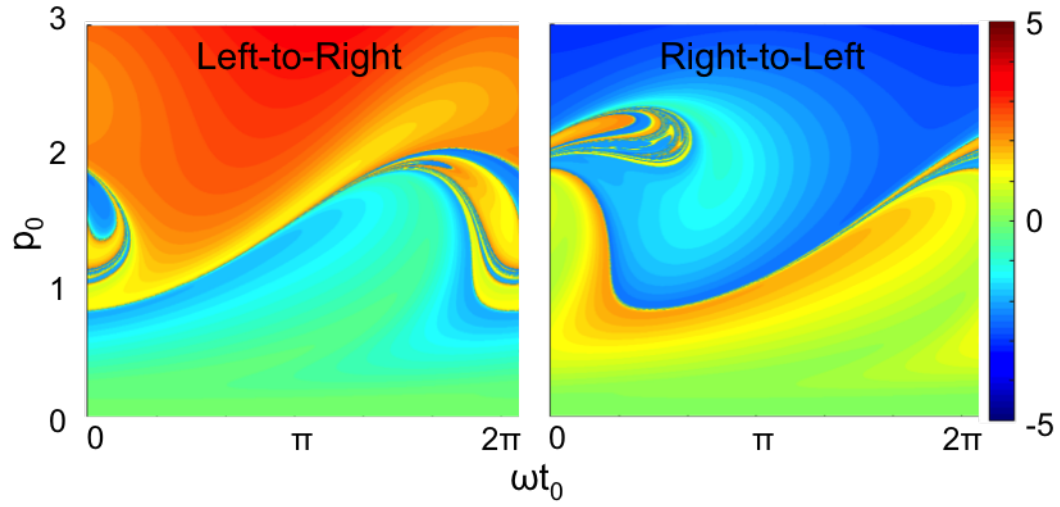
FIG. 6.16: Final momentum of particles scattered from a double Gaussian turnstile pump. The results of a grid of particles with initial momentum $p_0 = 0$ to 3 and launched over $\omega t_0 = 0$ to 2π. The color of each pixel corresponds to the final momentum of a particle at the particular initial position and launch time. The left (right) surface plot represents particles launched from left-to-right (right-to-left). Red and warm (blue and cool) shades correspond to particles which end with positive (negative) final momentum. In this case, FWHM $= 2$, $\omega = 1$, $U_0 = 1$, and the barriers are centered at $x_{0left} = -3$ and $x_{0right} = 3$.

We should also expect that increasing the barrier width or the barrier spacing will create even more complexity as we increase the chaotic region.

We can also see these differences in the surface of section plot for the double Gaussian turnstile in Figure 6.17. The presence of the two barriers is marked in the figure with gray bars having width equal to the FWHM of the Gaussian barriers. Some features are quite similar to the simpler single barrier case from Figure 6.4. Particles with $p_0 = \pm 2.5$ (red and blue curves) transmit over both barriers. Particles with $p_0 = \pm 0.5$ (orange and lime green curves) reflect from the first encountered barrier. The transmission or reflection of particles with $p_0 = \pm 1.5$ and ± 2 (pink, purple, forest green, and cyan) is extremely dependent upon initial position, so those lines end up tangled between the top right and bottom left quadrants. The region between the barriers, the so-called chaotic region is a new feature in this case. One can see that there is a tangle of trajectories, stemming largely from the line of particles with $p_0 = -2$ (forest green), but also from $p_0 = \pm 1.5$ (pink and cyan).

Zooming in on this region in Figure 6.18 shows the complicated nature of this area of phase space. In addition to the tangled trajectories of particles entering from the left or right of the pump, there are also two concentric rings of particles shown in black and gray. These rings represent particles which begin between the two barriers with insufficient momentum to ever make it out of the pump. They are forever trapped - "islands of stability amongst a sea of chaos" [86].

Finally, we can compute the pumping performance of the double Gaussian barrier turnstile pump. In Figure 6.19 we plot the sum of the final momentum of particles launched left-to-right and right-to-left toward a double Gaussian turnstile pump (rightmost plot), as well as the net momentum and particle pumping (center and leftmost plots, respectively). Once again, net momentum is defined by $\left[\sum_{\omega t_0} p_f(p_0) \right]/N$ where N is the total number of particles, while net particles pumped simply counts the number of particles on the left vs
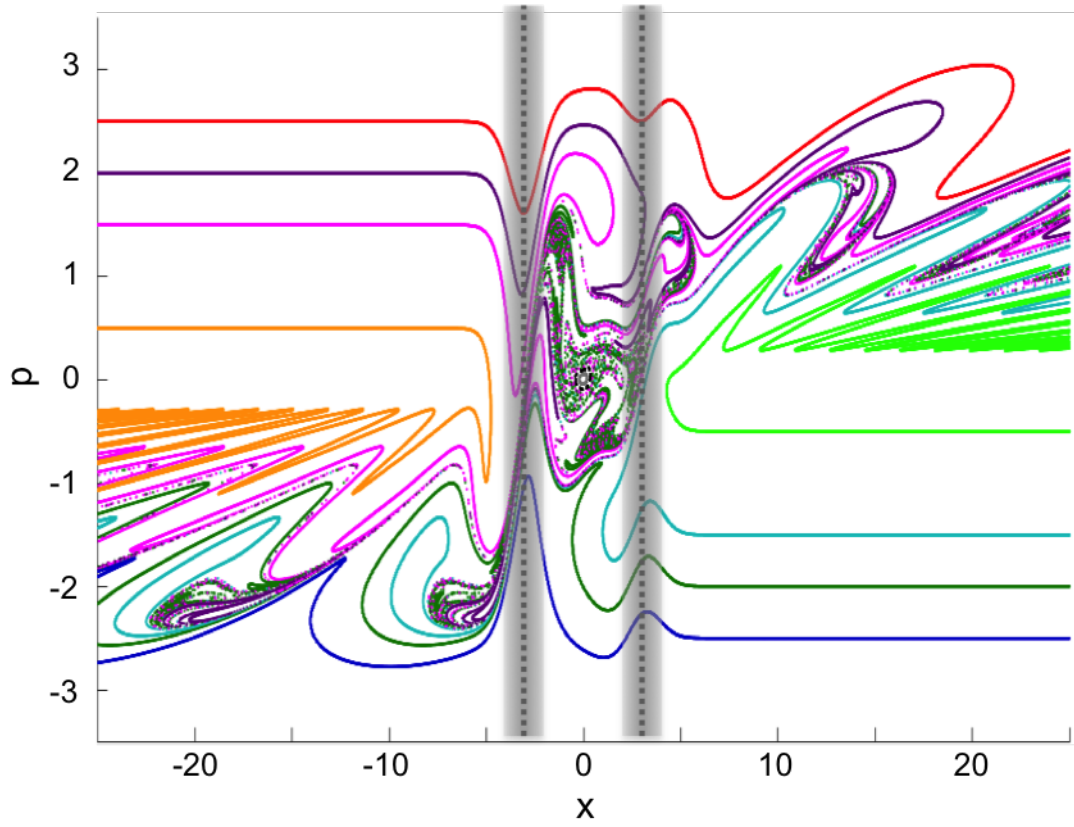
FIG. 6.17: Surface of section for a double Gaussian turnstile pump. Particles are launched towards a double Gaussian turnstile pump with $U_0 = 1$, $\omega = 1$, FWHM=2, and barriers located at $x_{0left} = -3$ and $x_{0right} = 3$. The shaded region indicates the FWHM size of the Gaussian barriers in the plot.
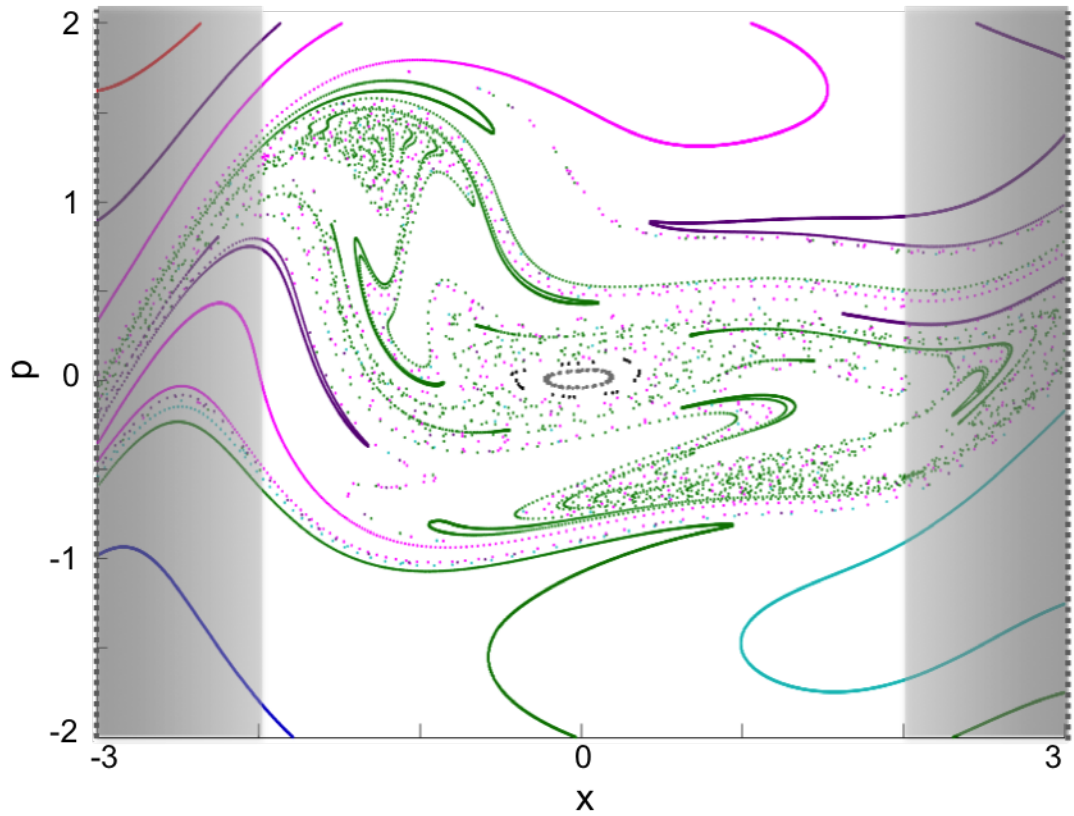
FIG. 6.18: Zooming in on the surface of section for a double Gaussian turnstile pump. We look more closely at the chaotic region between the barriers of the full surface of section given in Figure 6.17. Here we see a significantly tangled trajectories of particles which began with $p_0 = -2$ (forest green). At the very center are two concentric rings in black and gray representing particles which start in between the barriers and do not have sufficient momentum to escape to either side.

the number on the right for a single value of p_0 and normalizes the result with respect to N. Given the material in this chapter, there should be no surprises in the resultant plot of the final momentum on the left or the net momentum at each p_0 averaged over all ωt_0 on the right. For sufficiently large and small momenta, the averaged momentum goes to zero. Averaged over all possible p_0, the total pumping goes to zero. However, in between the large and small momenta, for small ranges of p_0, there are certainly regions of pumping.
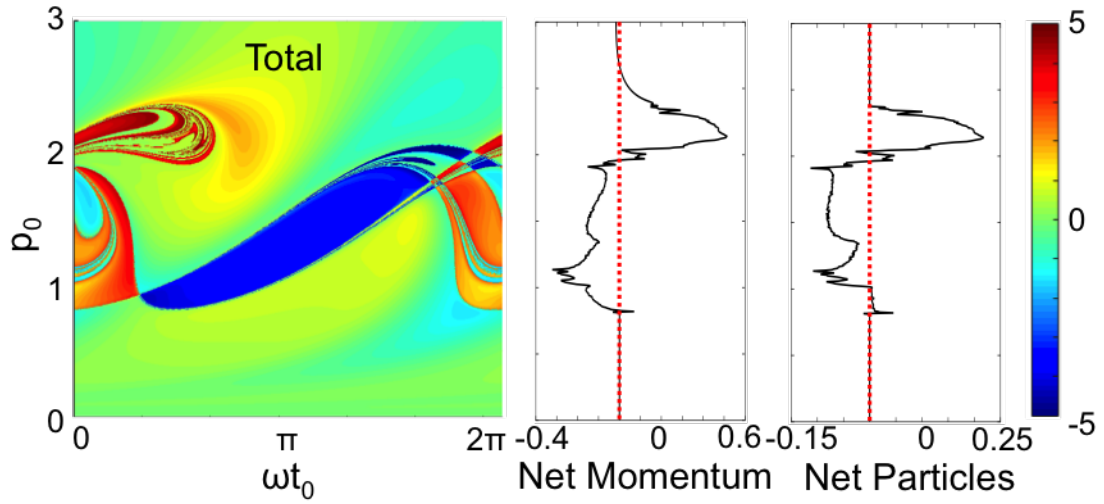
FIG. 6.19: Double Gaussian barrier total and average momentum and particle pumping. The left plot shows the sum of each plot from Figure 6.16. The center plot shows the average momentum for each p_0 on the y-axis summed over all possible ωt_0 on the x-axis. The left plot shows the average particles pumped for each p_0 on the y-axis summed over all possible ωt_0 on the x-axis. Regions of pumping for particular p_0 are obvious (where the color is not green in the left plot or where the net momentum or particles are not zero in the center and right plots).

6.5 The quantum picture

The quantum simulations of the scattering from oscillating Gaussian barriers involve propagating the wave packet by numerical integration of the Schrodinger equation [85]. These calculations have been carried out by AJ Pyle on code written by Kunal Das. The

results have been confirmed by Tommy Byrd, John Delos, and Kevin Mitchell using semi-classical theory. More details can be found in [85] and [87]. Here I focus primarily on the results of those detailed analyses and the stark contrast between the quantum and classical results.

For this thesis, we choose barriers broad enough to minimize the possibility of quantum tunneling through the barrier and a sufficiently elongated wave packet to allow for quantum interference effects, which play a key role in the scattering physics. While it is important to note that we are ultimately interested in the net current flow of particles, our simulations generally run a single packet from one side propagating in a single direction (towards the pump). For discussions of net current, we simply sum the results of the same packet from opposite sides of the pump. It is trivial to anticipate the net current flow if we were to launch packets from opposite directions for the single barrier problem. For the case with only one barrier, the system is entirely symmetric, so there will be no net current. For a net particle flow, we must somehow break this symmetry.

6.5.1 Single Gaussian barrier

As in the classical case, we begin simply with a single oscillating Gaussian barrier. We examine the scattering of a spatially elongated wavepacket with narrow momentum spread by looking at the final momentum distribution as we did in the classical case in Figure 6.15. The same parameters in the quantum simulations show a very different final momentum distribution than the classical simulations. Figure 6.20 shows the classical distribution from Figure 6.15 overlapped with the quantum distribution, plotted as $|\Psi(p)|^2$ on the y-axis. Rather than one smooth continuous distribution of final momenta, there are discrete peaks spaced by $\Delta E = \pm n\hbar\omega$ in energy space which appear as sidebands to a peak at the initial momentum. This is a dramatic difference from the continuous distribution in the

classical case.
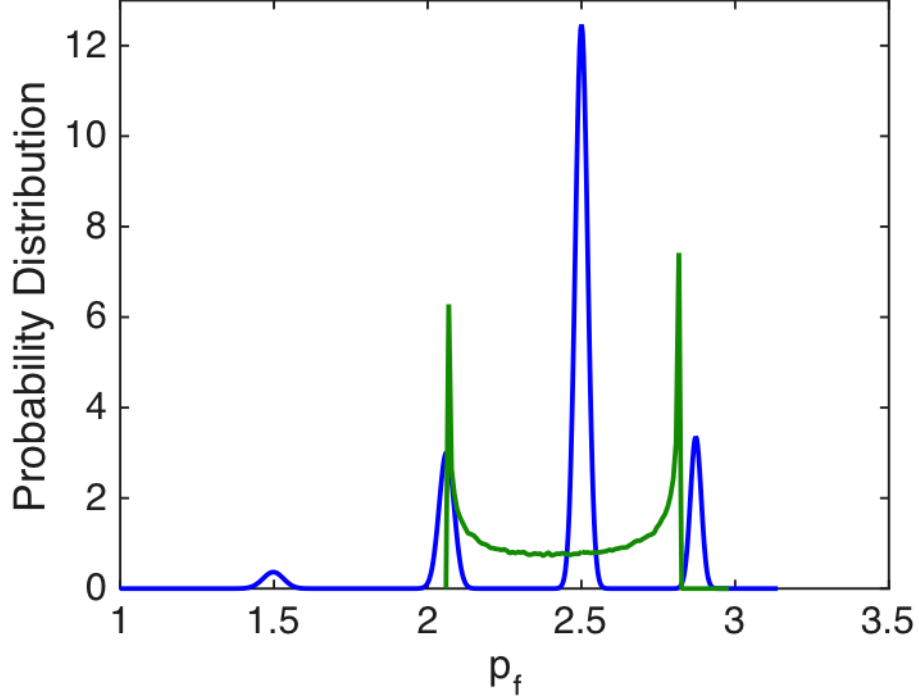
FIG. 6.20: Quantum and classical results for a single Gaussian barrier. Particles with $p_0 = 2.5$ are launched at a single oscillating Gaussian barrier with $U_0 = 1$, $\omega = 1$, FWHM=2, and located at $x_{0left} = -3$ and $x_{0right} = 3$. Both the quantum and classical results are overlayed to show the stark contrast between the two. In the classical case (green), the distribution is exactly the same as that shown in Figure 6.15 (scaled by $\times 100$). The quantum case (blue) plots $|\Psi(p)|^2$ as four visible Floquet states. The state at $p_f = 2.5$ lies entirely within the classically allowed region, and the state at $p_f \approx 2.1$ lies approximately half within the classically allowed region. Floquet states at $p_f = 1.5$ and ≈ 2.8 lie beyond the classically allowed region.

The presence of these peaks originates from our choice of a broad position-space wave packet and the periodic nature of our system. The peaks can be described by the Floquet theorem [88], which is the temporal analogue of Bloch's theorem in solid state physics [89]. Bloch's theorem describes the spatial wavefunction of a particle in a periodic potential, such as an electron in an ordered crystal. In our system, we have a particle in a periodic potential in time, so rather than manifesting in the spatial wavefunction, the Floquet peaks appear in the Fourier transform.

131

A detailed semi-classical study [87] elucidates the physics of the quantum scattering process and shows that the evenly spaced momentum peaks are due to constructive and destructive interference of scattered waves from different barrier oscillation cycles. This can be more clearly understood by examining this particular packet in the surface of section plot again. By drawing a horizontal line through the top right quadrant of Figure 6.4, it is easy to see that there are multiple initial positions within the single-momentum wavepacket with $p_0 = 2.5$ which lead to a given final momentum. It is the interference of these multiple paths which create the peaks in the quantum picture. We also note that diffraction(or momentum space tunneling) leads to the appearance of peaks outside of the classically allowed region.

Figure 6.20 is a simple case where paths interfere to produce four visible peaks - p_0 and two sidebands, one of which falls on the edge of the classically allowed region, and the other which falls just beyond it. Another small sideband is visible at $p_0 = 1.5$. Figure 6.21 is a more complicated version for the same system parameters but with $p_0 = 1.5$. In this case, the classically allowed region is broader than in Figure 6.20: It ranges from $p_f = \approx -2$ to ≈ 2.2 (green). This is a result of particles being both transmitted and reflected by the barrier. The Floquet states (blue) also appear across a much broader range, some of which have been both transmitted and reflected by the barrier. While the largest Floquet states fall within the classically allowed region, there are also peaks which appear beyond this region.

6.5.2 Double Gaussian barrier turnstile

The double Gaussian turnstile consists of two single oscillating Gaussian barriers. In the single barrier case, a particle with a single momentum encounters a barrier which separates it into several momentum peaks - for example, let us use the case that the single
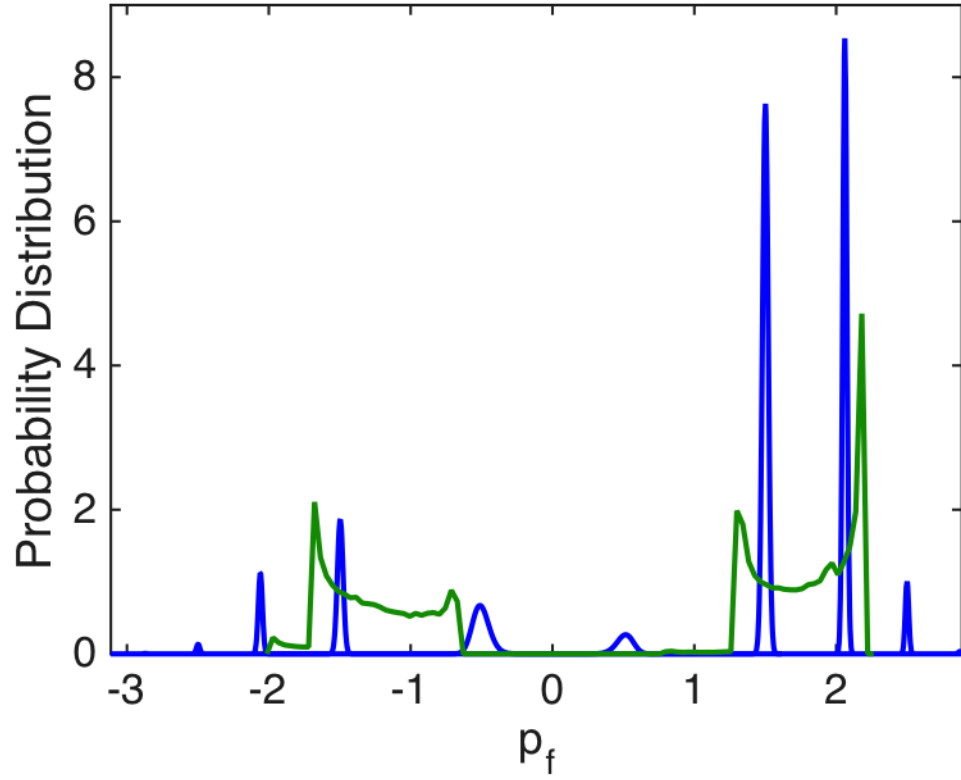
FIG. 6.21: Quantum and classical results for a single Gaussian barrier with both transmission and reflection. Particles with $p_0 = 1.5$ are launched at a single oscillating Gaussian barrier with $U_0 = 1$, $\omega = 1$, FWHM=2, and located at $x_{0left} = -3$ and $x_{0right} = 3$. Both the quantum and classical results are overlayed to show the stark contrast between the two. In the classical case (green), the distribution ranges from $p_f = \approx -2$ to ≈ 2.2 (scaled by $\times 50$). The quantum case (blue) plots $|Psi(p)|^2$ as several visible Floquet states which fall both within and beyond the classically allowed region.

input momentum is separated into three momentum peaks with energies $E_0 - \hbar\omega$, E_0, and $E_0 + \hbar\omega$. One can consider each of those peaks as a separate input momentum for the second barrier, each of which gets split into three additional momenta, as shown in the example cartoon in Figure 6.22. In the case of final momentum states that can be produced in several ways or paths (e.g. $E_0 \rightarrow E_0 - \hbar\omega \rightarrow E_0$, $E_0 \rightarrow E_0 \rightarrow E_0$, and $E_0 \rightarrow E_0 + \hbar\omega \rightarrow E_0$), the phases of the different paths must be included and will lead to destructive and constructive interference. The double barrier turnstile pump acts as a momentum space interferometer.
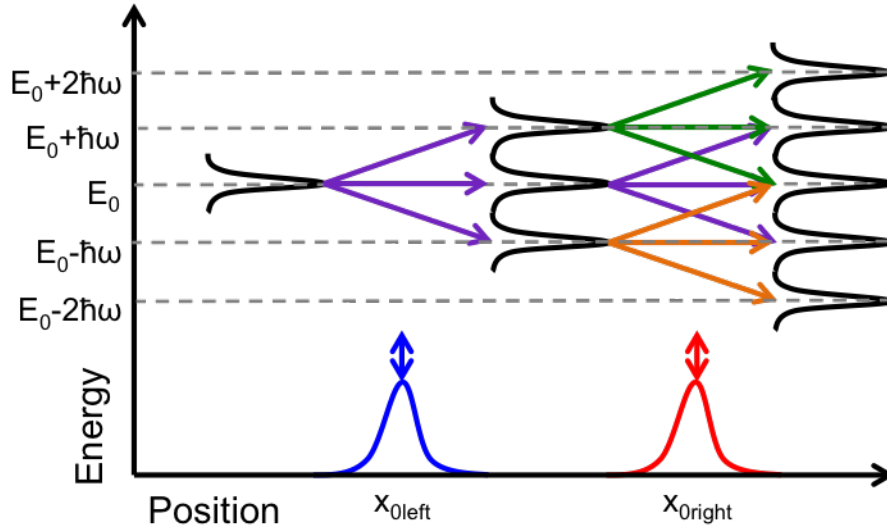
FIG. 6.22: Conceptual drawing of a momentum interferometer. A basic cartoon momentum interferometer would split a wavepacket with a single momentum state into several momentum states and then recombine them. Here, an oscillating barrier splits the wavepacket into several Floquet states. Each of these Floquet states encounters a second oscillating barrier which splits each of these. The resultant peak at the original energy is a recombination of the peaks.

Another application one could imagine is a diode. The diode would operate with one fixed barrier and one oscillating barrier as in Figure 6.23. The height of the fixed barrier U_0 is such that an incoming packet with a kinetic energy $E < U_0$ does not have sufficient energy to transmit over the fixed barrier: Particles approaching from the side of the fixed

barrier will be reflected. However, the quantum interference effects from the oscillating barrier create several Floquet states from the single wavepacket approaching from the side of the oscillating barrier. Some of these Floquet states can be sufficiently energetic to transmit over the second barrier, permitting pumping in only one direction [85]. (Note that transmission will also occur due to classical dynamics associated with the oscillating barrier.)
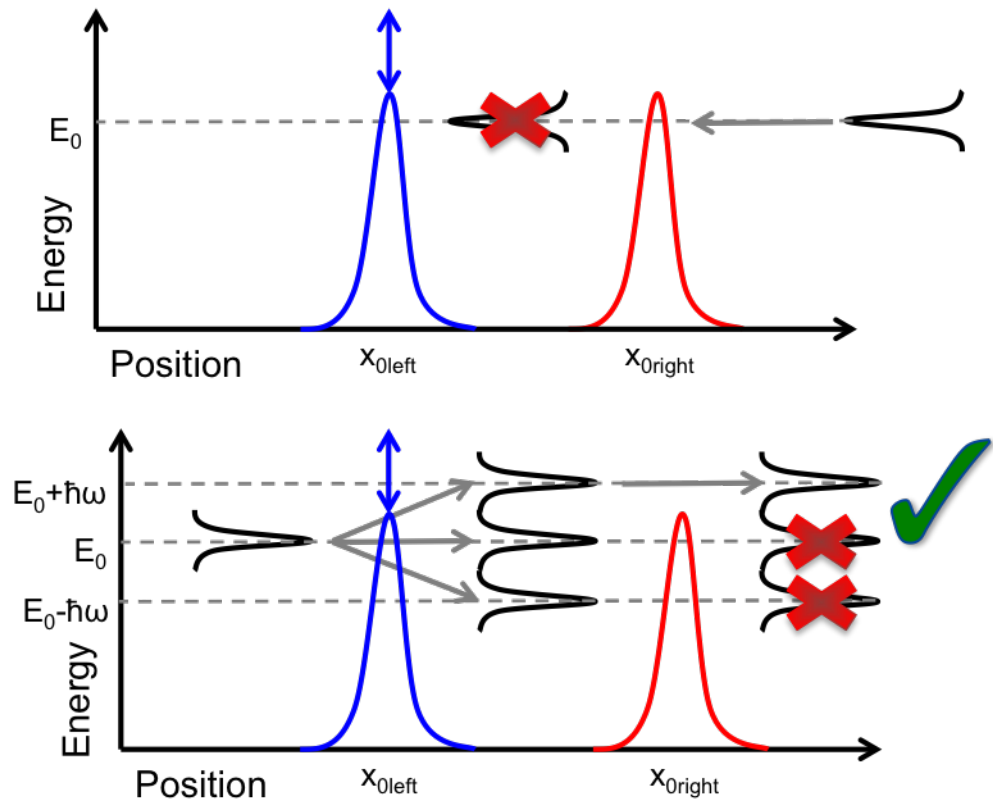
FIG. 6.23: Conceptual drawing of a quantum diode. A quantum diode consists of a single oscillating barrier (left) and a fixed barrier (right). The right barrier is high enough that a wavepacket with energy $E < E_0$ is reflected. Therefore particles approaching from the right are entirely reflected. Particles approaching from the left first encounter the oscillating barrier, which creates Floquet states of higher energy. The higher energy states transmit over the stationary barrier. The creates net pumping only in one direction.

A close corollary to the diode is a switch. Again, the switch would operate with one fixed barrier and one oscillating barrier, as in Figure 6.24. The momentum of the

wavepacket is small enough that it cannot transmit over the stationary barrier. However, when the oscillating barrier is turned on, the higher energy Floquet states can transmit over the stationary barrier. In this way, one can switch on and off the pumping in one direction.
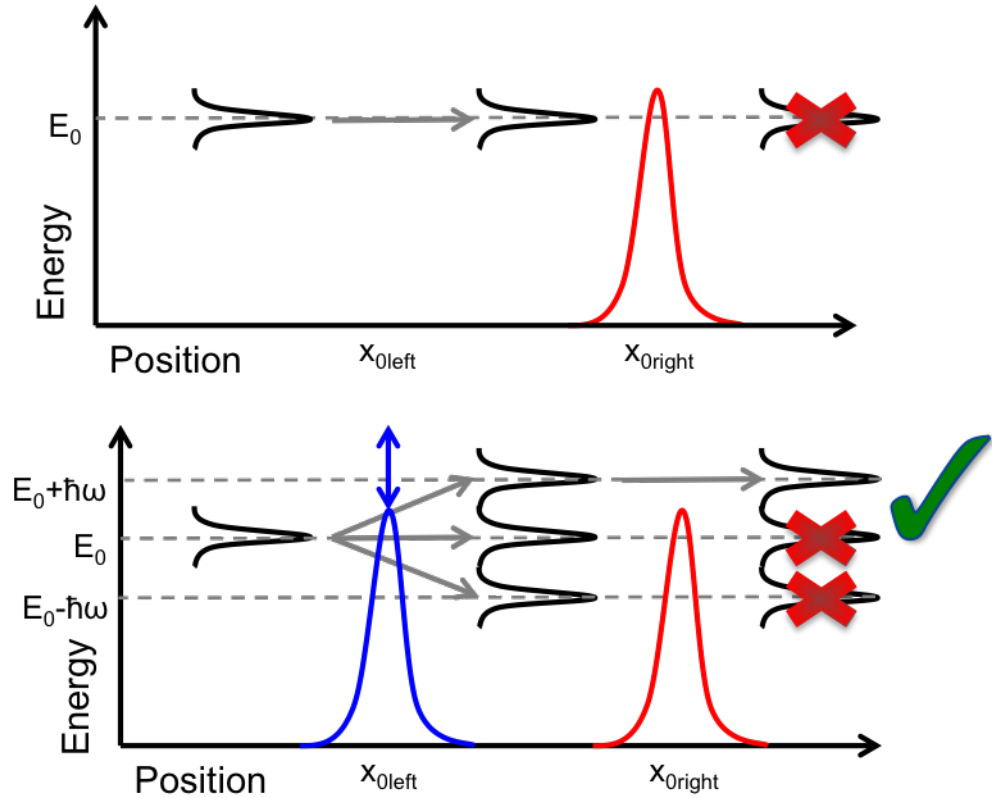
FIG. 6.24: Conceptual drawing of a quantum switch. Similar to the quantum diode, a quantum switch would allow one to switch a pumping current on or off. Once again, the switch operates with one oscillating barrier and one fixed barrier. The fixed barrier has a height which prevents the input wavepacket from transmitting over it. However, when the oscillating barrier is turned on, the higher Floquet states transmit over the fixed barrier. In this way, pumping only occurs when the oscillating barrier is turned on, and no pumping occurs when it is turned off.

136

6.5.3 Conclusion

It is clear that pumping can be both a classical and quantum process. Classically, there are extremely rich dynamics present which affect the overall pumping of both momentum and particles. Generally, chaos is detrimental to large pumping regions. In the quantum process, interference can play a large role in shaping the resultant final momentum distributions. The single oscillating Gaussian barrier shows a dramatic difference between the classical and quantum results and is an excellent candidate for exploring these differences in initial experiments.

CHAPTER 7

Experimental single barrier scattering

7.1 Introduction

Now that we have established the theoretical tools with which to understand this scattering problem, we can prepare to study it experimentally with ultracold atoms. As was shown in Chapter 5, the apparatus is capable of producing BECs of approximately 10^4 ^{87}Rb atoms on a chip. We can easily control the final temperature of our atoms by choosing a higher or lower RF value during our evaporation. This allows us to smoothly transition from thermal atom clouds which follow classical Maxwell-Boltzmann statistics (for $T >> T_c$, Bose-Einstein statistics approximate to Maxwell-Boltzmann statistics) to condensates which are quantum objects in which all of the atoms are in the same state, providing an excellent tool for probing both classical and quantum regimes outlined in the previous chapter.

In this chapter, we characterize the simple case of scattering from a single oscillating

Gaussian barrier, which shows obvious differences between the classical and quantum behavior. The basic objective of an early experiment is to see quantum peaks emerge as we transition from the classical to quantum distribution. Our approach is to launch a cloud of atoms at a single oscillating Gaussian barrier and try to detect the resultant peaks. There is more than one way of doing this. For example, we initially proposed waiting some sufficiently long time-of-flight to see the peaks manifest in the position space wavefunction. The resultant position space probability distribution for the case in Figure 6.20 is shown in Figure 7.1 after a t=500 time-of-flight. However, depending on the experimental parameters, it is possible that by the time the peaks manifest in position space, the cloud will have fallen out of the field of view of the camera or there would be no atom density signal due to lifetime issues. Therefore, we consider an alternative method.

We instead examine the resultant peaks from a single oscillating barrier using a method fondly termed "The Discriminator", which is similar to the conceptual cartoon of a quantum switch shown in Figure 6.24. The basic idea is that a cloud of atoms will begin with an initial momentum, scatter from an oscillating barrier giving it a spread of final momenta, and then encounter a second static barrier. Depending on the height of the second static barrier, the cloud can either transmit, reflect, or be partially transmitted and reflected. This second barrier will discriminate or select between low and high final momenta.

In this simple case, however, we do not yet have a second barrier in our toolbox. Clever use of our trapping potential allows us to demonstrate "The Discriminator" case with only a single barrier. The basic idea, depicted in 7.2, is to launch a cloud of thermal atoms with initial momentum p_0. As the cloud interacts with the oscillating barrier, it will acquire a spread of final momentum p_f. In the classical case, this spread will be a smooth distribution similar to the green curve in Figure 6.20. The quantum case will also end with multiple final momentum values, but having Floquet peaks similar to the peaks
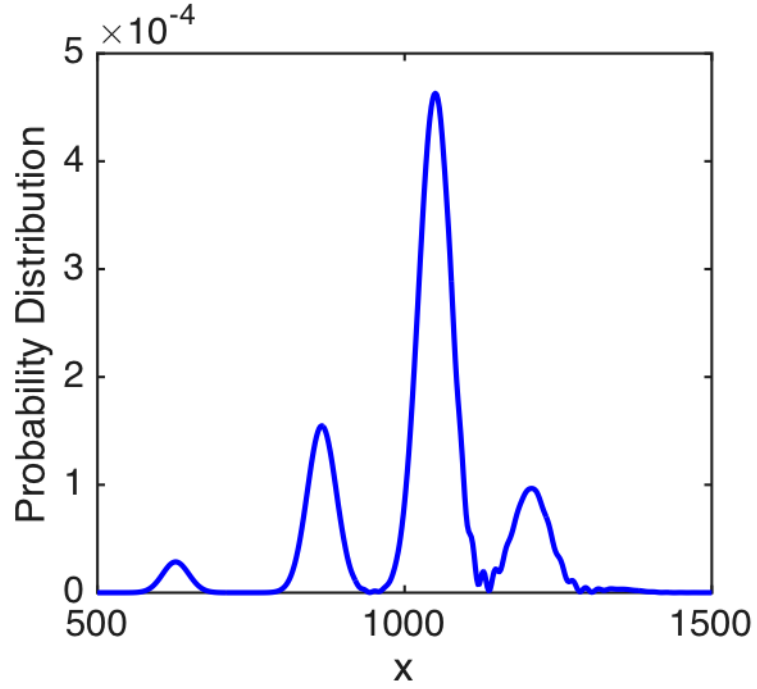
FIG. 7.1: Simulated quantum position space probability density after a long time-of-flight. After a sufficiently long time-of-flight (t=500 here), the quantum peaks manifest in the position space probability density. This is the position space probability density which corresponds to the position space probability density in Figure 6.20. In the theory units from Chapter 6, the parameters are $p_0 = 2.5$, FWHM $= 2$, $\omega = 1, U_0 = 1$, and $x_{0left} = 0$. To convert to experimental units, first determine the ratio of the real barrier width to the theoretical barrier width l_u. Then $\omega' = \frac{\hbar}{ml_u^2}\omega$, $U_0' = \hbar\omega'U_0$, and $p_0' = \sqrt{\hbar m\omega'}p_0$ where the primed units represent the experimental parameters.

in the blue curve in Figure 6.20. Because our atoms are trapped in a harmonic trap, they will interact with the oscillating barrier, reach the top of the harmonic bowl, and then reverse directions to interact with the barrier a second time. On the return trip, however, we choose a static barrier, which will either fully or partially reflect (and transmit) the particles depending on its height.
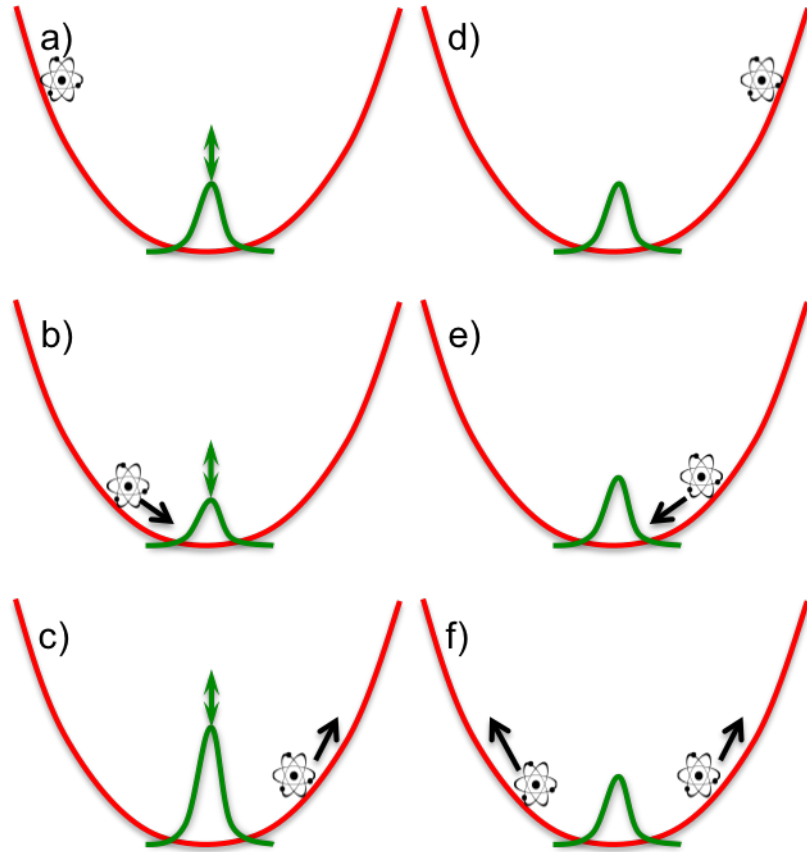
FIG. 7.2: "The Discriminator" scheme. a) Begin with atoms pushed up the side of the trap. b) The atoms slide down the side of the trap, gaining momentum as they approach the oscillating barrier. c) After interacting with the oscillating barrier, the atoms continue up the opposite side of the trap, now with a larger spread of momentum due to the barrier. d) The atoms eventually stop and reverse direction back towards the barrier. e) This time, the atoms approach a static barrier. f) Depending on the height of the static barrier, the atoms are reflected or transmitted. By measuring the number of atoms reflected or transmitted at varying static barrier height, one can determine the momentum spread imparted by the oscillating barrier.

With this method, we can produce plots of transmission of atoms over the barrier as

a function of barrier height. The transmission curves for the classical and quantum final momentum distributions from Figure 6.20 are shown in Figure 7.3. These transmission curves are determined by summing the probability distributions: Transmission $= 1 - \sum_0^{p_f}$(Probability Distribution).
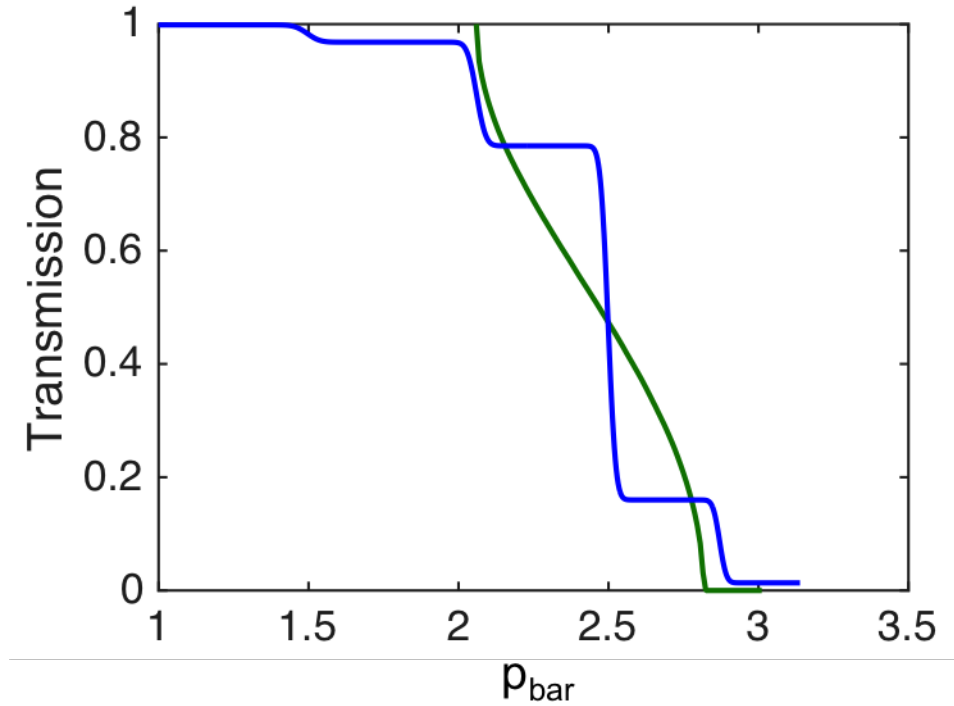
FIG. 7.3: Expected transmission curve for "The Discriminator" based on Figure 6.20. The transmission of atoms over a barrier with barrier height corresponding to $p_{bar} = \sqrt{2U_0}$ for a classical case (green) and a quantum case with four visible Floquet states (blue).

Experimental implementation in the lab requires:

1. A packet of atoms held in a quasi-1D conservative trap,

2. A Gaussian potential barrier that can be static or amplitude modulated, and

3. A way of imparting a narrow band of initial momentum to those atoms.

In this chapter, I detail the design, demonstration, and characterization of each of these components in the Aubin lab and show the classical results of a cloud of atoms interacting with the static barrier in "The Discriminator" scheme.

7.2 Conservative potential

We have two conservative potentials to choose from in our lab: 1) The magnetic chip trap potential, and 2) the optical dipole trap. The motivation behind the demonstration of the optical dipole trap described in Chapters 3 and 4 was to use it as the 1D potential for quantum pumping experiments. However, during my tenure, we became acutely aware of the severe impact of stray reflections and the surprisingly deep lattice potentials they create. Because of these concerns, we decided to perform the experiment described in this chapter in the magnetic chip trap potential .

The specific magnetic chip trap previously described in Chapter 5 is problematic for the proposed experiment due to its uneven potential. The dimple that delayed our achievement of BEC will also distort the motion of our atomic cloud in this experiment. Therefore, we relaxed the trap such that the potential minimum was $\approx 465\mu$m from the surface of the chip. At this distance, the dimple was no longer visible in the trap potential. To produce a trap at this distance, we ran 1 A of current through the Z-wire with $B_{Hold} = 4.64$ G and $B_{Ioffe} = 4.92$ G. The resulting calculated radial and axial trap frequencies are $\omega_r = 2\pi \times 46.8$ and 59.8 Hz in the radial vertical and horizontal directions, respectively, and $\omega_z = 2\pi \times 13.9$ Hz in the axial direction. We verified the axial trap frequency using the sloshing method described in Chapter 5 and measured $\omega_r = 2\pi \times 63(3)$ Hz and $\omega_z = 2\pi \times 13.5(5)$ Hz.

7.3   Gaussian barrier

The Gaussian barrier is produced with a tightly focused blue-detuned Gaussian laser beam. The beam is produced with a 532 nm laser (Coherent 532 nm DPSS) generously loaned to the Aubin lab by Dana Anderson of JILA for the completion of this work. The laser scheme (shown in Figure 7.4) overlaps the green laser with the path of the pump/probe beam used for axial imaging. We create a vertical sheet of light that cuts through the center of our cigar-shaped trap axially. This is done with a combination of a f=60 cm cylindrical lens which focuses the beam in the vertical axis (in and out of the page in Figure 7.4) followed by a f=6 cm achromat lens (Edmund 49-329) that collimates the vertical axis but focuses the horizontal axis (up/down in Figure 7.4). In order to maintain a collimated probe beam, a 1:1 telescope is formed with an additional spherical lens and the final f=6 cm achromat lens. The beams are combined on a dichroic mirror that passes 780 nm light but reflects 532 nm light.

The green beam is directed along the path in Figure 7.4 with a single-mode polarization maintaining fiber. Prior to being coupled to the fiber, an AOM and mechanical shutter provide fast switching of the green beam. Once through the fiber, a piece of glass is placed along the path of the green laser in order to monitor the power with a photo diode. We calibrate the output power with respect to the AOM voltage when the laser is in half power mode and full power mode. This allows us to monitor the height of the potential barrier. The power vs AOM calibration is shown in Figure 7.5. The amplitude control of the RF power to the AOM allows us to modulate the barrier or keep it static as desired.

Two mirrors allow us to align our beam to the approximate center of the atom cloud with 3 progressively more involved methods. The first method is the most coarse, and simply involves using the axial imaging camera in free-running mode to monitor the po-
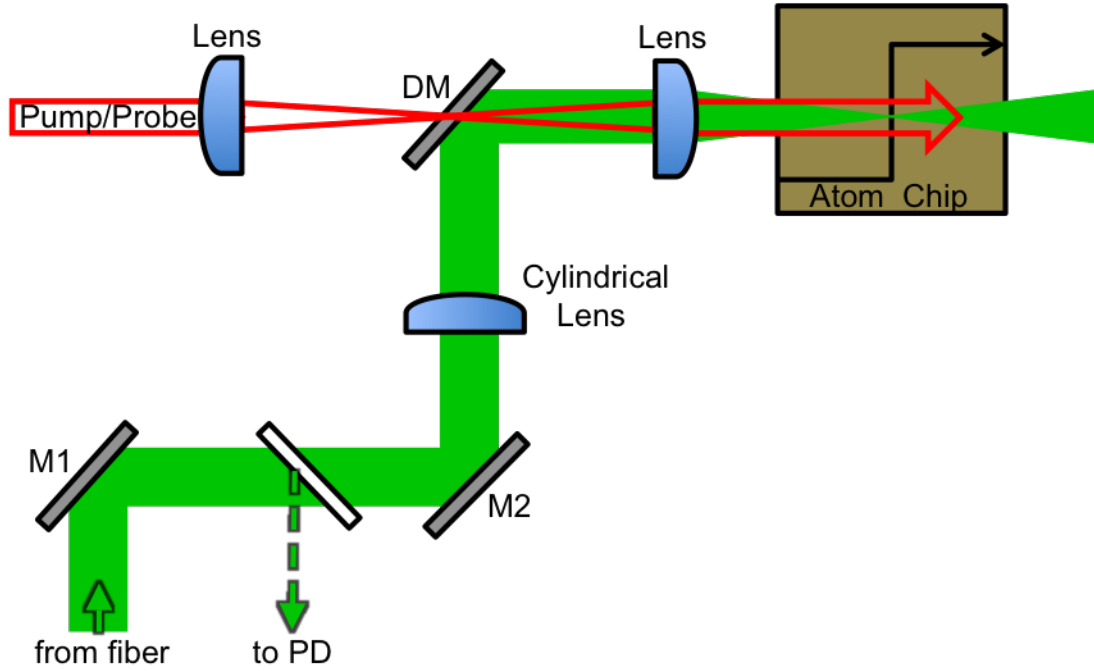
FIG. 7.4: Green beam Gaussian barrier scheme. The green beam is delivered to the system through an optical fiber. The beam is combined with the axial imaging pump/probe beam on a dichroic mirror (DM). The blue-detuned focused sheet of light is produced with a cylindrical lens that focuses the beam in/out of the page followed by a f=6 cm spherical lens that collimates the beam in/out of the page and focuses the beam up/down on the page. A piece of glass picks of a small reflection for monitoring power on a photo diode (PD). Alignment is done with two mirrors (M1 and M2) and a translation stage under the spherical lens for adjustments of the focus along the axis of propagation.
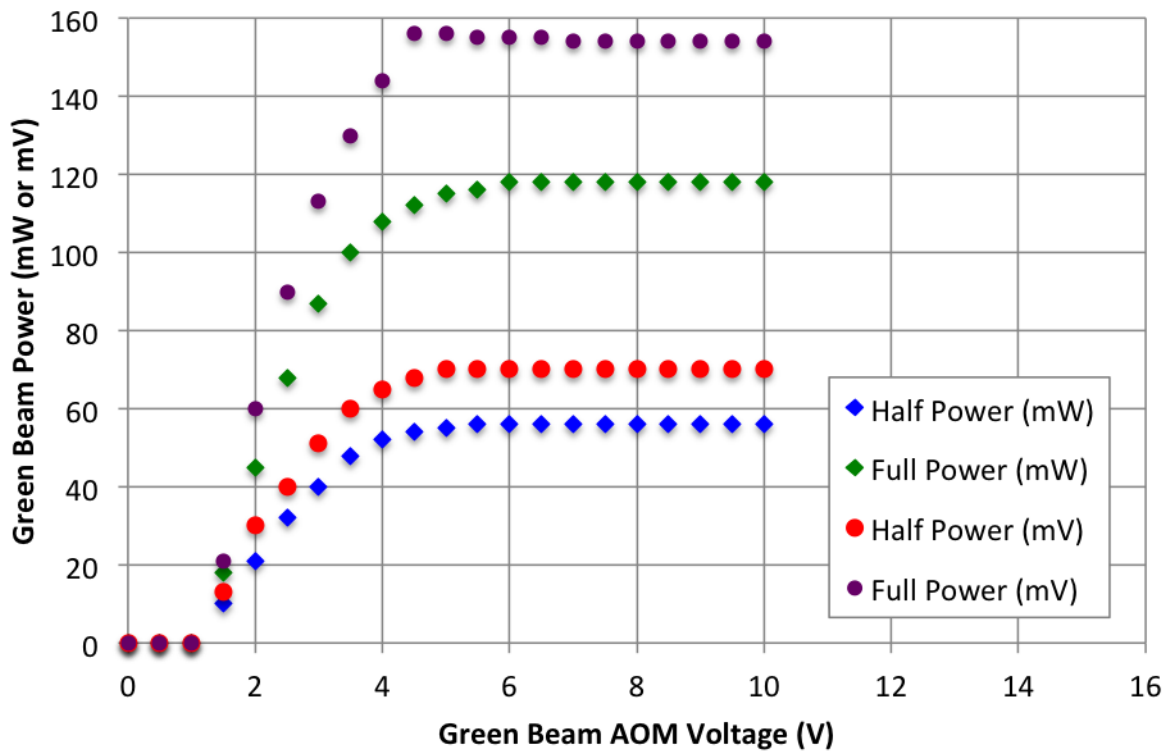
FIG. 7.5: Green beam power calibration. Green beam power and photodiode voltage at fiber output as a function of the AOM amplitude control voltage. The 532 nm laser has two settings: half power and full power. The power of the beam is measured with a power meter and monitored with a photodetector. Both the power and the photodetector voltage are plotted as a function of the AOM voltage.

146

sition of the green beam. Once the camera is focused on the atom cloud, we note the pixel position of the atom cloud on the camera. We then align the beam to that position. This horizontal/vertical alignment is done with the two mirrors. The longitudinal focus position is adjusted by translating the final f=6 cm achromat lens along the axis of propagation. We make this adjustment while minimizing the size of the beam's resultant line on the camera. When approximately aligned with this method, the camera shows the beam has FWHM = 1.4 pixels = 6.6 μm along the horizontal axis and FWHM = $\sigma_{vertical}$ = 40 pixels = 186 μm in the vertical direction. This alignment method will get us close in the longitudinal and transverse axes but not perfect. The camera imaging system we are using is designed for 780 nm, and there will be chromatic aberrations at 532 nm. Therefore, we expect the position of the focus to need further adjustments.

Now with the atoms present, we turn on the green beam to poke a hole in the cloud. The gap be observed visually in the absorption images with a narrow-pass 780 nm filter. Again, we adjust the horizontal/vertical alignment with mirrors and make longitudinal focus adjustments along the axis of propagation with the lens. The goal is to make the hole in the atom cloud as narrow as possible. Figure 7.6a is a typical absorption image of the atoms at 56 nK in the chip trap with the barrier on. One can see there is a line cut through the center of the atom cloud. That line is due to the presence of the barrier. We did our best to center the barrier on the bottom of the chip trap. Figure 7.6 shows the beam is displaced a few pixels from the center. This is due to alignment drift over time.

The final alignment tool relies upon the system dynamics to alert us if the atoms are sneaking around the barrier in the axis in and out of the camera. While the system approximates a 1D problem, the actual atom trap is truly 3D. Indeed, if the barrier is not focused on the atoms, then a video of sloshing atoms will show some of the atoms transmitting when they should be entirely reflecting. This can be corrected by fine tuning the focusing lens along the axis of propagation.
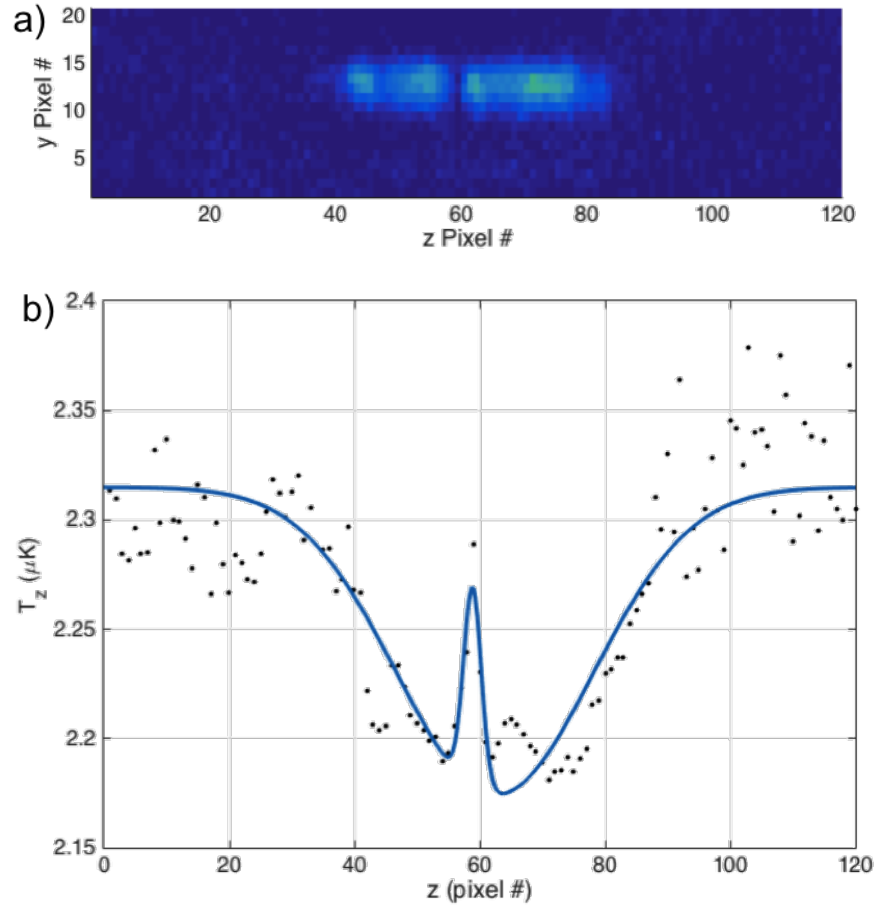
FIG. 7.6: Characterization of the potential barrier produced by the green beam. a) Absorption image of the atom cloud in the presence of the green sheet of light. The green vertical sheet is visible as a slice through center of the cloud where no atoms are present. b) Atom number density can be converted to trap potential (recall Chapter 5) to calibrate the width and height of the barrier using a measured atom temperature of 56 nK. This plot is generated from the sum of the pixels in a) along the y-axis. Here, we have fitted to Equation 7.1 with $a_1 = -141$ nK, $x_1 = 62$, $\sigma_1 = 22$ pixels, $a_2 = 92$ nK, $x_2 = 59$, $\sigma_2 = 2.0$ pixels, and $d = 2.3\mu$K.

148

We use the atom density images such as the one shown in Figure 7.6a to reconstruct the potential as was described in Chapter 5. Figure 7.6b shows this potential T_z fitted to a double Gaussian given by:

$$T_z = a_1 \exp(\frac{(x - x_1)^2}{\sigma_1^2}) + a_2 \exp(-\frac{(x - x_2)^2}{\sigma_2^2}) + d \tag{7.1}$$

where the first term fits to the trap potential and the second term fits to the barrier potential. In this particular image, the barrier has $\sigma_2 = 2.0$ pixels $= 9.3$ μm. From the average of 5 fits, we determine that our barrier has $\sigma_2 = 2.2 \pm 0.2$ pixels $= 10.2 \pm 0.9 \mu$m. We can also use this method to estimate the height of the barrier. From these same images, we determine that our barrier maximum height ($2U_0$) is between 70 and 110 nK tall.

Our second method of calibrating the height of the barrier involves launching a cloud of atoms with a known velocity at the static barrier and increasing the barrier height until half of the atoms transmit over the barrier and half of the atoms are reflected. This is shown in Figure 7.7 for an initial velocity 8.6 mm/s ($E/k_B = 388$ nK). The method for determining the initial velocity of the atoms is described in detail in Section 7.4. In the figure, atoms are launched from right-to-left. Approximately half of the atom cloud is reflected and half is transmitted for 58 mW of power. This tells us that 58 mW of power from the fiber produces a barrier with a height of approximately 388 nK. Note that a quick calculation such as those performed in Chapter 3 will produce a barrier much higher ($\approx 2\times$) than 388 nK with 58 mW of power. Therefore it is important to recall that 58 mW is the power output from the fiber. This is not the power that the atoms see. Power will be lost due to transmission in the mirrors and reflection at the piece of glass, lenses, and cell wall. It is not unreasonable to expect only 70 % of the light at the atoms, assuming only 4 % loss per surface along the way.
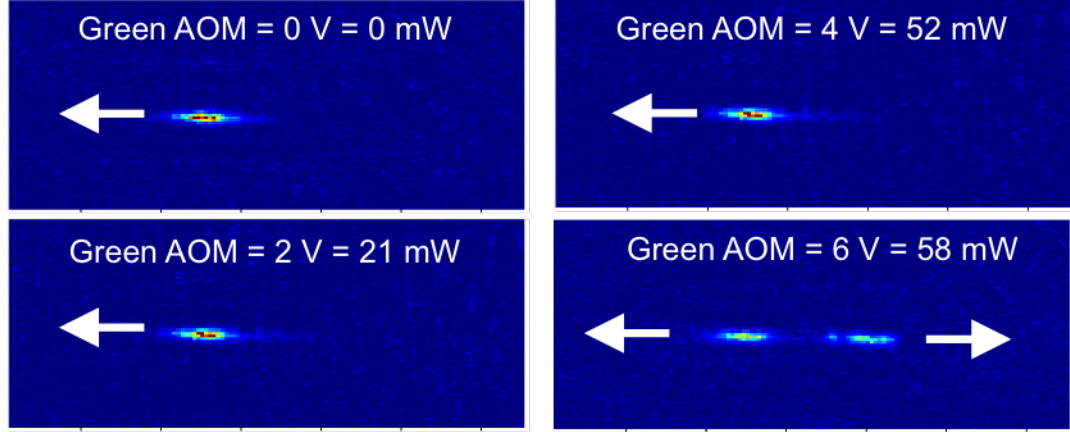
FIG. 7.7: Characterizing the height of the potential barrier using the energy of the atoms. A cloud of atoms with initial velocity 8.6 mm/s (388 nK) is launched right-to-left at a barrier with increasing height. At 58 mW of power, half of the cloud is reflected and half is transmitted, indicating a barrier height of approximately 388 nK.

7.4 Initial momentum

The initial momentum is imparted on the atoms by pushing the atoms up the wall of the magnetic chip trap and then releasing them. This push is provided by an external z-axis push coil, which produces a magnetic gradient along the z-axis. When current passes through the coil, the potential minimum of the chip trap is shifted axially. When quickly powered off, atoms find themselves on the side of the chip trap with some potential energy which quickly turns to kinetic energy as they slide down the trap wall. If we turn off the trap potential when the atoms reach the bottom of the trap, they will continue to translate at constant velocity, allowing us to measure that velocity with a series of time-of-flight images.

The coil for imparting the initial momentum is placed adjacent to the cell such that the strong axis of the coil is aligned to the z-axis (axial direction) of the trap. It is positioned around the radial imaging line-of-site, approximately 5 cm from the center of the trap. Most of the transmission scattering cases that we are interested in demonstrating

150

require an initial velocity $v_0 \geq 15$ mm/s, recalling that $p_0 = mv$. For ^{87}Rb, this velocity corresponds to an energy of 1.63×10^{-29} J or 1.18 μK (note: this is NOT the temperature of the atoms, but rather the temperature corresponding to this initial velocity given by $T = \frac{U}{k} = \frac{mv_0^2}{2k}$). This energy corresponds to a field of 0.0175 G. Given the axial trap frequency of $2\pi \times 13.9$ Hz, the coil will need to push the atoms 172 μm along the z-axis.

A round coil was designed to achieve these goals with an inner radius of 4.8 cm and 14 turns. We power the coil with one of the transport power supplies using a spare channel on the magnetic transport multiplexer. We calibrate the initial velocity produced by the coil in the following manner: i) We adiabatically ramp up the coil current to the desired current. ii) We quickly turn off the current and wait until the atoms reach the center of the trap. (We do this via trial and error. We know where the unperturbed center of the trap is. Therefore, we increase the time the atoms are held in the trap until an image with extremely short time-of-flight places them at the center.) iii) When the atoms reach the center of the trap, we quickly turn off all fields and measure the velocity by tracking the free-fall position of the clouds via time-of-flight. The results of this calibration are shown in Figures 7.8 and 7.9.

The points in Figure 7.9 are less linear than one would hope for producing easily calculable initial momenta based on current alone. This could be due to a number of reasons. For example, we have seen non-uniformity in our trapping potential before, and the structure in this data could signify structure in the harmonic trap. It could also be trace amounts of sloshing, though care was taken to turn the coil on sufficiently slow to minimize sloshing. The bumpiness of this plot should be noted as something that should be improved upon in future experiments. For this reason, rather than using the linear fit to determine initial momentum for a given coil current, we choose a coil current with a measured initial momentum and use the data point itself in the experiments detailed in the remainder of this dissertation.
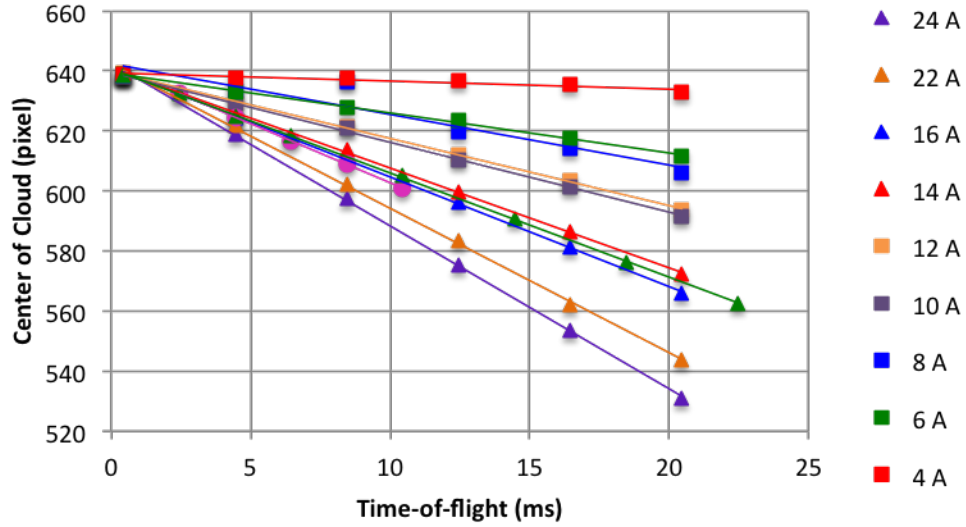
FIG. 7.8: Initial velocity from push coil. A coil with varying amounts of current provides a push along the z-axis to give the atoms initial momentum. The coil is slowly ramped on, then quickly turned off. Atoms will slide down the trap wall. At the bottom of the trap, all the potential energy is converted to kinetic energy and we turn the trap off and watch the atoms travel ballistically for a variable time-of-flight.

7.5 Classical experimental characterization of "The Discriminator"

A valuable lesson learned early on in attempts to demonstrate the classical momentum spread from 'The Discriminator' was the importance of the trap potential in the classical simulations that we attempt to produce. The simulations in Chapter 6 assume a flat potential except for the actual barriers. This is not the case in the experimental system. It is obvious from the images in Figure 7.6b that our potential is not flat. We must take into consideration the harmonic trap potential if we are to produce accurate simulations.

Adding the harmonic trap potential changes the shape of our final momentum distribution significantly. Figure 7.11 shows the original final momentum distribution without the harmonic trap potential in black and the new momentum distribution with the har-

152
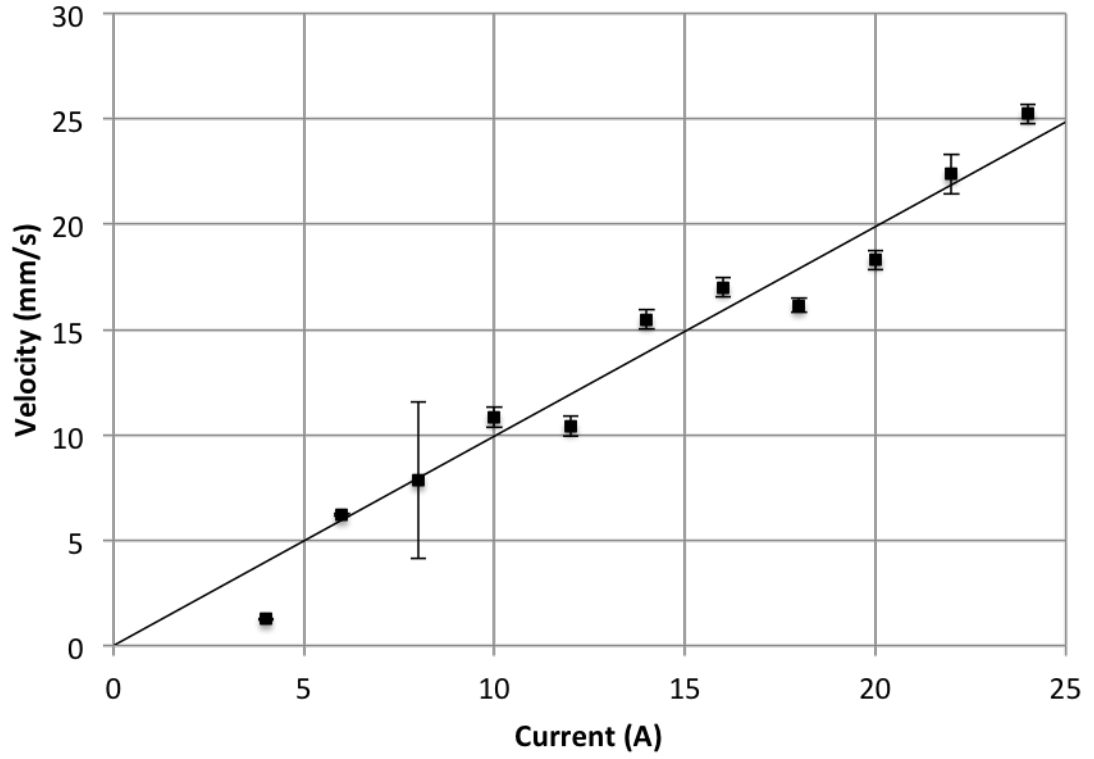
FIG. 7.9: Initial momentum characterization. The slopes of the fitted lines from Figure 7.8 give the velocity of the clouds for a given coil current. Here I plot the velocity dependence on the current. The atoms will travel at a velocity of 1.1(2) mm/s per Ampere of current. The error bars represent the 95% confidence bounds of the linear fits in Figure 7.8.

monic trap potential in red. The reason for this change in shape is that we cannot create an initial momentum exactly at a single value. There will be some spread. Due to the position size of the cloud (on the order of the barrier width), there will be a corresponding spread in momentum as we pull it up the side of the harmonic trap for the initial momentum. This issue is depicted in Figure 7.10 which shows the harmonic potential and the corresponding phase space diagram. The atoms that have been given an initial momentum by being released from the side of the harmonic trap have a significantly larger momentum spread than a typical cloud initiated at the bottom of a trap. In the experimental trap, the FWHM of our cold atom cloud is $\approx 44\mu$m. Pushing our cloud 264 μm up the axial wall gives an initial velocity of 22.4 mm/s. We were expecting the momentum spread to correspond only to atom temperature (a few mm/s spread). However, the wall of our trap is quite steep at that position, with a slope of about 1.9 mm/s per μm. This corresponds to a spread of several tens of mm/s, much larger than originally anticipated.

We discovered this problem during preliminary characterization of the static barrier in "The Discriminator" scheme. We attempted to measure the initial momentum spread of our cloud of atoms by repeatedly launching it at the static barrier as we increase the barrier height, producing a curve akin to the ones in Figure 7.11. The resulting distribution was expected to be narrow, since the final momentum distribution would match the initial momentum distribution in this case. However, we instead measured a large initial distribution, due to the reasons outlined above. This problem calls for a major change in course for future quantum pumping experiments. However, in this thesis, I will concentrate on characterizing "The Discriminator" method and the classical dynamics of the experimental system. I use these curves to further characterize the initial momentum and temperature of our atoms.

In "The Discriminator" measurement method, we measure the transmission of particles (having already passed through the oscillating barrier) over a static barrier of varying
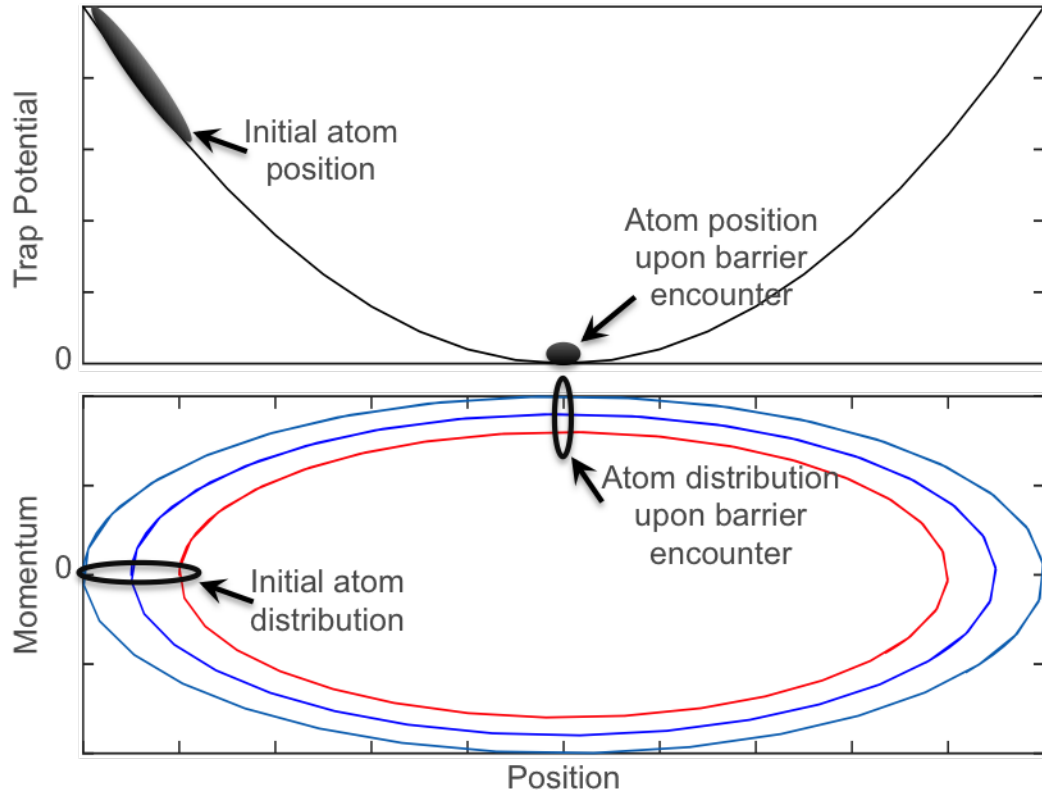
FIG. 7.10: Effect of harmonic trap on initial energy spread of the atoms. (top) Our initial momentum scheme of pushing the atoms up the side of the harmonic trap in order to ensure an initial momentum at the bottom of the trap is shown. (bottom) The phase space diagram of a harmonic potential illustrates the expected momentum spread at the bottom of the trap for particles released from the side of the trap. This method results in a larger than anticipated spread in momentum when the atoms encounter the barrier.
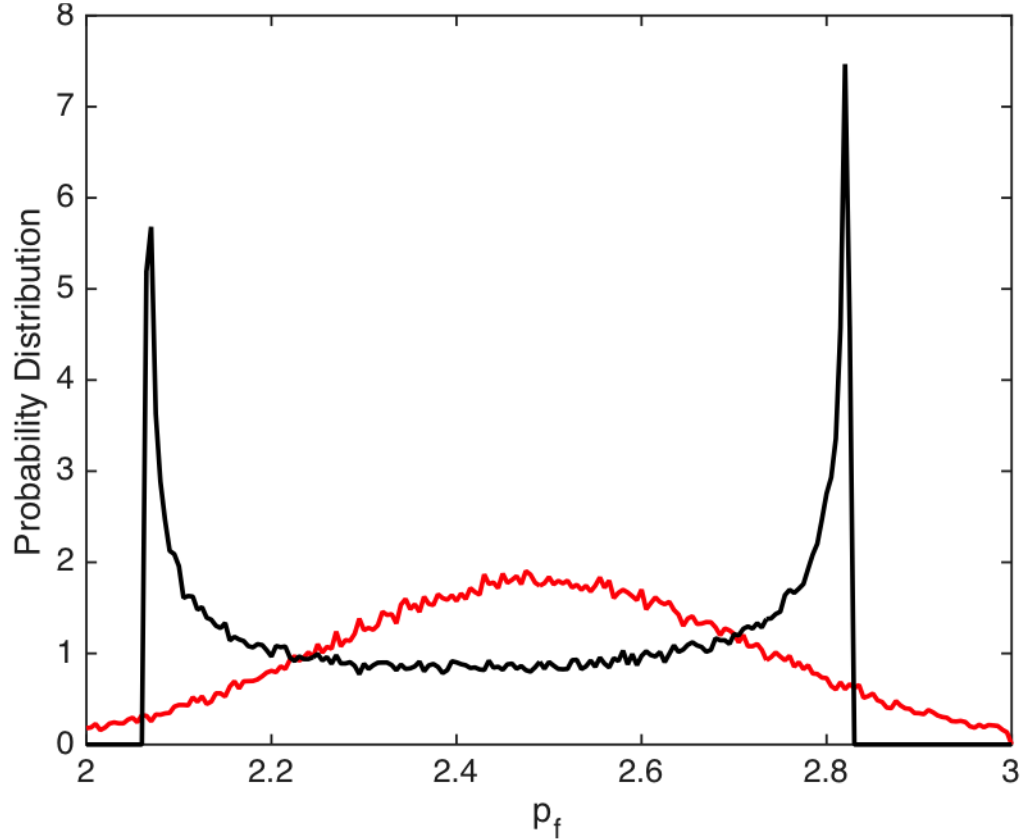
FIG. 7.11: Effects of harmonic trap potential on the final theoretical momentum distribution. The original probability distribution vs final momentum plot from Figure 6.15 (black) and the resultant probability distribution with the added harmonic trap potential (red). In the theory units from Chapter 6, the parameters are $p_0 = 2.5$, FWHM = 2, $\omega = 1$, $U_0 = 1$, and $x_{0left} = 0$. To convert to experimental units, first determine the ratio of the real barrier width to the theoretical barrier width l_u. Then $\omega' = \frac{\hbar}{ml_u^2}\omega$, $U_0' = \hbar\omega'U_0$, and $p_0' = \sqrt{\hbar m\omega'}p_0$ where the primed units represent the experimental parameters.

heights. For a low enough static barrier height, we expect that all the atoms will transmit over the barrier, while for a high enough static barrier, none of the atoms will transmit. The calculated equivalent of this transmission curve, based on the momentum distribution in Figure 7.11, is plotted in Figure 7.12. In this figure, the transmission curves for the both cases (with and without harmonic trapping potential) are plotted (in red and black, respectively). The red curve is the type of curve we reproduce in our experiment. The equivalent plot for the quantum picture would create a smoothed step function due to the Floquet peaks (recall Figure 7.3).
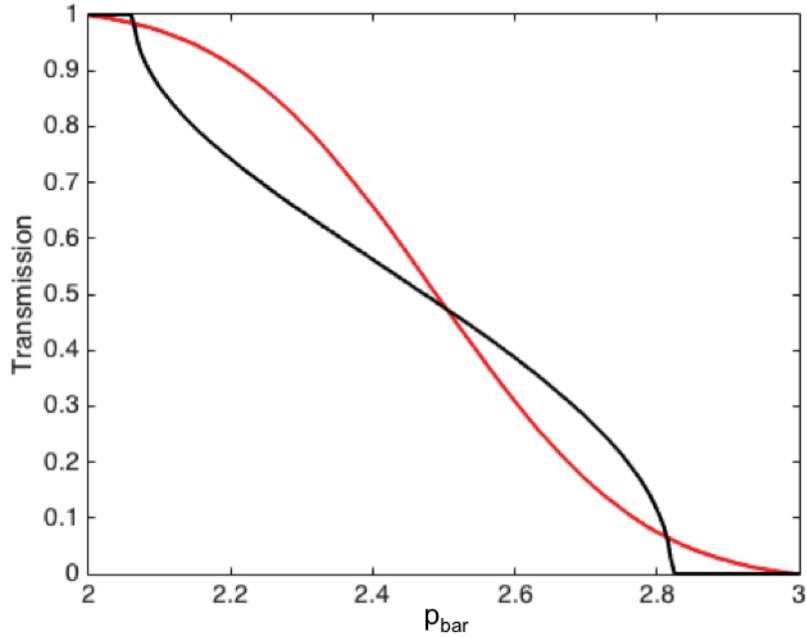
FIG. 7.12: Calculated transmission over "The Discriminator" as a function of barrier height with and without the harmonic trap potential. The classical transmission of atoms over a barrier of varying height corresponding to $p_{bar} = \sqrt{2U_0}$ with no trap potential from Figure 7.3 (black) compared to the classical transmission curve with a harmonic trap potential (red). The presence of the harmonic trap potential distorts the expected outcome. In the theory units from Chapter 6, the parameters are $p_0 = 2.5$, FWHM $= 2$, $\omega = 1, U_0 = 1$, and $x_{0left} = 0$. To convert to experimental units, first determine the ratio of the real barrier width to the theoretical barrier width l_u. Then $\omega' = \frac{\hbar}{ml_u^2}\omega$, $U_0' = \hbar\omega'U_0$, and $p_0' = \sqrt{\hbar m\omega'}p_0$ where the primed units represent the experimental parameters.

157

We conduct two main studies to characterize the classical dynamics of "The Discriminator" system. First, we study the transmission of the particles over the barrier as a function of barrier height as we vary the particle initial momentum. In this study, we expect the curve to shift to larger barrier heights as we increase the initial momentum. Next, we study the transmission of the particles over the barrier as a function of barrier height as we vary the particle temperature from thermal to BEC. Here, we expect the transmission curves to cut off more sharply as we decrease the temperature.

We first experimentally reconstruct the transmission curve as we vary the initial momentum of the particles. The results of this study are shown in Figure 7.13. This figure shows the transmission of atoms over a static barrier as the barrier height is increased. The height of the barrier is measured using the voltage signal on the photodiode in Figure 7.4. Each of these curves shows that atoms will fully transmit for low enough barriers, and fully reflect for high enough barriers. As the initial momentum of the atoms is increased, the barrier must be higher to fully reflect the atoms, as expected. The data points are averages of 2-5 experimental runs, with the standard deviation drawn as the error bars.

Here, the photodiode voltage plotted on the x-axis can be converted to energy or temperature using $1 \text{ mV} = 4.5(2) \times 10^{-31}$ J. This number is found by recording the photodiode voltage $V_{50/50}$ at which the experimental cloud is transmitting 50% and reflecting 50% for each velocity v. We average the conversion for each curve found by $\frac{mv^2}{2V_{50/50}}$.

The theoretical curves in Figure 7.13 are drawn as fits to the experimental data, with initial momentum values from the fits listed in the legend. Table 7.1 lists the theoretical parameters that we use to produce the theory curves to match the experimental data. In these theory calculations, we give the atoms zero initial momentum and use the initial position on the side of the harmonic potential to impart the potential energy which is entirely converted to kinetic energy by the time the atoms reach the barrier. Therefore, the sharpness of the cutoff from full transmission to full reflection in Figure 7.13 is due
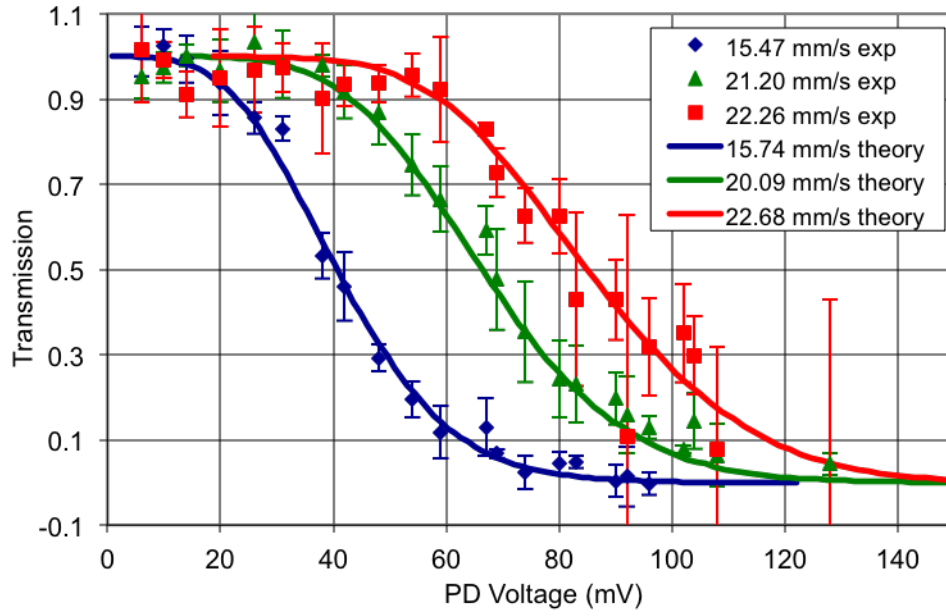
FIG. 7.13: Transmission vs initial momentum. Transmission of a cloud of atoms over a static barrier with height measured in PD voltage. As the initial momentum of the atoms is increased, the transmission curve shifts to higher PD voltage values. The atoms used here have a temperature of 17 nK. Each data point is the average of 2-5 data runs. The error bars represent the standard deviation of those data runs. The conversion between PD voltage to energy is 1 mV $= 4.5 \times 10^{-31}$ J.

to the initial size of the cloud along the axial direction of the trap. This initial size is dependent upon the temperature of the cloud. For the atoms in Figure 7.13, the variance of the Gaussian fit to the initially cooled atom cloud is 7.3 pixels or 33.9 μm.

TABLE 7.1: Parameters for producing theory curves in Figure 7.13.

Coil current	Initial position	Initial energy	Initial velocity
14.85 A	180 μm	1.80×10^{-29} J	15.74 mm/s
18.95 A	230 μm	2.93×10^{-29} J	20.09 mm/s
21.42 A	260 μm	3.74×10^{-29} J	22.68 mm/s

Next, as we anticipate future quantum pumping experiments that will explore both classical and quantum regimes by varying the temperature of the atom cloud, we study the transmission of atoms as a function of barrier height as we vary the temperature of the atoms. We adjust the temperature of the atoms simply by sweeping the RF knife higher or lower during the final evaporation stage. The results are shown in Figure 7.14 for atom temperatures of 64 nK, 36 nK, 17 nK, and BEC. The initial cloud size at these temperatures is given in Table 7.2. The data points are averages of 2-5 experimental runs, with the standard deviation drawn as the error bars. As one would expect, the transmission curve is much broader for higher temperatures, indicating a larger initial momentum spread.

TABLE 7.2: Initial cloud size as a function of temperature for producing theory curves in Figure 7.14.

Temperature	Initial size
BEC	5 pixels = 23 μm
17 nK	7 pixels = 34 μm
36 nK	11 pixels = 51 μm
64 nK	16 pixels = 73 μm

In Figure 7.14, the theory curves are not fits but actual theoretical calculations for a cloud with the same temperature and experimental parameters. To produce these theory curves, we must convert our calculated transmission curves, which are typically a function
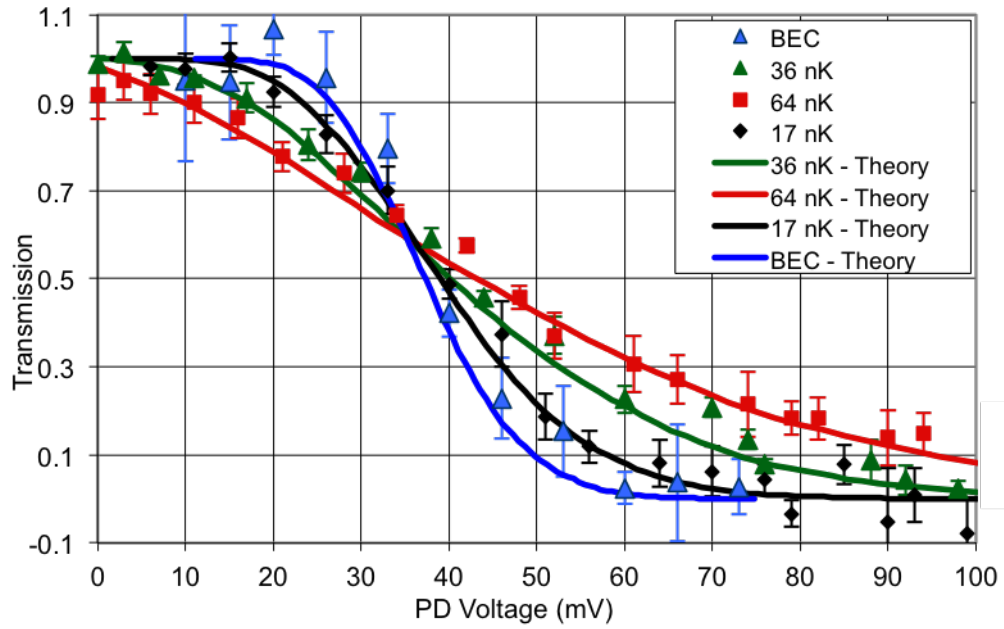
FIG. 7.14: Transmission vs temperature. Transmission of a cloud of atoms over a static barrier with height measured in PD voltage. As the temperature of the atoms is decreased to BEC, the transmission curve becomes sharper, indicating a smaller spread in initial momentum. The atoms used here have an initial velocity of 15.47 mm/s. Each data point is the average of 2-5 data runs. The error bars represent the standard deviation of those data runs. The intersection of the fits at 60% transmission (not 50% as one would expect) is likely due to long term experimental drift in the alignment of the barrier beam.

of momentum (recall Figure 7.12), to functions of photodiode voltage. To do so, we use the same method as above to match the voltage at which the cloud is transmitting 50% and reflecting 50% with the kinetic energy of the cloud. Table 7.3 shows the conversion factor for each cloud in the plot above. Though we use the same initial velocity for the clouds in this case and only vary temperature, it is clear that there is some drift in $V_{50/50}$ indicating that there are fluctuations in the experiment that we are not controlling.

TABLE 7.3: Conversion factors for producing theory curves in Figure 7.14.

Cloud Temperature	$V_{50/50}$	Conversion
64 nK	45 mV	4.6×10^{-31} J/mV
36 nK	42 mV	5.0×10^{-31} J/mV
17 nK	40 mV	5.2×10^{-31} J/mV
BEC	38 mV	5.5×10^{-31} J/mV

7.6   Conclusion

We understand the classical behavior of the experimental system quite well. We observe good agreement between the theory developed in Chapter 6 and the experiment described in this chapter. Armed with these tools, we have a much clearer picture of the characterization of each of the required tools in 'The Discriminator' scheme. There are also several improvements that can be made to truly probe the classical and quantum features of quantum pumping or even scattering from a single oscillating barrier. The realization that our initial momentum spread cannot be made as narrow as we require for these future experiments has given us the foresight to consider a different scheme for imparting initial momentum on the atoms. For that reason, a shift in experimental design began that was anticipated to take significant time, and I passed the experimental quantum pumping torch to AJ Pyle. In the remaining chapter, I detail some of the unanswered questions and potential experimental schemes to improve the setup towards future quantum pumping

experiments.

CHAPTER 8

Conclusion and Outlook

I assisted in the design, construction, testing, characterization, and optimization of a dual-species dual-chamber atom-chip apparatus for producing ultracold quantum gases from the ground up. The apparatus is capable of producing ^{87}Rb BECs of $\approx 10^4$ atoms in a magnetic chip trap. In anticipation of quantum pumping experiments with ultracold neutral atoms, I have laid the groundwork for such experiments with the following steps beyond demonstration of a BEC:

- Characterization of a quasi-1D channel which mimics the nanowire in mesoscopic quantum pumping schemes.

- Implementation of a Gaussian potential barrier which can be static or amplitude modulated, and characterization the width and height of that barrier.

- Development of a method of imparting an initial momentum to the atoms using a magnetic field gradient, and characterization of the initial momentum imparted to the atoms via this method.

- Establishment of a breadth of theory for modeling the classical dynamics of such a system and for comparing it to quantum effects in collaboration with John Delos, Kunal Das, Kevin Mitchell, Tommy Byrd, and AJ Pyle.

- Verification of the classical modeling by producing experimental transmission curves while varying the initial momentum of the atoms.

- Verification of the classical modeling and the tunability of the experimental system from classical thermal gases to quantum gases by producing experimental transmission curves while varying the temperature of the atoms.

In doing so, we have demonstrated excellent agreement between the predicted models from Chapter 6 and the experimental results in Chapter 7.

In addition, we have become intimately familiar with the capabilities of the experimental system which we have built and described in Chapters 4 and 5 while gaining insight into potential improvements and next steps. Perhaps the largest challenge which we have encountered as far as the quantum pumping experiments entail is the shortcoming of our initial momentum method to produce clouds with a sufficiently small spread of initial momentum. This is in fact so problematic that we have shifted experimental gears entirely for the next implementation. This next experiment will impart initial momentum to the atoms not by pushing them up the harmonic wall but instead by dropping them and allowing them to accelerate due to gravity. A significant difference between this next method and the one presented in Chapter 7 is the lack of a trapping potential while the atoms are accelerated. I recommend that care should be taken during these preliminary stages to ensure that this does not detrimentally impact the experiments proposed.

Other more complicated methods exist for producing narrower spreads in atom clouds. For example, one could push the atoms up the side of the harmonic chip trap with a magnetic gradient and then intentionally implement a hybrid magnetic trap + 1D optical

lattice trap as shown in Figure 8.1a. The 1D optical lattice would confine the atoms to discrete lattice sites with lattice spacing ≈ 532 nm. A single-site (or several-site) lattice addressing scheme could then be implemented to keep only the atoms in a narrow band of lattice sites. Figure 8.1b shows a field in blue that would preferentially eject atoms from all lattice sites but the center one. In this manner, the spatial and momentum spread of the cloud is reduced to 532 nm (see Figure 8.1c). Such a scheme is challenging to implement and could alone suffice as a dissertation topic. However, schemes such as this have been implemented to address atoms held in single lattice sites for applications such as qubit registries [90]. In the Aubin Lab, one could potentially use the Zeeman splitting already induced by the chip magnetic gradient and microwave potentials

There also exist additional improvements to the more general apparatus (not only impacting the quantum pumping experiments) which will enhance the performance of all experiments. These improvements primarily involve the stability and reproducibility of the system. We were eager to demonstrate an operational BEC-producing apparatus during my tenure at William and Mary, and we did so successfully while still developing an extremely versatile system with a variety of potential experimental endeavors. This eagerness has also left room for tweaking and optimizing in the future. Since my departure, the group has already improved the TA coupling and output, leading to larger atom numbers in the MOT as well as the BEC. I have no doubt that similar incremental improvements will be made throughout the years.

One of the main feats of the apparatus we have developed is the versatility it offers to the experimentalist. The apparatus is not only capable of producing magnetic chip trap BECs, but it is also capable of dipole trapping with long lifetimes in both the MOT and science chamber. This enables all-optical or hybrid magneto-optical BEC production in the MOT chamber [55], and possibly more continuous loading schemes for the science chamber. The apparatus is also capable of cooling and trapping several isotopes of rubidium and
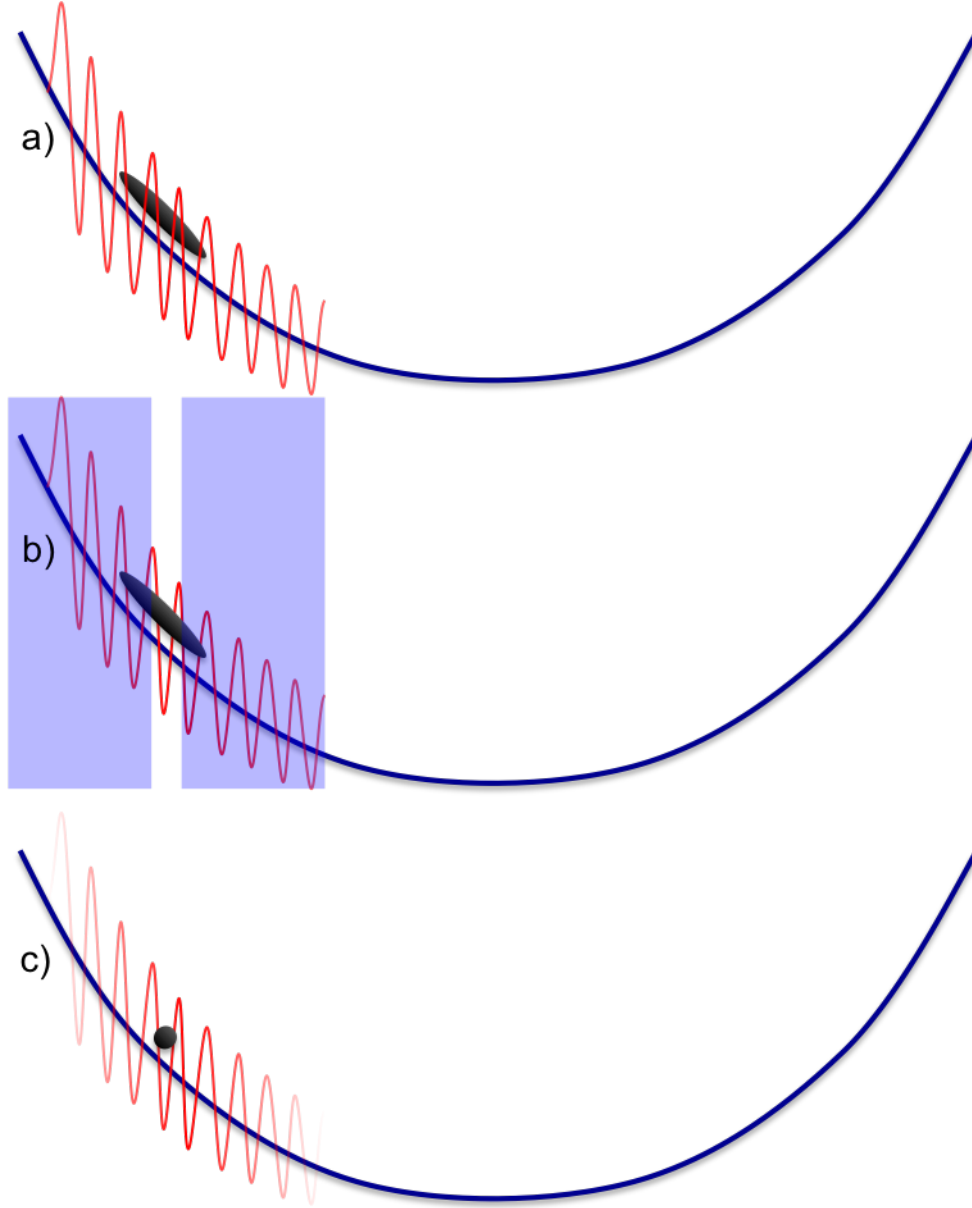
FIG. 8.1: Single-site addressing in an optical lattice for narrower momentum packets. a) We push the atoms up the side of the magnetic chip trap. b) We overlap the magnetic chip trap with an optical lattice thereby producing a hybrid magnetic trap + 1D optical lattice trap. Then we preferentially eject atoms from all but a single lattice site. c) This leaves a cloud of atoms with significantly smaller spatial and momentum spread. Single site addressing could be done with a scheme similar to one found in [90].

potassium, and I also initiated preliminary demonstrations of molecular photo-association have been performed. With the successful demonstration of BEC in this versatile apparatus, the Aubin Lab is well-positioned for pursuing not only quantum pumping experiments, but a number of experiments in fundamental physics and application development.

APPENDIX A

Dynamical monodromy

Dynamical monodromy is a term used to describe a system that, upon evolving around a closed path, does not return to its original state. In a collaboration with Professor John Delos and his student Chen Chen, I was asked to develop portions of two experimental schemes for observing dynamical monodromy. The first scheme is a purely classical realization of the theory using a magnetic puck on an air table. The second scheme uses a gas of ultracold atoms in a laser field. This latter scheme offers advantages such as the possibility of exploring the role of atom-atom interactions and quantum mechanical effects. My primary role in the publication attached below was the laser scheme design and early calculations of initial conditions in the second scheme, as well as carrying out the experiments on the air table (detailed in the Appendix of the attached paper).

Dynamical monodromy

C. Chen, M. Ivory, S. Aubin, and J. B. Delos[*]

Department of Physics, College of William and Mary, Williamsburg, Virginia 23187, USA

(Received 5 July 2013; published 28 January 2014)

Integrable Hamiltonian systems are said to display nontrivial monodromy if fundamental action-angle loops defined on phase-space tori change their topological structure when the system is carried around a circuit. In an earlier paper it was shown that this topological change can occur as a result of time evolution under certain rather abstract flows in phase space. In the present paper, we show that the same topological change can occur as a result of application of ordinary forces. We also show how this dynamical phenomenon could be observed experimentally in classical or in quantum systems.

PACS number(s): 05.45.−a, 37.10.Vz, 45.20.Jj

I. INTRODUCTION

The general goal of this type of research is to understand and control quantum systems by understanding and controlling the corresponding classical systems. In recent years there have been major advances in classical mechanics: nonlinear dynamics, chaos theory, the "butterfly effect," new understanding of periodic orbits and their bifurcations and proliferation and their organization into families, chaotic transport and fractals, and some recently uncovered phenomena called "Hamiltonian monodromy." In each case, new understanding of classical systems has led to new understanding of their quantum counterparts.

This paper deals with the last-mentioned topic. We display new aspects of Hamiltonian monodromy in classical systems, and we show how these phenomena might be observed in a macroscopic system and in a system of ultracold atoms.

The proper name of our topic is "dynamical manifestations of nontrivial monodromy of action and angle variables in Hamiltonian systems." Let us just call it "dynamical monodromy." Monodromy means "once around a closed path"; a system exhibits "nontrivial monodromy" if when we go around a closed path in some space, the system does not come back to its original state. The simplest example of functions that have nontrivial monodromy are $f(z) = z^{1/2}$ or $g(z) = \log(z)$ for complex z: On one circuit around the branch point, $z = 0$, these functions change their values. A function of two real variables (l,h) with the same property is $\alpha(l,h) = l \tan^{-1}(h/l)$. If l represents angular momentum and h represents energy, and we multiply by constants to get the units consistent, then this function gives an approximate formula for an action variable of the system we will study: It is a multivalued function of (l,h), and on one circuit around the origin of (l,h) space, it changes its value.

A Hamiltonian system is said to exhibit nontrivial monodromy if the system is integrable and action and angle variables can be constructed, but they are found to be multivalued. Angle variables are defined in such a way that they trace out fundamental loops on tori. For the systems we are considering, the angle variables change smoothly as (l,h) change, but when (l,h) undergo a circuit around the origin, the loops change their topological structure. Specifically, a

[*]Corresponding author.

loop that begins entirely on one side of a classically forbidden region ends by encircling that forbidden region. This is called a "static" manifestation of monodromy because it involves smooth connections among coordinates defined on "static" tori.

In Refs. [1,2] it was pointed out that this static manifestation of monodromy must have dynamical consequences: If a collection of particles is given initial conditions corresponding to an initial angle loop on a torus, and those particles are driven continuously around a monodromy circuit, then the loop of particles must undergo the same topological change that is seen in the angle loop.

The purpose of this paper is to answer two questions. (1) Can this phenomenon be seen using ordinary particles that obey Newton's laws of motion? (2) Can it be seen under less-than-ideal conditions, with particles having a distribution of energies and angular momenta? We show in this paper by computation that the answer to both of these questions is "Yes." We also present a design for an experimental measurement that would answer another question. (3) What happens in a quantum system? To what extent will these phenomena show up in an ultracold gas or a Bose-Einstein condensate?

In the next section we give a general introduction to Hamiltonian monodromy, so that we can pose questions (1) and (2) with more mathematical precision. Then in Sec. III we establish by computation affirmative answers to questions (1) and (2). Finally in Sec. IV and Appendix C we present designs for two experimental implementations of the theory. One is purely classical, involving pucks on a tilting air table, while the other, an ultracold gas or a BEC, brings forth quantum-mechanical issues that are not addressed by the computations presented in this paper.

II. STATIC AND DYNAMICAL MANIFESTATIONS OF MONODROMY

A. Tori and torus quantization

Let us begin with the primary theorem on bound integrable systems [3]. Given a phase space of dimension $2N$ with coordinates $\mathbf{z} = (z_1, \ldots, z_{2N}) = (q_1, \ldots, q_N, p_1, \ldots, p_N) = (\mathbf{q}, \mathbf{p})$, suppose there are N independent functions $\{F_\alpha(\mathbf{q},\mathbf{p})|\alpha = 1, 2, \ldots, N\}$ "in involution" with each other, i.e., their mutual

Poisson brackets all vanish,

$$[F_\alpha(\mathbf{z}), F_\beta(\mathbf{z})] = \sum_i (\partial F_\alpha/\partial q_i)(\partial F_\beta/\partial p_i)$$
$$- (\partial F_\alpha/\partial p_i)(\partial F_\beta/\partial q_i) = 0. \quad (1)$$

We use lowercase letters f_α to represent the values of these functions, and we call the space of values $\{f_\alpha | \alpha = 1, \ldots, N\}$ of these functions "spectrum space."

We examine the level sets Λ_f of these functions—the set of phase-space points $\mathbf{z}$ such that all $F_\alpha(\mathbf{z})$ are constants, f_α:

$$\Lambda_f = \{\mathbf{z} | F_\alpha(\mathbf{z}) = f_\alpha, \alpha = 1, \ldots, N\}. \quad (2)$$

The "Liouville-Arnold" theorem asserts that any such level set that is compact and connected is topologically equivalent to a torus [3]. Furthermore there exists a set of action and angle variables which make good coordinates for the tori. Each angle variable $\phi_i(\mathbf{z})$ varies from 0 to 2π when the phase-space point $\mathbf{z}$ goes around one of the fundamental loops of a torus, while the action variables $I_i(\mathbf{z})$ are constant on each torus because they depend on $\mathbf{z}$ only through their dependence on the set of functions $\mathbf{F}(\mathbf{z})$: $I_k(\mathbf{z}) = \mathscr{I}_k(F_1(\mathbf{z}), \ldots, F_N(\mathbf{z}))$. It is presumed that the Hamiltonian function for the physical system depends only on the functions $F_\alpha(\mathbf{z})$; there is presumed to be an invertible relationship between values $\mathbf{f}$ of these conserved quantities and values $\mathbf{i}$ of the action functions, so the Hamiltonian can also be expressed as a function of the action variables, $H(\mathbf{z}) = \mathscr{H}[I(\mathbf{z})]$. It follows that the motion of any phase-space function $g(\mathbf{z})$ is quasiperiodic (i.e., a Fourier transform of $g[\mathbf{z}(t)]$ shows N fundamental frequencies and all harmonics and combinations), and the fundamental frequencies ω_i are simply obtained from the Hamiltonian by differentiation, $\omega_j = \partial \mathscr{H}(I)/\partial I_j$. Also, good approximations to quantum eigenvalues and eigenfunctions are obtained by examining a discrete set of tori having appropriately quantized values of action variables.

These concepts, first formulated by Liouville, carried into the old quantum theory by Einstein in 1918, and revived starting in the 1970s by Percival [4–6], Marcus and Noid [7–16], and Berry [17], are a standard part of the repertoire of semiclassical physics and chemistry [18]. They have been used to study an immense variety of systems, such as simple nonlinear oscillators (e.g., the Henon-Heiles system) [19–22], molecular vibrations and rotations [23], excited states of hydrogen in electric and magnetic fields [24,25], doubly excited states of helium [26–28], spin-orbit coupling [29], and excited states of nuclei [30]. (Googling the phrase "torus quantization" gives over 3000 hits.) Torus quantization also arises in problems far afield from atomic, molecular, and optical (AMO) physics: In a study of a Buffon probability problem (when a needle is dropped in random positions on a tiled floor, what is the probability that the needle intersects n of the lines between the tiles?), it was found that torus quantization gives a step on the path to the solution [31]. Analysis and quantization of tori have been widely studied for so many years that it might come as a surprise that reexamination of the theory would lead to new and interesting phenomena.

B. Singular points and monodromy

In this beautiful and well-known theory, it is easy to fail to notice the little assumption that the functions $F_\alpha(\mathbf{z})$ must be independent, i.e., their phase-space gradient vectors $\nabla_z F_\alpha(\mathbf{z})$ must be linearly independent. However, in many systems there are points $\mathbf{z}_s$ at which the functions fail to be independent (among other things, one or more of the gradients might vanish). Phase-space points $\mathbf{z}_s$ at which the rank of the $N \times 2N$ matrix $DF = \partial F_i/\partial z_j$ is less than N are called singular points, and the corresponding values of the conserved quantities $\mathbf{F}(\mathbf{z}_s) = \mathbf{f}_s$ are called singular values. A value $\mathbf{f} = \mathbf{F}(\mathbf{z})$ is "regular" only if no phase-space point $\mathbf{z}$ in its preimage under $\mathbf{F}$ is singular, otherwise it is a singular value. A region of spectrum space is called "regular" if and only if all values of $\mathbf{f}$ in that domain are regular.

The importance of singular values is that *near such singular values, the structure of the embedding of tori in phase space might change*. A trivial example is a one-dimensional pendulum, in which $H = p^2/2 - \cos q$. Phase-space points $\mathbf{z}_- = (\mathbf{q} = 0, \mathbf{p} = 0)$ and $\mathbf{z}_+ = (\mathbf{q} = \pi, \mathbf{p} = 0)$ are singular (the gradient of H vanishes there), and the singular values are $E_- = H(\mathbf{z}_-) = -1$, $E_+ = H(\mathbf{z}_+) = 1$. For $E < -1$ there are no tori, while for each energy in the interval $-1 < E < 1$, a single torus corresponding to librational motion exists. For $E > 1$, we find at each value of E two tori, corresponding to rotation in a clockwise or counterclockwise sense. Thus at each of the singular points $E = \pm 1$, there is a structural change.

More substantial examples are given in the book by Cushman and Bates [32]. This book examines simple mechanical systems that appear in undergraduate textbooks (two-dimensional harmonic oscillators, tops, spherical pendula, etc.) and uses modern mathematical artillery to study them—Poisson algebras, Lie theory, Ehresmann connections, Morse theory, bifurcation theory, and especially global analysis. Global analysis focuses on how tori foliate phase space smoothly, or how the embedding of tori in phase space can change abruptly near a singular value.

Duistermaat [33] (apparently following a suggestion of Cushman) was the first to publish a paper discussing nontrivial consequences of singular values. Consider a system with two degrees of freedom having a Hamiltonian of the familiar kinetic plus potential energy form, in which the potential energy is cylindrically symmetric:

$$H(\boldsymbol{p}, \boldsymbol{q}) = \frac{\boldsymbol{p}^2}{2} + V(\rho) = h, \quad (3)$$

$$\rho = \sqrt{x^2 + y^2}, \quad (4)$$

$$V(\rho) = -a\rho^2 + b\rho^4 \quad (a, b > 0). \quad (5)$$

The potential-energy function has a well to confine particles within a certain region and a central potential-energy barrier. Conserved quantities are the angular momentum $L = xp_y - yp_x$, with numerical value $L(\boldsymbol{p}, \boldsymbol{q}) = l$ and the Hamiltonian $H(\boldsymbol{p}, \boldsymbol{q}) = h$. The derivatives of both $H(\boldsymbol{p}, \boldsymbol{q})$ and $L(\boldsymbol{p}, \boldsymbol{q})$ vanish at the origin in phase space $(x, y, p_x, p_y) = \mathbf{0}$, and therefore it is a singular point, and the corresponding origin in

spectrum space $(l,h) = \mathbf{0}$ is a singular value, or monodromy point.

A closed directed path $[l(s),h(s)]$ in spectrum space surrounding this singular value is called a monodromy circuit (s is a continuous timelike variable representing points along the path). If the canonical action functions $\mathscr{I}_k(l,h)$ are defined so that they vary smoothly as the system is carried around this circuit, then, when the system returns to the original (l,h), one of the action functions is changed. One of the two action functions is always

$$\mathscr{I}_1(l,h) = \frac{1}{2\pi}\oint L(\mathbf{z})d\phi = l,$$

$$I_1(\mathbf{z}) = L(\mathbf{z}) = xp_y - yp_x, \tag{6}$$

so it does not change when we carry the system around the monodromy circuit,

$$\mathscr{I}_1^f(l,h) = \mathscr{I}_1^i(l,h) = l^i = l^f \tag{7}$$

(superscripts i and f mean initial and final). The other action variable can initially be taken to be an integral around a "ρ loop":

$$\mathscr{I}_2^i(l^i,h^i) = \frac{1}{2\pi}\oint p_\rho(\rho;l,h)d\rho. \tag{8}$$

However, at the end of the monodromy circuit, this action function has changed to [33–35]

$$\mathscr{I}_2^f(l^f,h^f) = \mathscr{I}_2^i(l^i,h^i) - \mathscr{I}_1(l^f). \tag{9}$$

$\mathscr{I}_2$ is therefore a multivalued function of (l,h). The conjugate angle variables must also change on a passage around the monodromy circuit:

$$\phi_1^f = \phi_1^i + \phi_2, \tag{10}$$

$$\phi_2^f = \phi_2^i = \phi_2. \tag{11}$$

It is easy to verify that the transformation from $(\phi_1^i,\phi_2^i,I_1^i,I_2^i)$ to $(\phi_1^f,\phi_2^f,I_1^f,I_2^f)$ is canonical.

In Fig. 1, we show this static manifestation of monodromy. The figure in the center is a monodromy circuit in (l,h) space; in this case, any counterclockwise circuit surrounding the origin gives the same result. The outer figures show seven tori corresponding to seven different points in the (l,h) spectrum space. The tori are represented in (x,y,p_ρ) space [it is convenient to regard (x,y,p_ρ) as orthogonal axes]. When the system is carried around such a circuit surrounding the origin in (l,h) space and it returns to the original torus, the coordinate system defined by canonical angle variables on the tori changes smoothly into a different one. (The method used to calculate angle loops is given in Appendix A.)

On each torus two families of fundamental loops $[\gamma_1]$ (green curves online) and $[\gamma_2]$ (blue curves online) are shown, and they provide a coordinate system for each torus. Each toroidal loop γ_1 (green online) has a constant value of canonical angle variable ϕ_2, while ϕ_1 varies from zero to 2π. These loops are spaced by fixed steps of ϕ_2. Likewise each poloidal loop γ_2 (blue online) has a constant ϕ_1, while ϕ_2 varies from zero to

2π. Those loops are spaced by fixed steps of ϕ_1. One of the γ_2 loops is stressed by a heavy curve (black online).

The fundamental loops and the associated coordinate systems in the tori change smoothly as l and h change. Starting at $l = 0$, $h = -35$, the stressed γ_2 (heavy black loop) is perpendicular to the toroidal (green online) loops, and it is projected into the (x,y) plane as a line. Moving counterclockwise in the (l,h) plane, that loop is widened and tilted. For $h > 0$, as l decreases from $(l,h) = (5,6)$ to $(0,5)$, the "doughnut hole" shrinks, and the innermost point of any poloidal γ_2 loop approaches the origin in (x,y,p_ρ) space. For $l = 0$ this (x,y,p_ρ) projection of the torus is singular, and the γ_2 loops all rise vertically through the origin. When l continues to decrease for $h > 0$, the formerly poloidal (blue online) loops all go around the doughnut hole, and their projections into the (x,y) plane enclose the origin. Continuing around the monodromy circuit, the loops change smoothly; when we get back to the original torus $l = 0$, $h = -35$ the loops γ_2, and the associated canonical angle coordinate system, are topologically different from the original loops on that torus. The originally poloidal loop now goes around the torus in both poloidal and toroidal senses.

Also, examining the projections of the γ_2 loops into the (x,y) plane, wherein there is a classically forbidden region surrounding the origin, the topology of the projected loop has changed. Initially it is a "trivial" loop, which in configuration space could be shrunk to a point without passing through the forbidden region, while at the end it has winding number -1 about the forbidden region.

At the top of the monodromy circuit, at $(l = 0, h = 5)$ the (x,y,p_ρ) representation of the torus is singular. However, the torus itself and its basic loops are not singular there. To display this, we show in the top line of Fig. 1 a representation of the tori in another space, $(X = y + p_x, Y = y - p_x, P_y = x + p_y)$, where the tori and the poloidal loops (blue and black online) evolve smoothly from $(l = 5, h = 6)$ to $(l = -5, h = 4)$. This change of the topological structure of the family of fundamental loops $[\gamma_2]$ is a static manifestation of monodromy.

Quantum implications of multivalued action variables were first described by Cushman and Duistermaat [36]: The lattice of allowed semiclassical eigenvalues $\{E_{n,m}\}$, defined such that $\mathscr{I}_2(m,E_{n,m}) = (n + 1/2)\hbar$, $\mathscr{I}_1(m) = m\hbar$ has a defect. The global perspective was brought into AMO physics especially by Sadovskii, Zhilinskii, and their colleagues. They have used the new methods to show the presence of monodromy and related phenomena in the hydrogen atom in perpendicular fields [37–39], the CO_2 molecule [40–42], HCN [43], LiCN [44], systems with coupled angular momenta [45,46], and a number of model oscillator systems [47–49]. Quasilinear molecules are discussed at length in [50–52], diatomic molecules in fields in [53], and the hydrogen atom in tilted fields in [54,55]. Experimental observations in a classical swing-spring system were made in [56].

C. A dynamical manifestation of monodromy

The above discussion describes the properties of angle coordinates on each (l,h) torus, and how those coordinate systems change if we compare one torus with another. We call
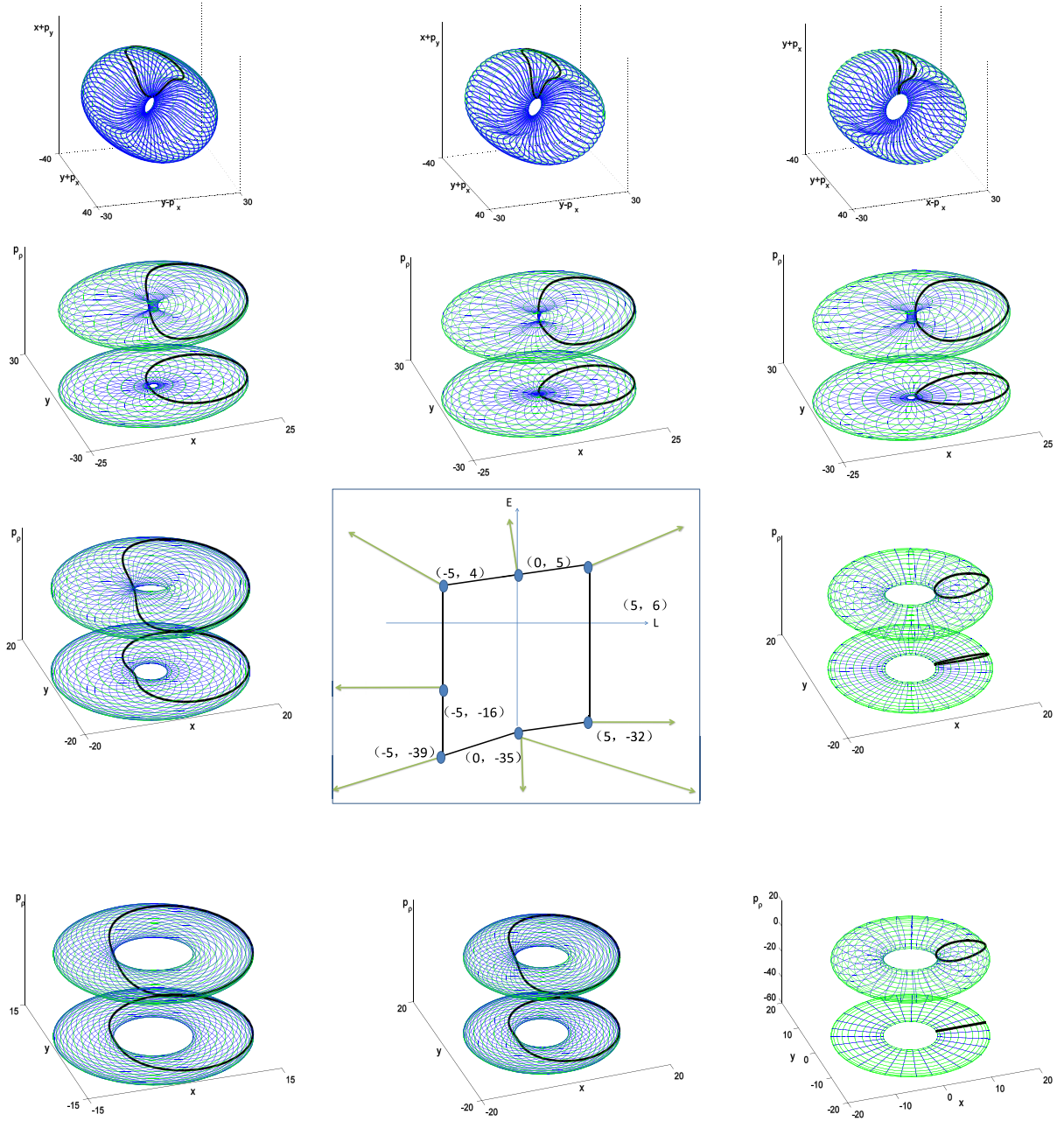
FIG. 1. (Color online) A static manifestation of Hamiltonian monodromy. Explanation is given in Sec. II B.

the phenomenon illustrated in Fig. 1 a static manifestation of monodromy because it is a property of static coordinate systems on static tori. A time variable t never appears in Sec. II B above; there is a path variable s for the monodromy circuit $(l(s),h(s))$, but motion in real time is not considered. Therefore it may seem that monodromy is an abstract geometrical property of abstract variables, with no interesting dynamical consequences. However, we now know that monodromy has significant dynamical consequences [1,2].

What happens if in addition to the forces represented by the Hamiltonian $H(\mathbf{z})$, we subject the system to an *additional* perturbing flow in phase space that changes the angular momentum and energy of particles in the system? Such additional forces and torques drive particles from one torus to another.

Specifically, suppose we begin with a collection of noninteracting particles on an initial torus having ($l = 0$, $h < 0$), and suppose that the positions and momenta of these particles

correspond to the initial γ_2 loop. Suppose then that all particles are made to change their angular momentum and their energy simultaneously, so that at every instant all particles have equal angular momentum and energy. Suppose furthermore that as they are driven from one torus to another, the change of torus leaves the value of the angle variables unchanged. (This statement requires a definition of the origin of coordinates on each torus, which we give in Appendix A.) Then the angle variables evolve with time as

$$\frac{d\boldsymbol{\phi}}{dt} = \boldsymbol{\omega}(l(t),h(t)). \tag{12}$$

We may think of this evolution as occurring in incremental steps. In the first half of each step, the particles move along a static torus with $d\phi/dt = \boldsymbol{\omega}(l,h)$, and in the second half of each step, each particle moves from a point on one torus to a point on an adjacent torus in such a way that the numerical values of the angle variables are unchanged $\boldsymbol{\phi}(l,h) = \boldsymbol{\phi}(l + dl, h + dh)$. We call this process "ideal" evolution. It is ideal in two senses: (i) the particles all begin on a single loop on a single torus, and that loop has a constant value of the angle variable ϕ_1^i; (ii) the particles move synchronously from one loop to another. This process is one type of ideal evolution.

Now suppose that the perturbing flow carries the particles in this way around a monodromy circuit in real time. In [2] we gave a full description of such "ideal" evolution, and we showed that a collection of particles distributed around a γ_2 loop remains always distributed around a γ_2 loop. At the end of the monodromy circuit, when all particles have returned to the original torus, they occupy the final γ_2 loop; that is, they have gone from a loop that is on one side of the potential-energy barrier to a loop that surrounds the potential-energy barrier. Thus the change in the angle coordinates on the tori is manifested in the dynamical behavior in real time.

The work in those references [1,2] left two important questions unanswered. (1) The ideal evolution defined therein arises from application of a perturbing flow in phase space which is (or can be) a Hamiltonian flow, but which cannot be derived from a single-valued Hamiltonian function. Can we implement a monodromy circuit by application of ordinary forces? (2) In any real system, the initial conditions cannot be a perfect γ_2 (poloidal) loop defined on a single torus; particles will have a distribution of initial angles, initial angular momenta, and energies. Can a monodromy circuit be implemented in a real system?

III. SIMULATIONS AND RESULTS

In this section, we show by computation that the answers to the two questions given at the end of Sec. II are "yes": (1) a monodromy circuit can be achieved by the application of ordinary forces, and (2) it can be achieved under reasonable experimental conditions. We have carried out calculations on a variety of two-dimensional circularly symmetric potential energies having a well and a central barrier, comparable to that given in Eq. (5). To change the angular momenta of the particles, we apply a torque. Also, since raising and lowering the energy of the particles would not be easy to implement in an experiment, we instead lower and raise the central barrier

(or equivalently, raise and lower the potential well). To answer the two questions separately, we carry out the calculations under two sets of initial conditions.

Single loop initial conditions (case a). We suppose that initially the particles all have the same energy and angular momentum, so their phase points lie on a single torus; we suppose that the particles are uniformly distributed on a single initial γ_2 loop on that torus, similar to the stressed (black online) loop in Fig. 1. Note that whereas the particles initially all have the same angular momentum and energy, as soon as a transverse force is applied, with the same force on all particles, each particle experiences a different torque, so their angular momenta do not remain equal. Also as the potential energy changes, they gain and lose different amounts of energy. However, the particles always occupy a single loop in phase space. That loop is close to a corresponding loop on a single torus, provided that the perturbing forces are applied slowly and gently, so that they do not change much during a radial oscillation of the particles. This is a kind of adiabatic implementation of the monodromy circuit. In our calculations, the entire monodromy circuit is implemented in approximately 30 cycles of radial oscillation. (Further discussion of adiabaticity is in Appendix D).

Cold-gas initial conditions (case b). The Heisenberg uncertainty principle tells us that we cannot fix both the angle and the angular momentum of particles, and practical experimental limitations tell us that we cannot fix the energy exactly. We suppose that the initial conditions involve a range of initial angles and angular momenta and energies, so that the phase-space points of the particles lie on different tori, but all are reasonably close to the initial γ_2 loop of case (a). The spread of angular momenta, angles, and energies is consistent with what can be done experimentally for a cold gas described in Sec. IV, so we call this case "cold-gas initial conditions." Again the applied forces change slowly compared to the period of radial oscillation. (However, note that if the forces change too slowly, so that the time required to go around the monodromy circuit is too long, then the gas particles will spread because of their thermal motion, and the change of character of the loop will not be visible. Computational experience has shown that the topological change is visible when the entire monodromy circuit is implemented in about 30 cycles of radial oscillation.)

To drive the particles around the monodromy circuit we use the following five steps. Every step is done sufficiently slowly that there are several radial oscillations of the particles in each step. In computations, we can start a collection of particles distributed around a single loop with zero angular momentum and fixed energy, or distributed with a broader range of initial angular momenta and energy comparable to the single-loop initial conditions. However, in an actual experiment, it is easier to start particles in a small packet near the inner turning point. Then after they have moved to the desired position, the process described below is begun.

(1) Keeping the cylindrically symmetric potential unchanged, add a rotating force $\boldsymbol{F}(t)$, the same force on all particles, to increase their angular momenta. The force is turned on and off gently and, in case (a), its direction is kept perpendicular to the position vector of the center of mass of the loop of particles. As a result, the force rotates counterclockwise

with a frequency close to

$$f = \frac{\Delta(\bar{l},\bar{h})}{\tau(\bar{l},\bar{h})}. \tag{13}$$

$\tau(l,h)$ and $\Delta(l,h)$ are, respectively, the "radial period" or time of first return, and the angle subtended in that time on the torus having angular momentum and energy respectively equal to (l,h). $\bar{l}$ and $\bar{h}$ are the mean values of angular momentum and energy at the time t (see Appendix A).

(2) Turn off the rotating force and raise the potential well so as to increase the energies of the particles to positive values. Equivalently, we may lower the central barrier; particle energies are defined relative to the value of the potential energy at the origin $\rho = 0$.

(3) Keeping the cylindrically symmetric potential fixed at the new values, apply the rotating force again the opposite way to reduce the angular momenta until they are negative. Again that force must rotate counterclockwise at a frequency close to that given in Eq. (13). In the "single-loop" computations of case (a) we keep the force perpendicular to the vector from the origin to the center of mass of the family of particles.

(4) Turn off the rotating force and lower the well to its original depth; this decreases the energy of each particle. Equivalently, we may raise the central barrier to its original height.

(5) Keeping the potential-energy function fixed at the new values (equal to the original values), apply the rotating force, still rotating counterclockwise with frequency (13), to increase the angular momentum of the particles, until the average angular momentum of those particles equals zero. Calculation shows that the average energy is then close to the initial energy.

Additional details about the potential energy and the perturbations are given in Sec. IV and Appendix B.

Figure 2 shows the resulting monodromy circuit for "single-loop initial conditions" and for "cold-gas initial conditions."
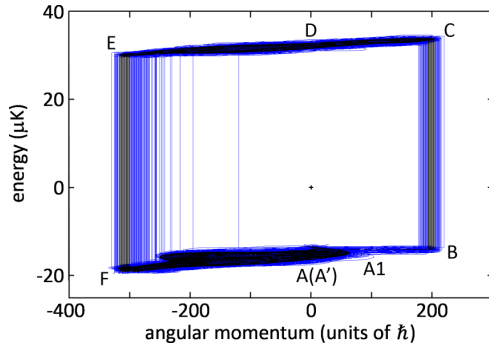

FIG. 2. (Color online) Spectrum-space paths, i.e., paths in angular momentum—energy space, (l,h). Each line represents the path $[l(t),h(t)]$ of one particle as it travels around the monodromy circuit starting at point A and proceeding through A1, B–F, and back to the final point A (called A′). Black lines represent particles with initial conditions on a single loop, and gray lines (blue online) are paths of particles having cold-gas initial conditions. Particles are driven around the monodromy circuit by applying a common force acting as a torque to change the angular momentum, and by raising or lowering the potential-energy well.

We see that the particles gain different amounts of energy and angular momentum as they traverse the monodromy circuit. However, they stay adequately close in angular momentum and energy.

Figure 3 shows the configuration space and velocity space behavior for the single loop and for cold-gas initial conditions. Two important things are shown by this simulation. First, it is possible to drive a collection of particles around a monodromy circuit using ordinary forces (rather than by using the ideal flow defined in Ref. [2]). Second, while we already know that the changed structure of the loop in configuration space provides a definitive signature of monodromy, also the structure in velocity space provides another clear signature.

Thus we have shown by computation that this dynamical manifestation of monodromy can be implemented in a real system by application of ordinary forces.

IV. EXPERIMENTAL REALIZATION

In this section and in Appendix C, we outline two experimental schemes for observing dynamical monodromy. The scheme described in the appendix uses motion of a magnetic puck on an air table, so it is a purely classical realization of the theory. The scheme described below uses a gas of ultracold atoms to implement dynamical monodromy. This experiment also offers the possibility of exploring the phenomenon in the presence of interparticle interactions, as well as quantum-mechanical effects such as interference and tunneling, which are beyond the scope of the theory presented in this paper. It is not an easy experiment, but it uses only standard tools of atomic physics.

A conclusive observation of dynamical monodromy should show experimentally that if one starts with a loop of initial condition points in phase space and then varies their energy and angular momentum along a closed path in spectrum space (such as in Fig. 2), then the initial and final configuration-space loops have a topologically different structure relative to the forbidden region surrounding the origin—i.e., the final, but not the initial loop encloses the energetically inaccessible region. The experimental system requires two main ingredients: (1) *precision control* for producing the initial phase-space loop, and for applying the torque and central potential barrier modulations to accurately implement the prescribed spectrum space path; and (2) *accurate measurements* of energy, angular momentum, position, and velocity to verify the phase-space and spectrum-space coordinates of the system at the start, end, and during the monodromy process.

The ultracold atoms scheme uses a ring-shaped optical trapping potential for ultracold ^{39}K atoms. Instead of running the full loop of initial conditions simultaneously, the atoms are placed in a short segment of the loop of initial conditions and then driven around the ring potential by the application of a uniform magnetic force, while the height of the central barrier is appropriately modulated to follow the monodromy circuit. The resulting energy and angular momentum of the atoms can then be tracked by both *in situ* and time-of-flight imaging as the system moves along the prescribed spectrum space path. The monodromy process for the full loop of initial conditions is reconstructed by combining the results of separate initial
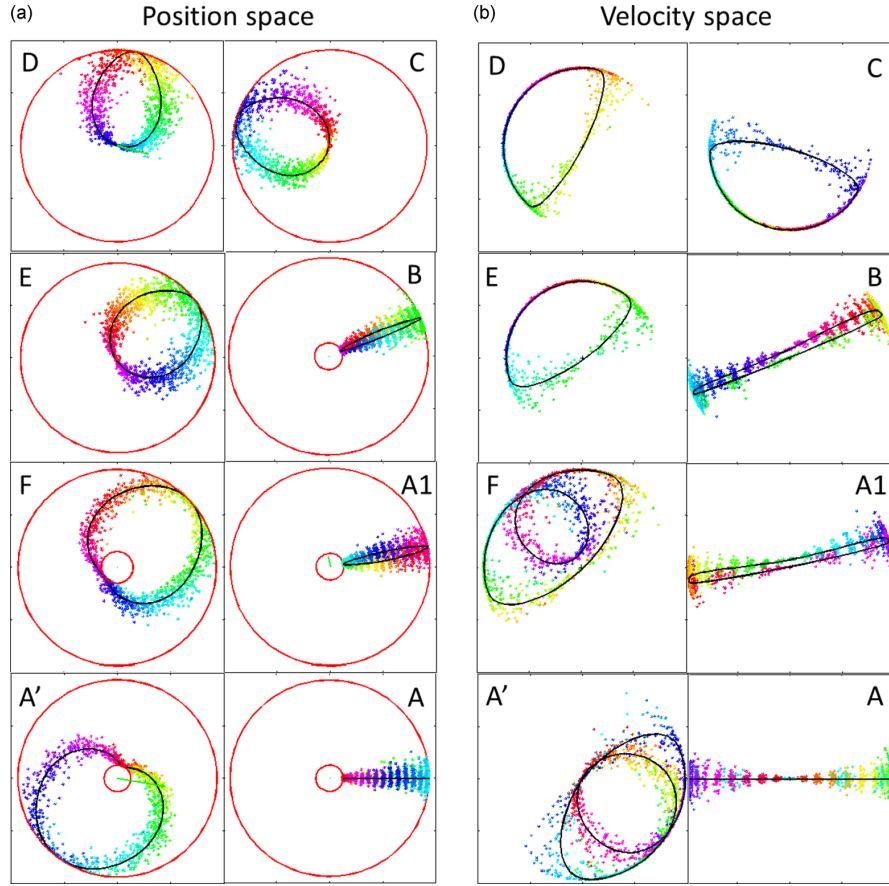
FIG. 3. (Color online) This is a collection of snapshots showing the evolution of the single loop and of the cold gas as the system traverses the monodromy circuit. The topological structure of loops of particles in configuration space changes during the monodromy circuit. Single-loop initial conditions are represented by the solid (black online) curve, while gas particles are represented by dots (color online). (A) and (A′) are points marked in Fig. 2. (a) Position space. Each square is a region 400×400 μm (± 200 μm about the origin). The inner and outer circles are boundaries of the classically allowed region for any single-loop particle that has $l = \langle l \rangle$ and $h = \langle h \rangle$. The vectors from the origin (green online) represent the applied rotating force. (A) Initially all single-loop particles have the same energy and angular momentum ($l = 0, h = h_0$) and they form a line in configuration space (x-y plane) while the "gas particles" have a spread in angle, angular momentum, and energy: $\langle h \rangle = h_0$, $\Delta h > 0$, $\langle l \rangle = 0$, and $\Delta l \Delta \phi = \hbar/2$. (A1) In the second snapshot, as angular momenta increase, the line evolves into a loop always linking the inner and outer boundaries. (B and C) The well is lifted (equivalently, the central barrier is lowered), so the central forbidden region is reduced to a size governed by the angular momentum. (C,D,E) With energy of the particles above the central barrier, the angular momentum is decreased from positive to negative. At some instant a single-loop particle having zero angular momentum passes over the center point $x = y = 0$; for that particle the central forbidden region has vanished for an instant. When it reappears, it is inside the loop. (E and F) The well is lowered (equivalently, the barrier is raised) and the central forbidden region gets larger. (F and A′) The angular momentum is driven back up to zero. Integration is stopped when $\langle l \rangle = 0$, and we find that $\langle h \rangle$ is close to the initial energy, h_0. Like the angle loop γ_2, the loop of particles has evolved into a topologically different loop. (b) Momentum space, (p_x, p_y). The units of momentum are 10^{-27} Kg m/s. Each square is a region 20×20, extending from ± 10 about $\mathbf{p} = \mathbf{0}$. From points A1–C, the loop does not enclose the origin. At D it touches the origin, and from E–A′, the winding number about the origin is 1. Initially particles are traveling equally to the left and right. At the end, they are dominantly going in a beam like a rotating searchlight.

condition segments, so that the new topology of the resulting phase-space distribution can be observed.

The experimental implementation requires a number of lasers to produce a ring potential and several external magnetic fields to produce a torque that changes the angular momentum of the atoms. Figure 4 shows how lasers and magnetic coils can be combined to produce the appropriate optical potential and magnetic force for the atoms, which are then detected

by a high resolution imaging system. We summarize the main suggested experimental parameters in Table I. In the following paragraphs, we describe the details of the ring trap, the atomic packet and its preparation in a segment of the ring of initial conditions, the torque force, and how to measure the total energy and angular momentum of the atomic packet.

Ring trap. The atoms are confined in a ring trap produced by two blue-detuned optical dipole potentials produced by two
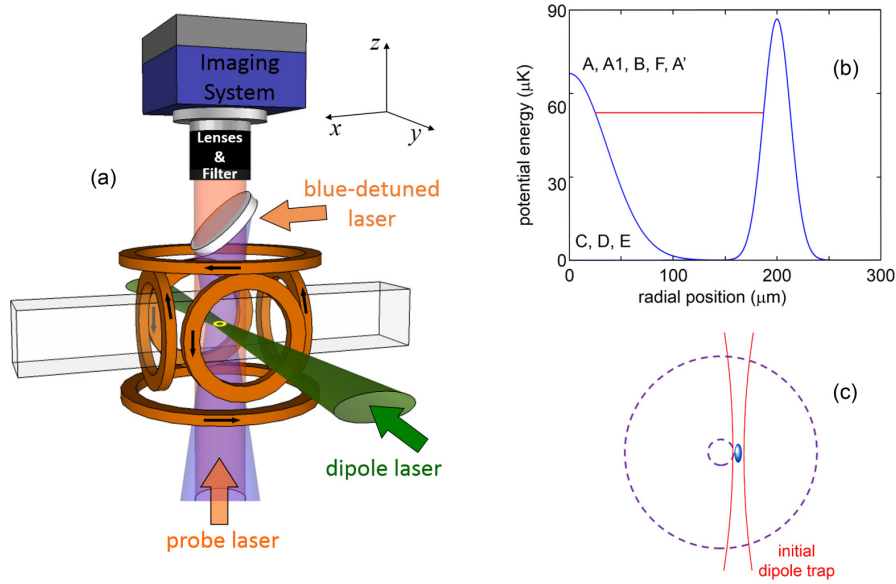
FIG. 4. (Color online) Proposed apparatus and optical potentials for observing dynamical monodromy. (a) Sketch of apparatus for observing dynamical monodromy: The atoms are confined in a ring trap formed by the vertical downward-directed blue-detuned laser beams and the horizontal laser beam (green online). The ring trap is the light (yellow online) ring in the intersection of these beams. Coils (orange online) generate magnetic fields for tuning the interactions to zero and producing the torque force. The camera is used for absorption imaging with an upward-directed laser probe beam (up-pointing arrow, orange online). (b) Planar ring-trap potential for the ultracold ^{39}K atoms. The potential consists of a central Gaussian barrier with a waist radius of 73 μm and an outer Gaussian wall at a radius of 200 μm with a waist of 26 μm. (c) Trap and release method for producing the atomic packet with total energy 53 μK.

vertically directed laser beams: a focused laser that serves as the central barrier and a concentric hollow laser beam that provides the outer wall of the trap. Hollow beams can be generated with a variety of optical elements such as axicon lenses [57], phase plates [58], and spatial light modulators [59]. Time-averaged doughnut beams can be produced by rapid rotation of a Gaussian beam using two crossed acousto-optic modulators [60]. The Gaussian ring potential of Fig. 4(b) is well suited for ultracold atom monodromy studies and can be produced with central barrier and outer wall laser powers of 0.4 and 2.5 W, respectively, at 750 nm. An additional red-detuned laser can be used to form a horizontal sheet of light that provides vertical confinement, while leaving the horizontal confinement potentials negligibly affected: For example, a 10 W laser beam at 1064 nm focused to horizontal and vertical

waist radii of 5 mm and 30 μm, respectively, will provide harmonic confinement of 360 Hz along the vertical axis with a trap depth of roughly 4 μK, but with a negligible 2 Hz confinement in the horizontal plane. Alternatively, vertical confinement can be provided by a one-dimensional optical lattice of horizontal "pancake traps" with the atoms spread over multiple layers. Based on simulations of atomic motion in the ring potential, the average scattering rate from all of the far off-resonant trapping light is estimated to be about 1 Hz per atom and so is negligible over the 100 ms duration of the proposed experiment.

Atomic packets. The atomic packets consist initially of a noninteracting Bose-Einstein condensate (BEC) of ^{39}K atoms designed to minimize the expansion of the atomic packet as it follows the spectrum space path. The BEC limits the expansion of the atomic packet to the Heisenberg-limited spread required of all quantum-mechanical systems, but must be carefully tailored by choosing an appropriate initial packet size: In our case, a ^{39}K BEC with radial and tangential half-widths of 0.3 and 2.25 μm, respectively, will expand with respective velocities of 2.7 and 0.4 μm/ms. Repulsive atom-atom interactions can also lead to relatively large expansion rates, but can be sufficiently suppressed by using the $|F = 1, m_F = +1\rangle$ hyperfine ground state of ^{39}K at a magnetic field of 350 G, which tunes the s-wave scattering length to zero due to a nearby Feshbach resonance [61]. (A slightly attractive interaction may be useful in reducing the Heisenberg-limited spreading of the packet, though simulating its precise effects on the atomic packet is beyond the scope of this paper.) Experimentally, the interactions are difficult to

TABLE I. Summary of ultracold atom experiment parameters.

Parameter	Value
Ring-trap laser power	2.9 W at 750 nm
Vertical trapping laser power	10 W at 1064 nm
Atomic state	$|F = 1, m_F = +1\rangle$ hyperfine state of ^{39}K
Atomic packet population	4×10^4
Energy of initial atomic packet	53 μK
Peak torque force	0.36 $m_K g^*$
Magnetic Feshbach zero	350 G
Duration of monodromy round trip	100 ms

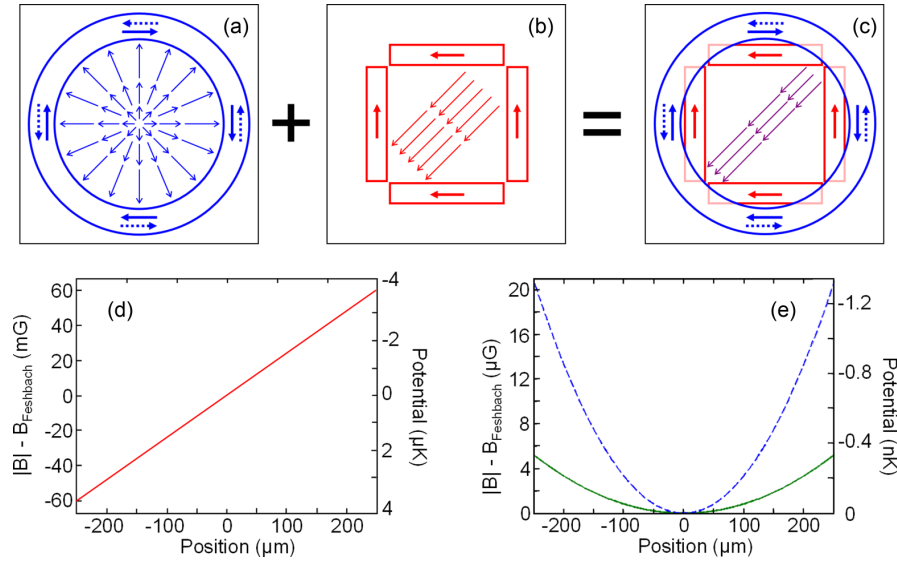*I.e. 0.36 times the weight of a potassium atom.

FIG. 5. (Color online) Magnetic fields for producing the torque force. The top three panels sketch how the quadrupole magnetic field [panel (a), thin arrows, blue online] generated by the anti-Helmholtz coil pair combines with the uniform horizontal magnetic field [panel (b), thin arrows, red online] produced by the two Helmholtz coil pairs to produce a magnetic gradient in the direction of the magnetic field [panel (c), thin arrows, purple online], whose orientation is determined by the relative currents in the two Helmholtz coil pairs. The magnetic field line sketches in panels (a), (b), and (c) are all in the horizontal plane (view from above) and are not to scale: The thick arrows represent the current in the coil, while the thick dashed arrows indicate the current in the hidden coil underneath. The two plots (d) and (e) show the magnetic field magnitude and its associated effective potential. Along the field direction (d) it is nearly linear (red online) while in the transverse directions (e) it is quadratic: Its horizontal variation is represented by the solid (green online) curve, and its vertical variation by the dashed (blue online) curve. Note the reversed right axes for the potential energy, since the $|F = 1, m_F = +1\rangle$ state is a strong field seeker.

eliminate altogether, but even if the scattering length is reduced to $a_s = 0.17a_0$, which for $\partial a_s/\partial B = 0.55a_0$ [61] corresponds to a magnetic field tuning precision of $\Delta B = \pm 0.3$ G, then interaction-induced spreading is negligible for packets with fewer than 8×10^4 atoms. However, the atom number must also be sufficiently large to allow for high-quality imaging: Simulations of time-of-flight experiments, such as in Fig. 7, show that atom numbers of 4×10^4 or more produce final atomic packets with optical depths of 0.5 or higher, which are suitable for absorption imaging methods [62].

Initial conditions. The BEC is inserted into the ring trap with a multistep process. As shown in Fig. 4(c), the BEC is initially trapped by a single-beam optical dipole trap produced by an additional laser that copropagates with the 1064 nm laser sheet [not shown in Fig. 4(a)]. The BEC is located at a radius of 25 μm, which corresponds to a potential energy of 53 μK. Upon turning off this single beam confining potential, the BEC is free to oscillate in the ring potential. The specific position-velocity combination of the ring of initial conditions for the atomic packet is chosen by applying the torque force at the appropriate time of the oscillation phase. Our simulations show that a radial positioning error of ± 1.25 μm can be tolerated. Alternatively, if a higher precision method is needed, a multiphoton Bragg pulse [63,64] can be used to impart a momentum kick (corresponding to a kinetic energy of 53 μK) to BEC atoms held at the minimum of the ring potential.

Torque force. The torque force can be produced by the magnetic gradient of a horizontally oriented quadrupole coil

pair with equal and opposite currents in its two coils, as shown in Fig. 4(a). As illustrated in the top three panels of Fig. 5, the central symmetry quadrupole field combines with the 350 G horizontal magnetic field required for suppressing interactions. At 350 G, the Zeeman shift of the $|F = 1, m_F = +1\rangle$ hyperfine ground state is -1.33 MHz/G. Modulation of the torque force as shown in Figs. 6(a) and 6(b) help to reduce the width of the packet in spectrum space. A maximum force of 2.3×10^{-25} N $= 0.36$ mg is required, which corresponds to a magnetic gradient of 2.6 G/cm. The combination of the uniform 350 G field with the weak quadrupole field results in a magnetic gradient along the direction of the 350 G field, while the gradients in the transverse horizontal and vertical directions contribute negligibly to the potential over the size of the ring trap. The orientation of the magnetic torque force can be easily rotated in the horizontal plane by changing the direction of the 350 G field, which is generated by two orthogonal Helmholtz-style coil pairs: Sinusoidal modulation of the coil pair currents ($\pi/2$ out of phase from each other) rotates the 350 G field and the magnetic gradient in a manner similar to the magnetic field modulations in a time-orbiting potential (TOP) trap [65]. Figure 6(b) shows the orientation of the torque force and 350 G field over the course of the monodromy process: The field maintains an average angle of roughly $\pi/2$ with respect to the angular position of the atomic ensemble and is rotated at rates of up to 330 Hz, which is substantially slower than in a TOP trap [65]. Finally, the magnetic gradient produces a negligible variation of the
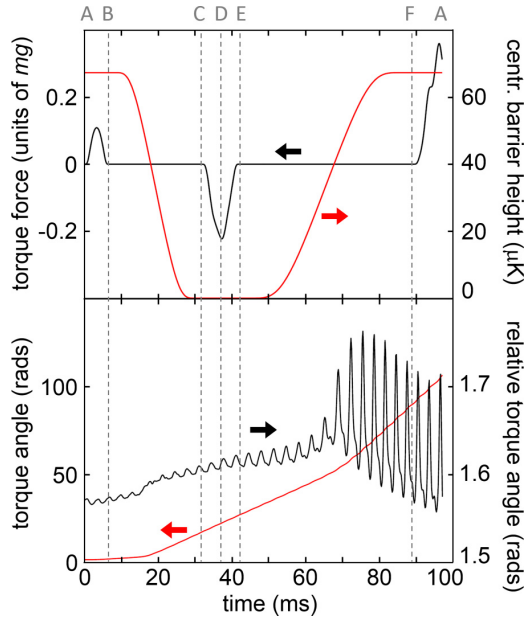
FIG. 6. (Color online) Torque force and central barrier modulation versus time required for completing the monodromy circuit. Top: Torque force magnitude (curve with arrow toward left axis, black online) and central barrier amplitude (curve with arrow toward right axis, red online) as a function of time. Bottom: Absolute torque angle with respect to starting position (arrow toward left axis, red online) and torque angle relative to full atomic ensemble center of mass (arrow toward right axis, black online). The letters on the top axis denote the monodromy circuit transit points of Fig. 2.

FIG. 7. (Color online) Time-of-flight method for measuring the total energy E. The plot corresponds to a packet that has completed the monodromy process and returned to point A (i.e., A′) on the spectrum space path of Fig. 2.

scattering length of at most $\Delta a_s = 0.06 a_0$ over the roughly 400 μm diameter of the ring trap.

Measuring the total energy E. The total energy E of the atomic packet can be measured by turning off the outer laser barrier of the ring trap while the atoms are climbing the inner central barrier. The atoms convert all of their potential energy to kinetic energy as they are pushed away from the central barrier and leave the ring potential region, so that their average velocity, kinetic energy, and thus total energy can be measured by time-of-flight imaging.

Figure 7 shows the results of a simulation of this process. The method relies on the compactness of the atomic packet to guarantee that there are no atoms in the outer barrier region when it is turned off, and to ensure that a measurement of average velocity is representative for all the atoms in the packet. Numerical simulations show that the method functions well for all initial conditions and points along the spectrum space path: To measure the total energy E at some point along the spectrum space path, the monodromy process is stopped at the desired point, and the outer barrier is turned off as the atoms are climbing the central barrier. Furthermore, the instantaneous kinetic energy of the atoms can be measured by turning off the entire ring potential and then measuring the velocity by time-of-flight imaging. In practice, the 1064 nm optical dipole laser and the torque force magnetic gradient will need to be turned off as well, since they provide very weak but

sufficient horizontal confinement to affect the time-of-flight measurements.

Measuring the angular momentum L. The angular momentum of the atomic packet can be measured by *in situ* imaging of the atoms as they travel around the ring potential. The inset of Fig. 8 shows a simulated image of the atoms in the ring potential, and the radially averaged atomic population as a function of angle from which the angular center of gravity of the packet can be determined from Gaussian fits of the distribution. A series of such images for different holding times shows the time evolution of the angular position of
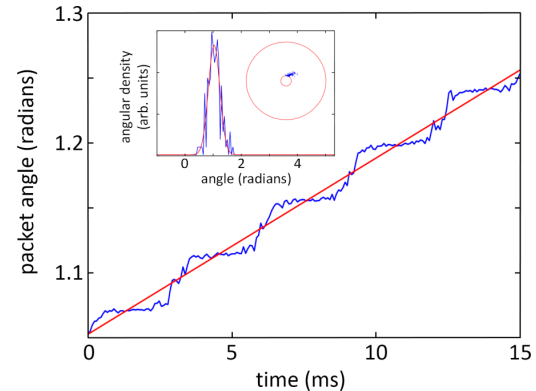
FIG. 8. (Color online) Angular momentum measurement method with *in situ* imaging. The main plot shows the average angular position of an atomic packet versus time (wiggly curve, blue online), along with a linear fit (straight line, red online) that gives the average angular velocity. The simulation is for an atomic packet that has returned to point A (i.e., A′) after completing the monodromy circuit of Fig. 2. Inset: Angular density of the packet (wiggly curve, blue online) and Gaussian fit (smooth curve, red online) versus angular position. The fit is used to determine the packet's average angle; the inset also shows a simulated image of the atoms (dots, blue online) in the ring potential along with the maxima and minima of the radial oscillations (circles, red online).

the packet. The main plot in Fig. 8 shows the results of a numerical simulation of this process: The average angular velocity $\langle\dot\theta\rangle$ is the overall slope of the angular time evolution, but the plot also contains a periodic step feature that reflects the radial oscillations of the atoms. The angular momentum L can be extracted from the time evolution of a packet's angular position, such as shown in Fig. 8, by determining the angle change $\Delta\theta_T$ over the course of one radial oscillation period ΔT_{radial} and then solving the following integral equation numerically for L [66]:

$$\Delta\theta_T = 2\int_{R_{\min}}^{R_{\max}} \frac{L\,dr}{r^2\sqrt{\frac{2}{m}[h-V(r)]-\frac{L^2}{m^2 r^2}}}, \qquad (14)$$

where h refers to the total energy of the atoms, $V(r)$ is the ring potential, and $R_{\min}$ and $R_{\max}$ are the inner and outer turning radii, respectively.

Extracting L requires knowledge of all the other quantities in Eq. (14). While $\Delta\theta_T$ can be determined from the step size of the "staircase" plot of average angular position versus time, it is more reliably obtained in our simulations from the relation $\Delta\theta_T = \Delta T_{\text{radial}}\langle\dot\theta\rangle$: The average angular velocity $\langle\dot\theta\rangle$ is the slope of a linear fit to the average angular position plot in Fig. 8, and the radial period ΔT_{radial} of the atomic packet in the ring potential can be obtained from a Fourier transform of the average angular position time series in Fig. 8. $V(r)$ can be determined experimentally by *in situ* absorption imaging of a cold thermal gas of temperature T_{thermal} in the ring potential: The image provides the radial atomic density $n(r)$ which can then be used to extract the potential through the relation $n(r) \cong \exp[-V(r)/kT_{\text{thermal}}]/\Lambda^3$, where $\Lambda = \hbar/\sqrt{2\pi m k T_{\text{thermal}}}$ is the thermal de Broglie wavelength [67]. The determination of the average total energy E of an atom in a packet was described in the previous section. The inner and outer turning radii can be determined from knowledge of the potential and the total energy or from *in situ* imaging. We find through numerical simulations of the above measurement method that L can be determined with an accuracy of 5%–10% over the course of the entire spectrum space path.

V. CONCLUSION

We have shown that a dynamical monodromy circuit can be implemented by ordinary forces, and we have described two ways to realize a dynamical monodromy circuit in a physical system—a puck on an air table, and an ultracold gas. All our calculations are classical, and presume no interaction between the particles, so measurements on a cold gas would raise questions about quantum behavior and about interactions between particles that are not addressed in this paper.

ACKNOWLEDGMENTS

APPENDIX A: NUMERICAL COMPUTATION OF CANONICAL ANGLE LOOPS

The method described here can be adapted for use in a great variety of systems, but we describe it here in detail for cylindrically symmetric systems. Given specified regular values of angular momentum $L(z) = l$ and energy $H(z) = h$ we presume that the corresponding torus is unique. For that specified (l,h), we choose a circle $\rho = \rho^0$ in the classically allowed region, and we choose an arbitrary point (ρ^0,ϕ^0) on that circle. At that point we set initial conditions on the momenta: $p_\phi^0 = l$ by definition, and p_ρ^0 is chosen as any value such that $H(p_\rho^0,p_\phi^0,\rho^0,\phi^0) = h$. Starting at that point, and time $t = t^0$ we integrate Hamilton's equations until the coordinate $\rho(t)$ passes again through the circle $\rho = \rho^0$ in the original sense (outward or inward, whichever way we started the trajectory), and we record the time of first return $\tau(l,h) = t - t^0$ and the subtended angle $\Delta(l,h) = \phi - \phi^0$, defined below. Now we define an effective Hamiltonian, which is a function of the four phase-space variables and two parameters (l,h),

$$\mathscr{H}(z;l,h) : \mathbb{R}^4 \times \mathbb{R}^2 \to \mathbb{R},$$
$$\mathscr{H}(z;l,h) \equiv \frac{[\tau(l,h)H(z) - \Delta(l,h)L(z)]}{2\pi}. \qquad (A1)$$

This is regarded as a function of the phase-space variables z, with l and h treated as fixed parameters. In other words, we derive equations of motion by differentiating $\mathscr{H}$ with respect to each z_i, holding l and h fixed. Here it is essential to distinguish between $[L(z),H(z)]$, the functions of positions and momenta, and their numerical values $[l,h]$, which are regarded as fixed parameters when Hamilton's equations are computed. In our case,

$$\mathscr{H}(z;l,h) \equiv \frac{1}{2\pi}\left\{\tau(l,h)\left[\frac{p_\rho^2}{2} + \frac{p_\phi^2}{2\rho^2} + V(\rho)\right] - \Delta(l,h)p_\phi\right\} \qquad (A2)$$

and, for example, denoting σ as the timelike variable,

$$\frac{d\phi}{d\sigma} = \frac{\partial\mathscr{H}}{\partial p_\phi} = \frac{1}{2\pi}\left[\frac{\tau(l,h)p_\phi}{\rho^2} - \Delta(l,h)\right]. \qquad (A3)$$

Equations of motion for other variables are obtained similarly. (For $h > 0$ it is best to integrate in Cartesian coordinates to avoid singular behavior near the origin.) Numerical integration of this path $z(\sigma)$ from $\sigma = 0$ to 2π produces a γ_2 loop.

As we change l and h, going from one torus to another, we need to define a connection between angle variables on the changing tori such that the transformation between phase-space points and variables (ϕ_1,ϕ_2,l,h) is a differentiable and invertible transformation. To do this, we must give a definition of the origin of angle coordinates $\mathbf{z}^0(0,0,l,h)$ such that the angles are differentiable functions of $\mathbf{z}$, and a definition of $\Delta(l,h)$ such that it is a differentiable function of (l,h). In the present case, we may choose the outermost point of each torus on the x axis to be the origin of angle coordinates.

When we define Δ so that it changes smoothly, we find that it is forced to be a multivalued function of (l,h). In our case, starting with $(l = 0,h < 0)$, $\Delta(l,h) = 0$. Increasing l from
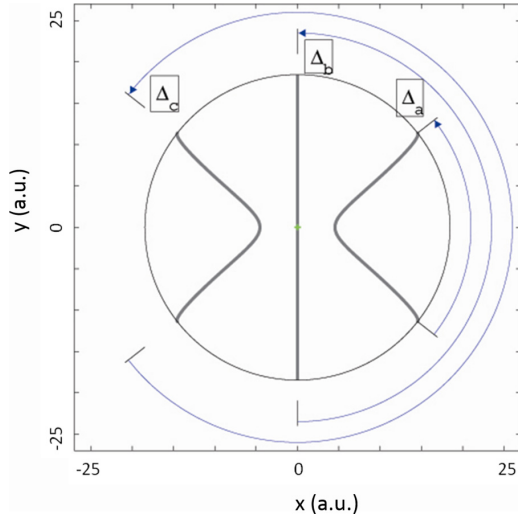
FIG. 9. (Color online) The angle $\Delta(l,h)$ must be defined such that it changes smoothly with l and h. As l decreases through zero with $h > 0$, $\Delta(l,h)$ must be defined so that it increases smoothly through π.

there makes $\Delta(l,h)$ small and positive. Proceeding around the monodromy circuit, $\Delta(l,h)$ increases until at $l = 0, h > 0$, $\Delta(l,h) = \pi$. As l goes negative with $h > 0$, $\Delta(l,h)$ must be defined so that it and all its derivatives with respect to l and h are continuous. This is done by defining $\Delta(l,h)$ as shown in Fig. 9. Δ is therefore a multivalued function of (l,h): The monodromy point $(l = 0, h = 0)$ is a branch point, and $\Delta(l,h)$ changes from 0 to 2π on its journey around the monodromy circuit.

The resulting γ_2 loop also evolves smoothly, and displays monodromy, as was shown in Fig. 1. This is the method we used to create that figure.

The corresponding multivalued action variable $\mathscr{I}_2(l,h)$ can be computed by integration around that γ_2 loop,

$$\mathscr{I}_2(l,h) = \frac{1}{2\pi} \oint_{\gamma_2} \boldsymbol{p}(s) \cdot \frac{d\boldsymbol{q}}{ds} ds. \tag{A4}$$

To show that this is all consistent with more familiar definitions, let us examine

$$\mathscr{I}_2'(l_1,h_1) = \frac{1}{2\pi} \oint p_\rho(\rho;l,h) d\rho,$$
$$\mathscr{I}_2'(l_2,h_2) = \frac{1}{2\pi} \oint p_\rho(\rho;l,h) d\rho - l, \tag{A5}$$

where (l_1,h_1) are any values of (l,h) on the first half of the monodromy circuit, (l_2,h_2) are any values on the second half, and

$$p_\rho(\rho;l,h) = \left\{ 2 \left[h - \frac{l^2}{2\rho^2} - V(\rho) \right] \right\}^{1/2}. \tag{A6}$$

One easily shows that $\mathscr{I}_2'$ defined in Eq. (A5) is the same as $\mathscr{I}_2$ defined in Eq. (A4), and

$$\frac{\partial \mathscr{I}_2'}{\partial h} = \frac{\tau(l,h)}{2\pi},$$
$$\frac{\partial \mathscr{I}_2'}{\partial l} = \frac{-\Delta(l,h)}{2\pi}. \tag{A7}$$

Hence we can write this action variable as a function of phase-space coordinates z with the notation

$$I_2(z) = \mathscr{I}_2'(L(z), H(z)), \tag{A8}$$

and its derivatives with respect to z are

$$\nabla_z I_2(z) = \left(\frac{\partial \mathscr{I}_2'}{\partial l} \right) \nabla_z L(z) + \left(\frac{\partial \mathscr{I}_2'}{\partial h} \right) \nabla_z H(z)$$

$$= \frac{1}{2\pi} [\tau(l,h) \nabla_z H(z) - \Delta(l,h) \nabla_z L(z)]. \tag{A9}$$

The conjugate angle ϕ_2 is obtained by using I_2 as Hamiltonian, and σ and ϕ_2 range from 0 to 2π on the γ_2 loop.

APPENDIX B: DETAILS OF THE APPLIED FORCES

The formulas for applied forces given below were obtained as a result of numerical experiments. We did not use any systematic optimization method to obtain these results, but only a modest number of trials. For single-loop initial conditions, we begin with N particles, all having angular momenta equal to 0, and all having the same initial energy, uniformly distributed around a γ_2 loop on the initial torus $[l(t_0) = 0, h(t_0) = h_0]$. At each instant they have a center of mass located at $\vec{r}_0(t)$, where

$$\vec{r}_0(t) = \frac{\sum_i^N m_i \vec{r}_i(t)}{\sum_i^N m_i} = r_0(t) \cos \varphi(t) \vec{i} + r_0(t) \sin \varphi(t) \vec{j}. \tag{B1}$$

$\vec{r}_i(t)$ and m_i are the instantaneous location vector and mass of the ith particle, and $r_0(t)$ and $\varphi(t)$ are the instantaneous length and azimuthal angle of the instantaneous center-of-mass vector $\vec{r}_0(t)$. As mentioned in the main section of this paper, the monodromy circuit is divided into five steps, with $t_{i-1} \leqslant t \leqslant t_i$ on the ith step.

The driving torque that changes the angular momentum is applied as follows. The same force $\vec{F}(t)$ is applied to all particles, and this force is nearly perpendicular to the center-of-mass vector $\vec{r}_0(t)$. The direction of the force is such that the angular momentum of the center of mass increases in step 1 and in step 5, and such that it decreases in step 3. Thus, in steps 1 and 5, $\vec{F}(t)$ is $\pi/2$ "ahead of" $\vec{r}_0(t)$:

$$\vec{F}(t) \equiv F(t) \cos \left[\varphi(t) + \frac{\pi}{2} \right] \vec{i} + F(t) \sin \left[\varphi(t) + \frac{\pi}{2} \right] \vec{j}, \tag{B2}$$

$$F(t) \equiv \frac{\dot{\Lambda}(t)}{\sqrt{\overline{r^2}(t)}}, \qquad \overline{r^2}(t) \equiv \frac{\sum_i^N m_i \vec{r}_i^2(t)}{\sum_i^N m_i}. \tag{B3}$$

$\overline{r^2}(t)$ is the mean square distance from the origin to the instantaneous location of each particle, and $\dot{\Lambda}(t)$ is a chosen average rate of increase of angular momentum. It is made to increase and decrease smoothly, as below. In steps 2 and 4,

$\dot{\Lambda}(t) = 0$, while in steps 1 and 3,

$$\dot{\Lambda}(t) = c_i \dot{\Lambda}_0 \text{sech}\left[\left(\frac{t_i - t_{i-1}}{2}\right)\left(\frac{1}{t_{i-1} - t} + \frac{1}{t_i - t}\right)\right]. \quad \text{(B4)}$$

$\dot{\Lambda}_0$ is a constant value which we take to be 0.9, and $c_i = 1, -2,$ and 3, respectively, in steps 1, 3, and 5. The negative sign in step 3 makes the force rotate in the same sense as the center of mass, but $\pi/2$ "behind," so the angular momentum is reduced in this step. Equation (B4) makes the torque change as a C^∞ function of time.

We found that a slightly different method worked best for step 5. We took for $t > t_4$,

$$\vec{F}(t) \equiv F_5 \cos\left[\varphi(t_4) + \omega t + \frac{\pi}{2}\right]\vec{i} + F_5 \sin\left[\varphi(t_4) + \omega t + \frac{\pi}{2}\right]\vec{j},$$
$$\text{(B5)}$$

where $\varphi(t_4)$ is the azimuthal angle of the center of mass at time t_4, and ω is a constant rotation rate chosen to be

$$\omega \equiv \frac{\Delta(l(t_4), h(t_4))}{\tau(l(t_4), h(t_4))}, \quad \text{(B6)}$$

where $(l(t_4), h(t_4))$ are the average value of angular momentum and energy when $t = t_4$, and $\Delta(l, h)$ and $\tau(l, h)$ are defined in Appendix A as subtended angle and time of first return as functions of angular momentum and energy. F_5 is a constant and set to be 0.15.

During steps 2 and 4, while there is no driving torque, the parameters of the well are changed by changing the height of the central barrier. In our calculations this is done by changing the power in the strongly focused laser so that the height of the central barrier $V(t)$ varies continuously between V_0 and V_1 as follows.

$$V(t) = V_0 \quad \text{if} \quad 0 \leqslant t \leqslant t_1$$
$$= V_0 + (V_1 - V_0)\left\{\tanh\left[\left(\frac{t_2 - t_1}{2}\right)\left(\frac{1}{t_1 - t} + \frac{1}{t_2 - t}\right)\right]\right.$$
$$\left. + \frac{1}{2}\right\} \quad \text{if} \quad t_1 < t \leqslant t_2$$
$$= V_1 \quad \text{if} \quad t_2 < t \leqslant t_3$$
$$= V_1 + (V_0 - V_1)\left\{\tanh\left[\left(\frac{t_4 - t_3}{2}\right)\left(\frac{1}{t_2 - t} + \frac{1}{t_4 - t}\right)\right]\right.$$
$$\left. + \frac{1}{2}\right\} \quad \text{if} \quad t_3 < t \leqslant t_4$$
$$= V_0 \quad \text{if} \quad t_4 < t \leqslant t_5. \quad \text{(B7)}$$

Integration is stopped when the average value of the angular momentum returns to zero, and that defines the time t_5.

APPENDIX C: CLASSICAL DYNAMICAL MONODROMY ON AN AIR TABLE

This scheme is considerably simpler than the proposed ultracold atom implementation, but it is purely classical, and so while it can illustrate dynamical monodromy, it cannot address the interesting questions associated with quantum systems. In this approach, a puck on an air cushion serves as a single test mass which can move with negligible surface friction over a
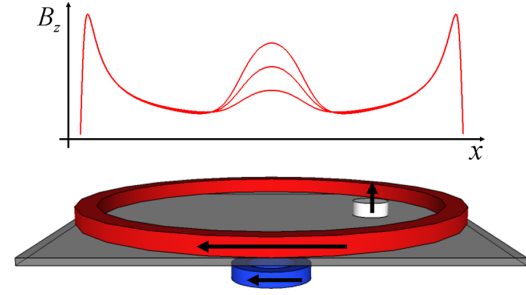

FIG. 10. (Color online) Magnetic confinement potential of the puck on the air table. Top: Plot of the magnetic field component normal to the air table, B_z, versus a radial horizontal axis. The horizontal confinement potential for the magnetic puck is proportional to B_z. The three curves plot B_z for central coil currents of $0.5I_0$, I_0, and $1.5I_0$, where I_0 is the current in the large outer coil. Both coils have the same number of turns. Bottom: Side view sketch of the air table (horizontal plane, gray online), large magnetic coil (red online), and central barrier magnetic coil (blue online). The arrows represent the direction of the current in the coils and the magnetic moment of the puck. The puck moves in a plane just above the surface of the air table.

horizontal planar surface. Magnetic forces are used to provide a ringlike confining potential in the horizontal plane, while the tilt of the air table away from horizontal provides an external force that exerts a torque on the puck. The motion of the puck can be recorded by a video camera placed directly above the air table. Repeating the circuit with different initial conditions and superposing the videos, one can watch the evolution of a loop.

Magnetic ring potential. A magnetic puck with a vertically oriented magnetization axis with magnetic moment $\overrightarrow{\mu}$ will experience a conservative potential in an external magnetic field, $\overrightarrow{B}$. The magnetic interaction Hamiltonian is $-\overrightarrow{\mu} \cdot \overrightarrow{B}$ and so it is proportional to the vertical component of $\overrightarrow{B}$. As shown in Fig. 10, a large diameter magnetic coil in the horizontal plane of motion of the puck provides the outer barrier of the ring potential, while a smaller concentric coil located below the air table provides the central barrier of the ring potential. The amplitude of the central barrier can be dynamically adjusted by varying the current flowing through it.

Torque force. The torque is provided by a uniform external force derived from Earth's gravity by tilting the air table by an angle ϑ from horizontal, in the desired direction of the force. The magnitude of the component of the force on the puck in the plane of the air table is then $mg \sin \vartheta$, where m is the mass of the puck. A directional and dynamically controlled tilt can be implemented by supporting the air table from below with a pivot point at its center and two electrically controlled actuator legs at adjacent corners. The height of the two legs can be modulated by independent computer controlled voltage signals. For a typical puck mass of 0.2 kg and a magnetic ring potential, such as in Fig. 10, with an outer radius on the order of 0.3 m produced by coils with currents on the scale of 200 amp-turns, our simulations show that the proper torque force can be produced with air table tilts on the order of 0.5° or less.

In this case, the equivalent spectrum space monodromy circuit can be completed on a time scale of 10–20 s.

Initial conditions. The puck is set in radial motion by holding it against the outer magnetic coil ring and then releasing it. The puck will travel radially, tracing out the ring of initial conditions in phase space, and the specific initial condition of interest is then selected by starting the monodromy process (i.e., the application of the torque force) when the puck has the required position and velocity.

Detection. The motion of the puck throughout the air table ring potential can be recorded by a video camera placed directly above the apparatus. The video provides the position of the puck as a function of time, from which the velocity of the puck can be derived. The position of the puck can be used to determine its magnetic potential energy (in combination with a magnetic field map), while the velocity gives its kinetic energy, and thus the total energy. The angular momentum can be derived from the velocity and radial position of the puck. The spectrum space path can thus be reconstructed from the energy and angular momentum of the puck.

Following a loop of initial conditions. The video would show each path $\mathbf{q}(t) = [x(t), y(t)]$, and superposition of the videos for different initial conditions would show the evolution of the whole loop.

APPENDIX D: MONODROMY AND HANNAY ANGLES

We are often asked about the relationship between monodromy and the phenomena associated with Hannay angles. There are some similarities, but there are also some essential differences.

Hannay [68] posed and answered the following question: Given an integrable Hamiltonian system; given that the trajectory begins on one torus; given that the Hamiltonian depends on one or more parameters; given that we change those parameters slowly so that they go around a cycle, returning to their initial values; then the adiabatic proposition asserts that the action variables will remain always constant, and therefore the system will return to its original torus. However, what happens to the angle variables?

Hannay showed that the angles evolve with time at the frequencies on the instantaneous tori, but with also a correction related to the integral of a certain 2-form. What are the similarities and differences from our description of monodromy? Both situations involve changes of canonical angles. In both cases, one component of the change is the frequency on instantaneous tori. However there are several important differences.

Hannay's theory applies to systems with one or more degrees of freedom, while monodromy can only appear in systems with two or more degrees of freedom. (2) The Hannay angle describes the change of position of particles along a loop. When one goes around a circuit in the parameter space, the loop returns to its original form, but the particles are not in the same location. In contrast, in a system with monodromy, not only do particles change their positions around a loop, but the whole loop changes its structure. (3) The correction in Hannay's case is a geometrical integral over an area subtended by changing parameters, and it can have any value. However, monodromy is a topological phenomenon. The change of structure of the loop does not depend on an area. When the system goes around any circuit enclosing a monodromy point in a given sense we get a change which is independent of path. (4) Hannay's formulas apply only to adiabatic traversals of a circuit. Monodromy is quite different. (a) In our case, we drive the system so that the angular momentum changes—but angular momentum is an action variable, so an action is changing, so the system is not undergoing strictly adiabatic evolution. (b) Nevertheless, one might argue that we are imposing a kind of adiabatic evolution because we make the particles undergo several radial oscillations while moving from one torus to another—this helps keep the particles moving together from torus to torus. That is a correct description—our implementation is adiabatic in this sense. (c) However, we claim that *in principle*, monodromy does not require any adiabatic traversal of a circuit. The kind of ideal evolution described in [2] will give the same result whether the system goes rapidly or slowly. (d) On the other hand, in practice, the only way we know how to implement a monodromy circuit in a real classical system with real forces involves a separation of time scales. In our case, we want all the particles to have nearly equal angular momenta; however, when the same force is applied to all particles, the ones at small radius experience a smaller torque and therefore a smaller change of angular momentum. Thus, in principle, monodromy does not require adiabaticity, but in actual implementation, it probably does.

[1] J. B. Delos, C. R. Schleif, and G. Dhont, J. Phys.: Conf. Ser. **99**, 012005 (2008).

[2] J. Delos, G. Dhont, D. Sadovskií, and B. Zhilinskií, Ann. Phys. **324**, 1953 (2009).

[3] V. I. Arnold, *Geometrical Methods in the Theory of Ordinary Differential Equations* (Springer, New York, 1988).

[4] I. C. Percival, J. Phys. B **6**, L229 (1973).

[5] I. Percival, in *Stochastic Behavior in Classical and Quantum Hamiltonian Systems*, edited by G. Casati and J. Ford, Lecture Notes in Physics Vol. 93 (Springer, Berlin, 1979), p. 259.

[6] I. Percival, in *Nonlinear Dynamical Aspects of Particle Accelerators*, Lecture Notes in Physics Vol. 247 (Springer, Berlin, 1986), pp. 12–36.

[7] D. W. Noid and R. A. Marcus, J. Chem. Phys. **62**, 2119 (1975).

[8] D. W. Noid and R. A. Marcus, J. Chem. Phys. **67**, 559 (1977).

[9] D. W. Noid and R. A. Marcus, J. Chem. Phys. **85**, 3305 (1986).

[10] D. W. Noid, M. L. Koszykowski, and R. A. Marcus, J. Chem. Phys. **71**, 2864 (1979).

[11] D. W. Noid, M. L. Koszykowski, and R. A. Marcus, J. Chem. Phys. **73**, 391 (1980).

[12] D. W. Noid, M. L. Koszykowski, and R. A. Marcus, Annu. Rev. Phys. Chem. **32**, 267 (1981).

[13] S. K. Knudson, J. B. Delos, and D. W. Noid, J. Chem. Phys. **84**, 6886 (1986).

[14] S. K. Knudson and D. W. Noid, Chem. Phys. Lett. **145**, 16 (1988).

[15] D. W. Noid, M. L. Koszykowski, and R. A. Marcus, in *Quantum Mechanics in Mathematics, Chemistry and Physics*, edited by K. E. Gustafson and W. P. Reinhardt (Plenum, New York, 1981), p. 133.

[16] B. G. Sumpter and D. W. Noid, Chem. Phys. Lett. **126**, 181 (1986).

[17] M. V. Berry, in *The Wave-Particle Dualism: A Tribute to Louis de Broglie on his 90th Birthday*, edited by S. Diner (Springer, Berlin, 1984), pp. 231–252.

[18] A. M. O. De Almeida, *Hamiltonian Systems: Chaos and Quantization* (Cambridge University Press, Cambridge, UK, 1990).

[19] R. Swimm and J. Delos, J. Chem. Phys. **71**, 1706 (1979).

[20] R. T. Swimm and J. B. Delos, J. Chem. Phys. **78**, 4795 (1983).

[21] M. K. Ali and S. S. Kipp, J. Phys. A: Math. Gen. **27**, 1953 (1994).

[22] K. M. Atkins and G. S. Ezra, Phys. Rev. E **51**, 1822 (1995).

[23] D. M. Wardlaw, D. W. Noid, and R. A. Marcus, J. Phys. Chem. **88**, 536 (1984).

[24] J. Gao and J. B. Delos, Phys. Rev. A **49**, 869 (1994).

[25] V. Kondratovich and J. B. Delos, Phys. Rev. A **57**, 4654 (1998).

[26] K. Richter and D. Wintgen, J. Phys. B **24**, L565 (1991).

[27] K. Richter, G. Tanner, and D. Wintgen, in *Quantum Chaos: Between Order and Disorder*, edited by G. Casati and B. Chirikov (Cambridge Uniuversity Press, Cambridge, 1995), p. 287.

[28] D. Wintgen and K. Richter, Comments At. Mol. Phys. **29**, 261 (1994).

[29] R. G. Littlejohn and W. G. Flynn, Phys. Rev. A **45**, 7697 (1992).

[30] M. T. Lopez-Arias, V. R. Manfredi, and L. Salasnich, La Rivista del Nuovo Cimento, Ser. 3 **17**, 1 (1994).

[31] B. H. Lavenda, Open Syst. & Information Dyn. **10**, 51 (2003).

[32] R. H. Cushman and L. M. Bates, *Global Aspects of Classical Integrable Systems* (Birkhäuser, Basel, 1997).

[33] J. J. Duistermaat, Commun. Pure Appl. Math. **33**, 687 (1980).

[34] L. M. Bates, Z. Angew. Math. Phys. **42**, 837 (1991).

[35] M. Zou, J. Geom. Phys. **10**, 37 (1992).

[36] R. Cushman and J. J. Duistermaat, Bull. Am. Math Soc. **19**, 475 (1988).

[37] R. Cushman and D. Sadovskii, Physica D **142**, 166 (2000).

[38] K. Efstathiou, D. A. Sadovskii, and B. I. Zhilinskii, Proc. R. Soc. London, Ser. A **463**, 1771 (2007).

[39] K. Efstathiou, O. V. Lukina, and D. A. Sadovskii, Phys. Rev. Lett. **101**, 253003 (2008).

[40] R. Cushman, H. Dullin, A. Giacobbe, D. Holm, M. Joyeux, P. Lynch, D. Sadovskii, and B. Zhilinskii, Phys. Rev. Lett. **93**, 024302 (2004).

[41] M. Sanrey, M. Joyeux, and D. A. Sadovskii, J. Chem. Phys. **124**, 074318 (2006).

[42] A. Giacobbe, R. Cushman, D. Sadovskii, and B. Zhilinskii, J. Math. Phys. **45**, 5076 (2004).

[43] K. Efstathiou, M. Joyeux, and D. Sadovskii, Phys. Rev. A **69**, 032504 (2004).

[44] M. Joyeux, D. Sadovskii, and J. Tennyson, Chem. Phys. Lett. **382**, 439 (2003).

[45] L. Grondin, D. A. Sadovskii, and B. I. Zhilinskii, Phys. Rev. A **65**, 012105 (2001).

[46] D. Sadovskii and B. Zhilinskii, Phys. Lett. A **256**, 235 (1999).

[47] K. Efstathiou, R. Cushman, and D. Sadovskii, Adv. Math. **209**, 241 (2007).

[48] N. N. Nekhoroshev, D. A. Sadovskií, and B. I. Zhilinskii, Compt. Rendus Math. **335**, 985 (2002).

[49] N. N. Nekhoroshev, D. A. Sadovskií, and B. I. Zhilinskií, Ann. Henri Poincaré **7**, 1099 (2006).

[50] B. P. Winnewisser and M. Winnewisser, in *Fourier Transform Spectroscopy*, edited by A. Sawchuk, OSA Trends in Optics and Photonics Vol. 84 (Optical Society of America, Washington, DC, 2003).

[51] B. P. Winnewisser, M. Winnewisser, I. R. Medvedev, M. Behnke, F. C. De Lucia, S. C. Ross, and J. Koput, Phys. Rev. Lett. **95**, 243002 (2005).

[52] M. Winnewisser, B. P. Winnewisser, I. R. Medvedev, F. C. De Lucia, S. C. Ross, and L. M. Bates, J. Mol. Struct. **798**, 1 (2006).

[53] C. A. Arango, W. W. Kennerly, and G. S. Ezra, Chem. Phys. Lett. **392**, 486 (2004).

[54] C. R. Schleif and J. B. Delos, Phys. Rev. A **76**, 013404 (2007).

[55] C. R. Schleif and J. B. Delos, Phys. Rev. A **77**, 043422 (2008).

[56] N. J. Fitch, C. A. Weidner, L. P. Parazzoli, H. R. Dullin, and H. J. Lewandowski, Phys. Rev. Lett. **103**, 034301 (2009).

[57] S. Kulin, S. Aubin, S. Christe, B. Peker, S. L. Rolston, and L. A. Orozco, J. Opt. B: Quantum Semiclassical Opt. **3**, 353 (2001).

[58] R. Ozeri, L. L. Khaykovich, N. Friedman, and N. Davidson, J. Opt. Soc. Am. B **17**, 1113 (2000).

[59] G. D. Bruce, J. Mayoh, G. Smirne, L. Torralbo-Campo, and D. Cassettari, Phys. Scr. T **143**, 014008 (2011).

[60] N. Friedman, L. Khaykovich, R. Ozeri, and N. Davidson, Phys. Rev. A **61**, 031403 (2000).

[61] G. Roati, M. Zaccanti, C. D'Errico, J. Catani, M. Modugno, A. Simoni, M. Inguscio, and G. Modugno, Phys. Rev. Lett. **99**, 010403 (2007).

[62] W. Ketterle, D. S. Durfee, and D. M. Stamper-Kurn, in *Proceedings of the Enrico Fermi International School of Physics, Course CXL*, edited by M. Inguscio, S. Stringari, and C. E. Wieman (IOS Press, Amsterdam, 1999), p. 67.

[63] S. Chiow, T. Kovachy, H. C. Chien, and M. A. Kasevich, Phys. Rev. Lett. **107**, 130403 (2011).

[64] D. M. Giltner, R. W. McGowan, and S. A. Lee, Phys. Rev. A **52**, 3966 (1995).

[65] W. Petrich, M. H. Anderson, J. R. Ensher, and E. A. Cornell, Phys. Rev. Lett. **74**, 3352 (1995).

[66] L. D. Landau and E. M. Lifshitz, *Mechanics: Course of Theoretical Physics* (Butterworth-Heinemann, Oxford, 1976), Vol. 1

[67] V. Bagnato, D. E. Pritchard, and D. Kleppner, Phys. Rev. A **35**, 4354 (1987).

[68] J. Hannay, J. Phys. A: Math. Gen. **18**, 221 (1985).

BIBLIOGRAPHY

[1] D. J. Thouless, "Quantization of particle transport," *Phys. Rev. B*, vol. 27, pp. 6083–6087, May 1983.

[2] P. W. Brouwer, "Scattering approach to parametric pumping," *Phys. Rev. B*, vol. 58, pp. R10135–R10138, Oct 1998.

[3] B. Kaestner, V. Kashcheyevs, S. Amakawa, M. D. Blumenthal, L. Li, T. J. B. M. Janssen, G. Hein, K. Pierz, T. Weimann, U. Siegner, and H. W. Schumacher, "Single-parameter nonadiabatic quantized charge pumping," *Phys. Rev. B*, vol. 77, p. 153301, Apr 2008.

[4] S. P. Giblin, M. Kataoka, J. D. Fletcher, P. See, T. J. B. M. Janssen, J. P. Griffiths, G. A. C. Jones, I. Farrer, and D. A. Ritchie, "Towards a quantum representation of the ampere using single electron pumps," *Nat Commun*, vol. 3, p. 930, 07 2012.

[5] S. K. Watson, R. M. Potok, C. M. Marcus, and V. Umansky, "Experimental realization of a quantum spin pump," *Phys. Rev. Lett.*, vol. 91, p. 258301, Dec 2003.

[6] M. Switkes, C. M. Marcus, K. Campman, and A. C. Gossard, "An adiabatic quantum electron pump," *Science*, vol. 283, no. 5409, pp. 1905–1908, 1999.

[7] P. W. Brouwer, "Rectification of displacement currents in an adiabatic electron pump," *Phys. Rev. B*, vol. 63, p. 121303, Mar 2001.

[8] Bose, "Plancks gesetz und lichtquantenhypothese," *Zeitschrift fr Physik*, vol. 26, no. 1, pp. 178–181, 1924.

[9] A. Einstein, *Quantum Theory of the Monatomic Ideal Gas*, vol. 1924. Akademie der Wissenshaften, in Kommission bei W. de Gruyter, 1924.

[10] A. Einstein, *Quantum Theory of the Monatomic Ideal Gas, Part II*, vol. 1925. Akademie der Wissenshaften, in Kommission bei W. de Gruyter, 1925.

[11] E. A. Cornell and C. E. Wieman, "Nobel lecture: Bose-einstein condensation in a dilute gas, the first 70 years and some recent experiments," *Rev. Mod. Phys.*, vol. 74, pp. 875–893, Aug 2002.

[12] W. Ketterle, "Nobel lecture: When atoms behave as waves: Bose-einstein condensation and the atom laser," *Rev. Mod. Phys.*, vol. 74, pp. 1131–1151, Nov 2002.

[13] D. J. Wineland, R. E. Drullinger, and F. L. Walls, "Radiation-pressure cooling of bound resonant absorbers," *Phys. Rev. Lett.*, vol. 40, pp. 1639–1642, Jun 1978.

[14] W. Neuhauser, M. Hohenstatt, P. Toschek, and H. Dehmelt, "Optical-sideband cooling of visible atom cloud confined in parabolic well," *Phys. Rev. Lett.*, vol. 41, pp. 233–236, Jul 1978.

[15] J. Prodan, A. Migdall, W. D. Phillips, I. So, H. Metcalf, and J. Dalibard, "Stopping atoms with laser light," *Phys. Rev. Lett.*, vol. 54, pp. 992–995, Mar 1985.

[16] S. Chu, L. Hollberg, J. E. Bjorkholm, A. Cable, and A. Ashkin, "Three-dimensional viscous confinement and cooling of atoms by resonance radiation pressure," *Phys. Rev. Lett.*, vol. 55, pp. 48–51, Jul 1985.

[17] J. Dalibard and C. Cohen-Tannoudji, "Dressed-atom approach to atomic motion in laser light: the dipole force revisited," *J. Opt. Soc. Am. B*, vol. 2, pp. 1707–1720, Nov 1985.

[18] A. Ashkin, J. M. Dziedzic, J. E. Bjorkholm, and S. Chu, "Observation of a single-beam gradient force optical trap for dielectric particles," *Opt. Lett.*, vol. 11, pp. 288–290, May 1986.

[19] C. Orzel, A. K. Tuchman, M. L. Fenselau, M. Yasuda, and M. A. Kasevich, "Squeezed states in a bose-einstein condensate," *Science*, vol. 291, no. 5512, pp. 2386–2389, 2001.

[20] W. D. Phillips, "Nobel lecture: Laser cooling and trapping of neutral atoms," *Rev. Mod. Phys.*, vol. 70, pp. 721–741, Jul 1998.

[21] M. K. Ivory, A. R. Ziltz, C. T. Fancher, A. J. Pyle, A. Sensharma, B. Chase, J. P. Field, A. Garcia, D. Jervis, and S. Aubin, "Atom chip apparatus for experiments with ultracold rubidium and potassium gases," *Review of Scientific Instruments*, vol. 85, no. 4, pp. –, 2014.

[22] S. Du, M. B. Squires, Y. Imai, L. Czaia, R. A. Saravanan, V. Bright, J. Reichel, T. W. Hänsch, and D. Z. Anderson, "Atom-chip bose-einstein condensation in a portable vacuum cell," *Phys. Rev. A*, vol. 70, p. 053606, Nov 2004.

[23] S. Aubin, M. Extavour, S. Myrskog, L. LeBlanc, J. Estve, S. Singh, P. Scrutton, D. McKay, R. McKenzie, I. Leroux, A. Stummer, and J. Thywissen, "Trapping fermionic 40k and bosonic 87rb on a chip," *Journal of Low Temperature Physics*, vol. 140, no. 5-6, pp. 377–396, 2005.

[24] S. Schneider, A. Kasper, C. vom Hagen, M. Bartenstein, B. Engeser, T. Schumm,

I. Bar-Joseph, R. Folman, L. Feenstra, and J. Schmiedmayer, "Bose-einstein condensation in a simple microtrap," *Phys. Rev. A*, vol. 67, p. 023612, Feb 2003.

[25] J. Reichel, W. Hänsel, and T. W. Hänsch, "Atomic micromanipulation with magnetic surface traps," *Phys. Rev. Lett.*, vol. 83, pp. 3398–3401, Oct 1999.

[26] M. A. Kasevich, "Coherence with atoms," *Science*, vol. 298, no. 5597, pp. 1363–1368, 2002.

[27] A. D. Cronin, J. Schmiedmayer, and D. E. Pritchard, "Optics and interferometry with atoms and molecules," *Rev. Mod. Phys.*, vol. 81, pp. 1051–1129, Jul 2009.

[28] T. Schumm, S. Hofferberth, L. M. Andersson, S. Wildermuth, S. Groth, I. Bar-Joseph, J. Schmiedmayer, and P. Kruger, "Matter-wave interferometry in a double well on an atom chip," *Nat. Phys.*, vol. 1, p. 57, Oct 2005.

[29] N. Hinkley, J. A. Sherman, N. B. Phillips, M. Schioppo, N. D. Lemke, K. Beloy, M. Pizzocaro, C. W. Oates, and A. D. Ludlow, "An atomic clock with 1018 instability," *Science*, vol. 341, no. 6151, pp. 1215–1218, 2013.

[30] B. J. Bloom, T. L. Nicholson, J. R. Williams, S. L. Campbell, M. Bishof, X. Zhang, W. Zhang, S. L. Bromley, and J. Ye, "An optical lattice clock with accuracy and stability at the 10-18 level," *Nature*, vol. 506, p. 71, Feb 2014.

[31] M. F. Riedel, P. Bhi, Y. Li, T. W. Hnsch, A. Sinatra, and P. Treutlein, "Atom-chip-based generation of entanglement for quantum metrology," *Nature*, vol. 464, p. 1170, Mar 2010.

[32] J. S. Douglas, H. Habibian, C. L. Hung, A. V. Gorshkov, H. J. Kimble, and D. E. Chang, "Quantum many-body models with cold atoms coupled to photonic crystals," *Nat Photon*, vol. 9, p. 326, May 2015.

[33] H. J. Kimble, "The quantum internet," *Nature*, vol. 453, p. 1023, Jun 2008.

[34] M. Greiner, O. Mandel, T. Esslinger, T. W. Hansch, and I. Bloch, "Quantum phase transition from a superfluid to a mott insulator in a gas of ultracold atoms," *Nature*, vol. 415, p. 39, Jan 2002.

[35] F. Gerbier, S. Fölling, A. Widera, O. Mandel, and I. Bloch, "Probing number squeezing of ultracold atoms across the superfluid-mott insulator transition," *Phys. Rev. Lett.*, vol. 96, p. 090401, Mar 2006.

[36] J. K. Chin, D. E. Miller, Y. Liu, C. Stan, W. Setiawan, C. Sanner, K. Xu, and W. Ketterle, "Evidence for superfluidity of ultracold fermions in an optical lattice," *Nature*, vol. 443, p. 961, Oct 2006.

[37] M. W. Zwierlein, C. H. Schunck, A. Schirotzek, and W. Ketterle, "Direct observation of the superfluid phase transition in ultracold fermi gases," *Nature*, vol. 442, p. 54, Jul 2006.

[38] E. L. Raab, M. Prentiss, A. Cable, S. Chu, and D. E. Pritchard, "Trapping of neutral sodium atoms with radiation pressure," *Phys. Rev. Lett.*, vol. 59, pp. 2631–2634, Dec 1987.

[39] A. L. Migdall, J. V. Prodan, W. D. Phillips, T. H. Bergeman, and H. J. Metcalf, "First observation of magnetically trapped neutral atoms," *Phys. Rev. Lett.*, vol. 54, pp. 2596–2599, Jun 1985.

[40] E. Majorana, "Nuovo cimento," vol. 9, no. 43, 1932.

[41] D. E. Pritchard, "Cooling neutral atoms in a magnetic trap for precision spectroscopy," *Phys. Rev. Lett.*, vol. 51, pp. 1336–1339, Oct 1983.

[42] U. Ernst, A. Marte, F. Schreck, J. Schuster, and G. Rempe, "Bose-einstein condensation in a pure ioffe-pritchard field configuration," *EPL (Europhysics Letters)*, vol. 41, no. 1, p. 1, 1998.

[43] K. Davis, M.-O. Mewes, M. Joffe, and W. Ketterle, *Fourteenth International Conference on Atomic Physics, Boulder, CO 1994*. AIP Conference Proceedings Series, New York: Springer-Verlag LLC, 1995. JILA Pub. 5383.

[44] W. Petrich, M. Anderson, J. Ensher, and E. Cornell, *Fourteenth International Conference on Atomic Physics, Boulder, CO 1994*. AIP Conference Proceedings Series, New York: Springer-Verlag LLC, 1995. JILA Pub. 5383.

[45] M. H. Anderson, J. R. Ensher, M. R. Matthews, C. E. Wieman, and E. A. Cornell, "Observation of bose-einstein condensation in a dilute atomic vapor," *Science*, vol. 269, no. 5221, pp. 198–201, 1995.

[46] D. A. Steck, "Rubidium 87 D Line Data." URL http://steck.us/alkalidata/rubidium87numbers.pdf.

[47] T. Tiecke, "Properties of potassium," *University of Amsterdam, The Netherlands, Thesis*, 2010.

[48] H. Katori, T. Ido, Y. Isoya, and M. Kuwata-Gonokami, "Magneto-optical trapping and cooling of strontium atoms down to the photon recoil temperature," *Phys. Rev. Lett.*, vol. 82, pp. 1116–1119, Feb 1999.

[49] Y. Takasu, K. Maki, K. Komori, T. Takano, K. Honda, M. Kumakura, T. Yabuzaki, and Y. Takahashi, "Spin-singlet bose-einstein condensation of two-electron atoms," *Phys. Rev. Lett.*, vol. 91, p. 040404, Jul 2003.

[50] A. Griesmaier, J. Werner, S. Hensler, J. Stuhler, and T. Pfau, "Bose-einstein condensation of chromium," *Phys. Rev. Lett.*, vol. 94, p. 160401, Apr 2005.

[51] M. Lu, S. H. Youn, and B. L. Lev, "Trapping ultracold dysprosium: A highly magnetic gas for dipolar physics," *Phys. Rev. Lett.*, vol. 104, p. 063001, Feb 2010.

[52] H. J. Metcalf and P. Van der Straten, *Laser cooling and trapping.* Springer Science & Business Media, 2012.

[53] M. Greiner, I. Bloch, T. W. Hänsch, and T. Esslinger, "Magnetic transport of trapped cold atoms over a large distance," *Phys. Rev. A*, vol. 63, p. 031401, Feb 2001.

[54] A. Ziltz, "Ultracold rubidium and potassium system for atom chip-based microwave and rf potentials," May 2015.

[55] Y.-J. Lin, A. R. Perry, R. L. Compton, I. B. Spielman, and J. V. Porto, "Rapid production of ^{87}Rb bose-einstein condensates in a combined magnetic and optical potential," *Phys. Rev. A*, vol. 79, p. 063631, Jun 2009.

[56] B. J. Verhaar, E. G. M. van Kempen, and S. J. J. M. F. Kokkelmans, "Predicting scattering properties of ultracold atoms: Adiabatic accumulated phase method and mass scaling," *Phys. Rev. A*, vol. 79, p. 032711, Mar 2009.

[57] E. G. M. van Kempen, S. J. J. M. F. Kokkelmans, D. J. Heinzen, and B. J. Verhaar, "Interisotope determination of ultracold rubidium interactions from three high-precision experiments," *Phys. Rev. Lett.*, vol. 88, p. 093201, Feb 2002.

[58] S. Falke, H. Knöckel, J. Friebe, M. Riedmann, E. Tiemann, and C. Lisdat, "Potassium ground-state scattering parameters and born-oppenheimer potentials from molecular spectroscopy," *Phys. Rev. A*, vol. 78, p. 012503, Jul 2008.

[59] M. Weidem'uller and C. Zimmermann, *Cold atoms and molecules.* John Wiley & Sons, 2009.

[60] W. Ketterle, D. S. Durfee, and D. M. Stamper-Kurn, "Making, probing and understanding Bose-Einstein condensates," *eprint arXiv:cond-mat/9904034*, Apr 1999.

[61] J. F. Sherson, C. Weitenberg, M. Endres, M. Cheneau, I. Bloch, and S. Kuhr, "Single-atom-resolved fluorescence imaging of an atomic mott insulator," *Nature*, vol. 467, p. 68, Sep 2010.

[62] R. Grimm, M. Weidemller, and Y. B. Ovchinnikov, "Optical dipole traps for neutral atoms," vol. 42 of *Advances In Atomic, Molecular, and Optical Physics*, pp. 95 – 170, Academic Press, 2000.

[63] D. Budker and M. Romalis, "Optical magnetometry," *Nature Physics*, vol. 3, no. 4, pp. 227–234, 2007.

[64] M. J. Piotrowicz, M. Lichtman, K. Maller, G. Li, S. Zhang, L. Isenhower, and M. Saffman, "Two-dimensional lattice of blue-detuned atom traps using a projected gaussian beam array," *Phys. Rev. A*, vol. 88, p. 013420, Jul 2013.

[65] A. E. Siegman, "Lasers, 4th edition," 1986.

[66] E. Hecht, "Optics, 4th edition," 2001.

[67] K. M. Maller, M. T. Lichtman, T. Xia, Y. Sun, M. J. Piotrowicz, A. W. Carr, L. Isenhower, and M. Saffman, "A Rydberg blockade CNOT gate and entanglement in a 2D array of neutral atom qubits," *ArXiv e-prints*, Jun 2015.

[68] S. Martnez, L. Hernndez, D. Reyes, E. Gomez, M. Ivory, C. Davison, and S. Aubin, "Note: Fast, small, and low vibration mechanical laser shutters," *Review of Scientific Instruments*, vol. 82, no. 4, pp. –, 2011.

[69] R. A. Nyman, G. Varoquaux, B. Villier, D. Sacchet, F. Moron, Y. Le Coq, A. Aspect, and P. Bouyer, "Tapered-amplified antireflection-coated laser diodes for potassium and rubidium atomic-physics experiments," *Review of Scientific Instruments*, vol. 77, no. 3, pp. –, 2006.

[70] A. Gozzini, F. Mango, J. Xu, G. Alzetta, F. Maccarrone, and R. Bernheim, "Light-induced ejection of alkali atoms in polysiloxane coated cells," *Il Nuovo Cimento D*, vol. 15, no. 5, pp. 709–722, 1993.

[71] M. Landini, S. Roy, L. Carcagní, D. Trypogeorgos, M. Fattori, M. Inguscio, and G. Modugno, "Sub-doppler laser cooling of potassium atoms," *Phys. Rev. A*, vol. 84, p. 043432, Oct 2011.

[72] V. Bagnato, D. E. Pritchard, and D. Kleppner, "Bose-einstein condensation in an external potential," *Phys. Rev. A*, vol. 35, pp. 4354–4358, May 1987.

[73] K. K. Das, S. Kim, and A. Mizel, "Controlled flow of spin-entangled electrons via adiabatic quantum pumping," *Phys. Rev. Lett.*, vol. 97, p. 096602, Aug 2006.

[74] D. Ferry, S. Goodnick, and J. Bird, *Transport in Nanostructures.*

[75] A. A. Zozulya and D. Z. Anderson, "Principles of an atomtronic battery," *Phys. Rev. A*, vol. 88, p. 043641, Oct 2013.

[76] S. C. Caliga, C. J. E. Straatsma, A. A. Zozulya, and D. Z. Anderson, "A Matterwave Transistor Oscillator," *ArXiv e-prints*, Aug. 2012.

[77] M. Gajdacz, T. Opatrn, and K. K. Das, "An atomtronics transistor for quantum gates," *Physics Letters A*, vol. 378, no. 2829, pp. 1919 – 1924, 2014.

[78] R. Labouvie, B. Santra, S. Heun, S. Wimberger, and H. Ott, "Negative differential conductivity in an interacting quantum gas," *Phys. Rev. Lett.*, vol. 115, p. 050601, Jul 2015.

[79] F. Giazotto, P. Spathis, S. Roddaro, S. Biswas, F. Taddei, M. Governale, and L. Sorba, "A josephson quantum electron pump," *Nat. Phys.*, vol. 7, p. 857, Nov 2011.

[80] J.-P. Brantut, J. Meineke, D. Stadler, S. Krinner, and T. Esslinger, "Conduction of Ultracold Fermions Through a Mesoscopic Channel," *Science*, vol. 337, pp. 1069–, Aug. 2012.

[81] K. K. Das, "Mesoscopic transport and interferometry with wave packets of ultracold atoms: Effects of quantum coherence and interactions," *Phys. Rev. A*, vol. 84, p. 031601, Sep 2011.

[82] K. K. Das and S. Aubin, "Quantum pumping with ultracold atoms on microchips: Fermions versus bosons," *Phys. Rev. Lett.*, vol. 103, p. 123007, Sep 2009.

[83] J. Avron, A. Elgart, G. Graf, and L. Sadun, "Transport and dissipation in quantum pumps," *Journal of Statistical Physics*, vol. 116, no. 1-4, pp. 425–473, 2004.

[84] K. K. Das, M. R. Meehan, and A. J. Pyle, "Quantum paddlewheel with ultracold atoms in waveguides," *Phys. Rev. A*, vol. 89, p. 063626, Jun 2014.

[85] M. K. Ivory, T. A. Byrd, A. J. Pyle, K. K. Das, K. A. Mitchell, S. Aubin, and J. B. Delos, "Ballistic atom pumps," *Phys. Rev. A*, vol. 90, p. 023602, Aug 2014.

[86] J. B. Delos *Frequent conversational quotes by Prof. John Delos*, 2007-present.

[87] T. A. Byrd, M. K. Ivory, A. J. Pyle, S. Aubin, K. A. Mitchell, J. B. Delos, and K. K. Das, "Scattering by an oscillating barrier: Quantum, classical, and semiclassical comparison," *Phys. Rev. A*, vol. 86, p. 013622, Jul 2012.

[88] G. Floquet, "Sur les équations différentielles linéaires à coefficients périodiques.," *Ann. de l'Éc. Norm. (2)*, vol. 12, pp. 47–89, 1883.

[89] C. Kittel, *Introduction to Solid State Physics.* John Wiley & Sons, 2005.

[90] D. Schrader, I. Dotsenko, M. Khudaverdyan, Y. Miroshnychenko, A. Rauschenbeutel, and D. Meschede, "Neutral atom quantum register," *Phys. Rev. Lett.*, vol. 93, p. 150501, Oct 2004.

VITA

Megan K. Ivory

Megan was raised in the outskirts of Sidman, Pennsylvania and spent much of her early childhood playing in the creek behind her house. Her father was a high school chemistry teacher, and her mother was an animal-loving, geographically challenged thespian. Aside from the nature she discovered in the woods, her earliest exposure to science was dry ice and reconstructed rodents from owl pellets that her mother tolerated displaying atop the living room entertainment system.

As academics drew Megan from the woods and into the classroom, she began to realize she was good at math. If she had been good at art too, she might be an architect right now. But she wasn't good at art, so she decided to stick to the hard sciences instead.

After graduating salutatorian from Forest Hills High School, Megan enrolled at Saint Vincent College in nearby Latrobe, Pennsylvania to study physics. While there, she made Dean's List every semester while participating in the women's Cross Country team as well as the college theater productions. She graduated Summa cum Laud with a BS in physics in 2007.

Before entering graduate school, Megan participated in two summer research excursions during the summers of 2006 and 2007. In 2006, Megan participated in the National Science Foundation's Research Experiences for Undergraduates through the College of William and Mary. She worked under Dr. Gwyn Williams at the Free Electron Laser at JLab to characterize a THz power meter. In 2007, she interned under Dr. Michael Martin at the Advanced Light Source at Lawrence Berkeley National Laboratory to facilitate users

on the IR Beamline and establish a method of remote data acquisition.

Having gained exposure to William and Mary during her REU, Megan eagerly set forth to pursue graduate studies there.